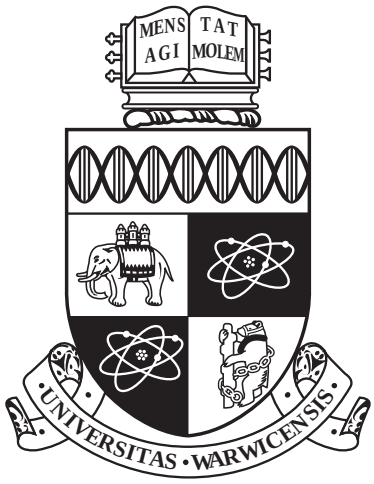

Stellar and planetary remnants in large area surveys

by

Nicola Pietro Gentile Fusillo

Thesis

Submitted to the University of Warwick

for the degree of

Doctor of Philosophy

Department of Physics

September 2015

THE UNIVERSITY OF
WARWICK

O sacrosante Vergini, se fami,
freddi o vigilie mai per voi soffersi,
cagion mi sprona ch'io mercé vi chiami.
Or convien che Elicona per me versi,
e Uranìe m'aiuti col suo coro
forti cose a pensar mettere in versi.

Dante Alighieri
Purgatorio, Canto XXIX

Contents

List of Tables

List of Figures

Acknowledgments

Time is up. After four years my PhD comes to an end. It has been a fantastic time, filled with challenges, sleepless nights and stressful deadlines, but most of all it has been inspiring and rewarding.

For giving me the opportunity to undertake this adventure, I want, first of all, to thank Boris Gänsicke. Thank you for taking me as a student, for teaching me so much, for your inexhaustible patience and, most of all, thank you for never letting my enthusiasm fade.

I also want to thank Joao, Simon and Jon for all the the small and the big things you thought me when I knew nothing. To Sandra, Phil, Penelope and Madelon, thank you for the fun times in the office and for your help in innumerable occasions. To Hristo, Vlad and Teo, thank you for the good times at ING.

For my funding, my thanks go to the Science and Technology Facilities Council and the European Research Council.

Ma niente di tutto quello che ho fatto sarebbe stato possibile senza il continuo supporto di chi mi vuole bene. Mamma, papà, Clementina e Gigia, non potrò mai ringraziarvi abbastanza.

E ad Angela, grazie per essermi stata accanto quando tutto è sembrato insormontabile.

Declarations

I declare that this thesis has not been submitted in any previous application for a higher degree.

Chapters 1−2 provide information gathered from various literatures sources. Chapter 3 outlines some common methods used through this work. In Chapters 4−8, I present my own work. Finally, in Chapter 9, I summarise the results and give an outlook of possible future applications of the presented work.

Chapters 4 is based on (Gentile Fusillo et al., 2015): Gentile Fusillo, N. P.; Gänsicke; B. T., Greiss, S.; "A photometric selection of white dwarf candidates in Sloan Digital Sky Survey Data Release 10", MNRAS, 448, 2260 (2015).

Chapter 5 is based on (Gentile Fusillo et al., 2015): Gentile Fusillo, N. P.; Rebassa-Mansergas, A.; Gänsicke, B. T.; Liu, X.-W.; Ren, J. J.; Koester, D.; Zhan, Y.; Hou, Y.; Wang, Y.; Yang, M.; "An independent test of the photometric selection of white dwarf candidates using LAMOST DR3", MNRAS, 452, 765 (2015).

Chapter 6 is based on the ongoing work towards the construction of a VST ATLAS catalogue of white dwarf candidates. A contribution to this work was made by Dr. Roberto Raddi at the University of Warwick.

Chapter 7 is based on: Gentile Fusillo, N. P.; Hermes, J.J.; Gänsicke, B. T.; "A search for variable white dwarfs in large area time domain surveys: a pilot study in SDSS Stripe 82.", submitted to MNRAS.

Large part of Chapter 8 is based on articles currently in preparation and significant elements of the data analysis were carried out by Prof. Detlev Koester at the University of Kiel and Dr. Jay Farihi at the University College of London.

Abstract

The advent of large-area digital sky surveys marked a turning point for the entire field of astronomy. Today, with multi-band photometry for hundreds of millions of objects readily at hand, the ability to mine data for specific rare objects of interest has become of fundamental importance.

The aim of this work was to study white dwarfs and planetary remnants by, first of all, developing efficient selection algorithms to identify these objects in large area surveys. Using SDSS DR7 we developed a routine which relies on colours and proper motion to calculate *probabilities of being a white dwarf* ($P_{\rm WD}$) which, in turn, enables a flexible selection of white dwarf candidates without recourse to spectroscopy. The application of this selection method to SDSS DR10 lead to the creation of a catalogue of $\simeq 66,000$ bright ($g \leq 19$) objects with calculated $P_{\rm WD}$ from which it is possible to select $\simeq 23,000$ high-confidence white dwarf candidates . The reliability of the method was further tested using a sample of spectroscopic objects from the LAMOST survey. This independent test confirmed the robustness of our algorithm and lead to the identification of 290 new white dwarfs. We also applied our selection routine to the recently released ATLAS DR2 to construct a preliminary catalogue of $\simeq$ 9000 ATLAS white dwarf candidates. This catalogue represents the first sample of white dwarfs candidates in the southern hemisphere.

We later exploited our catalogue in several science project. We developed a separate selection algorithm to identify variable white dwarfs in large area time-domain surveys. To test this method we carried out a pilot search for pulsating white dwarfs using 400 high-confidence white dwarfs candidates with available multi-epoch photometry in SDSS Stripe 82. This test proved the ability of our method to select different types of variable white dwarfs and allowed to identify 5 pulsating white dwarfs, 3 of which are new discoveries.

During the development of our catalogue, we also identified 64 new metal polluted white dwarfs. Recent studies have shown that the metal pollution in these objects is the result of accretion of remnants of planetary systems. In a few cases these planetary remnants form a circustellar debris disc which can be detected as an infrared excess. Here we present the results of high-resolution spectroscopic follow-up of 15 of the newly identified metal-polluted white dwarfs. Using accurate spectral analyses of the atmospheres of these white dwarfs we determined chemical compositions and masses of the accreted bodies, and discuss the impact of these finding on the current knowledge of extra-solar planetary systems. Using optical and infrared photometric data from various large-area surveys we carried out a search for infrared excess around our newly identified metal polluted white dwarfs, and high-confidence white dwarf candidates. We identified four metal polluted white dwarfs with possible debris discs and compiled a list of $\simeq$ 300 white dwarfs candidates with infrared excess ready for future spectroscopic follow-up.

Abbreviations

4MOST	4m Multi-Object Spectrograph
Al	Aluminium
BD	Brown Dwarf
CCD	Charge-Coupled Device
C	Carbon
Ca	Calcium
Cr	Chromium
CSS	Catalina Sky Survey
CV	Cataclysmic Variable
DxZ	Metal polluted white dwarf
ELM	Extremely Low-Mass
ESO	European Southern Observatory
Fe	Iron
FUV	Far-Ultraviolet
H	Hydrogen
He	Helium
IR	Infrared
ISIS	Intermediate dispersion Spectrograph and Imaging System
ISM	Interstellar medium
LAMOST	Large Sky Area Multi-Object Fibre Spectroscopic Telescope
LSST	Large Synoptic Survey Telescope
LT	Liverpool Telescope
Mg	Magnesium
MJD	Modified Julian Date
MS	Main Sequence
Ne	Neon
Ni	Nickel
NLHS	Narrow Line Hydrogen Star
NUV	Near-Ultraviolet
O	Oxygen
Pan-STARRS	Panoramic Survey Telescope and Rapid Response System
PTF	Palomar Transient Factory
P_{WD}	Probability of being a white dwarf
QSO	Quasar

RPM	Reduced Proper Motion
SDSS	Sloan Digital Sky Survey
SED	Spectral Energy Distribution
Si	Silicon
Ti	Titanium
UKIDSS	UKIRT Infrared Deep Sky Survey
UVB	Ultraviolet-Blue
VHS	Vista Hemisphere Survey
VIS	Visible
VLT	Very Large Telescope
WD	White Dwarf
WEAVE	WHT Enhanced Area Velocity Explorer
WDMS	White Dwarf Main Sequence binary
WHT	William Herschel Telescope

Chapter 1

Introduction

1.1 Brief overview of stellar evolution

Even by simply turning our eyes at night sky we can immediately see that the stars that surround us are in many ways different from each other. The astronomical tools at our disposal today allow us to explain these observed diversities in term of differences in physical parameters like mass, size, temperature and age.

One of the most powerful tools which has historically been used to distinguish between different classes of stars is the Hertzprung-Russell (H-R) diagram. Developed independently by Ejnar Hertzsprung in 1911 and Henry Norris Russell in 1913, it is a plot of temperature (or either spectral type or $B-V$ colour) against luminosity (or absolute magnitude). On this plot stars in different evolutionary states occupy distinct regions, such that the life cycle of a star can be described as a "path" on the H-R diagram.

Broadly speaking the entire life cycle of a star can be described by the processes that take place in its core. Stellar life begins with a gas cloud. In order to trigger star formation, the gas cloud has to contain enough mass to initiate spontaneous gravitational collapse. This minimum mass requirement is known as the Jeans mass (Jeans, 1902) and is given by the equation:

$$M_{\mathrm{J}} \simeq \left(\frac{5kT}{G\mu m_{\mathrm{H}}}\right)^{3/2} \left(\frac{3}{4\pi\rho_0}\right)^{1/2} \tag{1.1}$$

where k is Boltzman's constant, T is the temperature of the gas, G is the gravitational constant, μ is the mean molecular weight, m_{H} is the mass of the hydrogen atom and ρ_0 is the initial mass density of the cloud. If this condition is met the gas cloud begins to collapse, becoming denser and opaque to its own radiation. During this stage the mass of gas bound by self-gravity is known as a protostar. If the mass

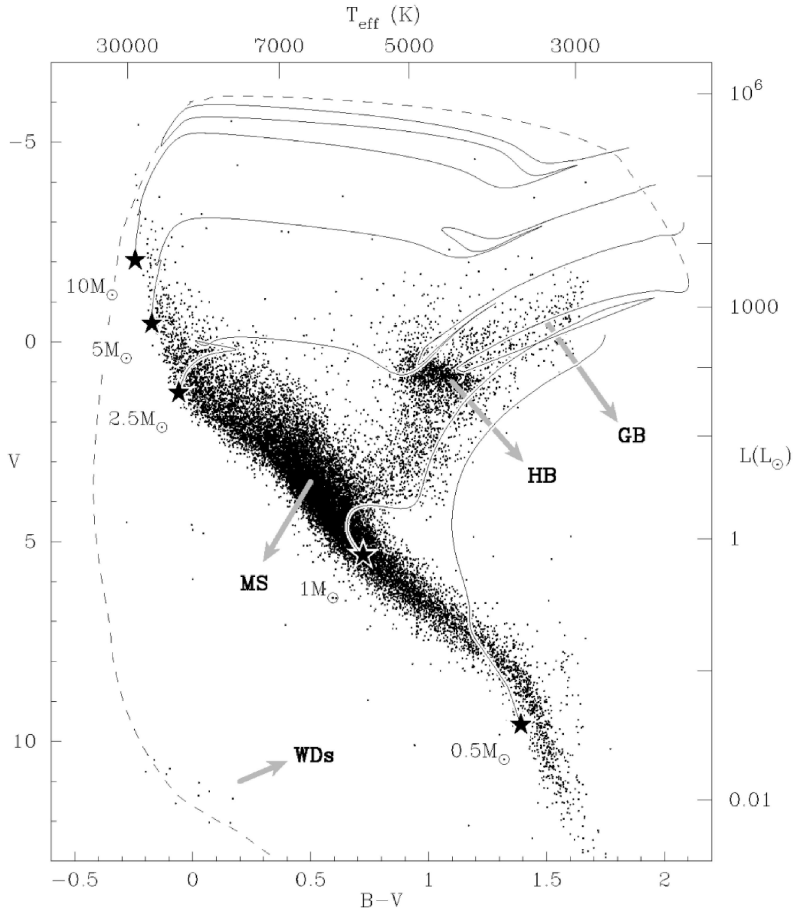

Figure 1.1: The Hertzprung-Russell diagram based on Hipparcos data of 20546 nearby stars. The arrows indicate the locii of the main sequence (MS), horizontal branch (HB), giant branch(GB) and white dwarfs (WDs). The diagram also includes evolutionary tracks up to the giant branch (solid lines) for stars with different main-sequence masses and up to a white dwarf (dashed line) for a $1\,M_\odot$ star. Courtesy of Marc van der Sluys.

of the protostar is below the critical value of $0.08M_\odot$, temperature and pressure in the core will not be sufficient to initiate nuclear fusion of hydrogen (H) into helium (He) while these low-mass objects will still undergo a phase deuterium burning in their core, they will not evolve as main-sequence stars. These "failed stars" are called brown dwarfs (BD) and are simply destined to cool down and fade into darkness (Laughlin & Bodenheimer 1993, Nakajima et al. 1995, Palla 2013). If, on the other hand, the minimum mass limit is reached, nuclear fusion of hydrogen will ignite in the core, and a new star is born. Once the outward pressure from the fusion reaction in the core and the gravitational forces driving the collapse of the gas reach a stable balance, the size of star settles and the star begins its lifetime on the main sequence. On the H-R diagram (Fig. 1.1) the main sequence runs diagonally across from cool, small, low-mass stars in the bottom-right, to the most massive, large, hot stars in the top-left. All stars spend the majority of their lifetime on the main

sequence (Hurley et al., 2000), but how long a star will stay on the main sequence and how it will evolve afterwords depends on the mass of the star. On the main sequence, stars continue to burn hydrogen and build up a He core and the reaction rate of these fusion processes strongly depends on the star's core temperature which, in turns, increases with increasing stellar mass. As a result, more massive stars age faster than less massive ones. Our Sun will spend approximately 10 billion years on the main sequence while the most massive stars will leave it after only few million years.

Once a main sequence star has depleted a significant fraction of the hydrogen reservoir in its core, the outward pressure will become unable to counters the gravitational inward pull. As a result the core starts to contract while its outer layers expand and cool down. At this stage the star leaves the main sequence and becomes a much larger cooler object: a red giant. in Fig. 1.1 these objects populate the so called giant branch: the sequence which sharply turns to the right of the main-sequence in the upper part of the diagram, i.e cool but very luminous stars.

As the temperature of the contracting core rises, hydrogen fusion continues in a narrow shell around the core itself (Prialnik, 2000). If the initial mass M of the star was $0.1\mathrm{M}_{\odot} \lesssim M \lesssim 0.7\mathrm{M}_{\odot}$ this shell burning will be the only active fusion process and the star will only ever develop a low-mass He core. However these low-mass stars evolve so slowly that none of them has left the main-sequence within the age of Galaxy (see Sect. 1.2).

On the other hand, in more massive stars the growing He cores will reach sufficiently high temperatures and pressures to fuse He into carbon (C) and oxygen (O). In stars with masses between $0.8\,\mathrm{M}_{\odot}$ and $2.0\,\mathrm{M}_{\odot}$ the necessary temperature is only achieved after extreme compression of the He core. Under such high pressure the gas in the core becomes degenerate before He fusion can be initiated. In a degenerate gas the pressure of is only dependent on the gas density and not on temperature. As a result, when, eventually, the temperature becomes high enough, nuclear fusion of the degenerate core is initiated in a thermally unstable process. The temperature rises dramatically, but the core does not expand causing the fusion to progress at extremely high reaction rate. In a short amount of time this process, known as helium flash, releases several thousand times more energy than fusion in non-degenerate material. This sudden energy outburst lifts the degeneracy of the gas allowing the core to adjust its size to match the increased temperature (Prialnik, 2000). In more massive stars the He core does not become degenerate and fusion can be initiated at a steady state. Eventually the He reservoir will also be depleted and fusion will stop. Without any internal pressure support, the core of these stars

shrink to an Earth sized radius, supported by electron degeneracy (see Sect 1.2). The outer layers of the star begin to expand and are slowly ejected until the small, hot, blue core is exposed. As the core continues to shrink, it also becomes hotter and, as a consequence, the star evolves with nearly constant luminosity moving across the top of the H-R diagram from right to left. This brief evolutionary phase takes the name of planetary nebula and its characterized by high mass loss, rapid cooling and ionization of the ejected gas by the ultraviolet emission from the hot central stellar remnant. As the central stars of planetary nebulae cool down, they move to the bottom-left corner of the H-R diagram (Fig. 1.1) and become known as white dwarfs. These stars are the object of study of this thesis and are described in more details in the next sections.

The most massive stars in the Universe face instead a more dramatic end. In stars with masses $M \gtrsim 10$ M$_\odot$ fusion continues beyond C and O creating neon, magnesium, silicon and iron in concentric shells around the core. The iron core becomes degenerate and keeps growing until it reaches a mass of $M_{\rm core} = 1.4$M$_\odot$ when even the electron degeneracy pressure can no longer counter the gravitational collapse (see Sect. 1.2). As a result the core begins to contract, the pressure becomes so high that all protons in the nuclei undergo electron capture, absorbing all electrons, and forming neutrons. In less than a second all that is left of the stellar core is a ball of neutrons about 10 kilometers in radius, supported by neutron degenerate pressure. The outer layers, which still contain most of the mass of star, free fall onto the newly formed neutron star heating up to billions of degrees and eventually rebounding off the extremely dense core. The outer layers are then ejected into space, in one of the brightest phenomena in the Universe: a core-collapse supernova explosion. As the supernova remnant keeps expanding in a cloud of stellar debris, only the small neutron star is left behind.

For few extremely massive stars the gravitational forces are able to overcome even the neutron degenerate pressure and star collapses in an object so dense not even light can escape its surface: a black hole. However several factors may influence whether as star will evolve into a neutron star or a black hole (e.g. rotation, metallicity) and the minimum main-sequence mass required to form a black hole is still very uncertain, raging from 25M$_\odot$ to over 100M$_\odot$ (Heger et al., 2003).

1.2 White Dwarfs

White dwarfs (WD) are the stellar remnants left over from the evolution of stars with main sequence masses $M > 0.8$M$_\odot$ and $M \leq 8 - 10$M$_\odot$ (Iben et al., 1997;

Smartt et al., 2009; Doherty et al., 2015). This mass range includes over 90% of all the stars in the Galaxy, making white dwarfs by far the most common stellar remnants. The other end products of stellar evolution, neutron stars and black holes, descend from much rarer massive stars and only constitute small minority. White dwarfs are small dense objects with radii similar to that of the Earth, and an average mass of $0.6\mathrm{M}_{\odot}$ (see Sect. 1.2.1). Unlike main-sequence stars, in white dwarfs the inward gravitational force is not countered by the pressure from fusion processes, but the star is instead supported by electron degeneracy pressure. The Pauli Exclusion Principle dictates that two electrons cannot simultaneously be in the same phase space and occupy the same quantum state. This leads to an effective outward pressure which in white dwarfs opposes the gravitational collapse. However there exist a maximum mass limit at which electron degeneracy pressure will no longer be able to counteract the gravitational force. This maximum mass is known as the Chandrasekhar limit ($1.44\,M_{\odot}$, Chandrasekhar 1931) and it is the threshold value which determines whether a star will evolve into a white dwarf or undergo a core collapse supernova event. Several unique properties of white dwarfs make them extremely interesting objects with possible science applications in many, diverse fields.

Astronomical laboratories: The structure, temperature, intense gravities, densities and magnetic fields of white dwarfs create some of the most extreme environments in astrophysics. White dwarfs can therefore be used as "astronomical laboratories" to test physics under conditions which cannot be achieved on Earth.

Stellar evolution: Since they descend from progenitors with main sequence masses $M > 0.8\mathrm{M}_{\odot}$ and $M \lesssim 8 - 10\mathrm{M}_{\odot}$, white dwarfs allow to study the final stages of the evolution of main sequence stars spanning this entire mass range. Our own Sun will one day evolve into a white dwarfs and the study of these objects lets us glimpse into the distant future of our solar system. The initial-to-final mass relationship of white dwarfs links the mass of a white dwarf with that of its main-sequence progenitor and this function is of paramount importance to understand mass loss in stellar evolution, determining the ages and distance of globular clusters and studying the chemical evolution of the Galaxy (e.g. Bragaglia et al. 1995; Ferrario et al. 2005; Catalán et al. 2008).

Astronomical clocks: White dwarfs are no longer powered by internal fusion reactions, and are therefore destined to simply cool down and decrease in luminosity. Since the supporting pressure in white dwarfs it is not dependent on temperature, they cool with nearly constant radius. Thanks to this property white dwarfs evolution can be described by a relatively simple cooling law (Mestel, 1952):

$$L(t)/\mathrm{L}_{\odot} = (2.3 \times 10^{-3}) \times M \times t^{-7/5} \tag{1.2}$$

where the mass, M, is expressed in solar units the time, t, in Gyrs. Equation 1.2 shows that the age of white dwarfs can therefore be directly deduced from their luminosity implying that white dwarfs can be used as reliable astronomical clocks and effectively trace the stellar formation history of Galaxy (e.g. Oswalt et al. 1996, Fontaine et al. 2001).

Low-mass companions: The intrinsic low luminosities of white dwarfs makes them perfect targets for searches of faint low mass companions. Such searches allow to probe the low end of the companion mass distribution and constrain the luminosity function of low-mass stars (e.g. Probst 1983a,b).

Planetary remnants: Some rare types of white dwarfs with traces of metal pollution in their atmospheres can even be used to characterize the composition of extra solar planetary systems (e.g. Alcock et al. 1986; Jura et al. 2012, see Chapter 8)

SN Type Ia progenitors: Supernovae Type Ia are extremely bright explosion events which trigger when a white dwarf somehow grows in mass and exceeds the Chandrasekhar limit. The use of Supernovae Type Ia as standard candles is one of the keystones of modern cosmology (Riess et al., 2000; Perlmutter et al., 1999). However the exact nature of the progenitor objects, whether a white dwarf accreting from a non degenerate companion, or a merger of two white dwarfs, is still matter of debate.

1.2.1 Structure and Mass distribution.

Even though there exists some diversity in the core and atmospheric composition of white dwarfs, their structure is overall very similar: in the center a highly degenerate core containing over 99.99% of the mass of the white dwarf (normally composed mostly of C/O), a surrounding non-degenerate layer of He and, finally, a thin H atmosphere (if all H was not consumed in the late stages of the progenitor evolution, Wood 1995; Althaus et al. 2013, Fig 1.2, Sect. 1.2.2). This clear differentiation of elements according to their atomic weight is a consequence of *gravitational settling*: the high surface gravity of white dwarfs causes heavy elements to rapidly sink such that the outer atmospheres can only be composed of the lightest elements (Fontaine & Michaud, 1979; Koester, 2009). However, not all white dwarfs have atmospheres completely dominated by gravitational settling. In hot white dwarfs photons carrying outward energy from the hot core are absorbed by metals in the atmosphere, effectively lifting them outward against gravitational settling. This phenomenon

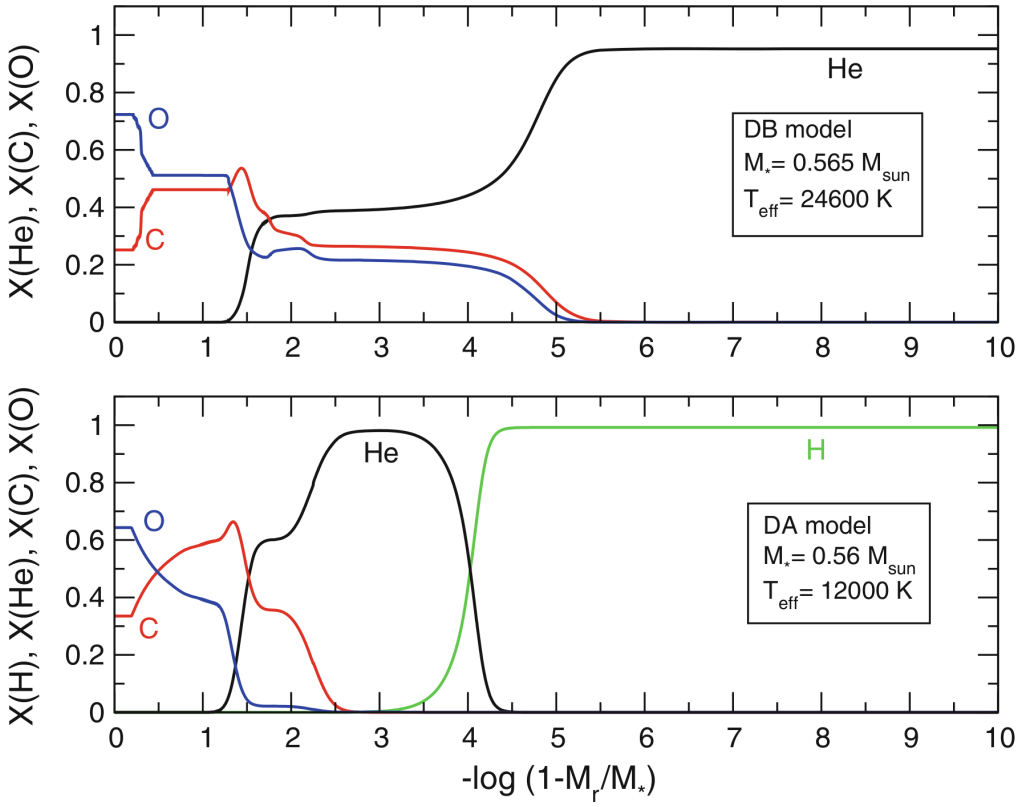

Figure 1.2: Cross section of the internal structure of a typical He-atmosphere (DB, top panel) and a typical H-atmosphere white dwarfs (DA, bottom panel). The letter X indicates the relative fraction of oxygen (O), carbon (C), helium (He)and hydrogen (H). The x-axis indicates the logarithm of the fractional mass depth, with the core of the white dwarf on the left and outer layers on the right. On this scale, the observable outer layers of the atmospheres are at values of 10 to 15, outside the right edge of the figure (Althaus et al., 2010).

is known as *radiative levitation* and, at $T_{\rm eff} \gtrsim 25,000\,{\rm K}$, it can sustain significant amounts of heavy elements in the outer atmosphere of a white dwarf (Chayer et al., 1995). At the other end of the temperature scale, cool white dwarfs develop convection zones which prolong the sinking timescales of heavy elements, and possibly dredge up core material (see Sect. 1.2.2).

As stated before, the majority of white dwarfs have a mass of $\simeq 0.6\,{\rm M}_{\odot}$, as measured from large samples of white dwarfs (Fig. 1.3). However, this mass distribution shows that, despite the strong peak at $\simeq 0.6{\rm M}_{\odot}$, the actual mass range spanned by the known population of white dwarfs is quite wide. Indeed different evolutionary scenarios can produce white dwarfs with masses ranging between 0.2 and 1.3 $\rm M_{\odot}$ (Brown et al. 2010, 2012; Dupuis et al. 2003).

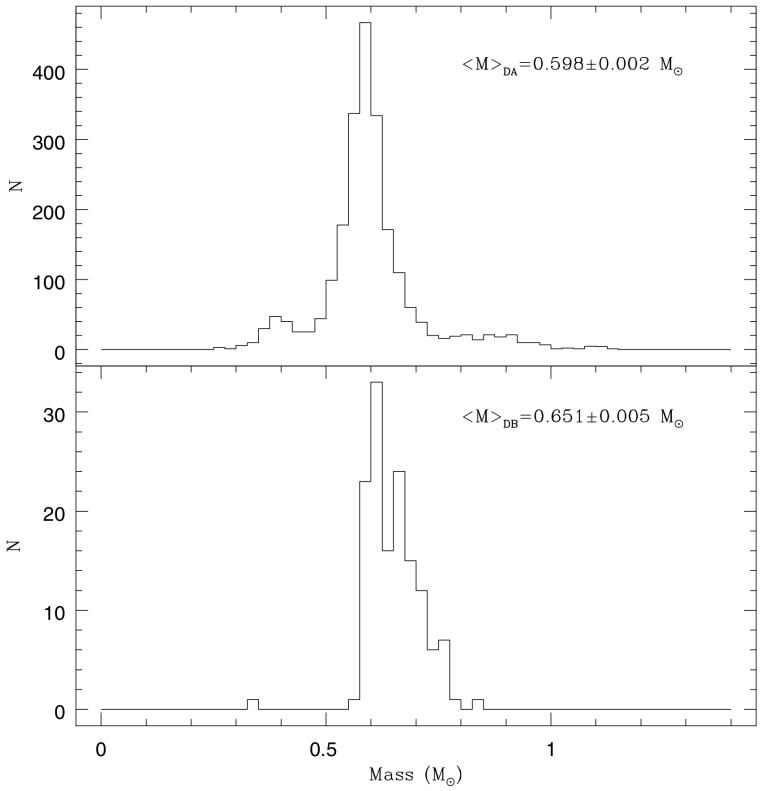

Figure 1.3: Mass distribution of the spectroscopic white dwarf sample from the seventh data release (DR7) of the Sloan Digital Sky Survey (SDSS). The top panel shows the mass distribution of H atmosphere (DA) white dwarfs with $T_{\rm eff} > 13,000$K. The bottom panel shows the mass distribution of He atmosphere (DB) white dwarfs with $T_{\rm eff} > 16,000$K. The labels indicate the mean white dwarf mass (Kleinman et al., 2013).

The low-mass end of the distribution is populated by He-core white dwarfs. As briefly mentioned above, main sequence stars with masses $\lesssim 0.7 M_\odot$ never initiate He fusion and eventually end their evolution as He core white dwarfs. However, their evolution proceeds extremely slowly, and their main-sequence lifetimes exceed the current age of the Galaxy ($\simeq 10$ Gyr Weidemann 2000). In fact, the observed population of low-mass white dwarfs is the result of evolution in interacting binaries (Marsh et al., 1995; Brown et al., 2010). The progenitors of these white dwarfs lost a fraction of their mass via interaction with the binary companion, eventually becoming unable to sustain fusion in their core. This process affectively truncated their evolution before He fusion could take place, leading to the formation of a He-core white dwarf.

The most massive white dwarfs, responsible for the high-mass tail in Fig 1.3, can have core compositions different from the majority of other white dwarfs. These

white dwarfs are either, the result of mergers (Giammichele et al., 2012; Rebassa-Mansergas et al., 2015) or descend from the highest mass progenitors which do not become core collapse supernovae ($\sim 8 - 10\,M_{\odot}$). In the core of these massive progenitors fusion can generate significant amount of Ne and the resulting massive white dwarf has a core dominated by O and Ne rather than C and O. However, because nearly all white dwarfs are shrouded in pristine H or He atmospheres, it is extremely difficult to actually probe the composition of their cores. Astroseismology of pulsating white dwarfs provides a valuable tool to peek past this outermost layer (see Sect 7.1.1), and the recent discovery of O rich white dwarfs, provided direct evidence of the O/Ne (rather than C/O) composition of the core of massive white dwarfs (Gänsicke et al., 2010).

1.2.2 Atmospheres and spectral classification

Since spectroscopic observation of white dwarfs can only reveal informations about the thin external atmosphere, white dwarf classification is based on the apparent composition of the star outermost layer (Sion et al., 1983).

Hydrogen atmosphere white dwarfs: DA

About 80 per cent of all, both young and old, known white dwarfs (Kleinman et al., 2013; Giammichele et al., 2012) have spectra dominated by pressure broadened Balmer lines from hydrogen absorption. These pure-hydrogen atmosphere white dwarfs are called DAs, and are found over a very large range of effective temperatures, from about 6000 K to over 100,000 K (Fig. 1.4). At temperatures below $\simeq$ 6000 K, H atoms have no electrons in the first excited state and hence Balmer series transitions are not possible. Once a DA cools down to these temperatures, its spectrum becomes featureless and the star is then classified as a DC. The shape and depth of the Balmer lines are particularly sensitive to temperature and pressure and fitting them with atmospheric models allows accurate measurement $T_{\rm eff}$ and $\log g$ of DA white dwarfs (Fig. 1.5, Koester et al. 1979; Weidemann & Koester 1984; Bergeron et al. 1992b; Rohrmann 2001; Koester 2010; Tremblay et al. 2013). Despite the relative simplicity of the structure of DA white dwarfs, atmospheric model fitting is a complex technique. As DA white dwarfs cool down to $T_{\rm eff} \simeq 13,000$ K they start to develop convection zones and accurate modelling of the energy transfer under these conditions is necessary to correctly estimated atmospheric parameters (Fig. 1.6, Bergeron et al. 1992b; Tremblay & Bergeron 2008). The most up-to-date atmospheric models account for convective mixing, as well as other physical phe-

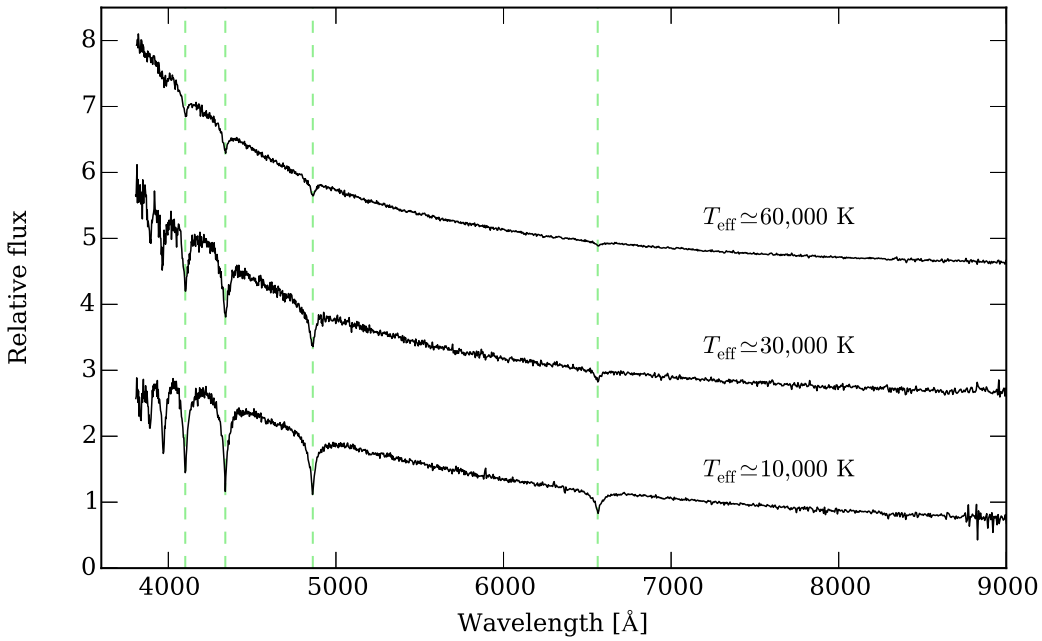

Figure 1.4: Sample SDSS spectra of DA white dwarf with different $T_{\rm eff}$. The characteristic broadened hydrogen absorption profiles are marked by the green dashed lines.

nomena, and their use in determination of atmospheric parameters is one of the cornerstones of white dwarf research.

Helium atmosphere white dwarfs: DO and DB

White dwarfs which exhibit spectra dominated by helium absorption features are subdivided into two categories. Hot helium rich white dwarfs ($T_{\rm eff} = 100,000 - 45,000\,{\rm K}$) normally have spectra dominated by single ionized helium and are known as DOs. Cooler helium rich white dwarfs with $T_{\rm eff}$ down to $\simeq 12,000\,{\rm K}$ mostly show absorption from neutral helium and are classified as DB (Fig. 1.7). The progenitors of DBs are believed to be DAs with thin H layers which transform into helium-atmosphere white dwarfs as convective mixing dilutes the hydrogen. (Fontaine & Wesemael, 1987). This formation scenario implies that DBs can only form once convection in thin-layer DAs becomes significant, so no hot DBs should exist. Indeed there is evidence of a so called "DB gap", a lack of observed DBs between the coolest DOs with $T_{\rm eff} \simeq 45,000\,{\rm K}$ and the hottest DBs with $T_{\rm eff} \simeq 30,000\,{\rm K}$ (Fig 1.12). However, in recent years, mostly thanks to SDSS some extremely hot DB stars have been discovered and the gap is beginning to fill (Eisenstein et al., 2006). Although the DB gap is still only sparsely populated there must exist a

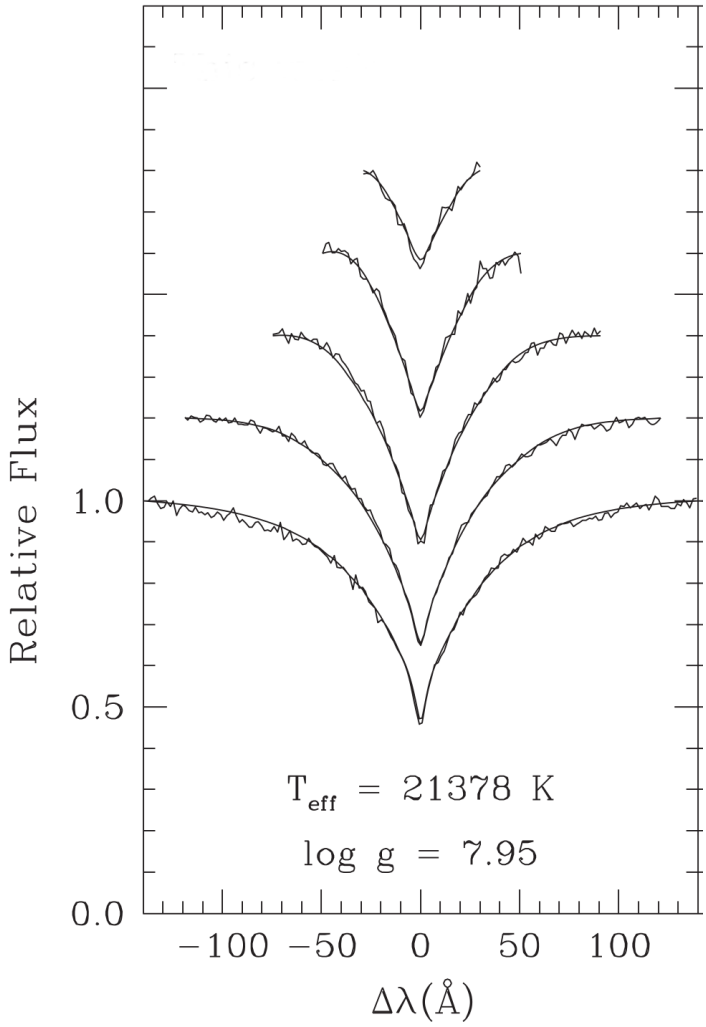

Figure 1.5: Example of a model fit to the Balmer lines of DA white dwarf (WD 0205+250) in order to estimate the atmospheric parameters, $T_{\rm eff}$ and $\log g$ (Tremblay & Bergeron, 2009).

separate formation channel for these extremely hot DBs. According to current theories a small fraction of white dwarf stars are born with negligible amounts of H in their envelope and simply have He dominated atmosphere for their entire evolution (Bergeron et al., 2011). Analogously to DAs, as they cool down, DB white dwarfs also develop convective atmospheres and eventually evolve into DCs. However in DB white dwarfs both effects happen at considerably higher temperatures, with convection becoming dominant at $T_{\rm eff} \simeq 30,000\,{\rm K}$ (Fig. 1.6) and the spectrum becoming featureless at $T_{\rm eff} \simeq 12,000\,{\rm K}$ (Bergeron et al., 1997).

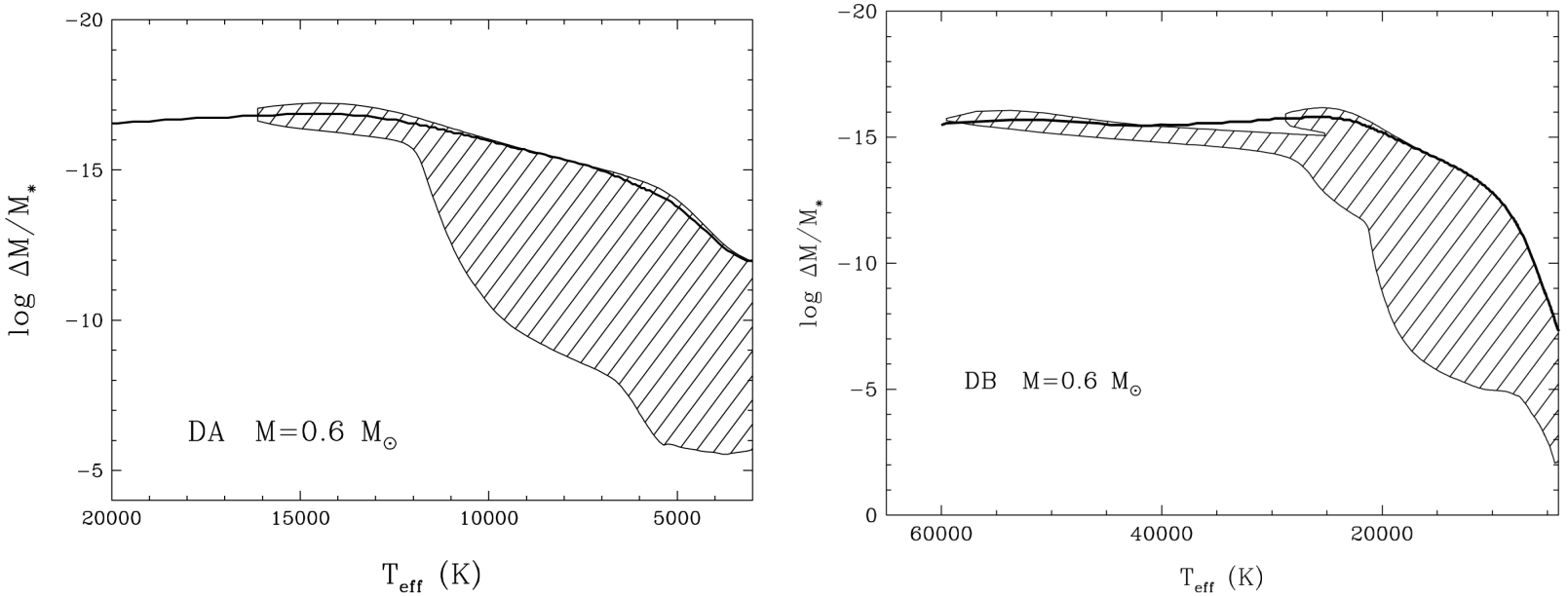

Figure 1.6: Location of the hydrogen convection zone (shaded area) for a 0.6 $M_{\odot}$ DA white dwarf (*left panel*) and of the He convection zone for a 0.6 $M_{\odot}$ DB white dwarf (*right panel*) as a function of $T_{\rm eff}$. The y-axis expresses the mass fraction M and the solid line indicates the location of the photosphere (Dufour et al., 2007b; Bergeron et al., 2011).

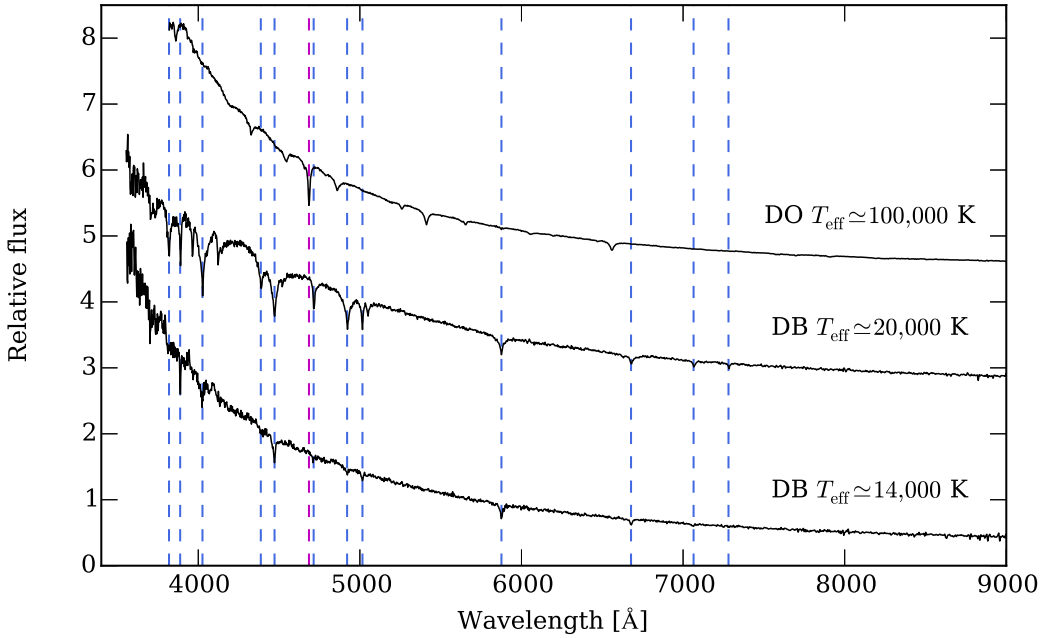

Figure 1.7: Sample SDSS spectra of two DB and one DO white dwarf. The neutral He and HeII absorption lines are marked by the blue and magenta dashed lines respectively.

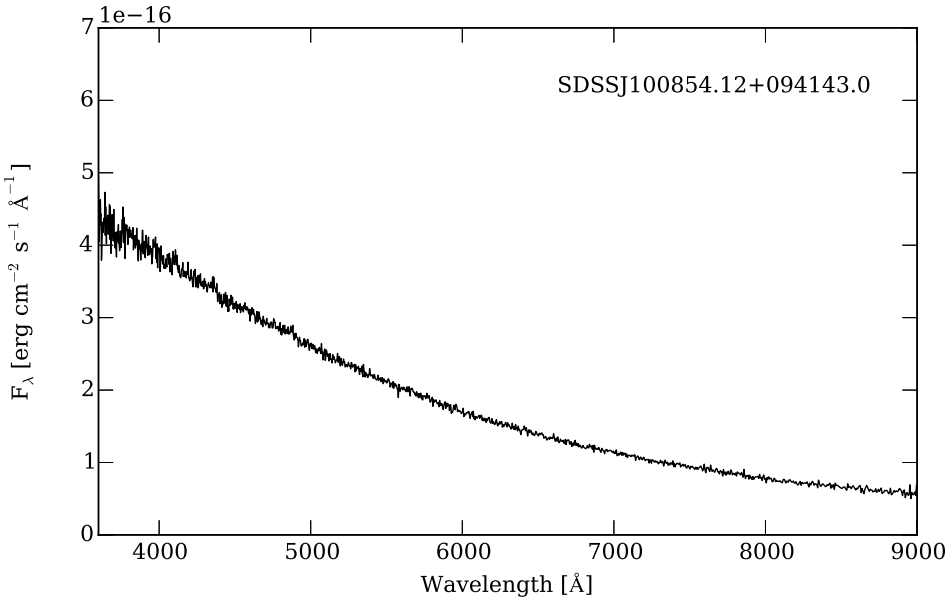

Figure 1.8: Sample SDSS spectrum of a featureless DC white dwarf.

Carbon atmosphere white dwarfs: DQ

White dwarfs which show carbon absorption features in their spectra are assigned the spectral type DQ. This rare class of white dwarf appears to be divided into two distinct sub-classes: cool DQ ($T_{\rm eff} < 11,000\,{\rm K}$, characterized by the presence molecular of C_2 Swan bands), and the even rarer *hot* DQ ($T_{\rm eff} \approx 18,000 - 24,000\,{\rm K}$ characterized by atomic C absorption). Cool DQs have He rich atmospheres and are believed to descend from DB white dwarfs where the C is dredged-up to the surface from the core by the deepening He convection zone (Pelletier et al., 1986; Koester & Knist, 2006; Dufour et al., 2007a). Similarly, in the recently discovered O dominated white dwarfs (here provisionally called DG), the atmospheric O is thought to be dredged-up from an O/Ne core (Fig. 1.10, Gänsicke et al. 2010). *hot* DQ white dwarfs, however, are found in a temperature range where DBs are still too hot to develop convection zones deep enough to dredge-up C. The origin of *hot* DQs is still matter of debate, but the most supported theory is that *hot* DQs descend from a peculiar type of progenitors of which H1504+65 is the archetype (Werner, 1991). H1504+65 is essentially a bare stellar nucleus produced by a particularly violent post-asymptotic-giant-branch very late thermal pulse that has removed in large part the remaining stellar envelope containing helium and hydrogen. The resulting descendant of H1504+65 would therefore be a white dwarf with an extremely small He layer and a large amount of C mixed in atmosphere (Dufour et al., 2007a). Recently Dunlap & Clemens (2015) proposed that *hot* DQs could instead form in the mergers of C/O-core white dwarf that were not tuned to explode as type Ia supernovae.

Metal polluted white dwarfs: DZ

White dwarfs which show traces of heavy elements (other than carbon) in their otherwise featureless optical spectra are collectively known as DZ. These objects are typically cool He-rich white dwarfs with $T_{\rm eff} < 12,000\,{\rm K}$ (as above this temperature He absorption would become visible in their spectra) characterized by the presence of the CaII H and K absorption lines (Fig. 1.11 Sion et al. 1990; Dufour et al. 2007b).

As mentioned before, the high surface gravity of white dwarfs causes heavy elements to rapidly sink to the bottom layers of the atmosphere, so presence if metals in DZs is not the result of a particular formation channel or of the natural evolution of the white dwarfs (Fig 1.12). This atmospheric composition is, in fact, the result of ongoing (or recent) accretion of tidally disrupted planetesimals (Koester & Wolff, 2000; Jura, 2003; Farihi et al., 2010b) . The origin of the accreted metals and the

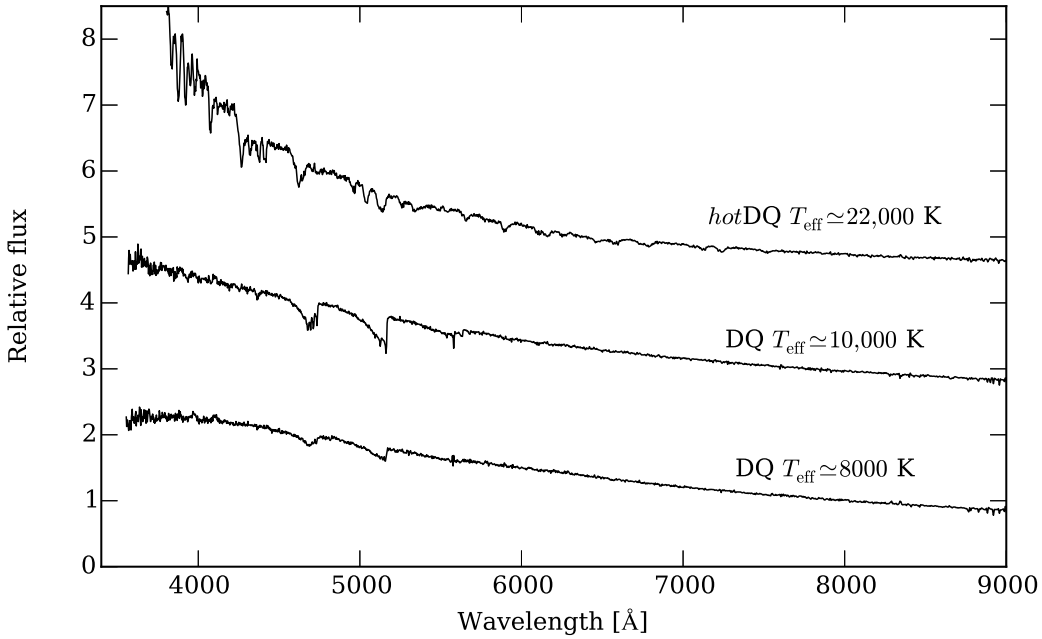

Figure 1.9: Sample SDSS spectrum of two DQ white dwarfs and one *hot* DQ. The two cooler DQs show broad C_2 absorption bands while the *hot* DQ exhibit atomic C absorptions.

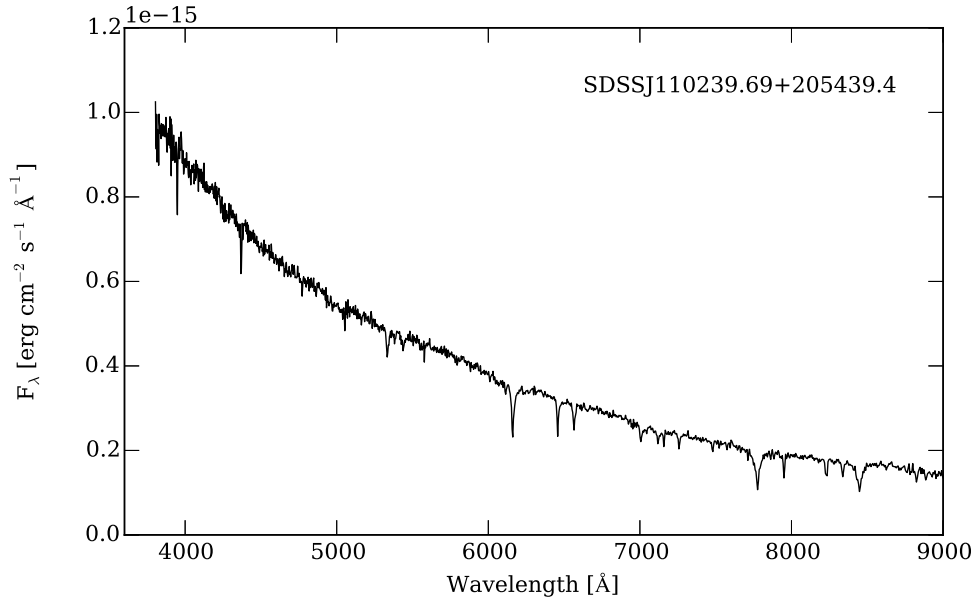

Figure 1.10: SDSS spectrum of SDSSJ110239.69+205439.4, one of the only three O rich white dwarfs known to date (here provisionally called DG).

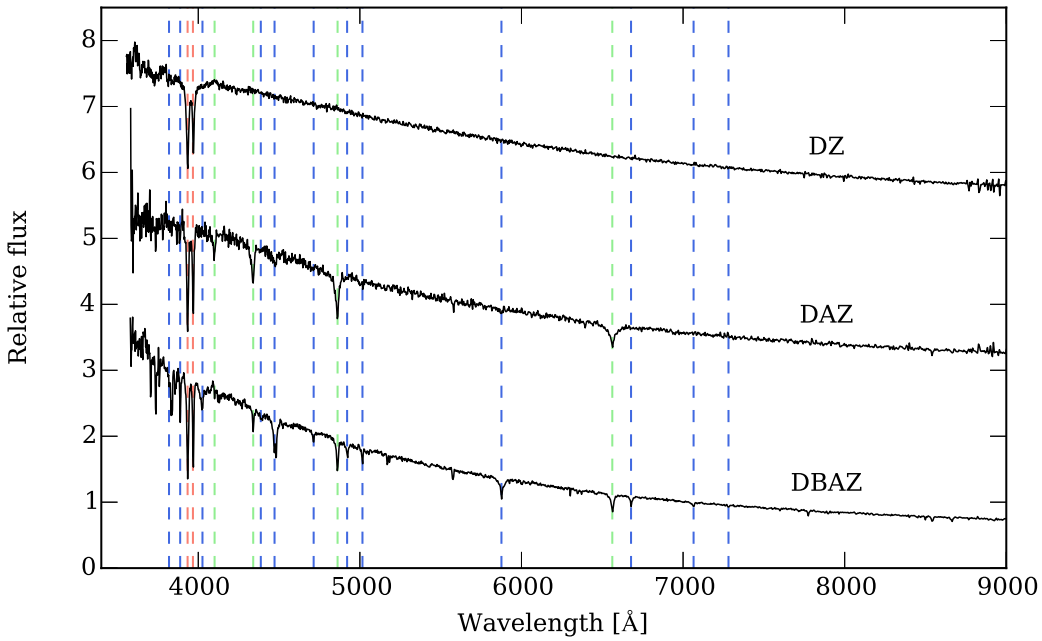

Figure 1.11: Sample SDSS spectra of a DZ, a DAZ and a DBAZ white dwarf. The spectrum of the hybrid type white dwarfs shows the presence of hydrogen (D**A**Z; DB**A**Z, green lines), helium (D**B**AZ, blue lines) and calcium (DA**Z**; DBA**Z**, red lines)

applications of DZs to exo-planet characterization are discussed in more detail in Chapter 8. The majority of known DZs have $T_{\rm eff} \gtrsim 6500\,{\rm K}$ (Dufour et al., 2007a), however Koester et al. (2011) unveiled the existence of a significant population of cool DZ with $T_{\rm eff} < 6000\,{\rm K}$. As a consequence of their strong metal pollution these cool DZs have unusual colours and spectra for white dwarfs and had been overlooked until recently.

Finally some white dwarfs may show in their spectra the defining features of more than one class (e.g. Balmer lines and CaII H and K doublet.). These hybrid objects are classified with the multiple letter classes, e.g. DAB, DBA, DAO, DAZ, DBZ and DABZ (Fig. 1.11) where the first letter denotes the visually most dominant element. However, it is important to underline that the element with the most dominant features in the spectrum may not be the main constituent of the white dwarf atmosphere. Archetypal examples are the white dwarfs GD 16 (Koester et al., 2005a) and GD 17 (see Chapter 8) which have spectra dominated by H, but are in fact He atmosphere white dwarfs.

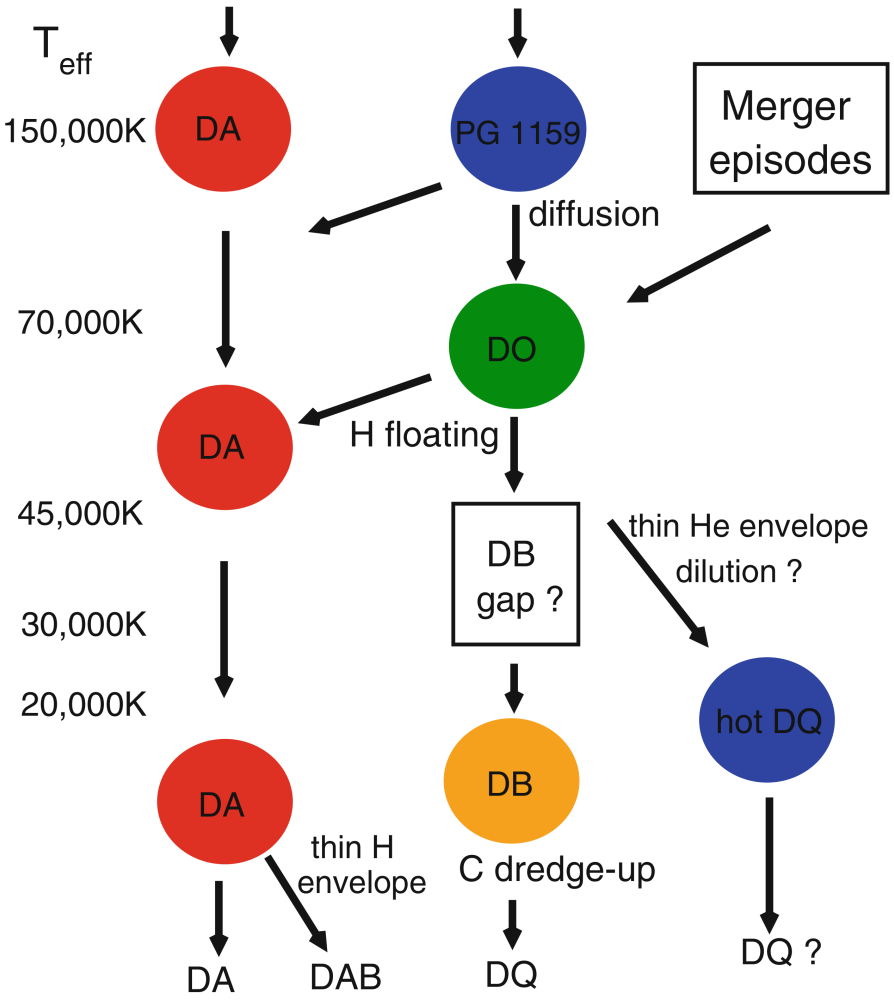

Figure 1.12: Schematic of possible evolutionary paths of white dwarf spectral types (Althaus et al., 2010). The left column indicates the effective temperature.

Other white dwarf classifications

A number of suffixes exist to denote specific subtypes of white dwarfs like the "H" suffix denoting magnetic white dwarfs with Zeeman splitting in their spectra, or the "V" suffix denoting pulsating white dwarfs (see Chapter 7). The full spectral naming convention of white dwarfs is summarized in Table 1.1.

Table 1.1: White dwarf spectral types naming convention (Sion et al., 1983; Koester, 2013)

Spectral type	Defining features	Temperature range [K]
DA	Balmer lines	100,000 - 6,000
DB	HeI lines	30,000 - 10,000
DC	Featureless continuum	$\lesssim$ 10,000
DZ	Metals lines only	-
DO	strong HeII lines	$>$ 45,000
DQ	C_2 Swan bands	$<$ 11,000
hot DQ	Atomic C lines	24,000 - 18,000
P	Magnetic white dwarfs with detected polarization	-
H	Magnetic white dwarfs with Zeeman splitting	-
X	Peculiar or unclassifiable spectrum	-
E	Emission lines are present	-
?	Uncertain assigned classification a colon (:) may also be used	-
V	Symbol to denote variability	-

Chapter 2

Astronomical observations and methods

2.1 Magnitudes ad photometry

In astronomy the brightness of celestial objects is commonly measured in units called magnitudes. This unit of measurement finds its roots in the work of the Greek astronomer Hipparchus who classified stars by their apparent brightness or perceived "size", hence magnitude. The magnitude scale was therefore chosen to keep some consistency with ancient tradition, but today it has necessarily acquired a formal definition.

Stellar flux is defined as the power received from an object at Earth per unit area. Magnitudes are a measurement, on a logarithmic scale, of the ratio of the stellar flux received from two objects, and are defined as:

$$m_1 - m_2 = -2.5 \log_{10} \left(\frac{F1}{F2} \right), \tag{2.1}$$

where m_1 and m_2 are the magnitudes of the two objects being compared. Two properties of magnitudes are immediately obvious from this equation: the scale is inverted, so the brighter the object, the smaller the magnitude, and the difference between magnitudes of two stars is proportional to the logarithm of the ratio of their fluxes. This definition of magnitude can be used to measure the difference between two objects, but, in order to give an absolute measurement of brightness, a standard comparison object (zero point) is required. The choice of the zero point is what defines and distinguishes different magnitude systems. The most commonly used systems are the Vega and the AB systems. In the Vega system the star Vega (or α Lyrae) is used as the reference object. Consequently, in the Vega system, Vega

is defined as having all magnitudes equal to zero. In the AB system, instead, the comparison object is a hypothetical star with constant flux per unit frequency interval (F_ν), i.e. a perfectly flat spectrum in F_ν. Measurements in the two magnitude systems are nearly equivalent in the central optical wavelength range but colour-dependent differences exists at other wavelengths. Stars and other celestial objects do not emit the same amount of flux at all wavelengths, so for accurate comparison magnitudes have to be defined over a specific wavelength range. This is normally achieved by observing through a filter which only lets through light in the desired wavelength window. Magnitudes measurements are therefore quoted together with filter that was used in the observation. The astronomical technique used to measure the flux an object, and to calculate its magnitude, is called photometry. Astronomical surveys image large areas of the sky carrying out photometric observations of millions of objects in a wide range of wavelengths (see Sect.3). The multi-band photometry provided by large area surveys constitutes the main data resource used in the work presented in this thesis.

2.2 Colour-colour diagrams

In astronomy the colour of an object is defined as the difference between magnitudes measured in two different band passes or filters (usually the shorter wavelength magnitude minus the longer wavelength one). The intensity of emitted light as a function of wavelength defines the spectral energy distribution (SED) of a star. Colour is therefore a measure of the gradient of the object's SED in the wavelength region covered by the two filters. Since the shape of the SED of a star is dependent on its temperature, surface gravity and atmospheric composition, colours are normally good temperature indicators and colour-colour diagrams can often be used to distinguish between different classes of objects. Some colours are more effective than others when trying to discriminate between specific objects. For example the strength of the Balmer jump (a broad Hydrogen absorption feature at $\simeq$ 3647Å) is sensitive to surface gravity so, over that wavelength region, white dwarfs have colours different from those of stars with similar temperature, but lower surface gravity (A−F stars). Indeed in $u-g$, $g-r$ colour-colour space, white dwarfs occupy a well defined locus distinct from that of main sequence stars (Fig. 2.1). During my work I have often used colour-colour diagrams to select or exclude specific object and to estimate effective temperature and other properties of white dwarfs.

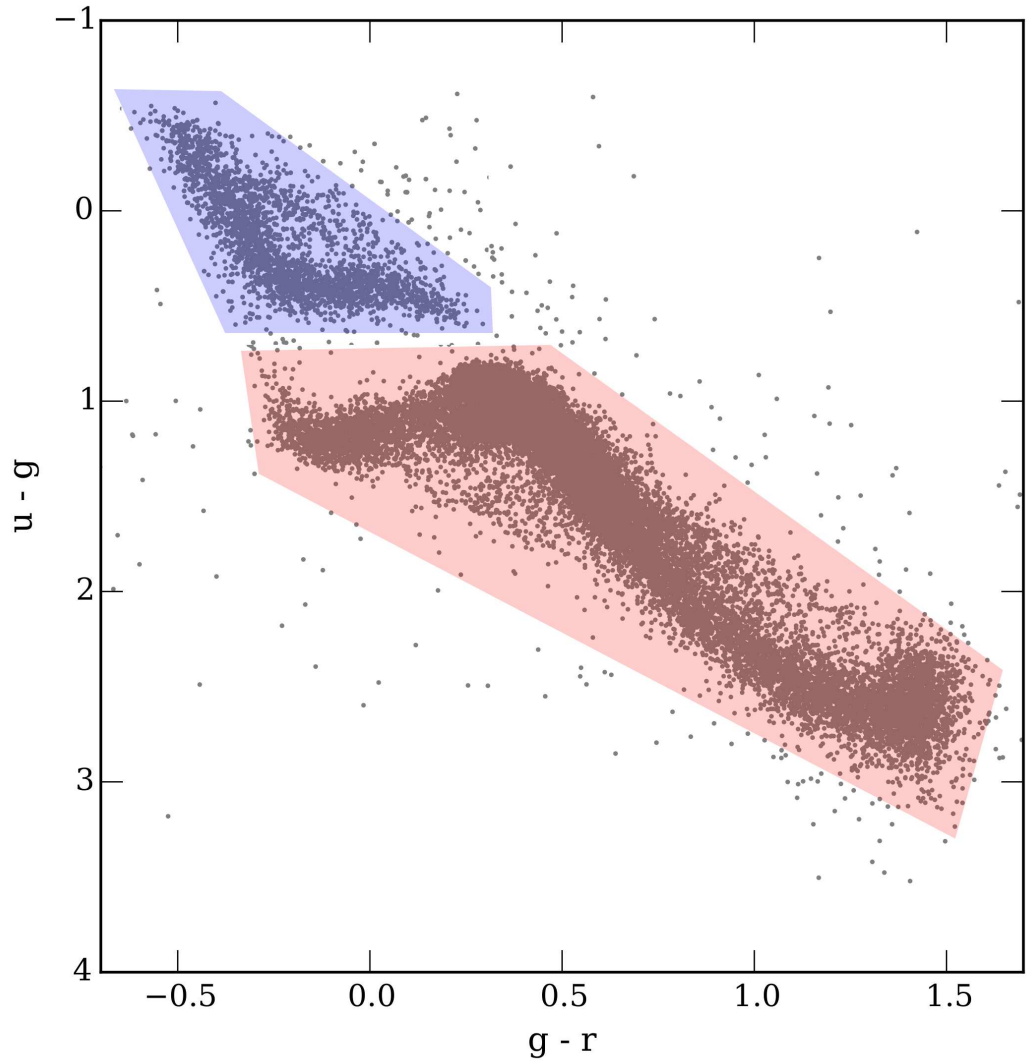

Figure 2.1: Colour-colour distribution of 25000 random objects from SDSS. The area shaded in blue marks the locus occupied by white dwarfs whereas the region shaded in red is occupied by main sequence stars.

2.3 Spectroscopy

As described before, photometry measures the brightness or intensity of light over a specific wavelength range. In other words photometric measurements are wavelength integrated observations of a specific section of an object's SED. However, photometry provides only one measurement for all of the star's flux within the wavelength interval. In contrast, a technique called spectroscopy is used to measure the continuous SED of an object over a chosen wavelength range. The absorption or emission lines in spectrum indicate the presence of specific chemical elements and there-

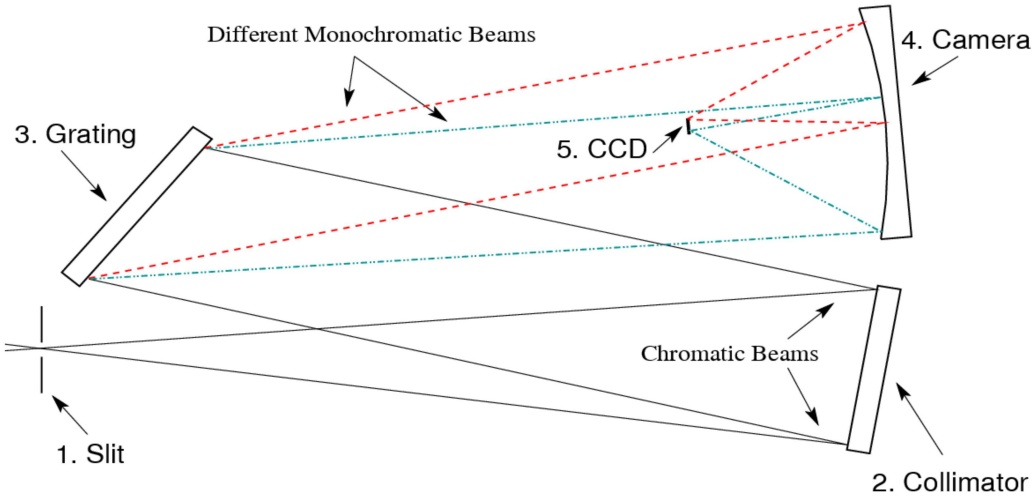

Figure 2.2: Schematic of the optical elements of a spectrograph.

fore allows to determine the composition of the atmosphere of the observed object. Furthermore the spectrum can be used to measure a star's effective temperature, surface gravity and the atmospheric abundances of certain elements (see Chapter 1 and Chapter 8). Spectroscopy is performed by focusing the collimated light from a source onto a diffraction or reflective grating. The grating spatially splits the light into its wavelength components which are then focused by the camera mirror or lens and recorded by a detector (Fig. 2.2). As part of the work described in these thesis I have obtained slit spectroscopy of individual objects and personally carried out the data reduction. In slit spectroscopy the light from the source passes through an adjustable slit before being directed into the diffracting element. The product of this type of observation is a 2D image (Fig. 2.3) with a spatial dimension (covering the length of the slit) and a spectral one (wavelength). In order to convert this image into the actual spectrum of a star some additional steps of data reduction are necessary:

- Bias removal: A bias frame is an image taken with zero exposure time and, therefore, only measures the electronic response of the detector. This electronic response corresponds to an offset in the number of counts measured by the detector in raw science images. In order to remove this offset a bias image is subtracted from the raw science one. In practice the electronic response varies randomly so several bias frames stacked together into a "master bias" are normally used. Additionally to the electronic response, extra noise (called readout noise) is also added by the electronics themselves in the conversions

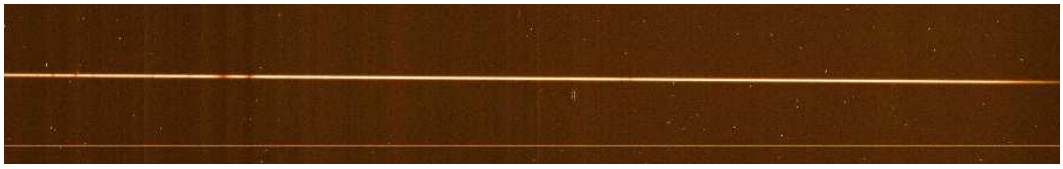

Figure 2.3: 2D spectrum of the white dwarf SDSS J0820+2530, observed with the Intermediate dispersion Spectrograph and Imaging System (ISIS) on the William Herschel Telescope (WHT). The horizontal axis corresponds to the spectral dimension (wavelength) and the vertical axis corresponds to the spatial dimension (covering the length of the slit). The bright horizontal line in the center of the image is the actual spectrum of the object. The Ca H and K absorption lines are clearly visible as the darker bands on the left. The thin bright line at the bottom of the image is a spurious features caused by the detector and is normally corrected for by the bias subtraction and flatfielding.

from analogue signals to digital number.

- Flat fielding: A flat field image is taken by uniformly illuminating the entire detector. This is normally achieved by "observing" the light from a tungsten lamp or by acquiring an image of the twilight sky. In the detector each pixel has different sensitivity. A flat field effectively maps these difference and allows to correct for them in the science image. In spectroscopy it also necessary to take into account the spectral shape of the flat field source (e.g. the tungsten lamp).

- Wavelength calibration: On the detector the dispersed light of different wavelengths is simply recorded on a pixel scale. In order to convert this pixel scale into wavelength units it is necessary to compare the science spectrum with a spectrum which has recognisable features at precisely known wavelengths. Normally the comparison spectrum used is that of a high pressure gas arc lamp with specific emission lines.

- Flux calibration: Similarly to wavelength calibration, also the measured flux has to be converted from detector counts to physical flux units. This is also done by comparing the science spectrum with a reference one. In this case, the reference spectrum is that of a spectrophotometric flux standard: a well studied star with a carefully characterized SED. For a reliable flux calibration, the reference star has to be observed with the same set-up as the science objects.

One of the main advantages of slit spectroscopy is that the spatial information is still available along the direction of the slit. However only one or two objects (if both are placed in the slit) can be observed at same time. Fiber-fed multi-

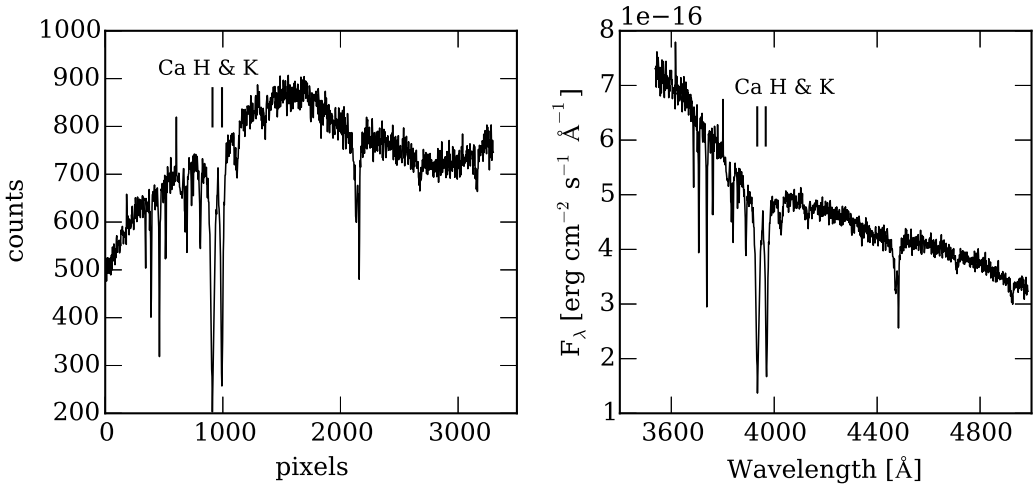

Figure 2.4: Reduced ISIS blue arm spectrum of the white dwarf SDSS J0820+2530. The left and right panels respectively shows the spectrum before and after wavelength and flux calibration.

objecs spectrographs instead allow to acquire multiple spectra simultaneously. These instruments use individual circular apertures for each observed object and the light is carried from the focal plane to the instrument along optical fibers. Large area surveys which use multi-objects spectrographs (e.g. SDSS) also have dedicated pipelines to reduce the raw data and provide spectra ready for science analysis. As part of the work described in these thesis I made extensive use of spectra from large area surveys (see Chapters 4 and 5).

Chapter 3

Large area surveys

3.1 The Sloan Digital Sky Survey

The Sloan Digital Sky Survey has been in continuous operation since 2000. It uses a dedicated 2.5° field of view, 2.5 meter altitude-azimuth telescope at Apache Point in New Mexico to carry out multi band photometric observation of the northern sky and follow-up spectroscopy of selected targets.

Photometric observations are taken in five filters (*ugriz*) and recorded by a mosaic of 30 2048×2048 Tektronix CCD cameras. SDSS photometry is only acquired for objects fainter than $\sim 15^{\text{th}}$ magnitude. Integration times are approximately 54 s and the 5σ detection limits during 1 arcsecond seeing conditions at 1.4 airmass are 22.3, 23.3, 23.1, 22.3 and 20.8 mag for u, g, r, i, z respectively. Observations in the different filters are not acquired simultaneously, but in the sequence *riuzg*, with observations in each filter separated by 71.72 s.

The filters have the following properties: u peaks at 3500 Å has full width at half maximum (FWHM) of 600 Å and effective wavelength 3560 Å, g is the green-blue passband centred at 4800 Å, with FWHM 1400 Å and effective wavelength 4680 Å, r is the red passband centred at 6250 Å, with FWHM 1400 Å and effective wavelength 6180 Å, i is the far red passband centred at 7700 Å, with FWHM 1500 Å and effective wavelength 7500 Å, z is the near infrared passband centred at 9100 Å, with FWHM 1200 Å and effective wavelength 8870 Å, the shape of the z response function at long wavelength is determined by the CCD sensitivity. The five filter curves are displayed in figure 3.1.

The photometric pipeline corrects for CCD defects, biases, sky subtraction, flat-fielding and provides PSF and Petrosian magnitudes. In g, r, i bands, mean errors are 0.03 mag at 20^{th} mag, and 0.12 mag at 22^{nd} mag. u and z bands are less sensitive with errors of 0.05 at 20^{th} mag, and 0.12 at 21^{st} mag. SDSS also provides

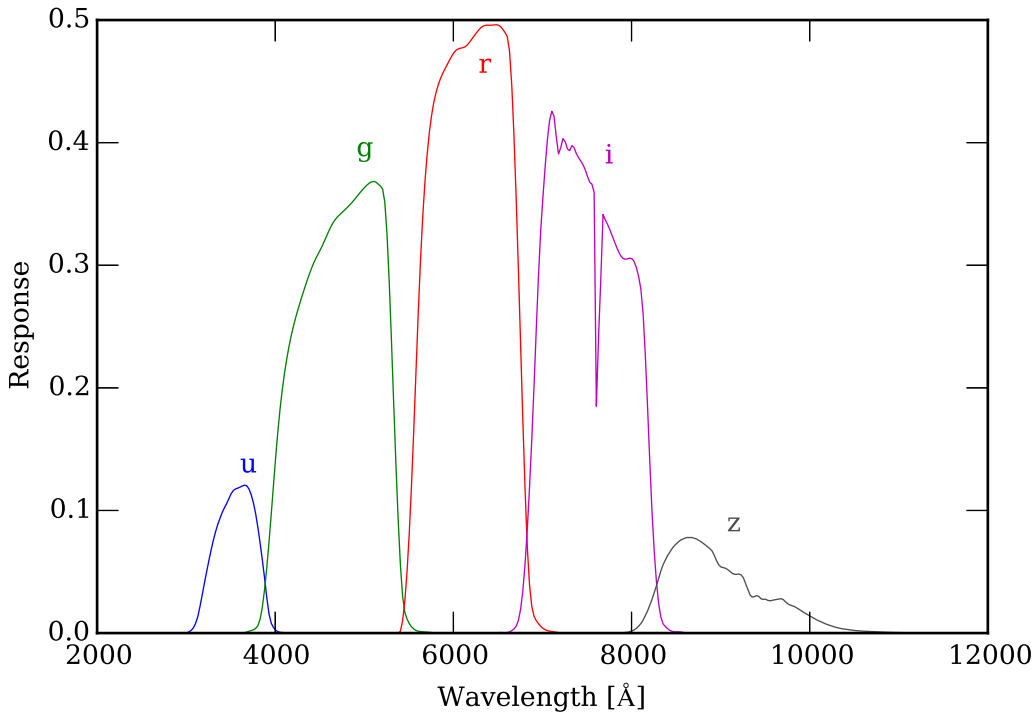

Figure 3.1: SDSS filter throughput curves.

proper motions derived by combining SDSS astrometry with USNO-B positions (Munn et al., 2004). For sources of magnitude $g \geq 19.6$ the completeness of proper motion catalogue drops with increasing values of proper motion. The catalogue is considered 94 per cent complete for objects with proper motion less than 20 mas/yr, dropping to about 70 per cent complete for objects with proper motions of 1000 mas/yr. Statistical errors in the component proper motions are roughly 3-3.5 mas/yr.

SDSS also carries out extensive spectroscopic follow-up programs of selected sources using a fiber fed multi object spectrograph. Spectroscopic targets are selected according to a series of colour cuts (e.g Stoughton et al. 2002; Dawson et al. 2013). The spectrograph used during its first and second operation phase (SDSS-I and SDSS-II, 2000−2008) had 640 fibers and covered the wavelength range 3800−9200 Å with resolution varying from 1850 to 2200. Each spectroscopic observation required a custom made aluminium plate with holes for fiber positioning drilled at the positions of the SDSS photometry. Each plate subtends 3 degrees of the sky, fiber holes are 3" wide and no fiber can be placed in the central 100" of the plate. Since the start of SDSS-III, a new improved spectrograph called BOSS

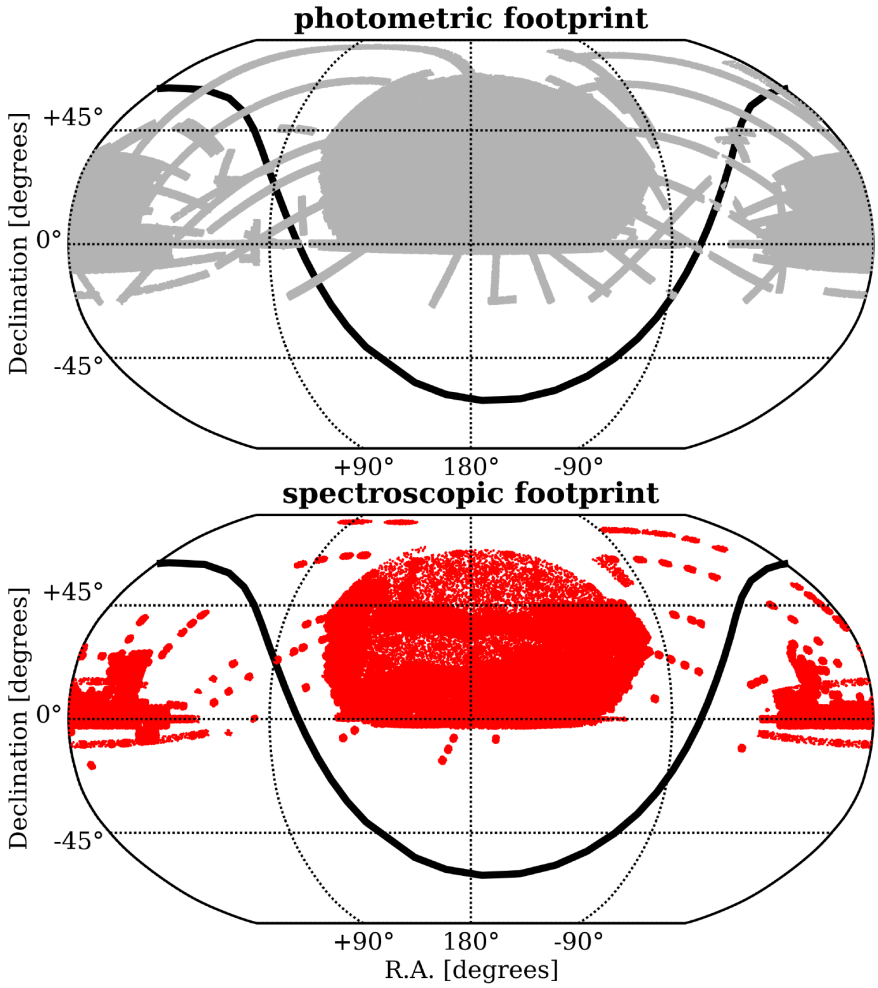

Figure 3.2: DR12 photometric (*top panel*) and spectroscopic (*bottom panel*) coverage of SDSS. The black line indicates the Galactic plane.

is used. BOSS uses new CCDs with improved red and blue response, it provides larger wavelength coverage ($3600 - 10400$ Å) as well as higher spectral resolution ($R \simeq 1560 - 2650$) Ahn et al. 2012). BOSS uses 1000 fibers each requiring only 2" holes, enabling better sky subtraction compared to the old spectrograph. SDSS spectra are typically combined from three or more individual exposures of 15 minutes each.

Alongside its imaging camera and multi object spectrograph, SDSS is also equipped with a high-resolution near infrared spectrograph (APOGEE) and an interferometer spectrograph(MARVELS). In my work I did not data from APOGEE and MARVELS, but more details about these instruments can be found in Ge et al. (2015); Hayden et al. (2015).

In the course my work I have made extensive use of the SDSS Data Release (DR) 7 (Abazajian et al. 2009), DR9 (Ahn et al. 2012) and DR10 (Ahn et al. 2014), which are, respectively, the last DR of the SDSS-II project and the second and third DRs of the SDSS-III project. SDSS has now reached completion of its third operation phase and the most recent data release is DR 12. To date SDSS has imaged 14555 $\deg^2$ and provides photometry of over 469 million sources and spectroscopy for over 4 millions unique objects (Alam et al., 2015).

The primary focus of SDSS is to map the structure and evolution of the Universe by acquiring spectroscopy and photometry of quasars (Richards et al., 2002) and galaxies (Strauss et al., 2002) within its footprint. Some projects within SDSS have, also been aimed at characterizing the Milky Way (SEGUE I-II, APOGEE) and about 3.5% of the BOSS fibers in SDSS-III were devoted to a series of 25 small ancillary projects. Particularly relevant to my work is the white dwarf and hot subdwarf ancillary project which targeted white dwarf and hot subdwarf candidates (Dawson et al. 2013, Ahn et al. 2014).

SDSS provides several different data access tools, each suited to a particular need. The Science Archive Server (SAS) offers a browser-based access to interactive spectra and image mosaics with the possibility to download FITS images for single objects or in bulk. The Catalog Archive Server (CAS) is an SQL database with fast search capabilities which contains the measured parameters for all SDSS photometric and spectroscopic targets. The CAS can be accessed via a stand-alone browser-based applications or using free-form SQL queries. In addition SDSS offers a number of other data access tools for astronomers and the general public alike.

In many aspects SDSS is the ideal survey for the work presented here and similar projects. It covers an extremely large area of the sky, offering multi-colour photometry, accurate proper motions and spectra. A small area of the SDSS footprint, Stripe 82, even received multi-epoch observations, and in Chapter 7 I show that these can be used to reliably identify variable objects. The SDSS photometric calibration are extremely reliable and often used as reference in other surveys. Furthermore the different data access tools and the extensive documentation allow to easily recover specific data subsets in bulk or quickly examine a single object. SDSS constitutes the backbone of my entire PhD work, from the development a selection method for white dwarf candidates (Chapter 4) to the search for planetary remnants (Chapter 8).

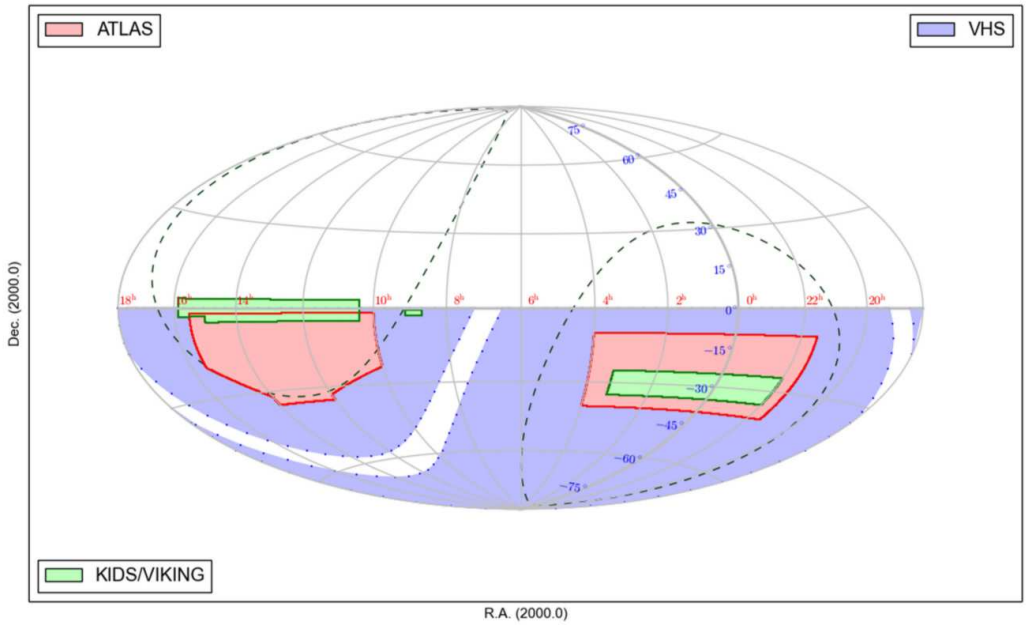

Figure 3.3: Planned ATLAS footprint in equatorial coordinates (red) compared to the other southern hemisphere surveys: VHS (blue) and KIDS (green). The dashed lines indicate regions $\pm 30°$ from the galactic plane.

3.2 VST ATLAS

The initial aim of ATLAS is to survey 4700 deg^2 of the Southern Sky at high galactic latitudes in five bands ($ugriz$) to comparable depths to the SDSS in the North. The ATLAS footprint is divided in two contiguous blocks in the North and South galactic caps. The ATLAS South Galactic Cap (SGC) area lies between $21^h30^m <$ RA $< 04^h00^m$ and $40° <$ Dec $< 10°$, whilst the North Galactic Cap (NGC) area lies between $10^h00^m <$ RA $< 15^h30^m$ and $20° <$ Dec $< 2.5°$ plus $10^h00^m <$ RA $< 15^h00^m$ and $30° <$ Dec $< 20°$ (Fig. 3.3).

The survey is carried out at the VLT Survey Telescope (VST), a 2.6 m, wide-field optical telescope located at Cerro Paranel in Chile. The VST has a 1 square degree field of view and observations are recorded on a 16000×16000 pixel detector mosaic composed of 32 CCDs (OmegaCAM). There are narrow gaps between the CCDs of OmegaCAM, and the overall geometric filling factor of the array is 91.4%. ATLAS uses the same band-passes as SDSS i.e. u, g, r, i, z. Exposures are taken in pairs for each filter and exposure times of 60 s for u, 50 s for g and 45 s for r, i and z. 5σ detection limits during 1"seeing conditions are 22.0, 23.1, 22.7, 22.0 and 20.9 mag for u, g, r, i, z respectively. The imaging data is reduced by the Cambridge Astronomical Survey Unit (CASU) using the VST data flow software. Images are

trimmed and debiased using nightly calibration frames and then flat-fielded using accumulated monthly stacked twilight sky flats. The frames are then corrected for crosstalk and defringed if necessary. The resulting imaging data comprise the combination of the two individual images for each of the original CCDs (Shanks et al., 2015).

The first data release (DR1) of ATLAS was recently made public via the ESO archive. This includes observations taken from the start of operations in August 2011 to the end of September 2012. In DR1 the area of sky covered in all filters is $\simeq 1200$, but a total area of $\simeq 1900\,\mathrm{deg}^2$ has already been covered in i and z. A second data release (DR2) has also been completed, and even though it is not public yet, we were granted early access to it. In Chapter 6 I present the application of my selection method for white dwarf candidates to the over 2 million objects with u, g, r, i, z photometry in ATLAS DR2. The primary aims of the ATLAS survey are cosmological. Similarly to SDSS, the multi-band photometry of ATLAS allows to select large numbers of quasars to study the structure and evolution of the early Universe. Because SDSS and other digital surveys have, so far, been limited to the northern hemisphere, the southern sky is, under many aspects, still a largely unexplored territory. As the largest and deepest optical digital survey to ever be carried out in the southern hemisphere, ATLAS represent the first step towards filling the aforementioned north-south observational gap.

3.3 LAMOST

LAMOST is a quasi-meridian reflecting Schmidt telescope of effective aperture $\simeq$4m located at Xinglong Observing Station in the Hebei province of China (Cui et al., 2012). LAMOST uses 16 fiber-fed spectrographs each equipped with a red and a blue channel CDD camera. Each spectrograph counts 250 fibers, thus LAMOST is able to obtain a total of 4,000 simultaneous spectra. The wavelength coverage of the spectra is $\sim$3800$-$9000 Å at a resolving power of $\sim$1,800. Although the flux calibration of the LAMOST spectra is relative (Song et al., 2012), the spectral energy distribution is correctly characterized and classifications based on visual inspection of the spectra can be considered as reliable.

LAMOST started operations in 2009 and began a five-year regular survey in 2012. This survey consists of two main parts with different science goals and target selection criteria (Zhao et al., 2012). The LAMOST Extra-Galactic Survey (LEGAS) studies the large scale structure of the Universe. The LAMOST Experiment for Galactic Understanding and Exploration (LEGUE) focuses on characterizing the

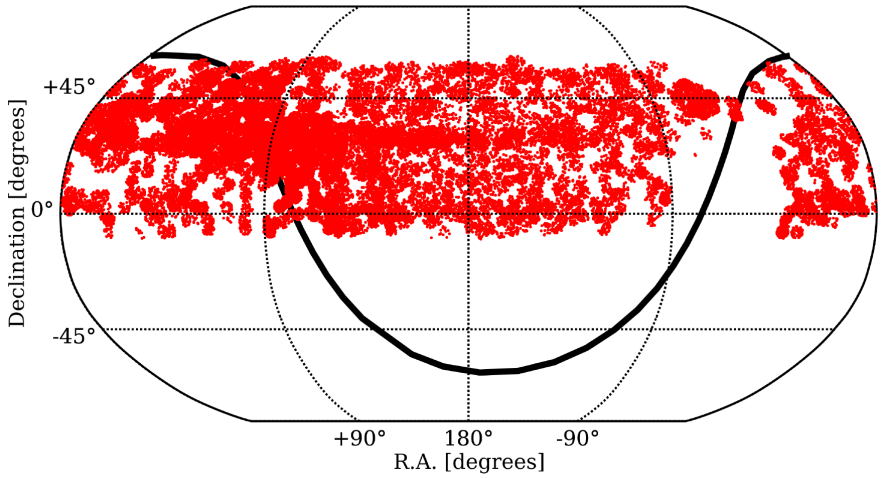

Figure 3.4: LAMOST DR3 pointings. The black line indicates the Galactic plane.

structure and evolution of the Milky Way (Deng et al., 2012) and is sub-divided into three sub-surveys (Carlin et al., 2012; Chen et al., 2012; Liu et al., 2014; Yuan et al., 2015): the spheroid, the disk, and the Galactic anti-center.

The current number of publicly available LAMOST spectra is ∼4.6 million. These include the full second data release (DR2) plus the first three months of data of the third data release (DR3). Even though the number of spectra acquired by LAMOST to date is comparable if not higher than those acquired by SDSS, the overall quality is distinctly inferior. Faint sources ($g \lesssim 18$) often have signal-to-noise ratios too low for accurate spectral analysis and sometimes even for reliable identification. This fact, combined with the lack of an absolute flux calibration limits the science impact of LAMOST spectroscopy compared to SDSS. Nonetheless LAMOST remains an extremely valuable resource and, in many aspects, it can be considered complementary to SDSS. For example LAMOST adopts a different targeting strategy from SDSS and covers areas of the sky which are specifically avoided by SDSS (e.g. the Galactic anti-center). Exploiting these key difference between SDSS and LAMOST, in Chapter 5 I used a sample of spectroscopically confirmed white dwarfs and contaminants from LAMOST DR3 to independently test my selection method for white dwarf candidates.

3.4 UKIDSS

UKIRT Infrared Deep Sky Survey (UKIDSS) is the collective name of a group of five near infrared surveys carried out at the 3.8 m United Kingdom Infrared

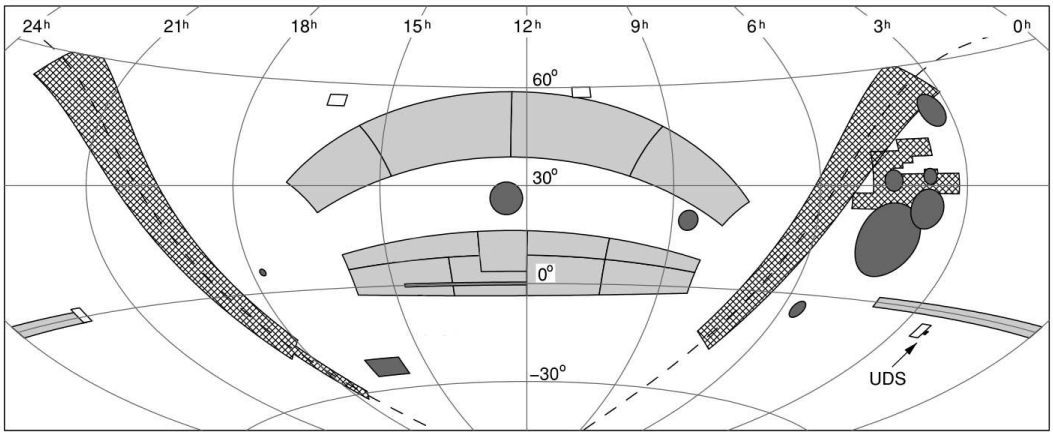

Figure 3.5: The UKIDSS sky coverage showing the LAS (solid light grey), GPS (cross-hatched), GCS (solid dark grey), DXS (empty squares) and UDS (as labelled, lying alongside the western-most DXS field). The dashed line indicates the galactic plane (Dye et al., 2006).

Telescope (UKIRT) in Hawaii (Hewett et al., 2006; Lawrence et al., 2007). The five surveys are: the Large Area Survey (LAS), the Galactic Plane Survey (GPS), the Galactic Cluster Survey (GCS), the Deep Extragalactic Survey (DXS) and the Ultra Deep Survey (UDS). Observations for these surveys are recorded by the Wide Field Camera (WFCAM), an imaging instrument composed of four 2048×2048 pixels Rockwell Hawaii-II PACE arrays. A single exposure of WFCAM covers a solid angle of 0.207 deg^2 and the standard exposure time is 5 s; each pointing consists of a set of 8 ($2 \times 2 \times 2$) exposures, and results in $4 \times 4096 \times 4096$ images, in which every pixel is exposed for 10 s. UKIDSS began operations in May 2005 and ha now reached formal completion of the surveys. Together, the 5 surveys imaged 7500 deg^2 of the Northern sky, covering both high Galactic latitudes and a large section of the Galactic plane (Fig. 3.5).

Each survey covers a separate part of the sky and has a unique main science aim, but overall UKIDSS aims range from finding the faintest objects in the solar neighbourhood (e.g cool brown dwarfs), through the structure of the Milky Way, to searching for the most luminous and distant object (e.g high-redshift starbust galaxies, galaxy clusters and quasars). Thanks to its large footprint overlap with SDSS, UKIDSS LAS was particularly relevant for my work. UKIDSS LAS provides imaging over 4000 deg^2 in four broad bands: Y, J, H, and K (see Figure 2.5), with limiting (Vega) magnitudes of 20.5, 20.0, 18.8 and 18.4, respectively. The most recent data release of UKIDSS is DR10 and the data is made available via the WFCAM science archive (Hambly et al., 2008).

The deep near-infrared photometry and high-resolution images of UKIDSS

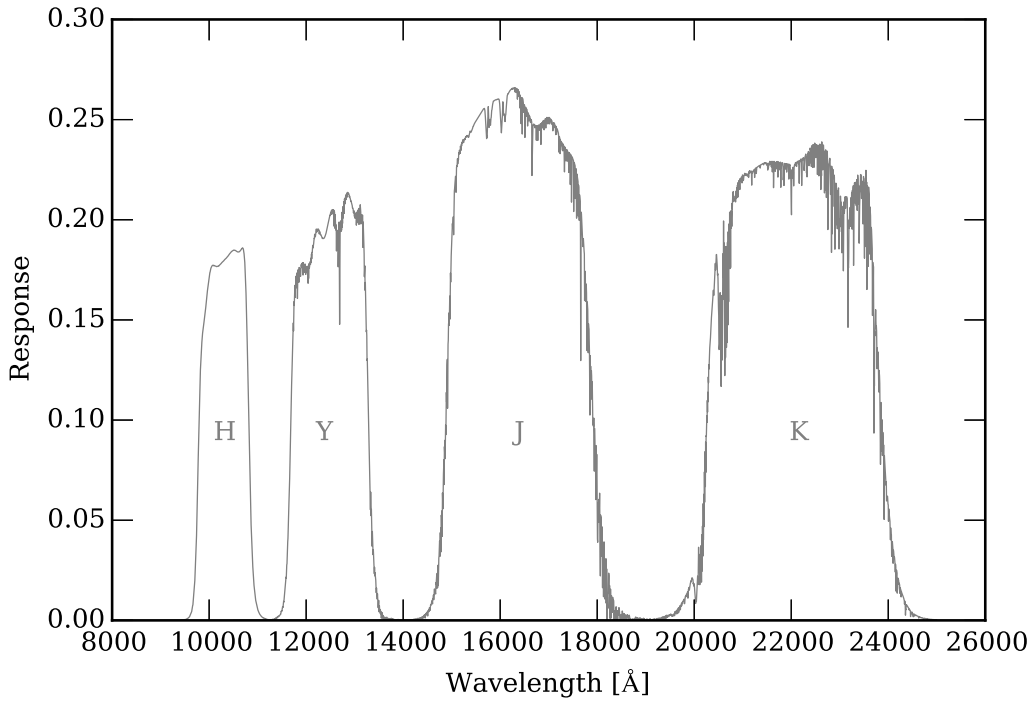

Figure 3.6: UKIDSS filters response curves.

perfectly complemented the data from WISE (see later) and were of fundamental importance in my search for white dwarfs with infrared excess (Chapter 8).

3.5 VHS

The VISTA Hemisphere Survey (VHS) consist of three near-infrared surveys which map different areas of the southern sky: the Galactic Plane Survey (GPS), the Dark Energy Survey (DES) and the ATLAS survey. All surveys are carried out at the 4 m Visible and Infrared Survey Telescope for Astronomy (VISTA) at ESO's Cerro Paranal Observatory in Chile. VISTA is equipped with an infrared camera (VIRCAM) composed of 16 Raytheon VIRGO 2048×2048 array detectors, with a pixel scale of 0.34" and a field of view per exposure of 0.59 $\deg^2$. Because of the gaps between detectors, six exposures are required to survey a contiguous area (tile) of 1.5 square degrees. Combining the three surveys VHS aims to obtain near-infrared coverage of the entire southern hemisphere ($\simeq 20,000$ $\deg^2$). VHS GPS will image $\simeq$ 8000 $\deg^2$ at low galactic latitudes ($5^\circ < |b| < 30^\circ$); VHS DES will scan $\simeq$ 4500 $\deg^2$ of the southern galactic cap and the remaining high galactic latitude regions will be covered by VHS ATLAS (Fig. 3.7). The three surveys also differ in the filter

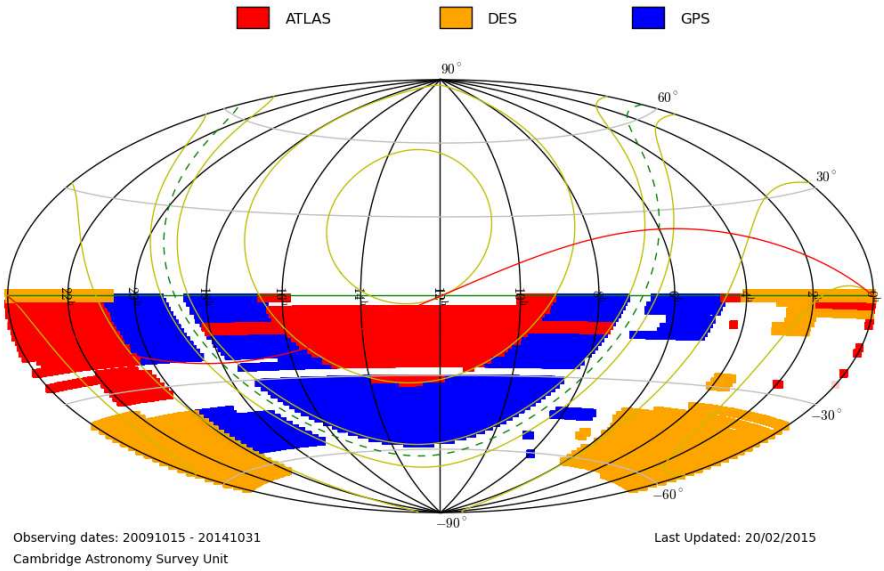

Figure 3.7: Area of sky already imaged in at least one filter by the three VHS surveys as of 20/02/2015.

used and the magnitude depth reached (McMahon et al., 2013):

- VHS GPS: 60 s exposures in J and K; limiting magnitudes (AB) 21.2 and 19.8.
- VHS DES: 120 s exposures in J, H and K; limiting magnitudes (AB) of 23.0, 21.6 and 20.2.
- VHS ATLAS: 60 s exposures in Y, J, H and K; limiting magnitudes (AB) of 20.9, 21.2, 20.6 and 19.8.

All VHS data is processed using the VISTA Data Flow System (VDFS; Hambly et al. 2004) operated by the Cambridge Astronomical Survey Unit. The final data products of the three surveys (catalogues and stacked images) are made public together in large VHS data releases accessible via the ESO archive. In my work I mostly used the latest data release currently available, DR3 (Fig. 3.7). Similarly to UKIDSS, VHS science goals are both galactic and extra-galactic, ranging from discovery of the lowest-mass stars to constrain properties of Dark Energy . Furthermore VHS will provide essential multi-wavelength support for other ESA missions (e.g XMM-Newton, Planck, Herschel and Gaia).

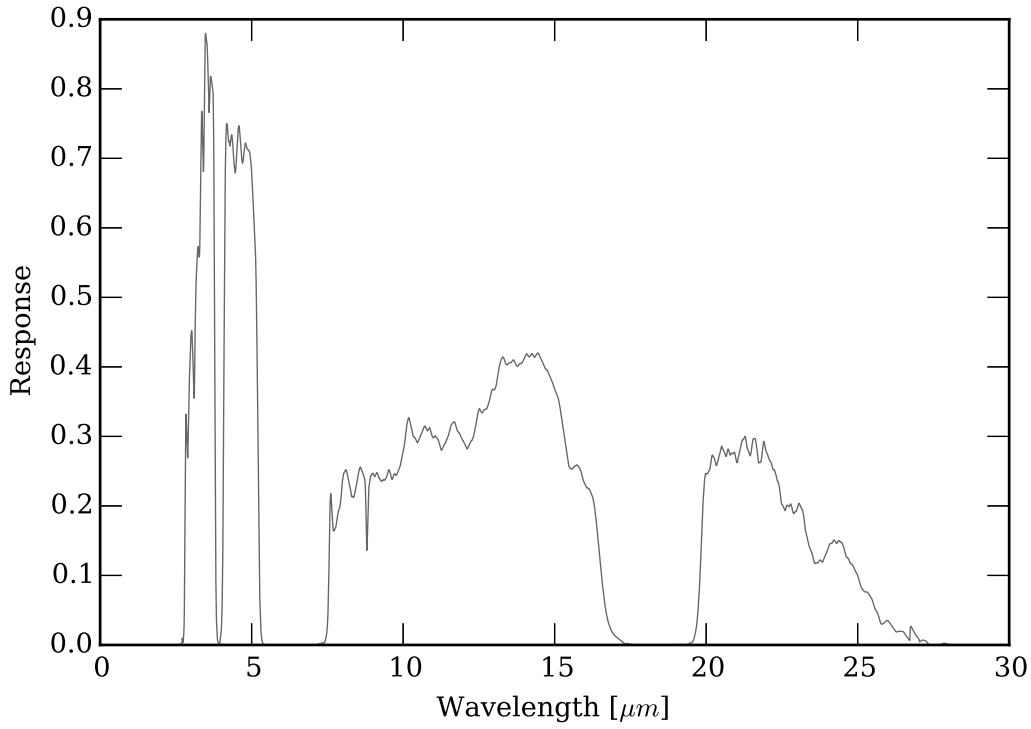

Figure 3.8: From left to right, $w1$, $w2$, $w3$ and $w4$ filters response curves.

In the search for white dwarf candidates with infrared excess presented in Chapter 8 I used VHS as the souther equivalent of UKIDSS to provide near-infrared photometry for the ATLAS white dwarf candidates.

3.6 WISE

The Wide-field Infrared Survey Explorer (WISE) is a NASA space telescope launched in December 2009 with the aim to survey the entire sky in four infrared bands. These bands, $w1, w2, w3$ and $w4$ have effective wavelength of 3.4, 4.6, 12 and 22 μm (Fig. 3.8; Wright et al. 2010). The satellite consists of a 40 cm telescope that images all four bands simultaneously every 11 s. Each image covers a 47 arcminute field of view, with a spatial resolution of 6". Each area of the sky was scanned at least 10 times with the number of repeated scans increasing towards the poles. Astrometric errors are less than 0.5" with respect Two Micron All Sky Survey (2MASS; Skrutskie et al. 2006). WISE achieved 5-sigma photometric sensitivity of 68, 98, 860, and 5400 Jy in $w1, w2, w3$ and $w4$ respectively.

The initial science goals of WISE were to identify brown dwarfs in the solar

neighbourhood, map dust in our Galaxy and discovery Ultra-Luminous Infrared Galaxies. The original WISE survey was officially completed in October 2010 when the spacecraft depleted its hydrogen coolant. However the program was extended for a four-month post-cryogenic mission named NEOWISE which aimed to detect near Earth asteroids and comets (Mainzer et al., 2011). WISE was eventually put into hibernation on February 1, 2011, but in September 2013, it was reactivated and assigned to detecting potentially hazardous asteroids.

The combined data from WISE and NEOWISE consists of images, positions, apparent motion measurements, four-band fluxes and flux variability statistics for over 747 million objects. All data is publicly available at the Infrared Science Archive (IRSA). Because of its all-sky coverage, WISE was the main infrared resource used in search for white dwarfs with infrared excess presented in Chapter 8.

Chapter 4

A photometric selection of white dwarfs candidates in SDSS DR10

4.1 Introduction

In the introduction to these thesis I emphasized how the advent of large area surveys triggered a huge leap forward in the field of white dwarfs. These surveys allowed to readily select larger and larger samples of white dwarfs, opening up uncountable science applications. Indeed, well-defined large samples of white dwarfs are the basis of all studies which aim to draw any statistical conclusions. Such large samples are required to reliably constrain fundamental parameters such as space density (Holberg et al., 2002, 2008; Giammichele et al., 2012; Sion et al., 2014), mass distribution (Bergeron et al., 1992a; Liebert et al., 2005; Falcon et al., 2010; Tremblay et al., 2013) and the luminosity function, which in turn can be used to determine the ages of the individual Galactic populations (Oswalt et al., 1996; De Gennaro et al., 2008; Cojocaru et al., 2014).

In addition, well defined large samples of white dwarfs are an extremely useful starting point for identifying rare white dwarf types: magnetic white dwarfs (e.g. Gänsicke et al. 2002; Schmidt et al. 2003; Kepler et al. 2013; Hollands et al. 2015), pulsating white dwarfs (e.g. Castanheira et al. 2004; Greiss et al. 2014), high/low mass white dwarfs (e.g. Vennes & Kawka 2008; Brown et al. 2010; Hermes et al. 2014b), white dwarfs with unresolved low mass companions (e.g Farihi et al. 2005; Girven et al. 2011; Steele et al. 2013), white dwarfs with rare atmospheric composition (e.g. Schmidt et al. 1999; Dufour et al. 2010; Gänsicke et al. 2010; Reindl et al. 2014), close white dwarf binaries (e.g. Marsh et al. 2004; Parsons et al.

2011), metal polluted white dwarfs (e.g. Sion et al. 1990; Zuckerman & Reid 1998; Dufour et al. 2007a; Koester et al. 2014) or white dwarfs with dusty or gaseous planetary debris discs (e.g. Gänsicke et al. 2006b; Farihi et al. 2009; Debes et al. 2011a; Wilson et al. 2014).

Despite the significant progress made in the last decade, because of their intrinsic low luminosity, finding white dwarfs remain a challenging task. The largest published catalogues have all been based on the spectroscopic data provided by SDSS (Eisenstein et al. 2006; Kleinman et al. 2013; Kepler et al. 2015). However SDSS spectroscopy is only available for less than 0.01% of all SDSS photometric sources and most of the SDSS white dwarfs are only serendipitous spectroscopic targets. The true potential of SDSS's vast multi band photometric coverage still remains to be fully mined for white dwarf research, but this requires a reliable method able to select white dwarf candidates without recourse to spectroscopy. Proper motions have been traditionally used to distinguish white dwarfs from other stellar populations. In particular many studies that contributed to the census of white dwarfs in the solar neighbourhood specifically targeted high proper motion objects (Holberg et al. 2002, Limoges et al. 2013). In this chapter we present a novel method which makes use of photometric data and proper motions to calculate a *probability of being a WD* ($P_{\rm WD}$) for any photometric source within a broad region in colour space. Unlike any previous similar work, our method does not use a narrow cut in colour or proper motion to generate a list of white dwarf candidates; instead it provides a generic catalogue of sources with an associated $P_{\rm WD}$. These $P_{\rm WD}$ can then be used to create samples of white dwarf candidates best suited for different specific uses, balancing the requirements on completeness and efficiency. By applying our method to the full photometric footprint of SDSS DR10, we created a catalogue which includes $\simeq 23,000$ bright ($g \leq 19$) high-fidelity white dwarfs candidates. Using this catalogue, we asses the spectroscopic completeness of the SDSS white dwarf sample.

4.2 SDSS data

The work presented in this chapter is based on the SDSS Data Release (DR) 7 (Abazajian et al. 2009), DR9 (Ahn et al. 2012) and DR10 (Ahn et al. 2014), which are, respectively, the last DR of the SDSS-II project and the second and third DRs of the SDSS-III project (Fig. 4.1). The early stages of the work described in this section were carried out almost exclusively on DR7 as, at the time, it was the most recent DR. Even though the focus of the work later shifted on DR9 and DR10,

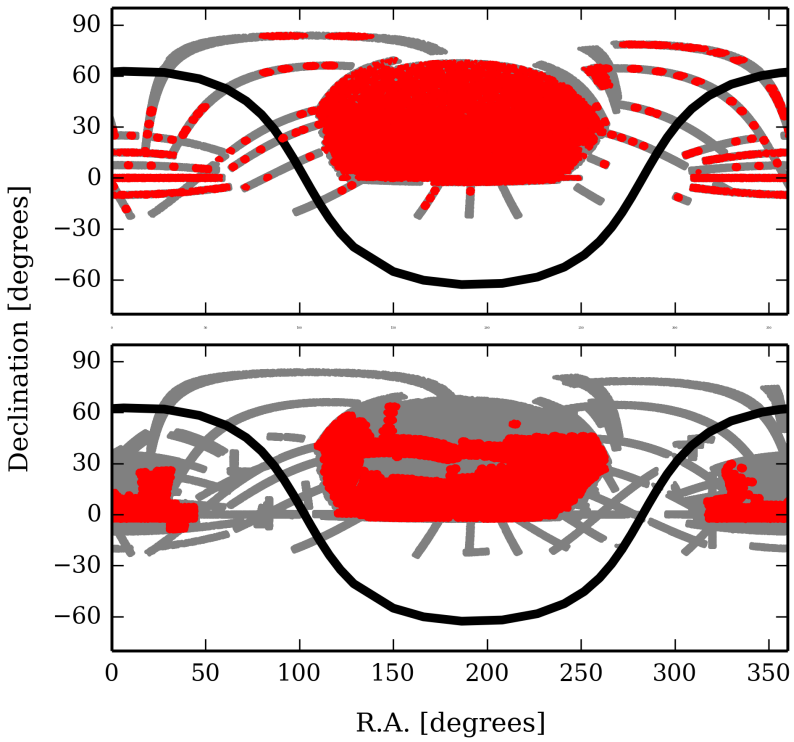

Figure 4.1: Photometric coverage (grey) of SDSS DR7 (top panel) and SDSS DR10 (bottom panel) in equatorial coordinates. The spectroscopic coverages of the SDSS-II spectrograph for DR7 and BOSS for DR10 are overlaid in red. The black line indicates the location of the galactic plane.

because of incongruences between DRs, we continued to make large use of DR7 data (see Sect. 4.7).

4.3 Developing a photometric selection method

We first retrieved spectra, *ugriz* photometry and proper motions for all the primary point sources with available spectra in DR7 within a broad region selected in the $(u-g, g-r)$, $(g-r, r-i)$, and $(r-i, i-z)$ colour-colour planes (Fig. 4.2, Table 4.2). The shape and extension of these colour-cuts were defined such that they included all of the objects which had been classified as either spectroscopically confirmed white dwarfs or as photometric white dwarf candidates by Girven et al. (2011). At this stage we were aiming to be as complete as possible and no real effort was made to avoid contamination.

In developing our selection method, we relied on visual classification of our

Table 4.1: Summary of the most relevant numbers presented in this chapter

magnitude limit of the catalogue	$g \leq 19$
Objects in main DR10 photometric catalogue (Sect. 4.5)	61,969
Objects in DR7 extension (Sect. 4.7.3)	3799
Objects with DR7 spectra in initial colour cut	28,213
Poor quality spectra or no proper motion	574
Objects in DR7 training sample (Sect. 4.3, Table 4.2)	27,639
WDs in the DR7 training sample	6706
Contaminants in the DR7 training sample	20,933
Object with SDSS/BOSS spectra in the catalogue	33,073
WDs with SDSS/BOSS spectra in the catalogue (Table 4.4)	8701
High confidence WDs candidates in the catalogue	$\simeq 23,000$
Of which with no SDSS spectra	$\simeq 14,000$
WDs from Kleinman et al. (2013) included in our catalogue (Sect. 4.8.1)	6689
Kleinman et al. (2013) WDs not classifed as WDs by us	30
Objects with a DR7 spectrum classified by us as WDs, not included in the Kleinman et al. (2013) catalogue	261

Table 4.2: Equations describing the colour and magnitude constraints used to select primary sources in the SDSS footprint.

Colour	constraint	
$(u-g)$	$\leq$	$3.917 \times (g-r) + 2.344$
$(u-g)$	$\leq$	$0.098 \times (g-r) + 0.721$
$(u-g)$	$\geq$	$1.299 \times (g-r) - 0.079$
$(g-r)$	$\leq$	0.450
$(g-r)$	$\geq$	$2.191 \times (r-i) - 0.638$
$(r-i)$	$\leq$	$-0.452 \times (i-z) + 0.282$
g	$\leq$	19
type	$=$	6

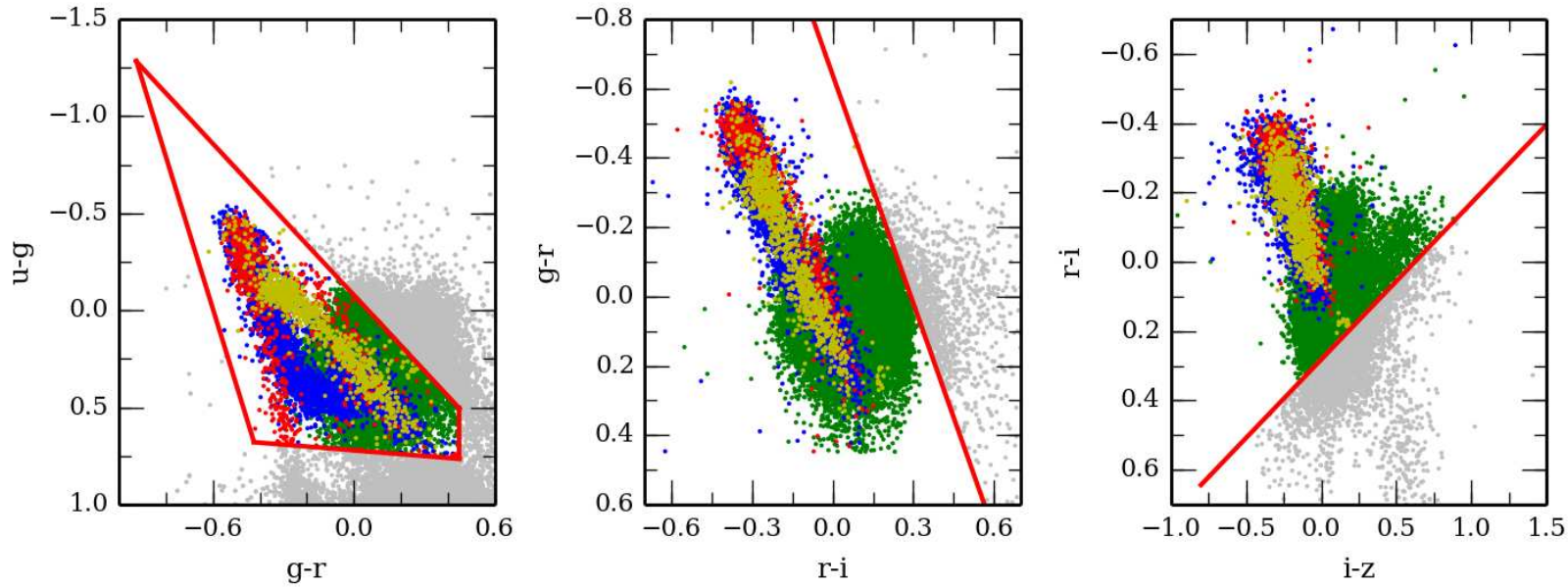

Figure 4.2: Colour-colour diagrams illustrating the location of the 27,639 DR7 spectroscopic objects that we used as training sample for our selection method. DA white dwarfs, non DA white dwarfs, NLHS and quasars are shown as blue, yellow, red and green dots respectively. The colour cuts that define our initial broad selection from Table 4.2 are overlaid as red lines. Objects outside this selection were not classified and are therefore plotted as grey dots.

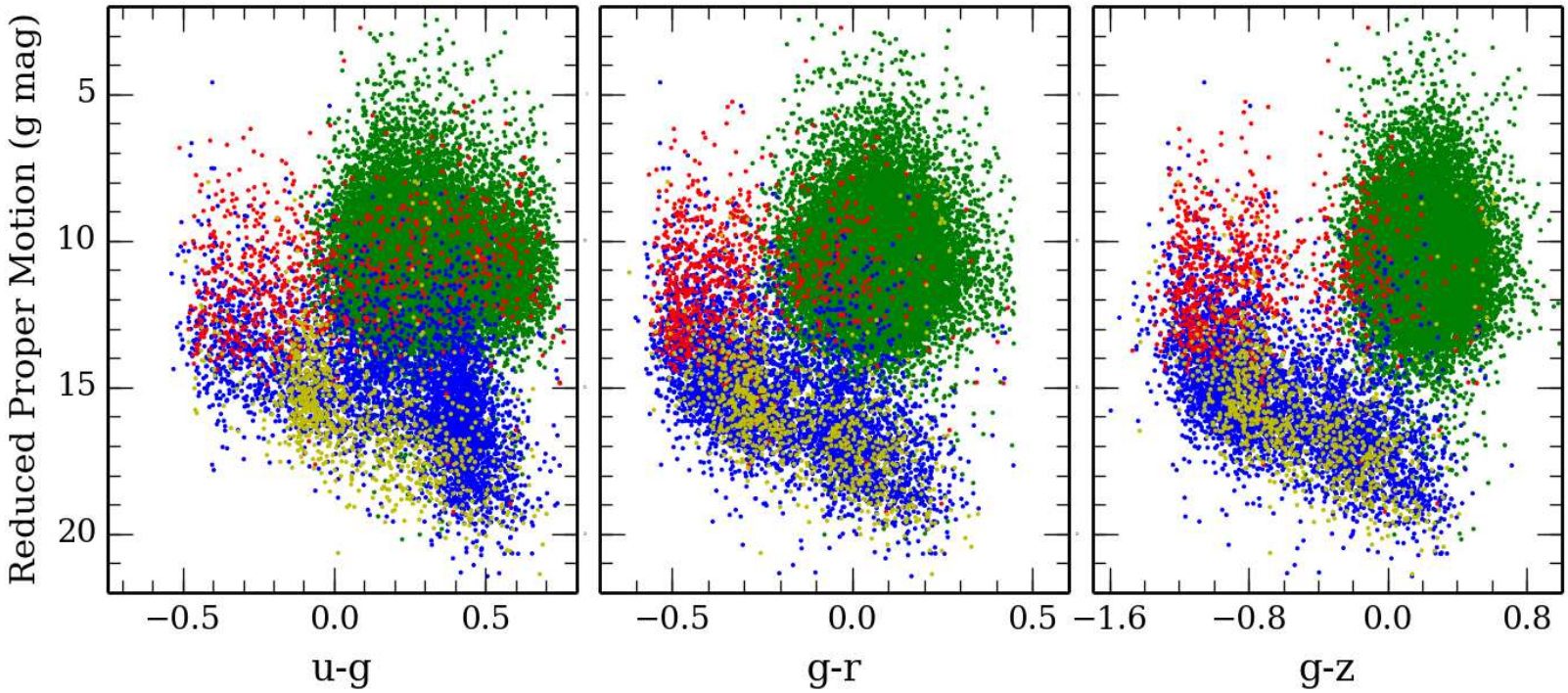

Figure 4.3: Reduced proper motion-colour diagrams illustrating the location of the 27,639 DR7 spectroscopic objects of our training sample (Table 4.3). DA white dwarfs, non DA white dwarfs, NLHS and quasars are shown as blue, yellow, red and green dots respectively.

Table 4.3: Classification of the 28,213 objects with available spectra and with $g \leq 19$ selected from DR7

Class	number of objects
DA	5271
DB	497
DAB/DBA	95
DAO	49
DC	404
DZ	111
DQ	120
Magnetic WD	134
WD+MS	197
CV	94
NLHS	1454
QSO	19739
Unreliable	36
Unclassified	12

initial spectroscopic sample and on proper motions. Sloan objects fainter than $g \simeq 19$ often have noisy spectra and missing or unreliable proper motions. For this reason we decided to limit ourself to bright sources ($g \leq 19$). In the sample we examined there was no object with a measured proper motion exactly equal to zero, but $\simeq 2\%$ of objects with magnitude $g \leq 19$ have no proper motion in the SDSS database. This is probably because these objects did not have a reliable match on the USNO-B photographic plates. From here on we will refer to these objects as having no proper motion, even though their proper motions have, probably, simply not been computed and are actually not zero in value. The initial spectroscopic sample included 28,213 objects which we classified according to spectral appearance. For the development of the selection method we only needed to classify these objects in 3 broad categories: "white dwarfs", "non white dwarfs" and "unreliable"(where the S/N was too low for classification). However we decided that a more detailed classification could help to diagnose biases during the development of the selection method and provide useful statistics. Therefore we subdivided the "white dwarfs" into 10 types (DA, DB, DC, Magnetic white dwarfs,... Table 4.3) and the "non WDs" into "QSOs" and a second category "Narrow Line Hydrogen Stars" (NLHS, a mixed bag of stars with low-gravity hydrogen dominated atmospheres, including subdwarfs, extreme horizontal branch stars and A/B type star). The NLHS sample may include a very small number of extremely low mass (ELM) white dwarfs. However we correctly identified all but one known ELM white dwarfs in our training sample (see

Sect. 4.7.2 for a detailed discussion). The results of our classification are summarized in Table 4.3.
After discarding 36 objects with "unreliable" spectra, we calculated reduced proper motions (RPMs) for all the objects in the sample,

$$H = g + 5 \log \mu + 5 \tag{4.1}$$

with the Sloan g magnitude and the proper motion μ in arcsec/year. 538 objects (of which 265 white dwarfs) did not have proper motions, reducing the size of our initial sample to 27,639 (Table 4.1). These 27,639 spectroscopically confirmed white dwarfs and contaminants with calculated RPM were the *training sample* on which we developed our selection method. RPM can be used as a proxy for absolute magnitude for a given transverse velocity and, with accurate photometry and astrometry, colour-RPM diagrams can show a very clean separation between main sequence stars, subdwarfs, white dwarfs and quasars.

The training sample was used to trace the loci occupied by white dwarfs and contaminants in RPM colour space and to explore the separation between the two types of objects achieved using different colours. We found that the strongest discrimination between white dwarfs and contaminants is obtained in $(g - z, \mathrm{RPM})$ space which we therefore adopted for our selection method (Fig. 4.3).

We then mapped the distribution of the white dwarfs and contaminants of our training sample in RPM colour space. In order to create a smooth continuous map, every object was included as a 2D Gaussian the width of which reflects the uncertainty of the RPM and $(g - z)$ colour of the object. The Gaussians were normalised so that their volume equals unity and therefore the integral over the map is equal to the number of objects in the training sample. In this way we produced a continuous smeared-out "density map" for white dwarfs, and another one for contaminants.

The proper motions computed by SDSS for objects with $g \leq 19$ are accurate to $\simeq 2.5$ mas/year (Ahn et al., 2012), but many objects (most of the QSO) have proper motion values < 2 mas/year and, consequently, large relative uncertainties. These values generate very large uncertainties in the computed RPMs and translate into Gaussians extremely stretched in the RPM dimension. These objects with poor proper motion measurements can, in fact, be smeared over the entire RPM dimension "polluting" even areas which should be populated only by the highest proper motion objects. Furthermore by visually inspecting the $(g - z, \mathrm{RPM})$ distribution of QSO it is instantly obvious that they all cluster in a well defined locus which has a far smaller extension in the RPM dimension than the uncertainties of these low

proper motions. To avoid such artifacts affecting our maps we decided to limit the maximum uncertainty in proper motion for any object to one third of the proper motion value. This correction only affects the objects with the lowest proper motions which, in the case of our training sample, are $\simeq 10,000$ QSOs and $\simeq 200$ other contaminants.

We then defined a map providing the *probability of being a white dwarf* ($P_{\rm WD}$), as the ratio of the white dwarf density map to the sum of both density maps (white dwarfs and contaminants). $P_{\rm WD}$ of any given object is calculated by integrating the product of its Gaussian distribution in the $(g-z, {\rm RPM})$ plane with the underlying probability map (Fig. 4.4). For any given photometric source this value directly indicates how likely it is for the source to be a white dwarf. Our DR7 training sample only contained few objects with very high RPMs and therefore the probability map is scarcely populated in the regime of extremely high RPM. This leads to a "patchy" probability map with blank areas with no information. When calculating $P_{\rm WD}$ for objects outside our training sample, the blank areas, caused by lack of data, would generate low probability values which would not reflect any actual likelyhood of being a white dwarf.

To obviate this problem we decided to define a line in $(g-z, {\rm RPM})$ space such that the $P_{\rm WD}$ of all objects below this line is assumed as 1.0. The line, given by

$$ {\rm RPM} > 2.72 \times (g-z) + 19.19 \tag{4.2} $$

was defined by inspecting the $(g-z, {\rm RPM})$ diagram of the spectroscopic sample and trying to include as much as the sparsely populated area as possible, while minimising the number of contaminants that would undergo such probability correction. (Fig. 4.4).

Using the calculated $P_{\rm WD}$ it is now possible to make different confidence selections by defining any object with an associated probability above an arbitrary threshold as a white dwarf candidate. When choosing such threshold value, completeness and efficiency are the key parameters one needs to compromise between. Reference values of completeness and efficiency can be calculated using again our training sample. For a given $P_{\rm WD}$ threshold, we define *completeness* as the ratio of the number of white dwarfs in the training sample with at least that associated probability to the total number of white dwarfs in the sample. Similarly *efficiency* is defined as the ratio of the number of white dwarfs selected by the probability cut to the number of all the objects retrieved by such selection. While testing the selection method we determined that we can generate from our DR7 training sample a 95% complete sample with 89.7% efficiency by selecting objects with $P_{\rm WD} \geq 0.41$

(Fig. 4.5). Fig. 4.5 clearly shows that the efficiency of any confidence cut increases sharply up to probability values of ~ 0.08 and more slowly after that. This effect is caused by the fact that the vast majority of the contaminants in our training sample are quasars with $P_{\rm WD} < 0.1$ while most of the white dwarfs in the training sample have $P_{\rm WD} > 0.8$. Fig. 4.6 illustrates the distribution of white dwarfs and contaminants in terms of their $P_{\rm WD}$ and shows that there are indeed only a few objects with probabilities between 0.1 and 0.8. Therefore even if a confidence cut at probabilities of 0.1 already yields an efficiency of $\sim$ 80%, much better completeness-efficiency compromises can be achieved using higher probability thresholds and $P_{\rm WD}$ so low should be chosen only when compiling a catalogue which aims to maximise completeness. Finally, in Fig.4.7 we use colour-colour diagrams to further illustrate the reliability of our selection method by comparing the a 95% complete photometric sample with the DR7 spectroscopic training sample.

4.4 White dwarfs with new spectra in DR9/10

Using again the broad selection described in Table 4.2, we retrieved *ugriz* photometry, proper motions and spectra for 8215 objects which received spectroscopic follow-up after DR7 up as part of SDSS-III. These are predominately objects observed with the BOSS spectrograph, including only 102 targets of the Segue-II program still observed with the old SDSS spectrograph. We classified the spectra by visual inspection (Table 4.4). The 3560 objects identified as white dwarfs form an independent sample of spectroscopically confirmed white dwarfs which we used to further test the reliability of our selection method. Furthermore 1752 of these white dwarfs did not have a spectrum prior to DR9 and are therefore new spectroscopically confirmed white dwarfs. We used the $(g-z, \mathrm{RPM})$ probability map to estimate $P_{\rm WD}$ for 3522 of these 3560 white dwarfs (since 38 of them did not have proper motion) and verify that their $P_{\rm WD}$ computed from the DR7 probability map are consistent with the spectroscopic classification. Fig. 4.9 clearly shows that the vast majority of the white dwarfs with new DR9/10 spectra have $P_{\rm WD} > 0.6$ and over 80% of spectroscopically confirmed contaminants have $P_{\rm WD} < 0.1$ confirming that our selection method can reliably distinguish between white dwarfs and contaminants. As a further test, we also decided to calculate values of completeness and efficiency using only objects with new DR9/10 spectra (Fig. 4.8) in the same way we did before using the DR7 training sample (Sect. 4.3). Even though this new spectroscopic sample is considerably smaller than the DR7 training sample, the calculated values of completeness and efficiency are similar; e.g. selecting objects with $P_{\rm WD} \geq 0.41$

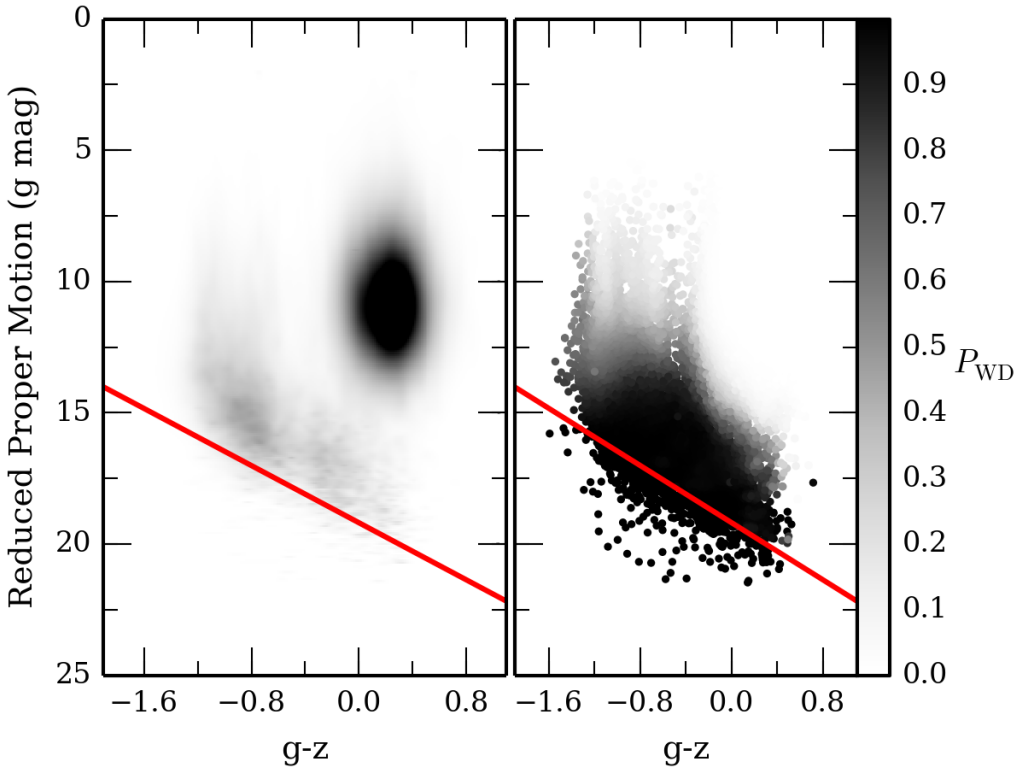

Figure 4.4: Distribution in $(g-z, \mathrm{RPM})$ of the 27,639 white dwarfs and contaminants of the DR7 spectroscopic sample. In the left panel the objects are included as 2D Gaussians to account for the uncertainties in their parameter and the gray-scale reflects the spatial density. In the right panel the grey-scale indicates the calculated $P_{\rm WD}$ with darker objects having higher values than lighter ones. All objects below the red line had their $P_{\rm WD}$ fixed to 1.0

achieves a completeness of 96% and an efficiency of 86.4% on the DR9/10 spectroscopic sample, comparable to the completeness of 95% and an efficiency of 89.7% achieved for the training sample.

4.5 A catalogue of photometric white dwarfs candidates in DR10

We retrieved *ugriz* photometry and proper motions for all the primary point sources in DR10 using the criteria described in Table 4.2, but adding the additional constraint that the selected objects must have proper motions. Furthermore, having to rely only on photometric data we decided to also exclude objects that were flagged as having too few good detections and saturated pixels. This results in a total of 61,969

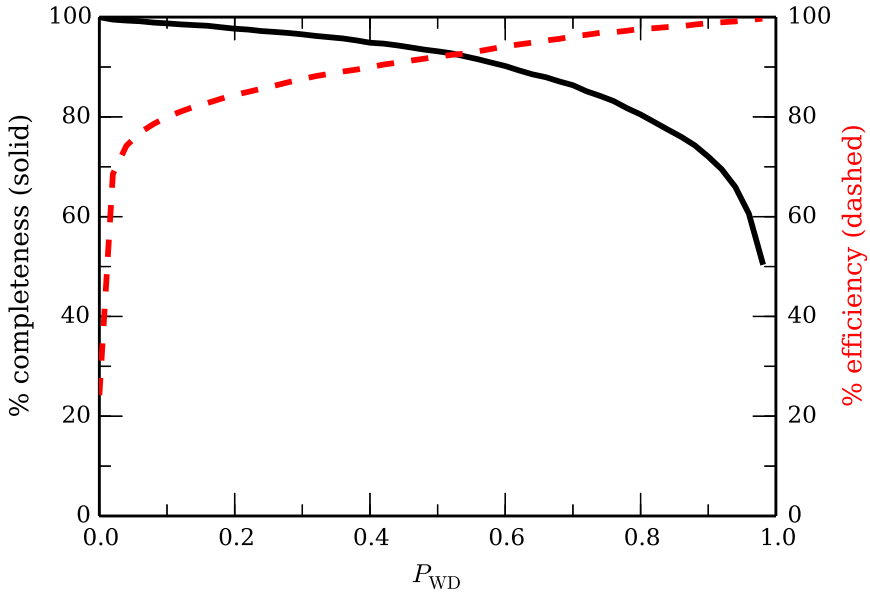

Figure 4.5: Completeness (solid line) and efficiency (dashed line) of samples of white dwarf candidates from our catalogue shown as functions of the minimum value of $P_{\rm WD}$ an object must have in order to be selected. These values of completeness and efficiency were computed using the spectroscopic DR7 training sample as a reference.

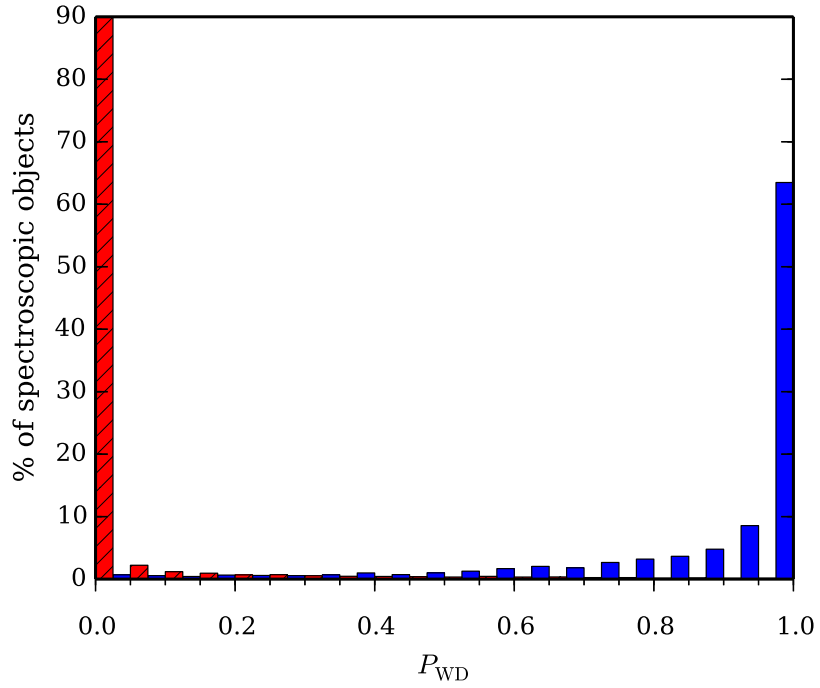

Figure 4.6: Distribution of 27,639 spectroscopically identified white dwarfs (blue) and contaminants (red, shaded) from the DR7 training sample as a function of $P_{\rm WD}$.

Table 4.4: Classification of the 8215 objects with spectra taken after DR7, with $g \leq 19$ within the initial broad colour-cut. The new spectroscopically confirmed white dwarfs had not received any spectroscopic follow up before DR9.

Class	number of objects
DA	2488
DB	408
DAB/DBA	127
DAO	46
DC	214
DZ	44
DQ	57
CV	27
Magnetic WD	60
WD+MS	89
NLHS	902
QSO	3735
Unreliable	16
Unclassified	2
New spectroscopically confirmed WDs	1752

photometric objects. We calculated RPMs for these objects and, using the probability map created with the DR7 training sample (Sect. 4.3), we calculated their $P_{\rm WD}$. Our catalogue can be easily used as the starting point for creating different white dwarf candidates samples according to the compromise between completeness and efficiency best suited for different specific uses. Table 4.5 illustrate the structure and the content of the catalogue, the full list of objects can be accessed online via the VizieR catalogue access tool.

Table 4.5: Format of the DR10 catalogue of white dwarf candidates. The full catalogue can be accessed online via the VizieR catalogue tool.

Column No.	Heading	Description
1	sdss name	SDSS objects name (SDSS + J2000 coordinates)
2	SDSS-III photoID	Unique ID identifing the photometric source in SDSS-III
3	SDSS-II photoID	Unique ID identifing the photometric source in SDSS-II
4	ra	right ascension (J2000)
5	dec	Declination (J2000)
6	ppmra	proper motion in right ascension (mas/yr)
7	ppmra err	proper motion in right ascension uncertainty (mas/yr)
8	ppmdec	proper motion in right declination (mas/yr)
9	ppmdec err	proper motion in right declination uncertainty (mas/yr)
10	probability	The *probability of being a WD* computed for this object
11	umag	SDSS u band PSF magnitude
12	umag err	SDSS u band PSF magnitude uncertainty
13	gmag	SDSS g band PSF magnitude
14	gmag err	SDSS g band PSF magnitude uncertainty
15	rmag	SDSS r band PSF magnitude
16	rmag err	SDSS r band PSF magnitude uncertainty
17	imag	SDSS i band PSF magnitude
18	imag err	SDSS i band PSF magnitude uncertainty
19	zmag	SDSS z band PSF magnitude
20	zmag err	SDSS z band PSF magnitude uncertainty

Table 4.5: Continued from previous page.

Column No.	Heading	Description
21	instrument	instrument used to take the most recent spectrum of the object (SDSS or BOSS)
22	specobjID SDSS-III	unique ID identifying the spectroscopic source in SDSS-III
23	specobjID SDSS-II	unique ID identifying the spectroscopic source in SDSS-II
24	human class	classification of the object based on our visual inspection of its spectrum
25	Kleinman class	classification of the object according to Kleinman et al. (2013)
26	Kepler class	classification of the object according to Kepler et al. (2015)
27	ancillary flag	1 indicates the object was part of the BOSS WD and subdwarfs ancillary program
28	SDSS WD	1 indicates that the objects was classified as a WD based on available SDSS spectra
29	BOSS WD	1 indicates that the objects was classified as a WD based on available BOSS spectra
30	Brown WD flag	1 indicates that the objects was classified as a WD in the the hypervelocity stars spectroscopic survey (Brown et al. 2006, 2007a, 2007b). 2 indicates that the object was classified as something other than a WD
31	Simbad classification	Currently available Simbad classifications
32	DR7 extension	1 indicates that the objects was included as part of the DR7 extension (Sect. 4.7.3)

4.6 SDSS spectroscopic coverage

4.6.1 SDSS objects with multiple spectra

About 24% of the objects in the spectroscopic samples inspected as part of this work have multiple spectra resulting from repeat observations of plates or overlapping regions between plates. Most of these have 2-4 spectra taken with either SDSS or BOSS, but we also found a few white dwarfs with up to 16 spectra. Concerning the work we describe in this chapter, multiple spectra where only inspected for objects with a dubious classification. However, these spectra are a precious resource which can be used to investigate systematic uncertainties in stellar parameter obtained by spectral modelling and to probe for variability of spectral features. For these reasons, in addition to our photometric catalogue of white dwarf candidates, we also provide a list of the available spectra (identifiable via *MJD, plate ID* and *fiber ID*) for all the objects in our catalogue (including the DR7 extension, Sect. 4.7.3).

4.6.2 SDSS white dwarf spectroscopic completeness

Using the $P_{\rm WD}$ in our catalogue and correcting for the completeness of the sample (Fig. 4.5) one can reliably estimate the total number of bright ($g \leq 19$) white dwarfs with $T_{\rm eff} \gtrsim 7000$ K in the SDSS photometric footprint. The ratio of spectroscopically confirmed white dwarfs to this total number of white dwarfs can be used as an estimate of the spectroscopic completeness of SDSS white dwarfs both in terms of spatial and colour distribution. As mentioned before, most of the SDSS white dwarfs are only serendipitous spectroscopic targets, so it comes with no surprise that the average spectroscopic completeness of SDSS white dwarfs is only ∼40%. However, this number is averaged over the entire SDSS photometric footprint, large areas of which have not yet received any spectroscopic follow up (Fig. 4.1). In Fig. 4.10 we show that over the spectroscopic footprint (which covers most of the northern galactic cap), the average spectroscopic completeness of SDSS white dwarfs is actually closer to ∼75%.

However, as shown in Fig. 4.11, the spectroscopic completeness is also very colour-dependent. Because quasars have always been one of the main targets of SDSS, the colour region populated by quasars has received more intense spectroscopic follow up. Consequently, the spectroscopic completeness of SDSS white dwarfs is highest for white dwarfs with colours similar to those of quasars and therefore $T_{\rm eff} \lesssim 10,000$ K. At this cool end in $(u-g, g-r)$ colour space the spectroscopic completeness can be as high as 85%. On the other hand, the colour space occupied by hotter white dwarfs ($T_{\rm eff} \gtrsim 10,000$ K) has received much sparser spectroscopic

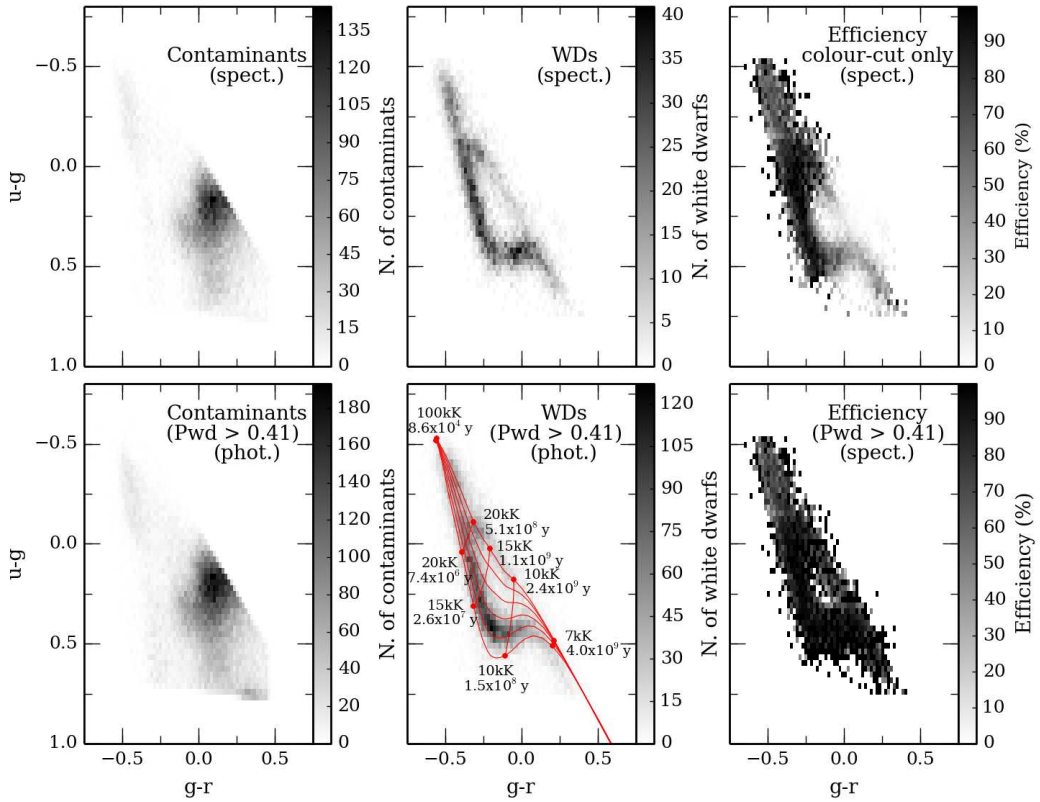

Figure 4.7: DR7 spectroscopic training sample (27,639 objects, top) and DR10 photometric sample (61,969 objects, bottom) within our initial $(u-g, g-r)$ colour-colour selection. The top left and top middle panels show, respectively, the distribution of the contaminants and the white dwarfs from our initial DR7 spectroscopic sample. The top right panel shows the ratio of spectroscopically confirmed white dwarfs to the total number of objects with spectra in DR7, $N_{\rm WD}/(N_{\rm WD}+N_{\rm Cont})$. The top right panel clearly illustrates the efficiency of a selection which only uses colour cuts. Such selection leaves areas of strong contamination at the red and the blue ends of the $(u-g, g-r)$ colour region. The bottom left panel shows the distribution of all sources from our DR10 photometric catalogue with $P_{\rm WD} < 0.41$; these objects would be considered contaminants when compiling a 95% complete sample. Similarly, the bottom middle panel shows the distribution of all sources from our DR10 photometric catalogue with $P_{\rm WD} \geq 0.41$, these objects would all be considered high-confidence white dwarf candidates when compiling a 95% complete sample. White dwarf cooling tracks are shown in the red overlay. Both photometric distributions are extremely similar to their spectroscopically determined counterparts (top panels). The bottom right panel shows the ratio of spectroscopically confirmed white dwarfs with $P_{\rm WD} \geq 0.41$ to the total number of objects with spectra in DR7 with $P_{\rm WD} \geq 0.41$. This diagrams effectively shows the efficiency of our selection method. Unlike the top right panel, this probability based selection is practically independent of the location in colour space.

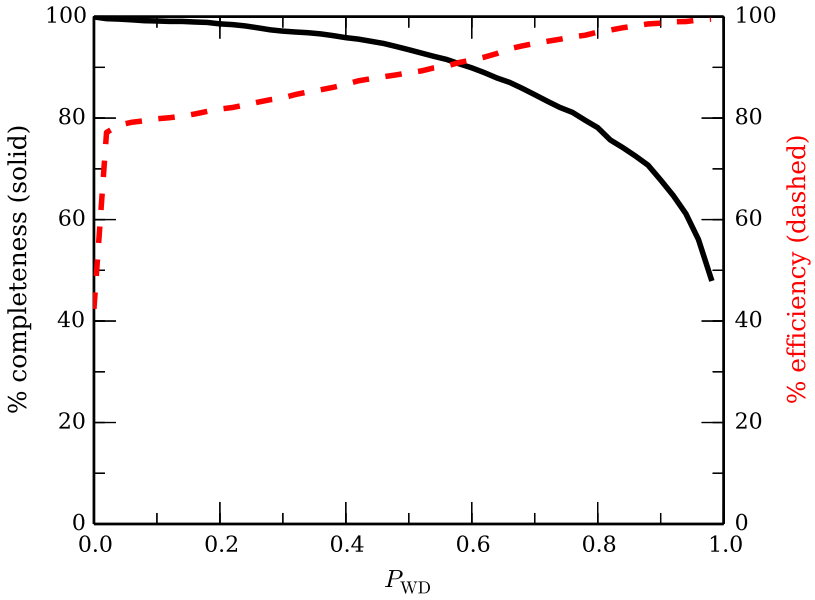

Figure 4.8: Completeness (solid line) and efficiency (dashed line) of samples of white dwarf candidates from our catalogue shown as functions of the minimum value of $P_{\rm WD}$ an object must have in order to be selected. These values of completeness and efficiency were computed using the SDSS-III spectroscopic sample as a reference.

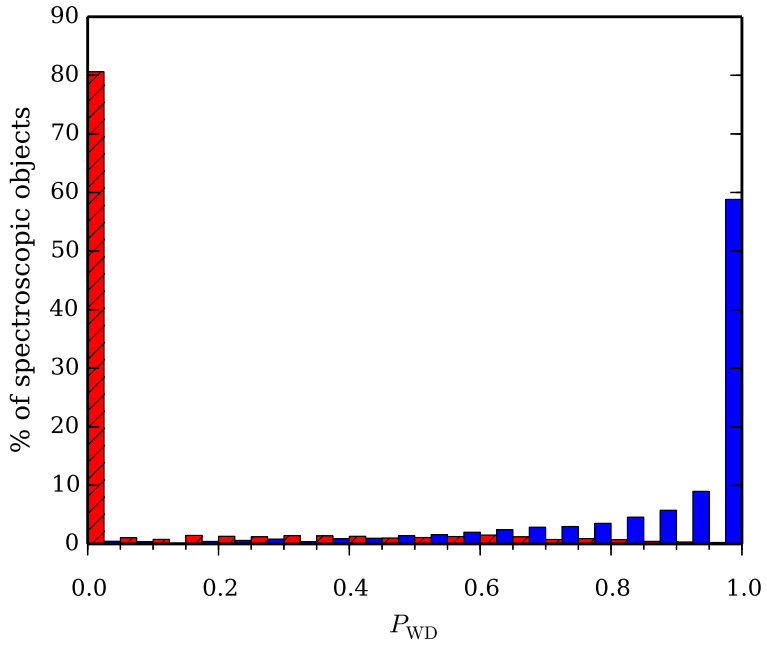

Figure 4.9: Distribution of 8034 spectroscopically identified white dwarfs (blue) and contaminants (red, shaded) with proper motions from the sample of objects with new DR9/10 spectra as a function of $P_{\rm WD}$.

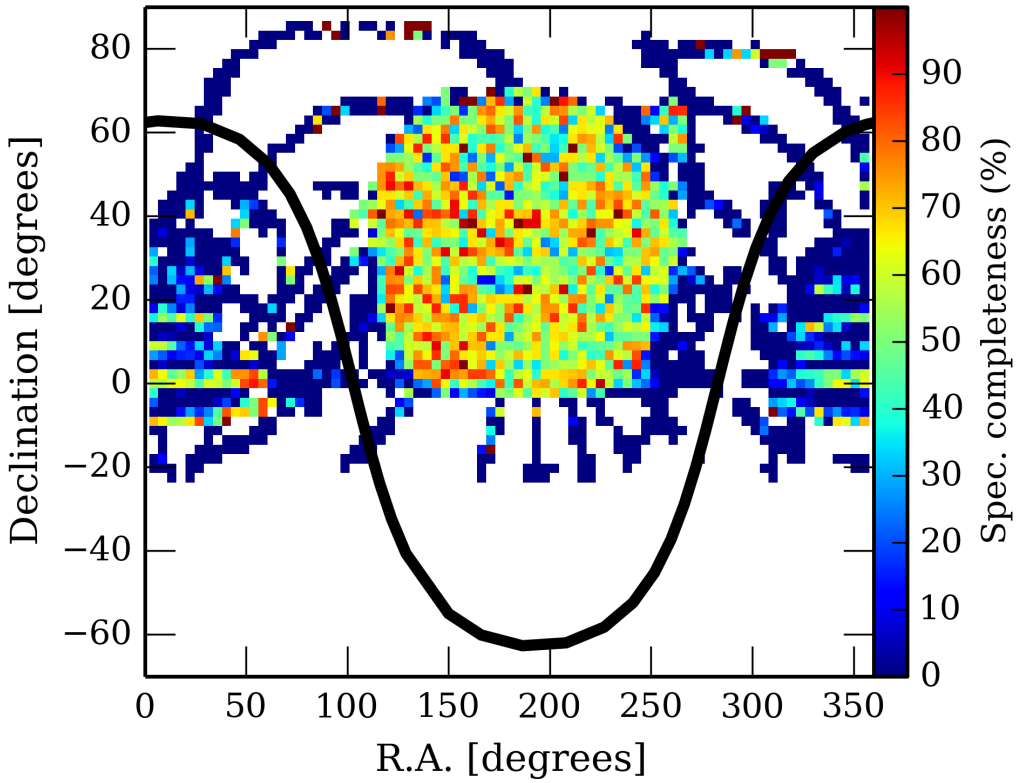

Figure 4.10: Spectroscopic completeness of SDSS white dwarfs satisfying the criteria in Table 4.2, computed as the ratio of spectroscopically confirmed white dwarfs to all high-confidence white dwarf candidates ($P_{\rm WD} \geq 0.41$) over the entire photometric footprint of SDSS (Table 4.5. The black line indicates the location of the galactic plane.

follow-up, which is reflected by the drop in spectroscopic completeness which varies between ∼20% and ∼40%. Even though these less complete colour regions have been specifically covered by SDSS's ancillary white dwarf follow-up programs (Dawson et al., 2013), the number of white dwarfs observed by these programs only marginally affects the overall completeness (Sect. 4.6.3). Fig. 4.10 and 4.11 clearly illustrate that the current sample of white dwarfs with Sloan's spectroscopy is inhomogeneous both in sky and colour distribution and extreme care should be taken when using it to compute any statistics. Each BOSS plates covers an area of 1.49 deg radius and has 1000 fibers. However, on average, only $\sim$ 4 white dwarfs were targeted on each BOSS plate, with only 2-3 plates having up to $\sim$ 20 white dwarfs and over 350 plates with no white dwarfs at all. Using our photometric catalogue of white dwarf candidates we estimated that on average $\sim$ 13 white dwarfs could have been targeted on each BOSS plate, with some more densely white dwarf-populated plates at low galactic latitudes (Fig. 4.12). Even these very simple estimates already

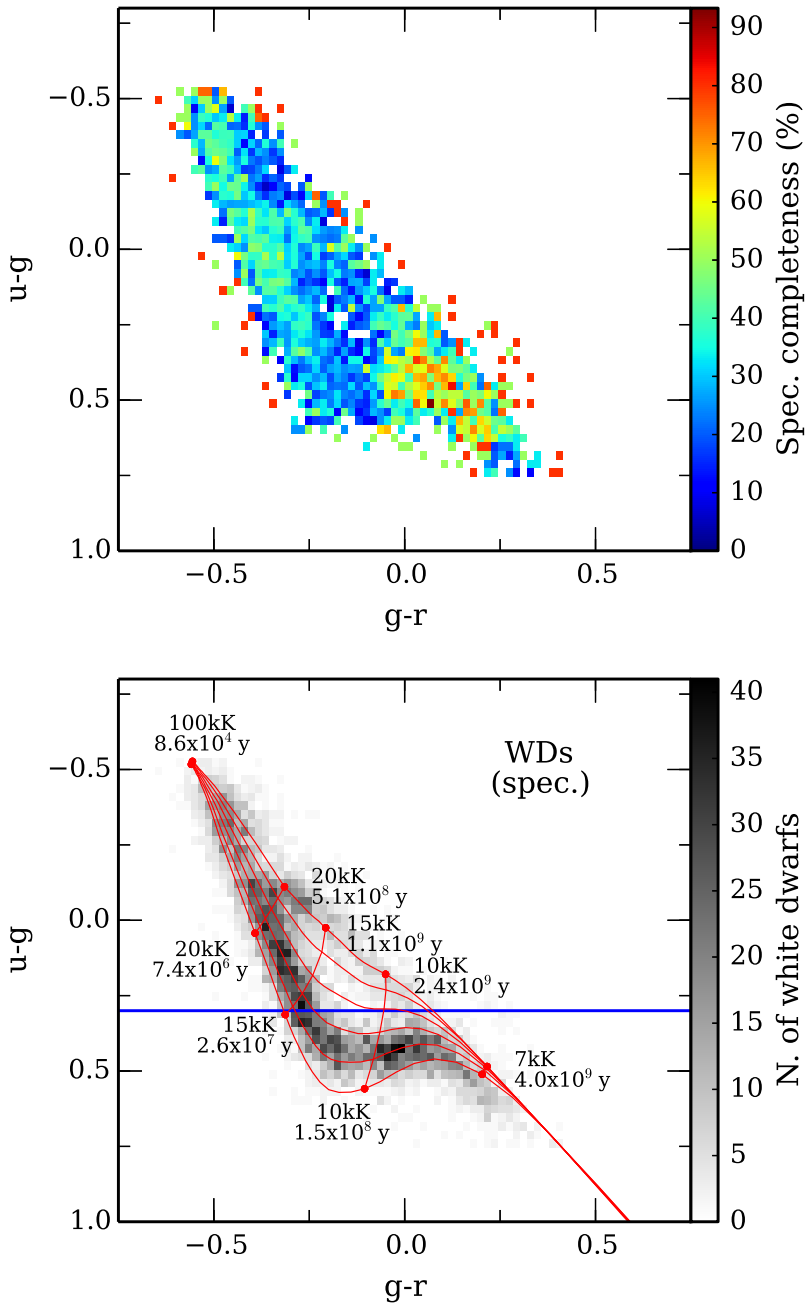

Figure 4.11: *Top panel*: Spectroscopic completeness of SDSS white dwarfs, computed as the ratio of spectroscopically confirmed white dwarfs to all high-confidence white dwarf candidates ($P_{\rm WD} \geq 0.41$) within our initial $(u-g, g-r)$ colour-colour selection. *Bottom panel*: Distribution of spectroscopically confirmed white dwarfs within our initial $(u-g, g-r)$ colour-colour selection with cooling tracks shown as overlay. The blue line indicates the $u-g$ cut applied by the SDSS-III white dwarf and hot subdwarf stars ancillary project target selection. Only objects above the blue line where targeted, excluding most of the cool white dwarfs.

Table 4.6: Constraints used to select the targets of the SDSS-III white dwarf and hot subdwarf stars ancillary project (Dawson et al., 2013).

Only areas of DR7 footprint with galactic extinction in r	$<$	0.5 mag
Colour	constraint	
$(u-g)$	$<$	0.3
$(g-r)$	$<$	0.5
$(g-r)$	$>$	-1
$(u-r)$	$<$	0.4
g	$<$	19.2
For objects with		
$(g-r)$	$>$	-0.1
$(u-r)$	$>$	-0.1
proper motion	$>$	20 mas/yr

show that SDSS, or any other similar multi-object spectroscopic survey (i.e. LAMOST; Zhao et al. 2013, Zhang et al. 2013, WEAVE; 4MOST), could easily provide spectroscopic follow-up of almost all bright white dwarf candidates with very little expenditure of fibers. In fact, a BOSS-like survey could produce a $> 95\%$ complete, magnitude limited ($g \leq 19$), spectroscopic sample of white dwarfs by dedicating just over 1% of its fibers to white dwarf follow up. With such a complete and well defined spectroscopic sample it would be possible to carry out extremely reliable and diverse statistical analyses and finally answer many of the open questions about the formation and evolution of white dwarfs and their progenitors. Furthermore such a large spectroscopic sample would include many rare types of white dwarfs.

4.6.3 SDSS-III white dwarf and hot subdwarf stars ancillary project

About 3.5% of the BOSS fibers in DR9 and DR10 were devoted to 25 small ancillary programs. One of these ancillary programs, the SDSS-III white dwarf and hot subdwarf stars ancillary project, specifically targeted 5709 white dwarf and hot subdwarf candidates selected using colour and proper motion as summarized in Table 4.6 (Dawson et al. 2013, Ahn et al. 2014). Using the corresponding ancillary target flag (Dawson et al., 2013) we retrieved spectra, *ugriz* photometry and proper motions of all the targets of this ancillary program. 4104 of these SDSS ancillary targets match the criteria (in either DR7 or DR10) in Table 4.2 and have proper motions and, therefore, must have been visually classified by us in either the DR7 training

Table 4.7: Results of the comparison of the SDSS-III white dwarf and hot subdwarf stars ancillary project with our classification of SDSS spectra.
After inspecting the spectra of the 904 ancillary targets not classified as white dwarfs by us, we are confident that these are most likely hot subdwarfs.

Total number of WDs from the ancillary program included in our catalogue including DR7 extension	4104
Number of ancillary program targets not classifed as WDs.	904

sample or the DR9/10 spectroscopic sample. When comparing our classification to the targeting selection of the ancillary project we established that 78% of the ancillary project targets included in our catalogue where classified as white dwarfs by us (Table 4.7), with the vast majority of the rest being subdwarfs. This comparison shows that the targeting strategy adopted in this ancillary program was very efficient, however the criteria in Table 4.6 limit the selection to white dwarfs with hydrogen dominated atmospheres (DA) hotter than $\sim 14,000$ K and white dwarfs with helium dominated atmospheres (DB) hotter than ~ 8000 K (Table 4.6). In conclusion the SDSS-III white dwarf and hot subdwarf stars ancillary project significantly contributed in increasing the number of SDSS white dwarfs with spectra, but the sample of white dwarfs produced is very incomplete and, because of the aforementioned observational biases, it should be handled with extreme care when used for statistical analysis.

4.7 Limitations and corrections

4.7.1 Proper motions

One of the main limitation of the selection method used to generate this catalogue is that our $P_{\rm WD}$ can only be calculated for objects with proper motions. 3.8% of all the spectroscopically confirmed white dwarfs we examined do not have proper motion and we can therefore expect that our DR10 photometric catalogue is incomplete by ~ 870 white dwarfs candidates on account of them not having proper motion.

4.7.2 Extremely Low Mass white dwarfs (ELM white dwarfs)

Even though our spectroscopic training sample, initially drawn from a broad colour selection (Fig. 4.2), includes the vast majority of single white dwarfs (see Sect.4.8) it does not include some rarer types of white dwarfs with more exotic colours.

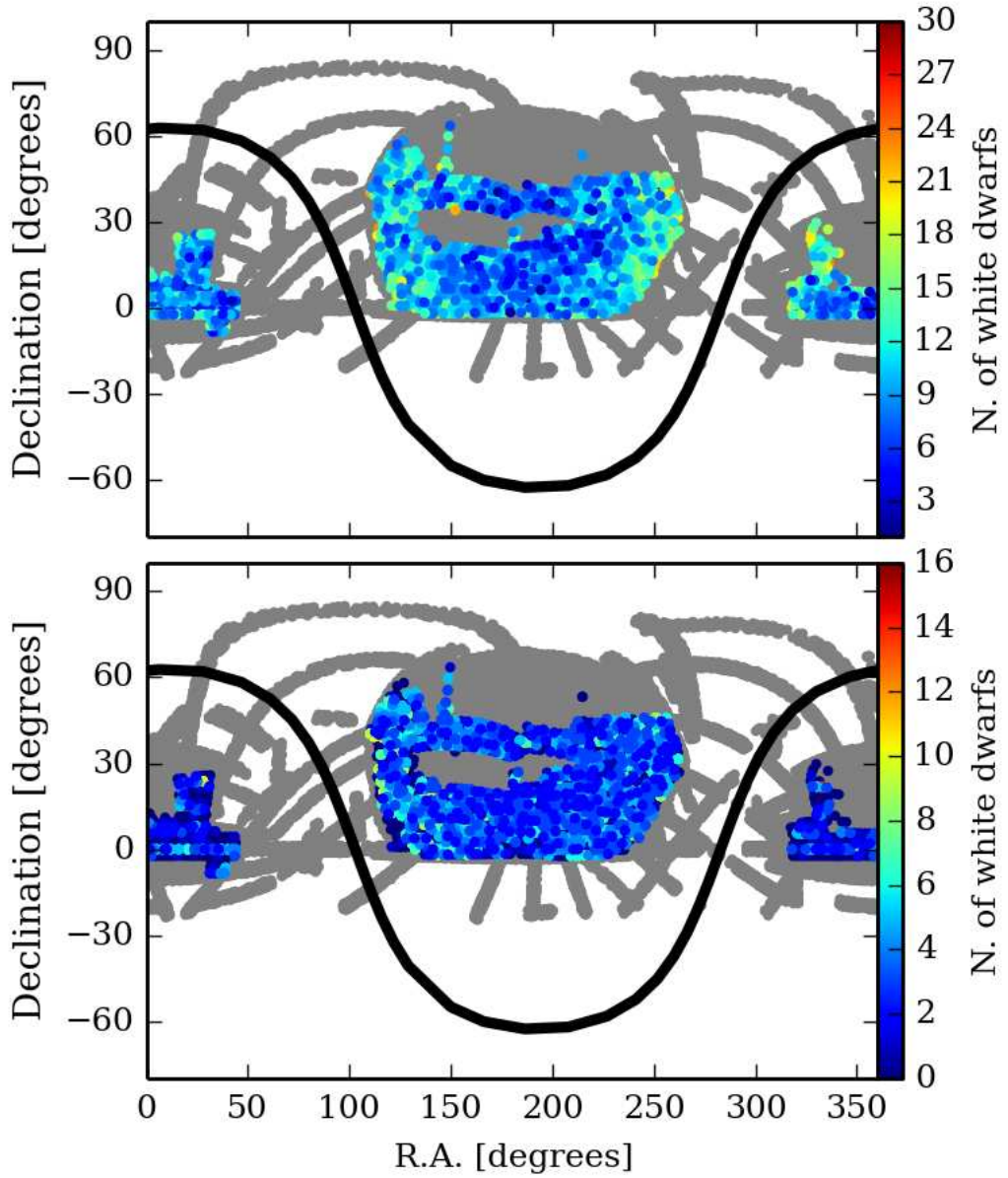

Figure 4.12: Location of BOSS plates overlaid on the DR10 photometric footprint (grey). The black line indicates the location of the galactic plane.
Top panel: The colour of the plates indicates the number of high confidence white dwarf candidates ($g \leq 19$) from our catalogue per plate.
Bottom panel: The colour of the plates indicates the number of spectroscopically confirmed bright ($g \leq 19$) white dwarfs which were observed on the BOSS plate and released in DR9/10.
Both panels clearly illustrate that the number of white dwarfs (or white dwarf candidates) per plate decreases with increasing distance from the galactic plane

Extremely low mass (ELM) white dwarfs are likely to be among such rare types (Brown et al., 2010). We tested the ability of our selection method to correctly identify ELM white dwarfs by retrieving the SDSS phototmetry of all bright ($g \leq 19$) ELM white dwarfs from Gianninas et al. (2014) and verifying whether or not they were recovered in our catalogue. We determined that only 17 out of 37 are included in our catalogue. One of the ELM white dwarfs was excluded because of bad photometry in SDSS, but the remaining 19 were simply outside our initial colour cut. Furthermore ELM white dwarfs have peculiar spectra which can make it hard to correctly classify them as white dwarfs. Of the 17 ELM white dwarfs in our catalogue 11 have either a SDSS or BOSS spectra and were therefore visually classified by us. Only one of these ELM white dwarfs was erroneously classified as a NLHS. Consequently we believe that miss-classification of ELM white dwarfs in our training sample does not significantly effect our selection method. In fact only 2 of the ELM white dwarfs in our catalogue have $P_{\rm WD} < 0.41$ while the remaining 16 have $P_{\rm WD} > 0.6$. We conclude that ELM white dwarfs within our colour regions would most likely be identified as high confidence white dwarfs candidates.

4.7.3 DR7 to DR10 miss-matches: the "DR7 extension"

When trying to retrieve the 6706 white dwarfs with proper motions of our DR7 spectroscopic training sample (Sect. 4.3) from our DR10 photometric catalogue, we noticed that some DR7 objects could not be correctly matched in DR10. The cross matching of DR7 spectra to DR10 photometric sources was done using modified Julian date (MJD), plate ID and fiber ID which, together, uniquely identify any spectrum in SDSS. This was faster and more reliable than a coordinate cross match using the entire DR10 photometric database or a specifically selected subset of it (some objects underwent changes in coordinates, photometry or flags in between data releases). Furthermore, in this way, we were able to check that the DR7 spectra were still available in DR10 and to check for other possible incongruences between the data releases. To our surprise we found that our DR10 photometric sample only included 6560 of the spectroscopically confirmed white dwarfs. We determined that 11 of the "missing objects" could not be matched to sources in DR10 because the MJD with which their spectra were identified changed between DR7 and DR10 [1]. However the objects are included in the DR10 photometric sample and therefore the cross-match was manually corrected and our count was updated to 6571 retrieved DR7 white dwarfs. The remaining 135 white dwarfs are missing

[1]From the spectra we examined, we determined that MJDs uniquely identifying SDSS spectra have changed between DR7 and 10 for the following plates: 0389, 2129, 2516, 2713, 2865.

Table 4.8: Detailed break down of the reasons why 135 white dwarfs from our DR7 training sample do not figure in the main DR10 photometric catalogue.
29 objects marked as "colours changed" experienced changes in their recorded *ugriz* magnitudes such that in DR10 they would not fall into our initial colour cut.
23 objects marked as "Not in SDSS-III database" either fall in the SEGUE-1 imaging scans which were not included in SDSS-III or are in areas of the sky where, probably because of the new SDSS-III sky subtraction, faint sources near a bright source were not identified (Ahn et al., 2012).

N. of WDs "missing"	Cause
17	$type \neq 6$ in DR10
63	$gmag > 19$ in DR10
29	colours changed
3	No recorded proper motion in DR10
23	Not in SDSS-III database
135	

from the photometric DR10 sample because of differences in their photometry or flags in DR10 compared to DR7 (Table 4.8).

In order to make our catalogue as complete as possible we decided to add a "DR7 extension" to our original list of 61,969 DR10 white dwarf candidates. This extension was created by recovering *ugriz* photometry for all reliable primary photometric sources in DR7 that satisfied the criteria described in Table 4.2 and then selecting only those objects that did not appear among the 61,969 DR10 photometric candidates. The cross-matching between DR9/DR10 and DR7 photometric sources was done by comparing sky coordinates using a 1 arcsecond matching radius which generated a list of 3799 DR7 objects. 689 of these do not have any counterpart in DR10 as they either fall in the SEGUE-1 imaging scans which were not included in SDSS-III or are in areas of the sky where, probably because of the new SDSS-III sky subtraction, faint sources near a bright source were not extracted (Ahn et al., 2012). The remaining 3110 are objects whose photometric data or flags have changed between data releases such that they no longer fulfil the criteria in Table 4.2 in DR9/10. As a final check we confirmed that the "DR7 extension" includes all of the 135 white dwarfs that were spectroscopically identified in DR7, but which were missing in our DR10 photometric catalogue (Table 4.8). Furthermore within the "DR7 extension" we were also able to identify and classify 29 new white dwarfs which only have BOSS spectroscopy (Table 4.9).

Table 4.9: Classification of the 297 objects with BOSS spectra, found in our "DR7 extension". 29 of the new spectroscopically confirmed white dwarfs had not received spectroscopic follow-up before DR9.

Class	number of objects
DA	32
DB	7
DAB/DBA	1
DAO	0
DC	4
DZ	0
DQ	1
Magnetic WD	0
WD+MS	6
CV	2
NLHS	21
QSO	222
Unreliable	1
Unclassified	0
New spectroscopically confirmed WDs	29

4.7.4 DR10 to DR7 miss-matches

In the previous paragraph we discussed how a few objects which fulfilled our selection criteria (Table. 4.2) in DR7 did not do so in DR10. Similarly we expected to find some sources with DR7 spectra which did not fulfil our selection criteria in DR7 but do so in DR10 and therefore would be included in our main photometric sample. From our 61,969 photometric candidates we selected all objects with SDSS-II spectroscopy which were not included in our initial DR7 spectroscopic sample, and therefore already classified. We identified 2071 of these SDSS-II spectroscopic sources which we had not yet inspected even though they were included in of our catalogue.

Once again the main reasons for the "appearance" of these sources in our DR10 selection are: changes in their g magnitude which may have moved an object below our $g \leq 19$ limit; corrections of flags of objects previously, erroneously, classified as "extended sources" and inclusion of proper motions for objects which did not previously have one. However, we also identified 31 sources in our DR10 sample with SDSS spectra which simply do not have any DR7 photometry (in our catalogue they lack a DR7 photometric ID). In order to keep our catalogue as consistent and complete as possible, we decided to retrieve spectra for these 2071 sources (using the DR7 photometric ID included in our table) and proceeded to visually classify

Table 4.10: Classification of the 2071 objects with SDSS spectra which did not fulfil our selection criteria in DR7 but did so in DR10

Class	number of objects
CV	6
DA	136
DB	12
DAB	27
DAO	1
DC	14
DZ	3
DQ	5
Magnetic WD	1
WD+MS	9
NLHS	95
QSO	1675
Unclassified	2
unreliable	84

them. The results of the classification of these 2071 objects are shown in Table 4.10.

4.8 Comparison with other catalogues

4.8.1 Kleinman et al 2013

The Kleinman et al. (2013) catalogue of spectroscopically identified DR7 white dwarfs contains 20407 spectra corresponding to 19712 unique objects of which only 7424 are brighter than g=19. Unlike our spectroscopic samples (DR7 training sample and DR9/DR10 BOSS sample) the Kleinman et al. (2013) catalogue does not have a set magnitude limit and includes spectra of extremely faint objects. Most of these have low signal to noise ratios making the classification, for at least some of them, inevitably less reliable. In order to carry out a comparison between our spectral classification and Kleinman's we proceeded to cross match the Kleinman et al. (2013) catalogue of DR7 white dwarfs with the DR10 *specphotoall* table using modified Julian date (MJD), plate ID and fiber ID and obtained SDSS-III IDs for these objects. Analogously to what is described in Section 4.7.4, 52 spectra could initially not be matched to DR10 sources because of changes in the MJD and another 149 spectra could not be matched because the corresponding photometric sources are not included in the DR10 photometric database. 861 more white dwarfs were rejected by our selection because of their colour, flags or lack of recorded proper motion (Table 4.11). After manually correcting the miss-matching MJDs and including

Table 4.11: Detailed break down of the reasons why 861 white dwarfs from the Kleinman et al. (2013) catalogue are not included in our main DR10 photometric catalogue. Most of these are white dwarfs with a main sequence companion. Note that 119 of these were recovered in our "DR7 extension" (sect 7.3)

Keinman WDs excluded in DR10 photometric catalogue	Cause
601	Excluded by criteria in Table 4.2
260	No proper motion
861	

the "DR7 extension" discussed before, we established that our catalogue includes 6689 objects classified as white dwarfs by Kleinman et al. (2013).

Inspecting the results of our spectroscopic classification, we find that we also identified 99.6% of these 6689 objects as white dwarfs. Only 30 (0.4%) of Kleinman's white dwarfs where classified as contaminants by us when preparing the spectroscopic training sample (Sect. 4.3). We closely re-examined all available spectra for these 30 objects. We confirm our initial classification of 20 objects as contaminants (18 NLHS and 2 QSO),and one object as "unclassified" because of the very low quality of its spectrum. However we concede that the remaining 9 objects are most likely white dwarfs and our initial classification was wrong.

Our catalogue also includes 261 objects with DR7 spectroscopy which we classified as white dwarfs, but which are not included in Kleinman et al. (2013) (Table 4.1). Kleinman et al. (2013) do not include a list of all spectra that they processed, and we have therefore no way to assess whether they inspected those objects. We conclude that our classification is remarkably close to Kleinman's and the disagreement over a very limited number of objects in our training sample does not effect our selection method.

Furthermore, unlike Kleinman et al. (2013), we aim to provide a well defined sample SDSS white dwarfs candidates without being limited by the availability of spectroscopy. Our catalogue contains $\simeq 23,000$ high-confidence bright ($g \leq 19$) white dwarfs candidates, over 3 times the number of white dwarfs in Kleinman et al. (2013) catalogue with the same magnitude limit, underlining the remaining potential for follow up spectroscopy.

4.8.2 Hypervelocity stars. I,II,III (Brown et al 2006, 2007a, 2007b)

The hypervelocity stars spectroscopic survey (Brown et al. 2006, 2007a, 2007b) identified a total of 260 white dwarfs serendipitously found among B star candidates.

48 of these white dwarfs have $g > 19$ and are therefore not included in our photometric sample; another 9 are excluded by our initial selection criteria (Table 4.2) and 23 more do not have proper motions in SDSS DR9/10. This leaves 180 white dwarfs spectroscopically identified by Brown et al. which are included in our DR10 photometric catalogue and which we flag as "known white dwarfs". Our catalogue also includes 296 hypervelocity survey targets which were classified as "non white dwarfs" by Brown et al. We flagged these objects to recognise them as "known contaminants". Even though this sample of confirmed white dwarfs and contaminants is quite small, it was selected and classified completely independently from our work. Therefore these white dwarfs and contaminants are valuable test objects to verify once more the reliability of our $P_{\rm WD}$.

We established that the vast majority of the 180 white dwarfs have $P_{\rm WD}$ greater than 0.9 and only 11 of them have probabilities lower than 0.6. Out of the 296 contaminants 34 have $P_{\rm WD}$ greater than 0.5, however only 11 of them have probability values higher than 0.7. In conclusion our $P_{\rm WD}$ seems to be somewhat weaker when trying to separate these contaminants as they were specifically selected as objects with colours similar to those of typical white dwarf *and* to have high proper motions.

4.8.3 Kepler et al. 2015

Soon after completion of the work presented in this chapter, Kepler et al. (2015) posted a catalogue of 9088 white dwarfs subdwarfs spectroscopically identified among the SDSS spectra obtained after DR7. For completeness, we compare our classification of objects with new DR9/10 spectra (Sect. 4.4) with Kepler's catalogue. Our catalogue includes 2041 white dwarfs and 590 subdwarfs from Kepler's catalogue. Inspecting the results of our spectroscopic classification, we find that we also identified 88.5% of these 2041 objects as white dwarfs. 234 (11.5%) of Kepler's white dwarfs where classified as contaminants by us (Sect. 4.4). We closely re-examined all available spectra for these 234 objects. We confirm our initial classification of NLHS for 223, but concede that the remaining 11 are likely white dwarfs.

Our catalogue also includes 57 objects with DR9/10 spectroscopy which we classified as white dwarfs, but which are not included in Kepler (Table 4.12). Kepler do not include a list of all spectra that they processed, and we have therefore no way to assess whether they inspected those objects.

Table 4.12: Result of the comparison between our classification of objects with spectra taken after DR7 and Kepler et al. (2015).

WDs from Kepler et al 2014 included in our catalogue	2041
subdwarfs from Kepler et al 2014 included in our catalogue	590
Kepler et al. WDs not classified as WDs by us	234
Kepler et al. subdwarfs classified as WDs by us	5
Objects with a DR9/10 spectrum classified by us as WDs, not included in the Kepler et al. (2014)catalogue	57

4.8.4 Follow-up spectroscopy: 11 new white dwarfs

As a final test for our selection method we selected 17 white dwarfs candidates from our catalogue which did not have a SDSS or BOSS spectrum (at the time of DR9) and spanned a wide range of $P_{\rm WD}$. On June 7^{th} and 8^{th} 2013, we obtained spectroscopy of these 17 objects using the double-armed Intermediate Resolution Spectrograph[2] (ISIS) on the William Herschel Telescope (WHT) on the island of La Palma. We observed under 1" seeing conditions. We used the R600R and R600B gratings in the ISIS blue and red arms respectively, with a 1" slit. The blue arm was centred at 4351Å and the red arm at 6562Å. The blue spectra covered a total wavelength range from ∼3700Å to ∼5000Å and the red spectra ranged from ∼5700Å to ∼7200Å. The spectral resolution is ∼2 Å and ∼1.8 Å in the red and in the blue arm respectively. Two consecutive 10 minute exposures were taken in order to increase the signal-to-noise ratio (S/N) of the average spectrum. We adopted a standard reduction and calibration for the spectra (Greiss et al., 2014). The spectra allowed us to classify our candidates and corroborate the validity of our $P_{\rm WD}$: the 9 targets with $P_{\rm WD} \geq 0.89$ were all confirmed as white dwarfs, out of 4 intermediate probability candidates ($> 0.45, < 0.7$) only the highest probability candidate was confirmed as a white dwarf and finally only one of the 4 low probability targets (< 0.39) is a white dwarfs (Table 4.13, Fig.4.13, Fig.4.14). The release of DR10 added new BOSS spectra, compared to DR9, and 3 of the photometric candidates we spectroscopically followed-up now also have BOSS spectra (SDSSJ1354+2530, SDSSJ1439+2344, SDSSJ1306+1333; marked with * in Table. 4.13). Visual inspection of these BOSS spectra confirmed our classification based on the ISIS spectra.

[2]http://www.ing.iac.es/Astronomy/instruments/isis/

Table 4.13: Results of classification of the newly acquired ISIS spectra for 17 white dwarfs candidates from our catalogue. In the case of DA white dwarfs we also include effective temperature and surface gravity calculated by fitting the spectra with 1-D atmospheric models.

SDSS name	probability of being a WD	classification	$T_{\rm eff}$ (K)	log g
SDSSJ141455.36+240839.0	1.000	DA	15071±72	7.560±0.018
SDSSJ134231.80+043517.4	0.999	DA	20566±65	7.770±0.019
SDSSJ135024.28+052252.3	0.999	DA	22037±94	8.010±0.020
SDSSJ143953.64+234453.6*	0.993	DA	24726±9	8.080±0.010
SDSSJ160726.61+532246.7	0.991	DA	12976±98	8.010±0.030
SDSSJ131825.92+500351.7	0.985	DC	–	-
SDSSJ154621.86+560325.8	0.941	DA	15422±103	7.950±0.017
SDSSJ135451.45+253048.0*	0.933	DA	28389±54	7.960±0.024
SDSSJ132936.48+532211.3	0.891	DA	17707±68	7.860±0.016
SDSSJ134614.32+080411.2	0.696	DA	16525±91	8.260±0.022
SDSSJ145042.93+094055.9	0.566	NLHS	–	-
SDSSJ121910.44+230020.7	0.523	NLHS	–	-
SDSSJ144601.03+483057.7	0.455	NLHS	–	-
SDSSJ130625.92+133349.2*	0.355	NLHS	–	-
SDSSJ154843.29+472936.2	0.315	DB	–	-
SDSSJ143554.16+544448.2	0.288	NLHS	–	-
SDSSJ134700.48+111123.8	0.250	NLHS	–	-

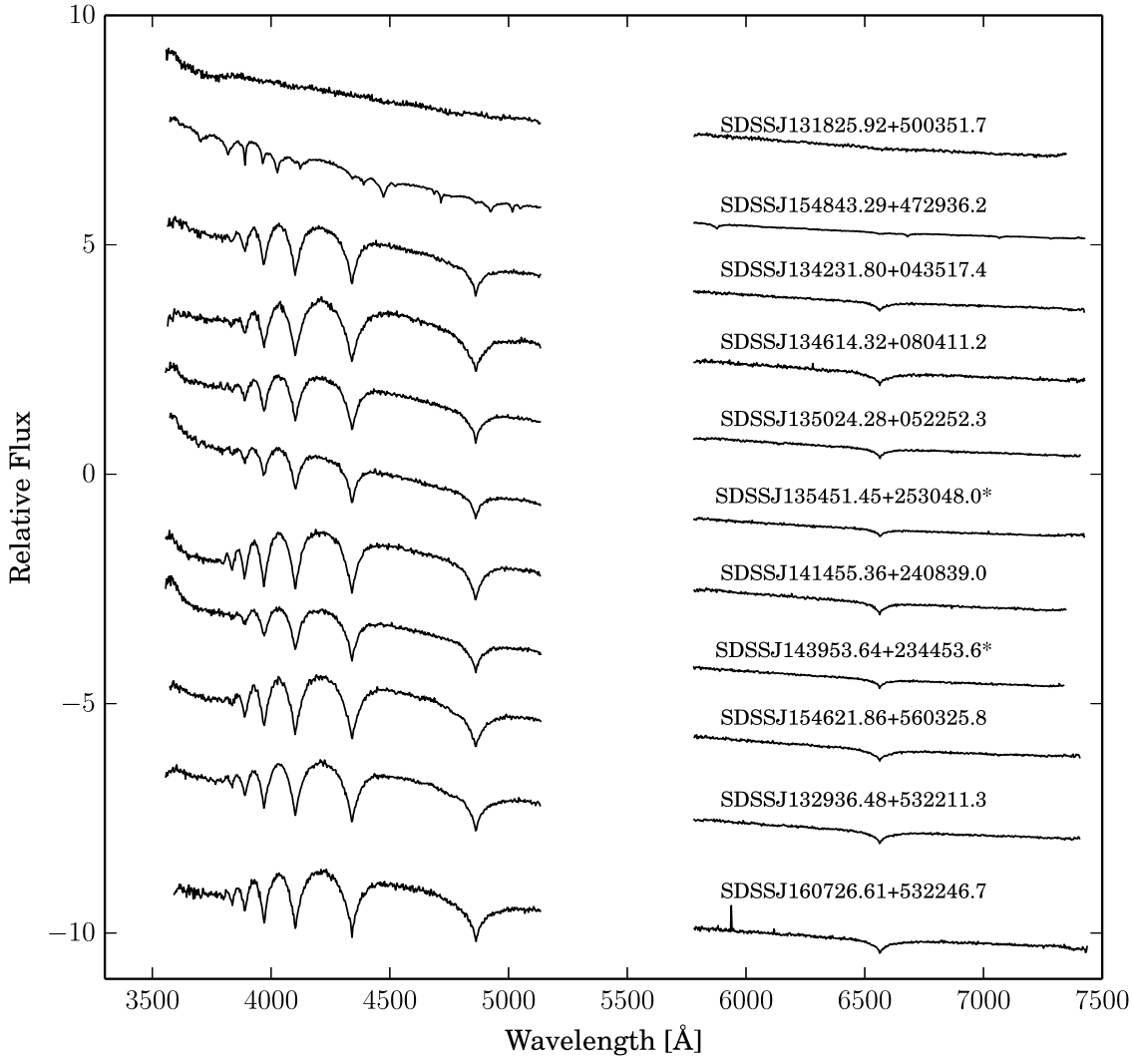

Figure 4.13: WHT ISIS spectra (blue arm + red arm; R600 grating) of the 11 confirmed high-confidence ($P_{\rm WD} \geq 0.6$ except for SDSSJ154843.29+472936, see Table 4.13) white dwarf candidates. Each spectrum is labelled with the SDSS name. Objects marked with * have a new BOSS spectrum released in DR10

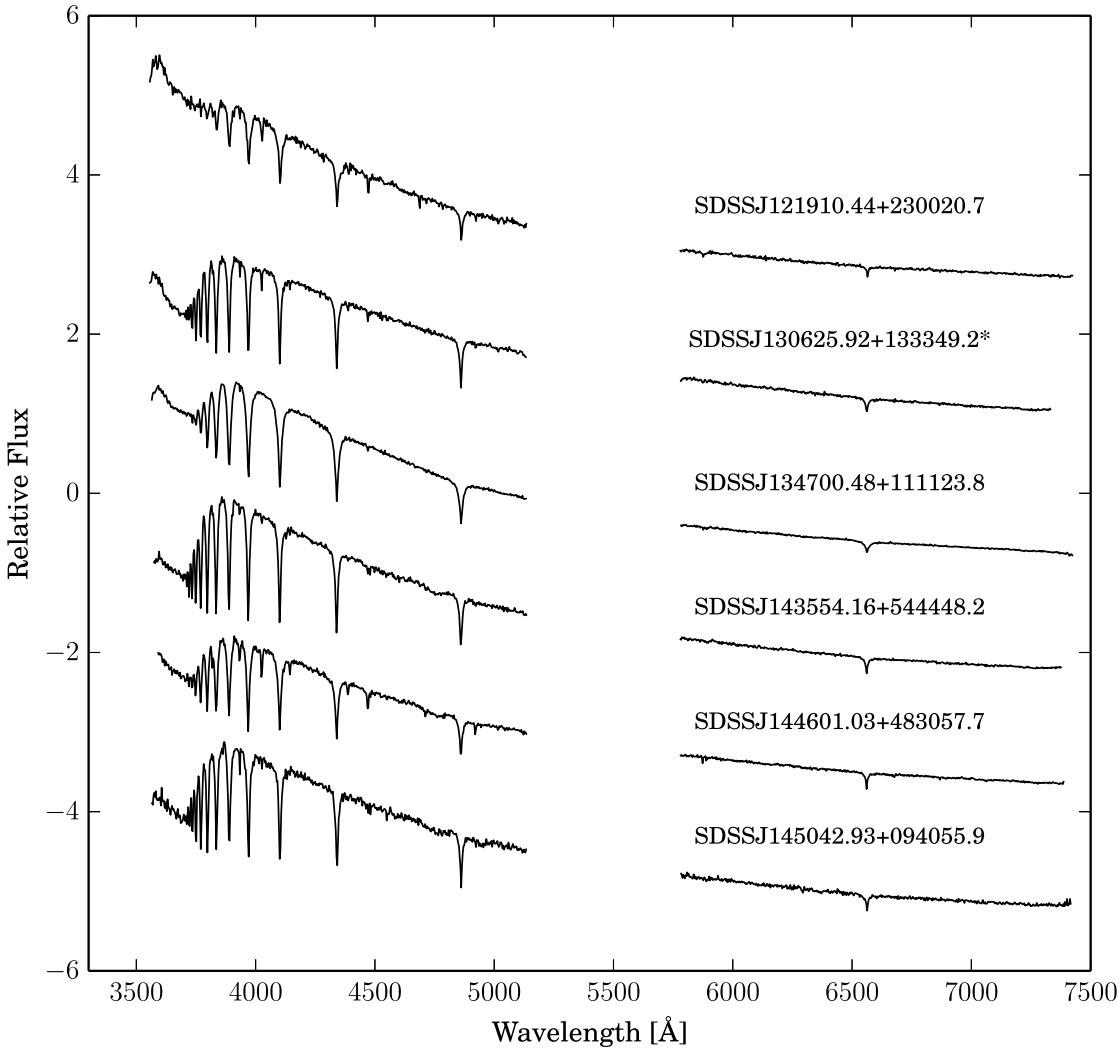

Figure 4.14: WHT ISIS spectra (blue arm + red arm; R600 grating) of the 6 low-confidence ($P_{\rm WD} < 0.6$, see Table 4.13) white dwarf candidates which were later classified as NLHS. Each spectrum is labelled with the SDSS name. Objects marked with * have a new BOSS spectrum released in DR10

4.9 Conclusions

We developed a selection method which allows to reliably select white dwarf candidates relying on their colours and reduced proper motion. By using the distribution of a large sample of spectroscopically confirmed white dwarfs and contaminants in colour-RPM space we calculate a *probability of being a WD* ($P_{\rm WD}$) for any object with available multi-band photometry and proper motion.
The spectroscopic sample used to develop our selection method was created by classifying over 27,000 spectra of blue objects from SDSS DR7. In developing our selection method we decided to limit our efforts to bright objects ($g \leq 19$) as fainter sources are less likely to have reliable detections on the historic photographic plates, necessary to calculate proper motions. We used our selection method to calculate $P_{\rm WD}$ for 61,969 primary photometric point sources selected from SDSS DR10 and for 3799 primary point sources selected from SDSS DR7 which fulfilled our selection criteria in DR7, but have incomplete data in the following DRs. This catalogue of over 65,000 objects with calculated $P_{\rm WD}$ contains 8699 objects with available Sloan spectroscopy which we classified as white dwarfs. Using different values of $P_{\rm WD}$ as threshold, one can produce white dwarf candidates samples based on the compromise between completeness and efficiency best suited for different specific uses. We estimate that our SDSS DR10 photometric catalogue contains $\simeq 23,000$ high confidence white dwarf candidates of which $\simeq 14,000$ have not been followed up spectroscopically. These statistics imply that the spectroscopic sample of SDSS white dwarfs is currently, on average, only $\sim 40\%$ complete for white dwarfs with $T_{\rm eff} \gtrsim 7000$ K and $g \leq 19$, underlining the remaining potential for follow-up spectroscopy.

In Chapter 5 we also present a further test of our selection method using an independent sample of spectroscopically confirmed white dwarfs and contaminants from the LAMOST survey.

The possible applications of our catalogue of white dwarfs candidates span various areas of white dwarf research. In particular, in Chapter 7 we use our catalogue as the starting point of our search for variable white dwarfs in SDSS Stripe 82 and in Chapter 8 we present its application in our search for metal polluted white dwarfs with debris discs.

While we developed our method using SDSS DR7 and present here its application to SDSS DR10, it can be used on any sample of objects having multi band photometry and proper motions, e.g. in Chapter 6 we present a preliminary application to the VST ATLAS surveys.

Chapter 5

An independent test of the photometric selection of white dwarf candidates using LAMOST DR3

5.1 Introduction

The recently initiated Large Sky Area Multi-Object Fiber Spectroscopic Telescope (LAMOST; Luo et al. 2015) survey provides hundreds of thousand of spectra per year and its sky coverage overlaps to a large degree with the photometric footprint of SDSS (Fig 4.1). Here we crossmatch our catalogue of photometric SDSS white dwarf candidates (Chapter 4) with the over 4 million spectra obtained to date by LAMOST and find spectra for 309 white dwarfs. We use this new set of white dwarfs to test our photometric selection method, as well as to analyse the effects of the target selection algorithm of LAMOST on the observed white dwarf population. We also provide the stellar parameters of the newly-identified DA (hydrogen dominated atmosphere) white dwarfs, namely the effective temperatures, surface gravities and masses.

5.2 SDSS photometric white dwarf candidates observed by LAMOST

The catalogue presented in Chapter 4 includes 65,768 bright($g \leq 19$) point sources selected according to their available SDSS photometry and colours. The catalogue contains not only white dwarfs, but also quasars and other blue stars, however each

Table 5.1: Summary of the cross-matching of SDSS white dwarf candidates with LAMOST DR3

	n. of objects	n. of spectra
All objects from cross-match	5173	6101
SDSS and LAMOST spectra	3500	3964
of which WDs	774	1177
LAMOST spectra only	1673	2137
of which WDs	309	387
already published	64	97
unpublished	245	290

object has an associated $P_{\rm WD}$ calculated from its $g-z$ colour and reduced proper motion.

We estimate that our catalogue contains $\simeq$14,000 white dwarfs which have not yet received spectroscopic follow up in the latest data release of SDSS (DR12). The vast number of available LAMOST spectra, combined with the large overlap in the SDSS and LAMOST footprints (Fig. 4.1), implies that a considerable number of white dwarf candidates have most likely been observed by LAMOST. Consequently combining our catalogue of SDSS white dwarfs candidates with all available LAMOST spectra is not only a quick and reliable way to identify new white dwarfs, but also provides a further test to corroborate the reliability of our selection method.

We cross-matched all 65,768 objects from the Gentile Fusillo et al. (2015) catalogue with the list of the 4.6 million LAMOST spectra and retrieved 6,101 spectra corresponding to 5173 unique objects (Table 5.1). 3500 of these have also received SDSS spectroscopic follow up and 64 further objects had already been identified on the base of their LAMOST spectra as white dwarfs or white dwarf binaries by Zhang et al. (2013); Zhao et al. (2013); Ren et al. (2014); Rebassa-Mansergas et al. (2015).

Since the main goal of this project is to test our photometric selection method using an independent spectroscopic sample of white dwarfs, we limited ourselves to objects which have no SDSS spectroscopic counterpart. This reduced the sample to 2,040 spectra corresponding to 1,609 unique LAMOST objects; plus the 64 known LAMOST white dwarfs mentioned above. Finally we visually classified all remaining white dwarf candidates with unpublished LAMOST spectra. We subdivided the identified white dwarfs into 10 types (Table 5.2, Fig. 5.1), and the contaminants

Table 5.2: Classification of the 2,040 unpublished LAMOST spectra of 1,609 white dwarf candidates from the Gentile Fusillo et al. (2015) catalogue.

Class	n. of objects	n. of spectra
DA	196	222
DB	5	6
DAB/DBA	2	2
DO	3	5
DC	10	12
DZ	3	3
Magnetic WD	2	2
WD+MS	4	4
CV	19	33
Planetary nebula	1	1
NLHS	393	538
QSO	546	678
K/M stars	3	3
Unreliable	422	531

into 3 types: "K/M stars", "Quasars" (QSOs) and "Narrow Line Hydrogen Stars" (NLHS), in which we group different stars with low-gravity hydrogen dominated atmospheres such as subdwarfs, extreme horizontal branch stars and A/B type stars. We also marked as "unreliable" all spectra which had a signal-to-noise ratio too low for a reliable classification. The results of our classification are summarized in Table 5.2.

Inspection of the Table reveals that we have identified 245 white dwarfs (with a total of 290 spectra), of which over 80 per cent have hydrogen dominated atmospheres (DA). DAs are known to constitute the vast majority of all white dwarfs (McCook & Sion, 1999), so the ratio above is unsurprising. Querying the SIMBAD astronomical database, we find that 57 of our 245 white dwarfs had already been identified as such (as single stars or part of binary systems) in other studies. In conclusion we report the discovery of 188 new white dwarfs.

5.2.1 Cataclysmic variables in the LAMOST sample

During the classification of LAMOST spectra we identified 19 cataclysmic variables (CV, Table 5.2). 10 of these objects are known CVs while the remaining nine are new discoveries. Considering the limited size of our white dwarf sample the number of CVs found is remarkably high. However, we are not aware of any aspects of the targeting strategy of LAMOST which could have led to preferential observation of

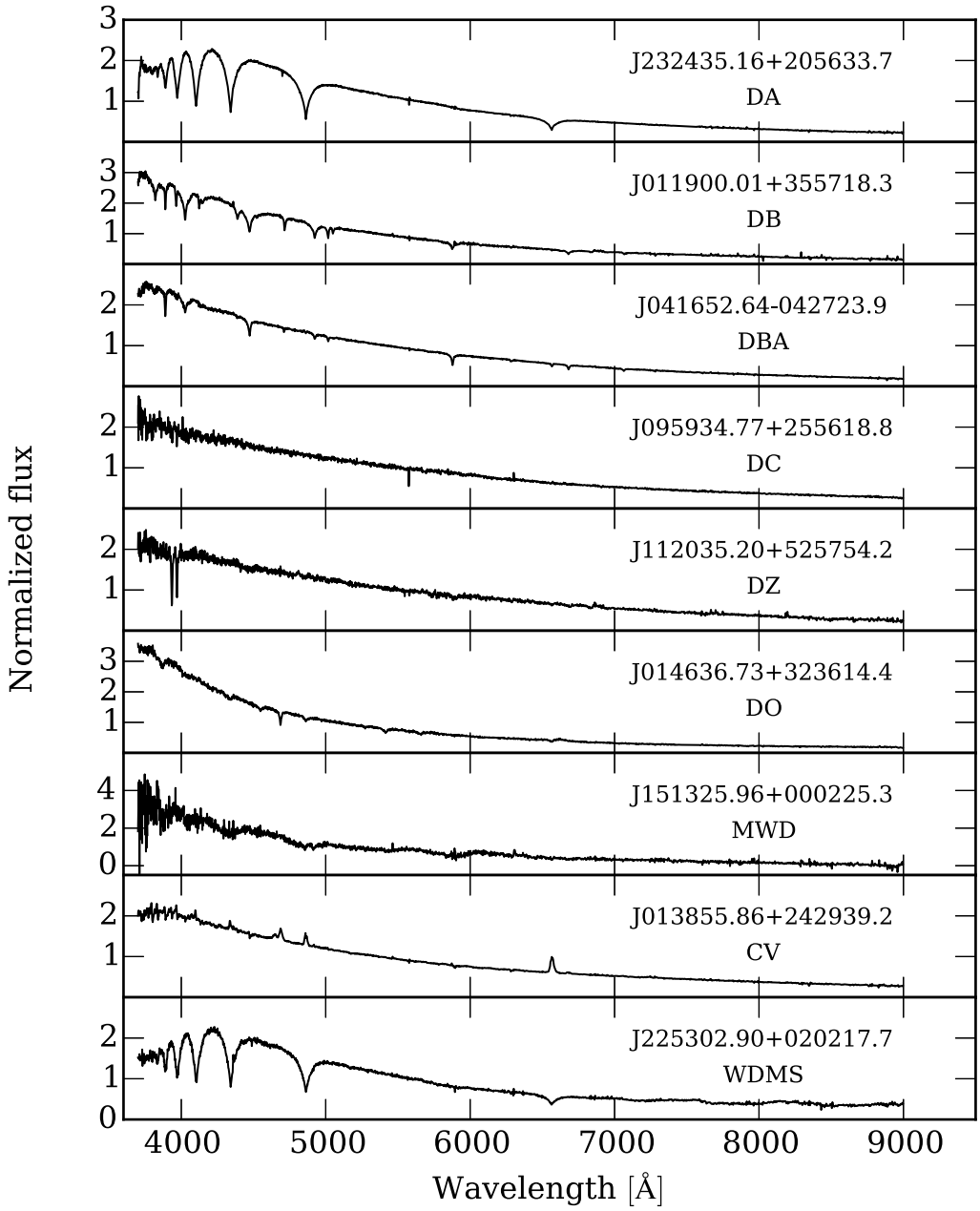

Figure 5.1: Sample LAMOST spectra of different types of white dwarfs

Table 5.3: LAMOST objects identified as previously unknown CVs.

Name	CRDR2 lightcurve
J003005.80+261726.3	yes
J010903.02+275010.0	yes
J013317.01+305329.8	yes
J013855.86+242939.2	yes
J052602.79+285121.3	no
J062402.64+270410.2	no
J074037.68+254109.4	yes
J171630.84+444124.5	yes
J172308.28+392455.2	yes

CVs. A possible cause of this bias towards CVs may be that the strong emission features which characterize CVs can be easily recognized even in very noisy spectra. Indeed we find that most of the inspected LAMOST spectra of CVs are of low quality. In order to verify our classification of these objects we cross-matched our nine new CVs with the second data release of the Catalina survey (CSDR2, Drake et al. 2009). CSDR2 provides multi-epoch photometry for over 500 million objects and has been an extremely useful resource for various campaign which searched for CVs (e.g. Breedt et al. 2014, Drake et al. 2014). Two of our new CVs are not within the CSDR2 sky footprint, but we were able to recover and inspected Catalina light curves for the remaining seven (Table 5.3). A complete analysis of these light curves is beyond the scope of this article, but we conclude these objects indeed show variability compatible with that of a CV.

5.3 An independent test of the Gentile Fusillo et al. 2015 white dwarf selection method

In Gentile Fusillo et al. (2015) we tested the reliability of our white dwarf candidate selection method using a sample of 6,706 spectroscopically confirmed white dwarfs and over 20,000 contaminants with available SDSS spectra. For a given $P_{\rm WD}$ threshold, we defined *completeness* as the ratio of the number of white dwarfs in the spectroscopic sample with at least that associated probability to the total number of white dwarfs in the sample. Similarly *efficiency* was defined as the ratio of the number of white dwarfs selected by the probability cut to the number of all the objects retrieved by such selection. We concluded that our $P_{\rm WD}$ can be reliably

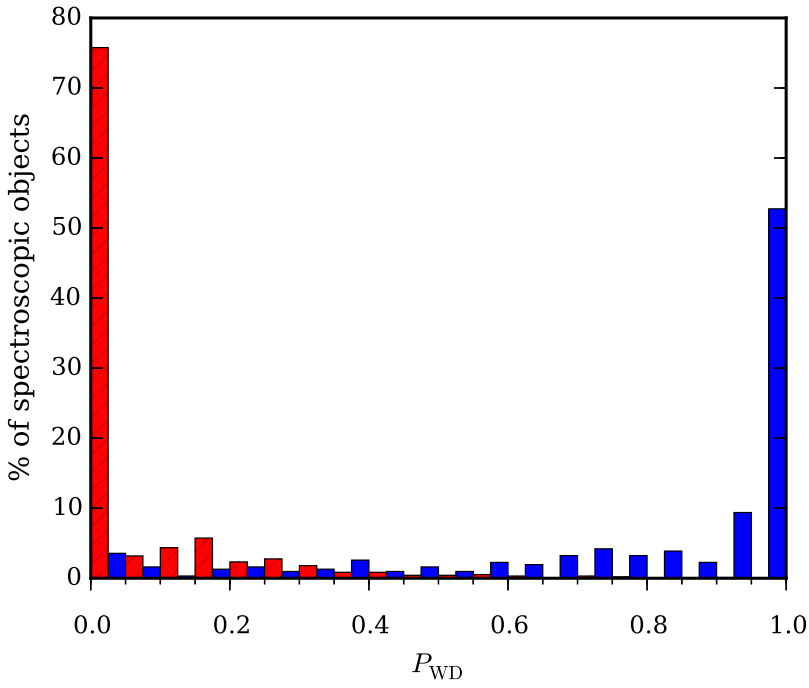

Figure 5.2: Distribution of all spectroscopically confirmed LAMOST white dwarfs (blue) and contaminants (red, shaded) as a function of $P_{\rm WD}$.

used to discern between white dwarfs and contaminants. For example, selecting all objects with a $P_{\rm WD} \geq 0.41$ resulted in a sample of white dwarf candidates which is 95 per cent complete and 89.7 per cent efficient. One of the main strengths of the selection method of Gentile Fusillo et al. (2015) is that, even though it was developed using SDSS, it can in principle be applied to any large area survey which provides multi band photometry (e.g. VST ATLAS, APASS, SkyMapper, Pan-Starrs). The possibility of applying the selection method to surveys other than SDSS, however, stresses the need to test the robustness of our $P_{\rm WD}$ values on a sample of spectroscopically confirmed white dwarfs completely independent from SDSS. Even though our sample of 309 (64 known ones and 245 identified as part of this work) confirmed LAMOST white dwarfs and 876 contaminants is small compared to the SDSS spectroscopic sample, it provides a welcome opportunity to verify the reliability of our $P_{\rm WD}$ values. Figure 5.2 clearly shows that over $\simeq$80 per cent of all LAMOST contaminants have $P_{\rm WD} < 0.2$ and virtually no contaminant has $P_{\rm WD} > 0.5$. Similarly, the vast majority of LAMOST white dwarfs have $P_{\rm WD} > 0.5$. Further inspection of Figure 5.2 reveals also that $\simeq$10 per cent of the LAMOST white dwarfs have $P_{\rm WD} < 0.4$ and would be missed by the most reasonable selections based on $P_{\rm WD}$,

i.e. a probability cut at $P_{\rm WD} \geq 0.41$. Inspection of these low probability objects reveals that the vast majority of these are CVs (see Sect 3.1). CVs have peculiar colours distinct from those of most single white dwarfs and the selection method of Gentile Fusillo et al. (2015) is not optimized for them. Nonetheless the statistic we compute on our LAMOST white dwarfs sample confirms the reliability of our selection method. The $P_{\rm WD}$ can confidently be used to select different samples white dwarfs according to the specific work one intends to carry out.

5.4 Spectroscopic completeness of the white dwarfs identified by LAMOST

In Gentile Fusillo et al. (2015) we find that, to date, the SDSS white dwarf spectroscopic sample is $\simeq$40 per cent complete. However, this number is averaged over the entire SDSS photometric footprint, large areas of which have not yet received any spectroscopic follow up. Furthermore, as we show in Fig. 5.3 (left panel), the spectroscopic completeness of SDSS white dwarfs is also very colour-dependent. For example, the spectroscopic completeness is highest for relatively cool white dwarfs with colours similar to those of quasars, a simple consequence of the target selection algorithm of SDSS. The LAMOST observing strategy differs from SDSS's both in terms of area of sky covered and target selection. Even though white dwarfs are only serendipitous or secondary targets for both surveys, the resulting spectroscopic samples are, to a certain degree, complementary. Figure 5.3 (right panel) illustrates that the spectroscopic completeness of LAMOST over the SDSS footprint does not dramatically depend on colour, although it does rise slightly in quasar-dominated areas. Naturally the number of white dwarfs increases at higher magnitudes as a larger volume is observed. However LAMOST observed mostly bright objects ($g \simeq 14-16$, Fig. 5.4) and therefore did not target the vast majority of photometrically selected white dwarfs. Consequently, even though the LAMOST white dwarf sample is less biased by colour it is limited in size, and the overall white dwarfs spectroscopic completeness is much lower than the SDSS one.

In order to compute the white dwarfs spectroscopic completeness of LAMOST we used the entire sample of 1083 white dwarfs resulting from our initial cross match of LAMOST targets with the catalogue of Gentile Fusillo et al. (2015) (newly identified LAMOST WDs + already published LAMOST WDs + LAMOST WDs with SDSS spectra). However it is important to keep in mind that the final sample of new white dwarfs presented is not representative of all the white dwarfs observed by LAMOST. The catalogue of white dwarf candidates of Gentile Fusillo et al. (2015)

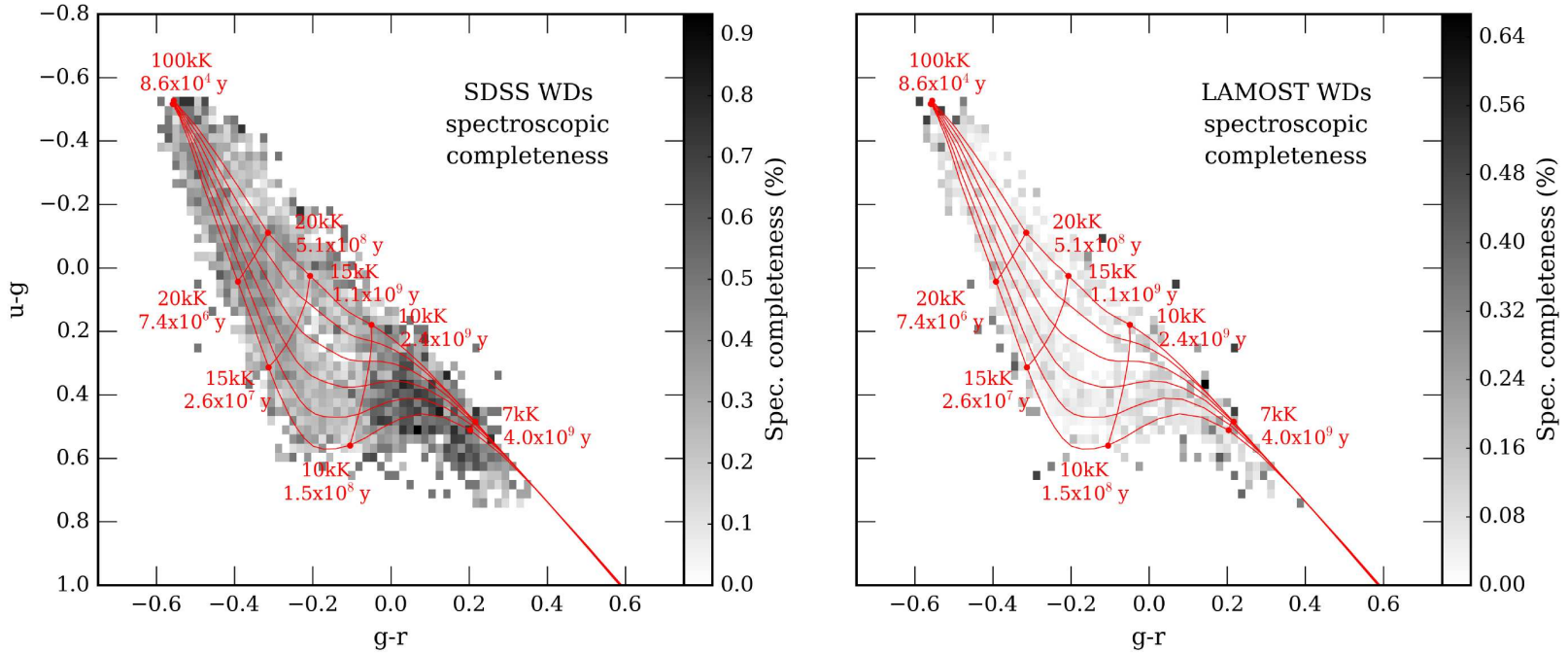

Figure 5.3: Spectroscopic completeness of SDSS white dwarfs (left panel) and LAMOST white dwarfs over the SDSS footprint (right panel). The values were computed as the ratio of spectroscopically confirmed white dwarfs to all high-confidence white dwarf candidates ($P_{\rm WD} \geq 0.41$) within the $(u-g, g-r)$ colour-colour selection used in Gentile Fusillo et al. (2015). To correctly compute the spectroscopic completeness of LAMOST over the SDSS footprint, we used the entire sample of 1083 white dwarfs resulting from our initial cross match of LAMOST targets with the catalogue of Gentile Fusillo et al. (2015) (newly identified LAMOST WDs + already published LAMOST WDs + LAMOST WDs with SDSS spectra). White dwarf cooling tracks from Holberg & Bergeron (2006) are shown as overlay (red solid lines). The left panel clearly shows an area of higher spectroscopic completeness caused by the SDSS target selection algorithm, which favours the observations of QSOs (see sect.5).

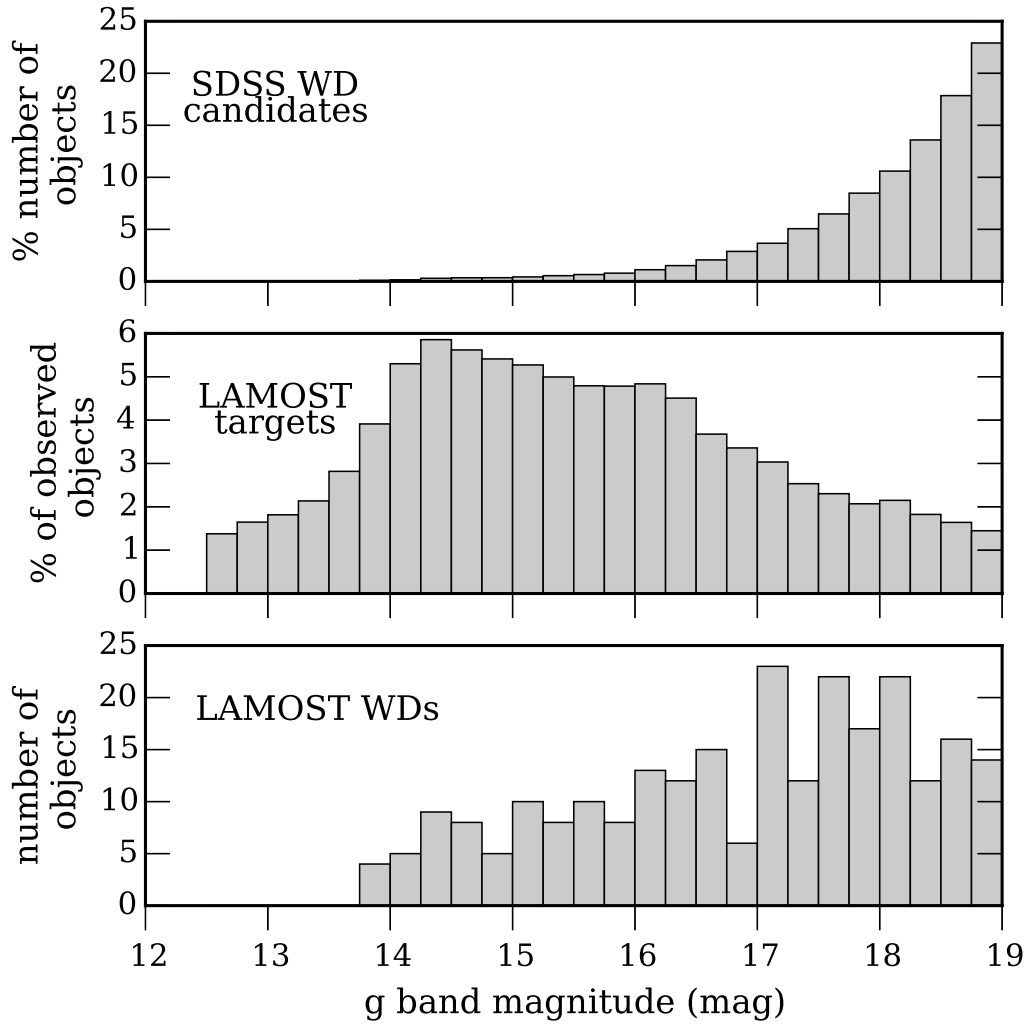

Figure 5.4: *Top panel*: g-band magnitude distribution of all SDSS white dwarf candidates from Gentile Fusillo et al. (2015).
Middle panel: g-band magnitude distribution of a random sub-set of 100,000 objects with LAMOST spectroscopy.
Bottom panel: g-band magnitude distribution of the newly identified LAMOST white dwarfs.

can only be considered complete for white dwarfs with available proper motions, $T_{\rm eff} \gtrsim 8000$ K and $g \leq 19$. Consequently the LAMOST white dwarf sample discussed here is affected by these same limitations. Even though cool white dwarf are particularly faint and LAMOST mostly targeted bright objects ($g \simeq 14 - 16$), we expect that among the 4.6 million spectra collected to date there should be some cooler nearby white dwarfs which were not included in this work. Finally, LAMOST has also extensively covered areas of the sky which lie outside the SDSS footprint (e.g. the Galactic anti-center;Yuan et al. 2015) and any white dwarf observed in those areas would, by definition, not be included in the catalogue presented here.

5.5 Stellar parameters

In this section we derive the stellar parameters of the newly identified LAMOST DA white dwarfs (Table 5.2). We do this following the fitting routine developed by Rebassa-Mansergas et al. (2007, 2010) adaptedto LAMOST spectra (Rebassa-Mansergas et al., 2015). The fitting procedure was carried out by Dr. Rebassa-Mansergas at the Kavli Institute for Astronomy and Astrophysics at Peking University, but I personally performed the subsequent statistical work. A brief description of the procedure used is given here, and we refer the reader to the references above for further details.

To determine the effective temperature ($T_{\rm eff}$) and surface gravity ($\log\, g\, [{\rm g\,cm\,s^{-2}}]$) we fit the normalised Hβ to Hϵ line profiles of each spectrum with the DA model grid of Koester (2010) using a mixing-length parameter (ML2/α) of 0.6. Since the equivalent widths of the Balmer lines go through a maximum near $T_{\rm eff} = 13,000$ K, the line fitting provides two possible solutions, i.e."hot" and "cold" solutions. We break this degeneracy fitting the entire white dwarf spectrum (continuum plus lines). The continuum spectrum of a DA WD is mostly sensitive to $T_{\rm eff}$, therefore the best-fit value from the entire spectrum generally indicates which of the two solutions is the most reliable one. However, because of uncertainties in the LAMOST flux calibration (Section 3.3), the best-fit to the entire spectrum may be subject to systematic uncertainties. Thus, the choice between hot and cold solution is further guided by comparing the ultraviolet GALEX (Galaxy Evolution Explorer; Martin et al., 2005; Morrissey et al., 2005) and optical SDSS photometry to the fluxes predicted from each solution (where the SDSS fluxes are derived directly from the SDSS u, g, r, i, z magnitudes). Spectroscopic fits that use 1D atmosphere spectra models are known to systematically overestimate surface gravities for cool ($\lesssim$12,000 K) white dwarfs (Koester et al., 2009a; Tremblay et al., 2011). To overcome this effect we applied the

3D corrections of Tremblay et al. (2013) to $T_{\rm eff}$ and $\log g$ determined above. Finally we obtained the masses of our white dwarfs by interpolating the obtained $T_{\rm eff}$ and $\log g$ values with the tables of Renedo et al. (2010).

The $T_{\rm eff}$, $\log g$ and masses we have determined are provided in the online catalogue which accompanies this article (Table 5.4). Inspection of the table reveals that these values are subject to large uncertainties in many cases. This is due to the low signal-to-noise ratio of many of the LAMOST spectra. In Figure 5.5 we show the $T_{\rm eff}$ distribution for DA white dwarfs with relative errors $\leq$10 per cent and the mass and $\log g$ distributions for DA white dwarfs with errors in mass $< 0.075 M\odot$. This results in 49 and 154 white dwarfs in the $\log g$ and $T_{\rm eff}$ histograms respectively.

The mass distribution displays a broad and clear peak at $0.6-0.7 {\rm M}_{\odot}$, as typically found in many previous studies (e.g. Liebert et al., 2005; Kleinman et al., 2013; Kepler et al., 2015). It also reveals the existence of both low-mass ($\lesssim 0.5 {\rm M}_{\odot}$) white dwarfs that may harbour unseen companions (Rebassa-Mansergas et al., 2011; Kilic et al., 2012) and high-mass ($\gtrsim 0.8 {\rm M}_{\odot}$) white dwarfs, some of which may be the result of mergers (Giammichele et al., 2012; Rebassa-Mansergas et al., 2015).

The $T_{\rm eff}$ distribution shows that our newly identified white dwarfs have generally 10,000$-$20,000 K, similar to the distribution obtained from SDSS spectroscopically selected white dwarfs (Kepler et al., 2015).

5.5.1 Comparison with stellar parameters from SDSS spectra

As mentioned in Section 5.2, 3500 objects from our initial sample have both SDSS and LAMOST spectra and 774 of them are white dwarfs (Table 5.1). This sample of objects provides a useful opportunity to compare DA white dwarf the stellar parameter obtained from LAMOST spectra with those obtained from SDSS spectra. In this comparison we decided to limit ourselves to DA white dwarfs with LAMOST spectra with a signal-to-noise ratio > 10. Applying these criteria results in a sample of 108 white dwarfs. We derive $T_{\rm eff}$ and $\log g$ from both the SDSS spectra and the LAMOST spectra following the same procedure described in Section 5.5. Figure 5.6 shows that the uncertainties in the LAMOST stellar parameters are generally significantly larger than the SDSS ones, this is caused by systematically lower signal-to-noise ratio of the LAMOST spectra. In order quantify the discrepancy between LAMOST and SDSS $T_{\rm eff}$ and $\log g$ we define a quantity τ :

$$\tau = \frac{\rm SDSS\,value - LAMOST\,value}{\sqrt{\rm SDSS\,\sigma^2 + LAMOST\,\sigma^2}} \tag{5.1}$$

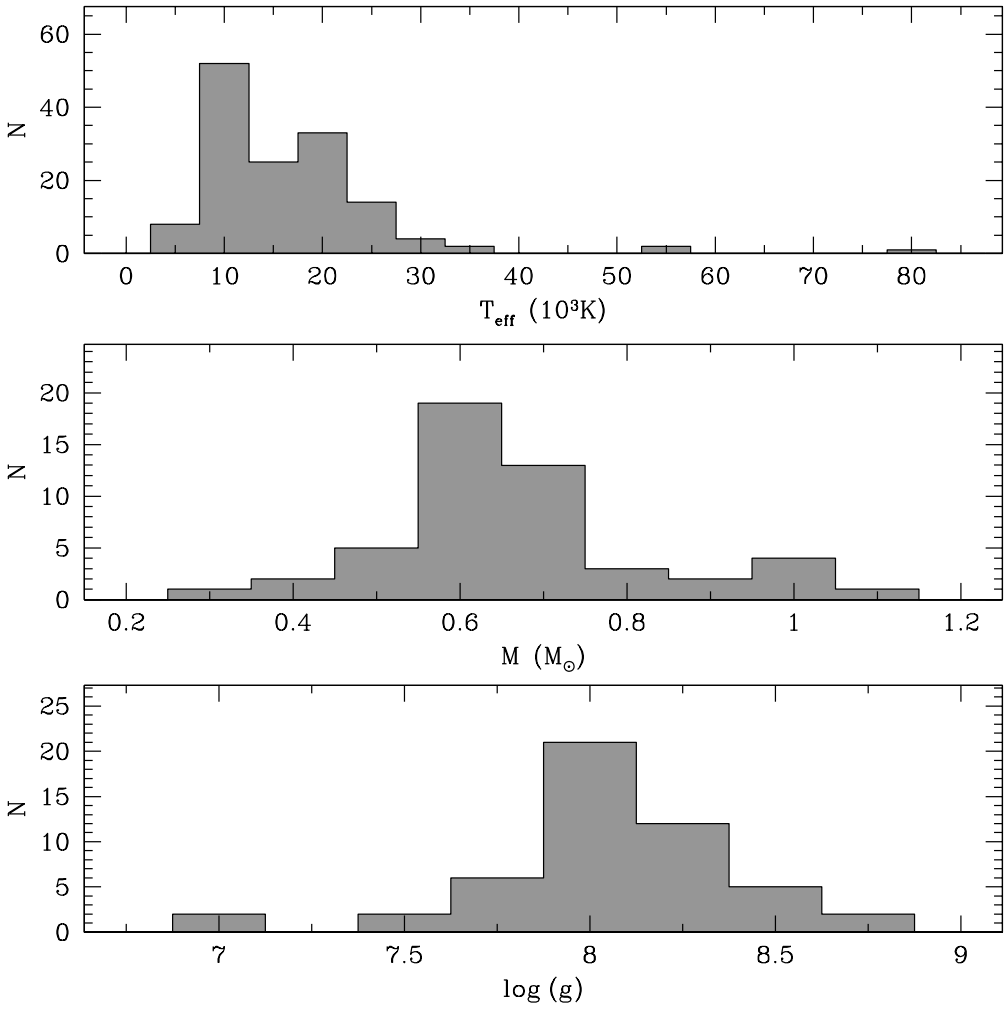

Figure 5.5: From top to bottom: effective temperature, mass and surface gravity distributions of the new LAMOST DA white dwarfs identified in this work.

We find that in 11 per cent of the cases the LAMOST $T_{\rm eff}$ values are overestimated by more than 2 τ compared to the SDSS ones. When comparing the $\log g$ values only 5.6 per cent of the objects show a comparable disagreement ($\tau > 2$). We can conclude that the stellar parameters computed using SDSS and LAMOST spectra are broadly in agreement.

5.6 Summary and conclusions

By cross matching all photometrically selected SDSS white dwarf candidates from the catalogue presented in Chapter 4 with the over 4 million spectra currently provided by the LAMOST DR3 we identified 309, bright ($g \leq 19$) white dwarfs with available LAMOST spectra of which only 64 were previously published as LAMOST white dwarfs. We inspected and classified the remaining 245 objects according to their spectral type and obtained $T_{\rm eff}$, $\log g$ and masses for the DAs (which make up 80 per cent of the sample). We also find that 188 of these white dwarfs were previously unknown and are therefore new discoveries. Since LAMOST targeted mainly object with $g \simeq 14 - 16$, the sample of LAMOST white dwarfs presented here is limited in size. However, because SDSS and LAMOST follow different targeting strategies, the sample of LAMOST white dwarfs is not affected by the known and heavy biases of the SDSS white dwarf spectroscopic sample and constitute therefore a valuable complementary addition.

We also inspected the LAMOST available spectra of 864 additional SDSS photometric sources from our catalogue of white dwarf candidates and classified them as non-white dwarfs, i.e. contaminant objects. We used the spectroscopic samples of newly confirmed white dwarfs and contaminants to test the reliability of the selection method developed in Chapter 4. Even with the relatively small size of our LAMOST spectroscopic sample we were able to verify that our *probabilities of being a white dwarf* can be reliably used to select samples of white dwarfs with completeness and efficiency close to 90 per cent. These results show that similar searches to the one presented here may be repeated in the near future (e.g with the forthcoming new data release of LAMOST) in a much more efficient way by relying more on the values of $P_{\rm WD}$ and therefore drastically reducing the amount of data to inspect by eye. Since our selection method for white dwarf candidates can be applied to any multi-band photometric survey, future searches may also not be limited to the SDSS footprint.

Our catalogue only includes SDSS white dwarf candidates with $g \leq 19$, $T_{\rm eff} \gtrsim 8000K$ and reliable proper motions (see Chapter 4). Furthermore, LAMOST

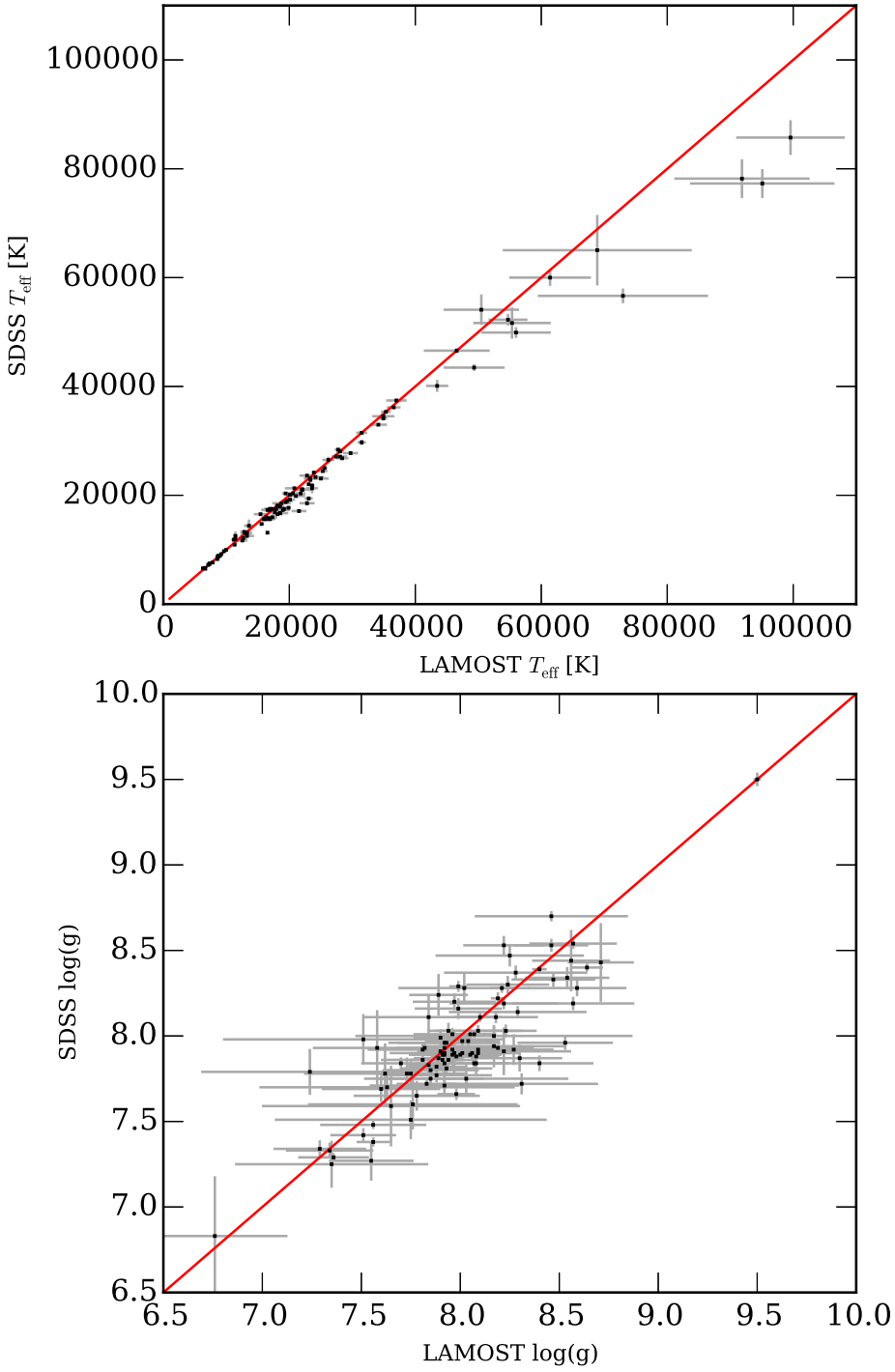

Figure 5.6: Comparison of stellar parameters (top: $T_{\rm eff}$, bottom: $\log g$) obtained by fitting the available SDSS and LAMOST spectra of 108 DA white dwarfs. Only objects which had a LAMOST spectrum with S/N > 10 were used. The red lines reflect a simple 1:1 relationship.

specifically targeted areas of the sky (e.g the Galactic anti-center) which were instead avoided by SDSS. Hence, the catalogue of new LAMOST white dwarfs presented here is not complete and should be considered as complementary to the work done in Chapter 4, as well as a contribution to the total sample of known spectroscopic white dwarfs.

In the near future further multi-band photometry of LAMOST targets will become available thanks to the Panoramic Survey Telescope & Rapid Response System (Pan-STARRS, Morgan et al. 2014). Our selection method for white dwarf candidates could be applied to the Pan-STARRS database. Such application will lead to a new search for LAMOST white dwarfs outside the SDSS footprint.

Table 5.4: Format of the catalogue of LAMOST white dwarfs. The full catalogue can be accessed online via the VizieR catalogue access tool.

Column No.	Heading	Description
1	sdss name	SDSS objects name (SDSS + J2000 coordinates)
2	ra	right ascension
3	dec	declination
4	probability	The *probability of being a WD* computed for this object in Gentile Fusillo et al. (2015)
5	umag	SDSS u band PSF magnitude
6	umag err	SDSS u band PSF magnitude uncertainty
7	gmag	SDSS g band PSF magnitude
8	gmag err	SDSS g band PSF magnitude uncertainty
9	rmag	SDSS r band PSF magnitude
10	rmag err	SDSS r band PSF magnitude uncertainty
11	imag	SDSS i band PSF magnitude
12	imag err	SDSS i band PSF magnitude uncertainty
13	zmag	SDSS z band PSF magnitude
14	zmag err	SDSS z band PSF magnitude uncertainty
15	ppmra	proper motion in right ascension (mas/yr)
16	ppmra err	proper motion in right ascension uncertainty (mas/yr)
17	ppmdec	proper motion in right declination (mas/yr)
18	ppmdec err	proper motion in right declination uncertainty (mas/yr)
19	Simbad classification	Currently available Simbad classifications

Table 5.4: Continued from previous page.

Column No.	Heading	Description
20	LAMOST spec ID	Unique spectra identifier composed of MJD (modified Julian date) of the observation, plate ID, spectrograph ID and a fiber ID
21	LAMOST class	classification of the object based on our visual inspection of its LAMOST spectra
22	$T_{\rm eff}$	effective temperature calculated for DA white dwarfs (sect. 6)
23	$T_{\rm eff}$ err	uncertainty in the effective temperature calculated for DA white dwarfs (sect. 6)
24	$\log g$	surface gravity calculated for DA white dwarfs (sect. 6)
25	$\log g$ err	uncertainty in the surface gravity calculated for DA white dwarfs (sect. 6)
26	$M/M_{\odot}$	mass of the white dwarfs calculated for DA white dwarfs (sect. 6)
27	$M/M_{\odot}$ err	uncertainty in mass the of the white dwarfs calculated for DA white dwarfs (sect. 6)

Chapter 6

White dwarf candidates in VST ATLAS

6.1 Introduction

Despite the fact that some of the largest and most advanced observatories in the world are located in the southern hemisphere, the southern sky is still today a largely unexplored territory. This difference between north and south is particularly marked for faint objects like white dwarfs. Thanks to large area surveys, most notably SDSS, we have discovered thousands of white dwarfs and reliable white dwarf candidates, but most of these surveys only scanned the northern hemisphere. As a result our knowledge of white dwarfs in the southern hemisphere is limited to the few hundred brightest stars (Fig.)

VST ATLAS is one of the first surveys to provide deep optical multi-band photometric coverage over a large area in the southern skies. The selection method described in Chapter 4 is not limited to SDSS and can be applied to any multi-band photometric survey. In this chapter I present a preliminary application of my selection method for white dwarf candidates to VST ATLAS DR2 and the resulting first sample of $\simeq 2500$ southern hemisphere high-confidence white dwarf candidates.

6.2 ATLAS vs SDSS

The ATLAS survey is carried out at the VST, a 2.6 m wide-field optical telescope located at Cerro Paranel in Chile (see Chapter 3). VST ATLAS uses the same optical filters as SDSS (*ugriz*) and in many ways aims to be the southern hemisphere counterpart of SDSS. However, there exist some fundamental differences between ATLAS and SDSS which need to be taken into account before we can apply our se-

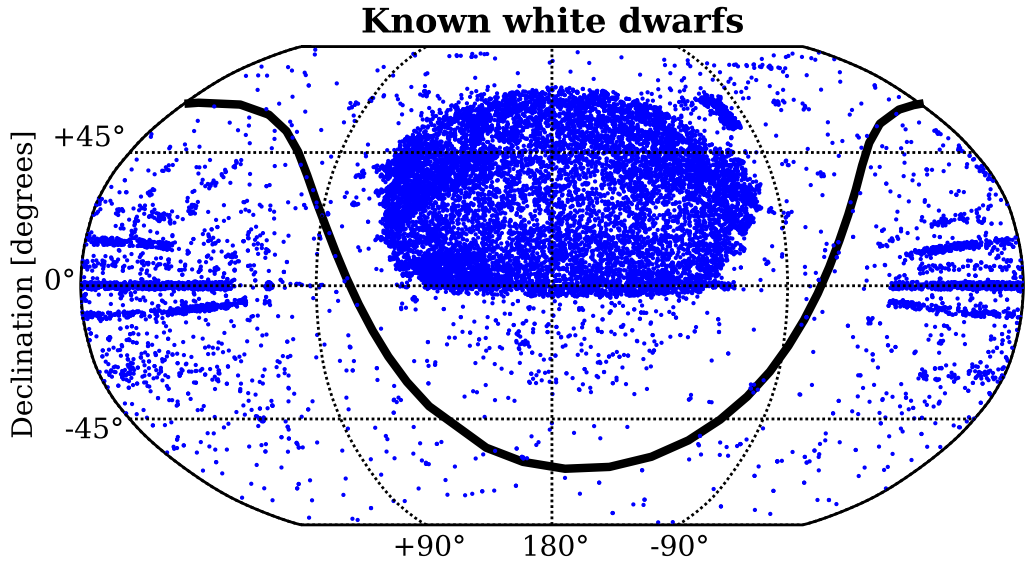

Figure 6.1: Sky distribution of 20,000 known white dwarfs from McCook and Sion catalogue of spectroscopically identified white dwarfs (McCook & Sion, 1999), the ESO Supernova Ia Progenitor Survey (SPY, Voss et al. 2007; Koester et al. 2009b) and SDSS (identified as part of the work described in Chapter 4). The plot illustrates the low number of known white dwarfs in southern hemisphere compared to the northern one. Only about 17% of the white dwarfs in this sample are located in the southern hemisphere.

lection method to ATLAS photometry. First of all ATLAS magnitude measurements are initially provided in the Vega system while SDSS ones are in the AB system. Even though the g band is roughly equivalent in the two magnitude systems, for the other bands there exist significant colour-dependent offsets. Furthermore, though the filter used in SDSS and ATLAS are nominally the same, the actual filter transmission curves have small differences, the detectors are not the same, the observing conditions at the telescope sites are different, and the flux calibration is conducted in different ways. As a result ATLAS and SDSS magnitudes, and therefore colours, are not perfectly equivalent.

Shanks et al. (2015) carried out an AB system recalibration of ATLAS photometry using the AAVSO Photometric All-Sky Survey (APASS) as reference. These recalibrated magnitudes are not yet publicly available but are included in ATLAS DR2.

ATLAS and SDSS overlap over an equatorial region of $\simeq 300$ deg^2 covering parts of both the north galactic cap ($10\mathrm{h} \lesssim \mathrm{RA} \lesssim 15\mathrm{h}\,30\mathrm{m}$; $-3.5^\circ \lesssim \mathrm{Dec} \lesssim -2^\circ$) and the south galactic cap ($22\mathrm{h}\,40\mathrm{m} \lesssim \mathrm{RA} \lesssim 3\mathrm{h}$; $-11^\circ \lesssim \mathrm{Dec} \lesssim -9^\circ$). Shanks et al. (2015) compared their ATLAS (AB) magnitude with the SDSS ones for objects in

Table 6.1: Summary of the most relevant numbers presented in this chapter.

ATLAS objects in initial colour cut	9402
Of which with no proper motion	499
Magnitude limit of final sample	$g \leq 19$
Objects in final sample of white dwarf candidates (Sect. 6.4)	8903
In common with SDSS DR10 catalogue of white dwarf candidates	544
Of which confirmed white dwarfs	54
Of which confirmed contaminants	117
High confidence white dwarf candidates in the final sample	~ 2500

the northern galactic cap overlapping region and developed a set of colour dependent equations to convert ATLAS (AB) magnitude in equivalent SDSS magnitudes:

$$\begin{aligned} u_{\rm SDSS} &= u_{\rm ATLAS} + 0.01(u-g) + 0.27 \\ g_{\rm SDSS} &= g_{\rm ATLAS} + 0.05(g-r) - 0.06 \\ r_{\rm SDSS} &= r_{\rm ATLAS} + 0.03(g-r) - 0.035 \\ i_{\rm SDSS} &= r_{\rm ATLAS} - 0.025 \\ z_{\rm SDSS} &= z_{\rm ATLAS} - 0.04(i-z) + 0.04 \end{aligned} \tag{6.1}$$

We started our white dwarf selection by retrieving recalibrated ATLAS (AB) *ugriz* photometry for all point sources in DR2 which have been observed in all five filters. We then applied the equations 6.1 to our dataset and calculated SDSS-equivalent magnitudes ($\rm ATLAS_{SDSS}$ from here on). In order to evaluate the robustness of this magnitude transformation we retrieved the available SDSS photometry of all the ATLAS sources in the overlapping regions with g mag ≤ 19.5 and clean SDSS photometry ($\sim 112,000$ objects). We compared the $\rm ATLAS_{SDSS}$ magnitudes with the SDSS ones (Fig. 6.2) and found that the mean values of SDSS $-$ $\rm ATLAS_{SDSS}$ magnitudes for objects in our overlapping samples are: u=0.0086±0.0004, g=0.0094 ±0.0002, r=0.0073±0.0002, i=0.0098±0.0002, z=0.0062±0.0003. These mean differences are smaller than the typical uncertainties in SDSS and ATLAS magnitude. We therefore conclude that $\rm ATLAS_{SDSS}$ magnitudes are, for most intent and purposes, equivalent to SDSS ones and our selection method for white dwarfs candidates (chapter 4) can be directly applied to them.

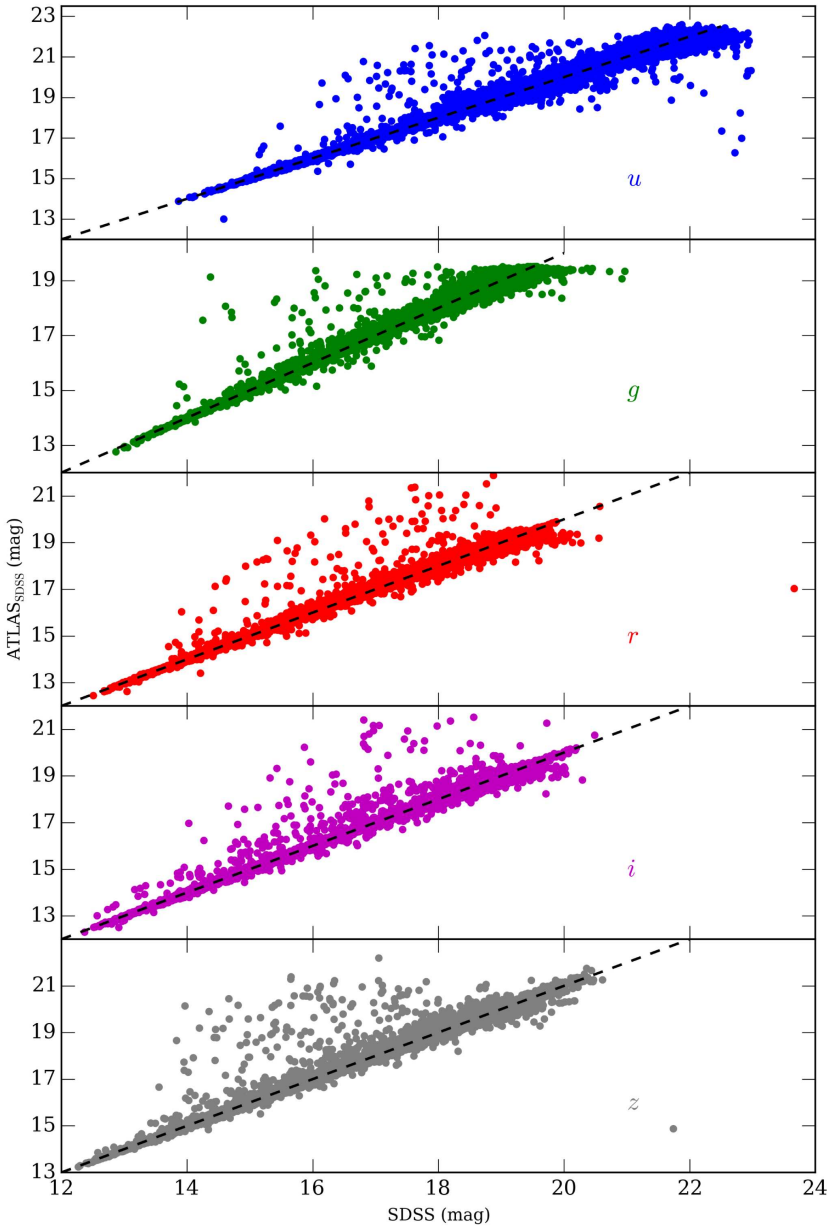

Figure 6.2: Comparison of ATLAS$_{\rm SDSS}$ and SDSS magnitudes for a sample of $\sim 112,000$ point sources. The dashed black lines indicate a 1:1 relationship. The comparison objects were chosen as SDSS objects with clean photometry. In ATLAS DR2 not all photometric flags have been fully implemented and it was not possible to accurately select objects with clean ATLAS photometry. As a consequence there is a clear increase in the data scatter above the 1:1 lines.

6.3 Colour selection and proper motions.

Using $\mathrm{ATLAS_{SDSS}}$ photometry we applied the colour cuts described in Table 4.2 in chapter 4. This broad colour cut resulted in a sample of 9402 blue ATLAS sources. Unlike SDSS, ATLAS does not provide proper motion measurements so these need to be retrieved from other surveys. We decided to use the PPMXL catalogue of positions and proper motions (Roeser et al., 2010). PPMXL combines USNO-B1.0 and 2MASS astrometry to provide proper motion for about 900 million objects over the entire sky to a magnitude limit $V \simeq 20$. However, the astrometry of PPXML and ATLAS can, in cases, correspond to observations taken years apart. White dwarfs can have high proper motions, and their coordinates may change by more than 1 arcsecond in the space of ten years. A simple cross match with a fixed radius may therefore lead to several miss-matches or missed objects.

To obtain more reliable results we divided our cross-matching procedure in three separate steps. We first retrieve every PPXML source in radius of 30 arcseconds (typically 4 to 8 objects) and compare the MJD of the ATLAS observation with that of the PPMXL matches (by definition at epoch J2000). We then use the proper motions and J2000 positions from PPMXL to compute predicted positions at the epoch of the ATLAS imaging for all objects in the first cross-match (Fig. 6.3). This coordinate "forward evolution" is carried out according to the equations:

$$\begin{aligned} \mathrm{RA} &= \mathrm{RA_{PPMXL}} + \left(\frac{\mathrm{pmRA}}{\cos(\mathrm{Dec_{PPMXL}})}\right) \times \frac{(\mathrm{MJD_{ATLAS}} - \mathrm{MJD_{PPMXL}})}{365.5} \\ \mathrm{Dec} &= \mathrm{Dec_{PPMXL}} + \mathrm{pmDec} \times \frac{(\mathrm{MJD_{ATLAS}} - \mathrm{MJD_{PPMXL}})}{365.5} \end{aligned} \tag{6.2}$$

Where pmRa and pmDec are the object proper motions in right ascension and declination respectively. Finally we consider a true match the closest object whose "evolved" coordinates fall within two arcseconds of the ATLAS ones. In case there is more than one matching object within two arcseconds we consider the closest object as the true match.

Following this procedure we obtained proper motion for 8903 of our objects. The "missing" proper motions for the remaining 499 objects are probably the result of these objects not having a reliable match on the USNO-B photographic plates used by PPMXL.

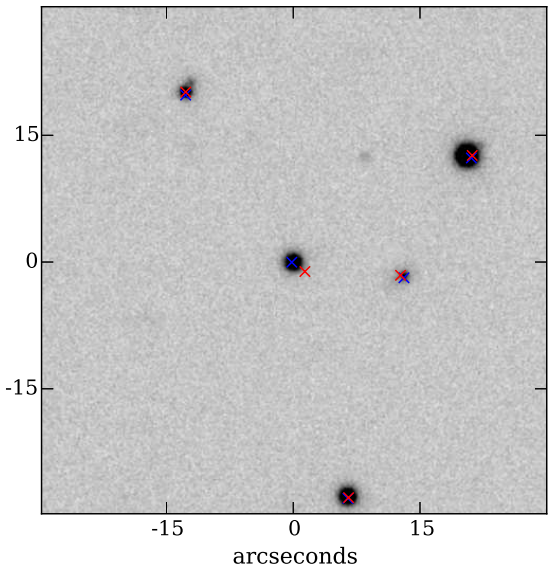

Figure 6.3: ATLAS g band image centered at the position of one of our white dwarf candidates. The blue crosses indicate the ATLAS coordinates of all sources in the image whereas the red crosses indicate the PPMXL coordinates. The two sets of coordinates are consistent to less than 1" for all objects except for the central high-proper motion white dwarf candidate which has moved by $\simeq 2.5$".

6.4 Candidate selection

Using the $\text{ATLAS}_{\text{SDSS}}$ magnitudes and the PPMXL proper motions we calculated RPMs for all ATLAS objects in our sample. Since $\text{ATLAS}_{\text{SDSS}}$ photometry is equivalent to the SDSS one, the distribution of ATLAS sources in RPM-colour space should be virtually identical to that of SDSS sources. Therefore we can calculate P_{WD} of ATLAS objects using the same probability map created with the SDSS DR7 spectroscopic training sample (Sect. 4.3, chapter 4). The final product of this process is a catalogue of 8903 ATLAS white dwarf candidates with computed P_{WD}.

6.5 Diagnostics

For our SDSS catalogue of white dwarf candidates we used an independent samples of spectroscopically confirmed white dwarfs and contaminants to test the strength of the selection method (SDSS DR9/10, chapter 4; LAMOST, chapter 5). However similar large spectroscopic samples do not exist for the southern hemisphere and therefore we cannot test the reliability of this application of the selection method to ATLAS in the same way. Nonetheless, as a result of the overlap of ATLAS with

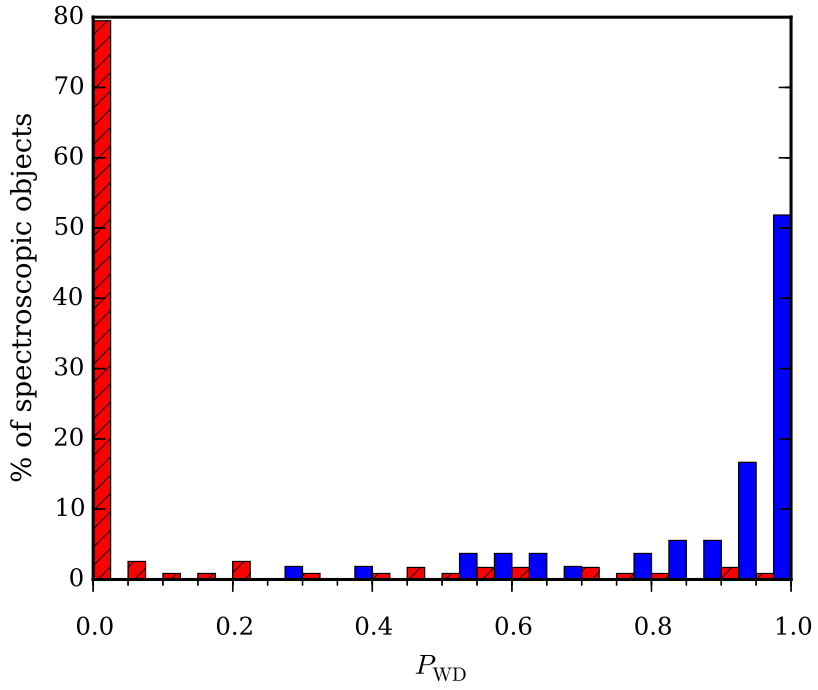

Figure 6.4: Distribution of 171 spectroscopically confirmed white dwarfs (blue) and contaminants (red, shaded) from the SDSS and ATLAS overlap sample as a function of $P_{\rm WD}$. For comparison with the distribution obtained using the $P_{\rm WD}$ calculated from SDSS, see Fig 4.6in Chapter 4.

SDSS, 544 objects appear in both our SDSS DR10 catalogue of white dwarf candidates and our ATLAS one. This overlapping sample includes 54 spectroscopically confirmed white dwarfs and 117 contaminants and these objects enables us to carry out some valuable test on the ATLAS sample of white dwarf candidates.

Figure 6.4 shows that over 80% of the 117 contaminants have $P_{\rm WD}$ (ATLAS) < 0.2 while over 80% of the 54 white dwarfs have $P_{\rm WD}$ (ATLAS) > 0.8. Though limited to small numbers it is evident that the $P_{\rm WD}$ calculated from ATLAS and PPMXL data provide a clear discrimination between white dwarfs and contaminants.

Using the same spectroscopic sample we can also calculate that a confidence cut which includes all ATLAS objects with $P_{\rm WD} \geq 0.41$ would result in a 96% complete and 78% efficient white dwarf selection. The same probability cut on our SDSS DR10 catalogue results in sample with the same completeness, but an efficiency of 86%. These preliminary results suggests that the application of our selection method to ATLAS photometry and PPMXL proper motions is slightly less efficient than the SDSS DR10 application. The dominant cause of this lower

efficiency is most likely the larger errors of PPMXL compared to SDSS. Typical errors in PPMXL proper motions are, in fact, $\simeq 6.5$ mas/yr, roughly double those of SDSS. Nonetheless reliable selections can still be achieved by adjusting the $P_{\rm WD}$ threshold and changing the compromise between efficiency and completeness.

The common ATLAS and SDSS white dwarf candidates also allows us to directly compare $P_{\rm WD}$ values calculated using ATLAS and PPMXL with those calculated using SDSS data. We find that the $P_{\rm WD}$ values are largely consistent with an average difference ($P_{\rm WD}$ (ATLAS)$-P_{\rm WD}$ (SDSS))$=0.06\pm0.01$. There exists however some isolated outliers with very inconsistent $P_{\rm WD}$ values. Close inspection of these objects reveals that the cause of such difference in $P_{\rm WD}$ is a marked discrepancy in the SDSS and PPMXL proper motions. In a few cases these discrepancies are caused by errors in our cross-matching procedure, but the dominant cause is actually erroneous proper motion measurement in PPMXL. For example, we are aware that QSOs can erroneously be associated with high-proper motions as, at different epochs, their coordinates are sometimes matched with different positions on the extended host galaxy. In the near future the first Gaia data release should provide accurate position of most of the objects in our ATLAS sample. In principle it should be possible to compare the coordinates of our objects at the ATLAS and Gaia imaging epochs and so correct or entirely replace the currently used PPMXL proper motions.

We consider our current sample of ATLAS white dwarfs candidates only a preliminary catalogue as further tests are still needed to fully evaluate the robustness of this application of our selection method. In particular we will require an independent sample of spectroscopically confirmed white dwarfs and contaminants spanning different values of $P_{\rm WD}$. We will also need to explore in more detail the reliability of our cross-matching routine and the difference between SDSS and PPMXL proper motions. Nonetheless we are confident that the current values of $P_{\rm WD}$ are sufficiently robust to select high-confidence dwarf candidates, i.e. Fig. 6.5 clearly illustrate that the $P_{\rm WD} \geq 0.41$ sample has a colour-colour distribution remarkably similar to that spectroscopically confirmed white dwarfs. Taking into account the values of completeness and efficiency calculated before, we estimate that our sample contains ~ 2500 high-confidence white dwarf candidates.

6.6 Conclusion

We present an application of our selection method for white dwarf candidates described in Chapter 4 to the photometry of ATLAS DR2. We adopted the trans-

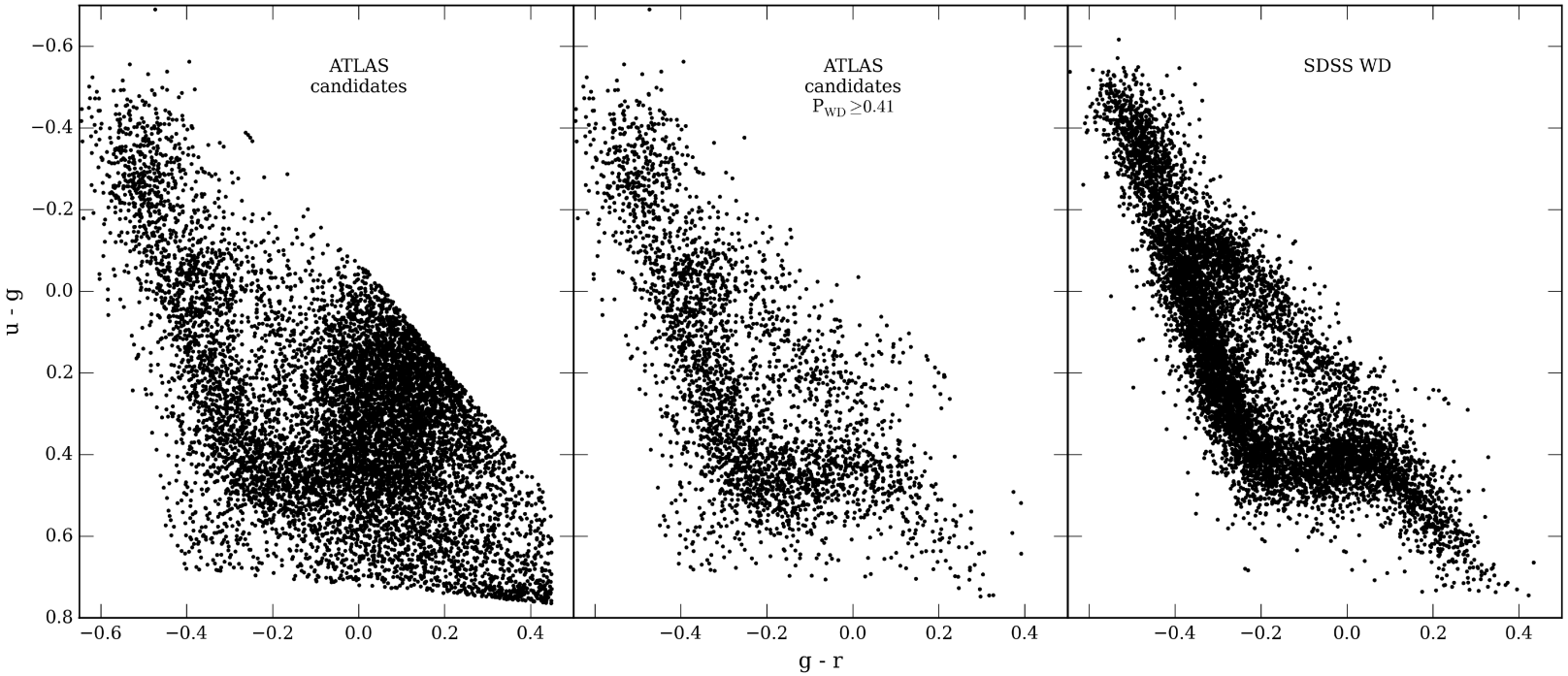

Figure 6.5: $u-g, g-r$ color-color distribution of (from left to rigth): all 8903 ATLAS objects in our final sample; 3190 ATLAS objects in our sample with $P_{\rm WD} \geq 0.41$; 8398 spectroscopically confirmed white dwarfs from Gentile Fusillo et al. (2015)

formations introduced by Shanks et al. (2015) to convert ATLAS magnitudes into SDSS equivalent magnitudes and confirmed the robustness of the conversion by comparing the photometry of over 112,000 objects in the overlapping regions of SDSS and ATLAS. We then used the PPMXL catalogue to retrieve proper motions for all ATLAS sources within an initial broad colour cut . The final result of this application is a sample of 8903 ATLAS white dwarf candidates with computed $P_{\rm WD}$. Preliminary tests using a small number of SDSS spectroscopically confirmed white dwarfs and contaminants suggest that the application of the selection method to ATLAS+PPMXL data is slightly less efficient than the original application to SDSS DR10. Specifically, a confidence cut at $P_{\rm WD} \geq 0.41$ produces a sample of white dwarfs 96% complete with efficiency of 78%; while the same cut on our SDSS DR10 catalogue achieved an efficiency of 86%. We estimate that this preliminary catalogue contains $\simeq$ 2500 high-confidence ATLAS white dwarf candidates, however, further tests and spectroscopic confirmation of a sample of candidates are still required to fully evaluate the robustness of this selection.

Chapter 7

A search for variable white dwarfs in large area time domain surveys: a pilot study in SDSS Stripe 82

7.1 Introduction

Many white dwarfs show some degree of variability in their apparent brightness. These brightness changes can be very different in nature: bright eruptions in interacting binaries (cataclysmic variables or classical novae; Warner 1995), eclipsing binaries (e.g Green et al. 1978; Orosz & Wade 1999; Parsons et al. 2015), rotationally variable magnetic white dwarfs (Barstow et al. 1995; Brinkworth et al. 2004, 2013; Lawrie et al. 2013), pulsating white dwarfs (Lasker & Hesser, 1971; Bergeron et al., 1995; Mukadam et al., 2004; Nitta et al., 2009) and even systems in which the cause of variability is still unexplained (Maoz et al., 2015; Holberg & Howell, 2011). Each one of these classes offers a unique and different channel to explore white dwarf structure and evolution. Pulsating white dwarfs, in particular, are extraordinary tools to probe their interior structure.

7.1.1 Pulsating white dwarfs

In 1968 the American astronomer Arlo Udell Landolt serendipitously detected rapid luminosity variations in the DA white dwarf HL Tau 76 (Landolt, 1968). Even though it was not initially recognized as such, this was the first pulsating white dwarf discovered. Since then the study of these objects has made great progress both

observationally, with over 200 pulsating white dwarfs found, and theoretically with accurate models to describe and exploit the observed pulsations. Today we known that pulsations are cause by non-radial gravity waves and arise as white dwarfs cool through narrow temperature ranges which define several instability strip (e.g Bergeron et al. 2004; Winget & Kepler 2008; Fontaine & Brassard 2008). Therefore it is thought that all white dwarfs will experience similar conditions as they cool through the instability strips, i.e. the appearance of pulsations is a natural phase in their evolution (Dziembowski & Koester, 1981; Winget et al., 1981). Pulsating white dwarfs are divided into three classes.

- DAVs or ZZ Ceti Stars. Named after the second pulsating white dwarf discovered (Lasker & Hesser, 1971), these are pulsating white dwarfs with H-dominated atmospheres. ZZ Cetis are by far the most common type of pulsating white dwarfs. As DA white dwarfs cool through the temperature range $12,500 - 11,000\,\mathrm{K}$, partial recombination of H in their atmospheres causes a dramatic increase in the envelope opacity which, in turn reduces the flow of radiation causing the pulsations (Fontaine & Brassard, 2008). Recently Hermes et al. (2013) discovered that extremely low-mass (ELM), He-core white dwarfs ($\mathrm{M} < 0.25\mathrm{M}_{\odot}$) also undergo pulsations. These white dwarfs also have H-dominated atmospheres, but are often considered a separate class from ZZ Cetis. The pulsation periods of ZZ Cetis typically range from 100 to 1400s (Mukadam et al., 2004) and can even reach up to 1.7h in ELM white dwarfs.

- DBV or V777 Her. The existence of pulsating white dwarfs with He-dominated atmospheres was predicted by Winget et al. (1981), before the actual discovery of one a year later (Winget et al., 1982). Similarly to the driving mechanism in ZZ Cetis, pulsations in DBV are caused by partial recombination of the outer envelope. Because of the higher ionisation potential of He, this happens at a higher temperature than in ZZ Cetis: pulsations in DBs arise in the temperature range $29,000 - 21,000\mathrm{K}$ (Nitta et al., 2009). However, with only $\simeq 20$ known to date (Kilkenny et al., 2009; Nitta et al., 2009), a robust definition of a DBV instability strip is still an ongoing challenge.

- PG 1159 or GW Vir. These extremely hot ($75,000\mathrm{K} \lesssim T_{\mathrm{eff}} \lesssim 200,000\mathrm{K}$) pre-white dwarfs have atmospheres composed of helium, carbon and oxygen in roughly comparable amounts. This peculiar atmosphere composition is thought to be the result of violent mixing events caused by He flashes in late stages of the progenitor evolution (Werner & Herwig, 2006). The origin of pulsations in PG 1159 is the so called κ-mechanism, a process caused by the

cyclic ionization of the K-shell electrons of carbon and oxygen (Quirion et al., 2007).

- Another class of variable white dwarfs are the recently discovered *hot*DQ stars (Dufour et al. 2007a, Sect. 1.2.2). As mentioned in the introduction, these are hot ($T_{\rm eff} \approx 18,000 - 24,000$K) white dwarfs with C dominated atmospheres. Some studies speculated that *hot*DQs may constitute a new class of pulsators, but the origin of the observed variability is still matter of debate (e.g Fontaine et al. 2008; Lawrie et al. 2013).

Traditionally, the physical parameters of white dwarfs, including their effective temperature ($T_{\rm eff}$) and surface gravity ($\log g$) are determined from spectroscopic analysis (Sect 1.2.2, Fig 1.5, Bergeron et al. 1992b). However, spectral information is restricted to the outermost layers of of the star. As a consequence, our understanding of white dwarfs is often, literally, superficial. Pulsating white dwarfs, however, provide a unique opportunity to look past the outermost atmosphere and probe the interior of these objects. Asteroseismological tools can be used to study pulsating white dwarfs and investigate the structure, composition and mass of both the core and envelope (Winget & Kepler 2008; Fontaine & Brassard 2008; Althaus et al. 2010). Furthermore, asteroseismology can be used to probe internal rotation profiles (Charpinet et al., 2009), measure weak magnetic fields (Winget et al., 1991) and even search for planetary companions via pulse timing variations (Mullally et al., 2008).

Historically, this unambiguous identification of pulsating white dwarfs required several hours of continuous high cadence photometry (e.g. Mukadam et al. 2004; Nitta et al. 2009), which is observationally expensive. Candidate selection has so far relied on colours and/or $T_{\rm eff}$ and $\log g$, estimated from model fits to spectra, with efficiencies ranging from 30% to 80% (e.g. Mukadam et al. 2004).

In recent years, the opportunity to repeatedly survey large areas of the sky has rapidly advanced the field of time-domain astronomy. Time-domain exploration of the sky is at the forefront of modern astronomy with many wide-field surveys in operation, or soon to come on-line (e.g. CRTS, Drake 2014; PTF, Law et al. 2009; EVRYSCOPE, Law et al. 2015; Pan-STARRS, Morgan et al. 2014; Gaia, Walton 2014; LSST, Ivezic et al. 2011). In order to fully exploit these vast resources we will need to develop efficient a robust method to identify pulsating white dwarf candidates that reduces, or removes, the need for high-cadence identification photometry.

Here, we investigate the feasibility of using multi-epoch photometry from large-area surveys to reliably identify pulsating white dwarf candidates based on

Stripe 82 of the Sloan Digital Sky Survey (SDSS). Several successful studies have made use of Stripe 82 multi-epoch observations to search for variable objects (eg. Sesar et al. 2007; Bramich et al. 2008; Becker et al. 2011). However these studies mainly focused on identifying large-amplitude variable sources (e.g eclipsing binaries or flaring stars) and the potential of identifying low amplitude variability (like that of pulsating white dwarfs) has not yet been explored. Starting from a sample of 400 high-confidence white dwarfs candidates from the catalogue of Gentile Fusillo et al. (2015), we recover, recalibrate and quality-control all available multi-epoch photometry to identify variable candidates. Even though Stripe 82 offers only low and irregular cadence over a relatively limited area, our study demonstrates promising results. In the near future a similar methodology, applied to superior time-domain surveys (e.g. Pan-STARSS, Gaia and LSST) will completely change the way we identify variable stars, including pulsating white dwarfs.

7.2 SDSS Stripe 82

SDSS has obtained *ugriz* multi-band photometry, in the magnitude range $g \simeq 15-22$ mag, for over a third of the sky, and spectroscopic follow up of over 4 million objects (Alam et al. 2015, see chapter 3).

A particular region of the SDSS footprint, Stripe 82, has received multiple observations as part of different programs (most notably the SDSS-II Supernova survey, Frieman et al. 2008; Sako et al. 2008). Stripe 82 covers an area of 300 deg^2 on the celestial equator spanning 8 hours in right ascension ($-50° < \mathrm{RA} < 59°$) and 2.5 degrees in declination ($1.25° < \mathrm{Dec} < 1.25°$, see Fig. 7.1). The stripe consists of two scan regions which have been repeatedly imaged over approximately ten years with a total of 303 imaging runs. A specific imaging run may cover the entire length of the stripe or just a specific region, and several runs overlap in certain areas (Abazajian et al., 2009).

7.3 Data selection and correction

We retrieved photometry for 400 high-confidence white dwarf candidates from the catalogue of Gentile Fusillo et al. (2015) which fall in Stripe 82 and have *probability of being a white dwarf* ($\mathrm{P_{WD}}$) ≥ 0.75. We found that, on average, each white dwarf had been observed between 60 and 200 times. Only about one-quarter of the Stripe 82 scans were obtained in photometric conditions; the rest were taken under variable clouds and often poorer than normal seeing. As a consequence, the default

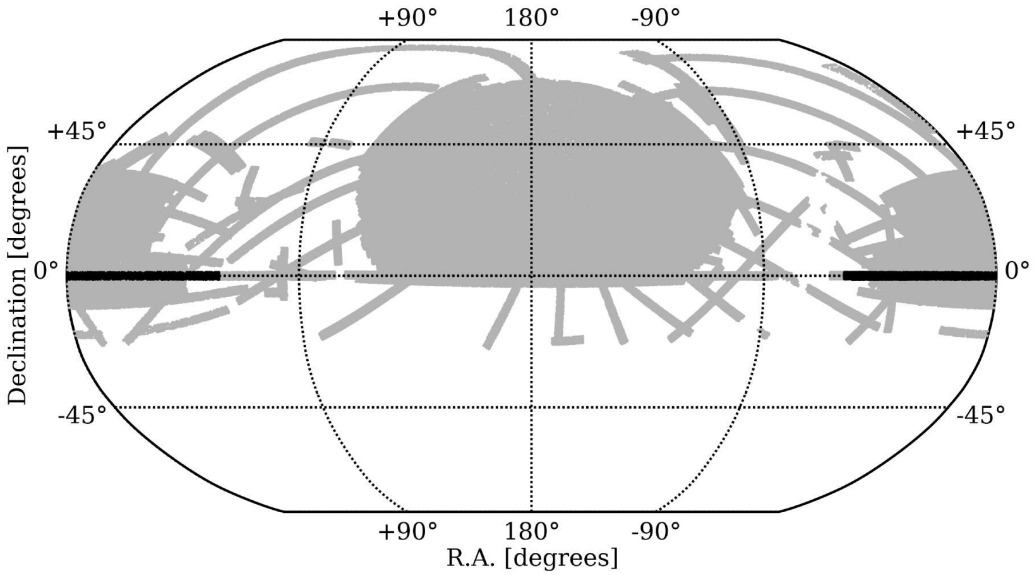

Figure 7.1: Current photometric footprint of SDSS (data release 12, Alam et al. 2015; $\simeq 14,000$ deg^2). The 300 deg^2 of Stripe 82 are shown in black.

calibration of the Stripe 82 photometry is insufficient to identify low-amplitude variables. In fact, all 400 white dwarf candidates (and their neighbouring objects) show significant low-amplitude variability (up to $\simeq 0.2$ mag) in their Stripe 82 lightcurves.

In the standard procedure to correct for varying atmospheric conditions in time-series photometry, *relative (or differential) photometry*, simultaneous observations of one or more neighbouring objects are used to calibrate the photometry of the science target. Changing atmospheric conditions affect neighbouring objects in the same way and can therefore be measured and corrected for. We followed this approach using the neighbouring stars of our white dwarf candidates to recalibrate the Stripe 82 observations, and identify unreliable detections. For each white dwarf candidate we retrieved Stripe 82 photometry of all point sources with "clean" photometry within a five arcminute radius, which were observed at the same time as the white dwarf. We defined an "individual nightly offset" as the difference between the *ugriz* magnitudes of an object as detected on a given night and the median of all Stripe 82 measurements of that object. Calculating the median of the "individual nightly offsets" for all neighbours, then defined a "median nightly offset" which we used to correct the Stripe 82 magnitude of the white dwarf on that night.

However, several effects (such as irregular cloud coverage or intrinsic variability of a neighbour) can cause irregular variations from object to object, hence in certain nights the "individual nightly offsets" are not consistent with each other

and can therefore not be used to re-calibrate the field. We compare the "individual nightly offsets" of all neighbours with the "median nightly offset" and calculate reduced χ^2 values. If a significant scatter is observed (${\chi^2}_{\rm red} > 3$) we conclude that the "median night offset" cannot be considered reliable and discard the night. Furthermore we also consider unreliable those nights in which less than four neighbours were observed. Following this strict selection criteria, 85 of our white dwarfs candidates were left with less than eight epochs of reliable data, which we deemed insufficient for a robust variability analysis. Consequently, we dropped these objects, reducing our sample size to 315. For each of these white dwarf candidates, we quantify the scatter of the recalibrated g-band magnitudes with respect to their median value (and therefore the degree of variability) by calculating reduced χ^2 values (Fig. 7.2). We defined ${\chi^2}_{\rm red} > 2.0$ as the threshold for selecting 26 variable white dwarf candidates. For each of these stars, we constructed multi-epoch light curves (e.g. Fig. 7.3)calculated amplitudes, and retrieved SDSS images and spectra (where available; Table 7.1). The amplitude of the scatter in the data was calculated from the observed light curves using a Monte Carlo method. We randomly varied the magnitude of each data point using a Gaussian probability distribution whose width was set to the uncertainty in the Stripe 82 magnitudes. For each re-sampling we calculate the amplitude as half of the difference between the brightest and faintest detection. The reported amplitudes are the averages of 1000 re-samplings. These values reflect the minimum expected amplitude of variability required to cause the observed scatter in the Stripe 82 data. All but one of our candidates (SDSSJ2157+0037, see Sect. 7.5.8) have an SDSS spectrum. Combining all available data (spectra, SDSS colours and images, ${\chi^2}_{\rm red}$ and light curves) we then attempted to assess the nature of the observed variability.

In our analysis of Stripe 82 data we made the fundamental assumption that all photometric errors are uncorrelated. However, trends related to changing airmass, atmospheric conditions and/or telescope tracking may be present (Pont et al., 2006). This type of systematic noise is known as red noise and it can alter the threshold of detectable variability. A commonly used approach to assess the impact of red noise on a dataset is to evaluate the scatter and correlation of the rms of the lightcurve with magnitude, for a large sample of non variable objects (e.g. Smith et al. 2006). In the case of this work on Stripe 82, our sample of non variable stars if far too small to carry out a statistically significant evaluation of red noise effects. Furthermore the Stripe 82 database is currently not accessible in its full format and it is therefore impossible to recover additional data. As such we are not able to make a statement on the possible limitations due to red noise.

Table 7.1: Stripe 82 photometric parameters of the 26 variable white dwarf candidates and the three non-variable white dwarfs (below the dashed line) selected as "control" objects. Median g magnitudes were calculated from all re-calibrated, reliable Stripe 82 photometry. g scatter were calculated via a Monte Carlo method, and represent the minimum expected amplitudes of variability required to cause the observed scatter in the Stripe 82 photometry. Colours were calculated using median magnitudes. Objects marked with † were later dropped as spurious candidates (see Sect. 7.3.1 and Sect. 7.3.2).

SDSS name	RA	Dec	median g mag	$u-g$	$g-r$	χ^2	g scatter (mag)
SDSS J0028−0012	00 28 03.34	−00 12 13.2	18.55	0.39	−0.26	3.3	0.10 ± 0.02
SDSS J0050−0001	00 50 13.52	−00 01 30.3	18.64	0.13	−0.31	3.4	0.10 ± 0.01
SDSS J0050−0023	00 50 47.61	−00 23 16.9	18.80	0.32	−0.089	2.7	0.12 ± 0.02
SDSS J0102−0033	01 02 07.32	−00 33 00.1	18.19	0.43	−0.11	2.7	0.09 ± 0.02
SDSS J0106−0014	01 06 22.99	−00 14 56.2	18.18	0.48	−0.20	4.3	3.71 ± 0.39
SDSS J0121−0028	01 21 02.30	−00 28 12.0	18.45	0.52	−0.15	8.7	0.11 ± 0.02
SDSS J0134−0109	01 34 40.94	−01 09 02.3	18.12	0.49	−0.03	2.6	0.09 ± 0.02
SDSS J0158−0000	01 58 01.11	−00 00 00.2	18.62	0.36	−0.22	5.1	0.16 ± 0.02
SDSS J0209+0050	02 09 27.68	+00 50 21.0	18.41	−0.03	−0.37	3.5	0.10 ± 0.02
SDSS J0247+0003	02 47 46.29	+00 03 31.6	16.26	0.24	−0.38	3.4	0.07 ± 0.01
SDSS J0318+0030	03 18 47.09	+00 30 29.5	17.86	0.42	−0.13	2.7	0.08 ± 0.02
SDSS J0321−0050	03 21 43.49	−00 50 25.6	18.89	0.27	−0.26	2.4	0.10 ± 0.02
SDSS J0326+0002	03 26 15.34	+00 02 21.6	18.44	0.08	−0.30	3.0	0.17 ± 0.02
SDSS J0326+0018	03 26 19.44	+00 18 17.5	17.41	0.39	−0.20	7.8	0.13 ± 0.01
SDSS J0342+0024†	03 42 29.96	+00 24 17.8	16.47	0.09	−0.18	5.7	0.29 ± 0.02
SDSS J0349−0059	03 49 17.40	−00 59 19.2	17.65	−0.39	−0.34	2.7	0.07 ± 0.01
SDSS J2109+0111	21 09 33.63	+01 11 10.6	18.96	0.12	−0.33	3.0	0.13 ± 0.02
SDSS J2156−0046	21 56 28.27	−00 46 17.2	18.38	0.55	−0.06	3.8	0.07 ± 0.01

Table 7.1: Continued from previous page.

SDSS name	RA	Dec	median g mag	$u-g$	$g-r$	χ^2	g scatter (mag)
SDSS J2157+0037	21 57 13.51	+00 37 14.8	17.41	0.51	−0.12	9.3	0.11 ± 0.01
SDSS J2157−0044†	21 57 11.87	−00 44 34.9	18.63	−0.35	−0.39	44.7	3.40 ± 0.25
SDSS J2218−0000	22 18 28.59	−00 00 12.2	18.09	0.15	−0.20	2.2	0.07 ± 0.01
SDSS J2220−0041	22 20 30.69	−00 41 07.3	17.48	0.43	0.11	2.8	0.07 ± 0.01
SDSS J2237−0101	22 37 26.85	−01 01 10.8	18.88	0.46	−0.11	4.8	0.12 ± 0.02
SDSS J2318−0114	23 18 41.50	−01 14 43.1	18.74	0.14	−0.32	2.2	0.15 ± 0.02
SDSS J2330+0100	23 30 40.50	+01 00 47.6	17.52	0.66	0.25	3.2	0.13 ± 0.02
SDSS J2333+0051	23 33 05.08	+00 51 55.6	18.55	−0.06	−0.32	5.0	0.16 ± 0.02
SDSS J0327+0012	03 27 27.52	+00 12 52.5	17.83	0.44	−0.17	0.8	0.04 ± 0.02
SDSS J2245−0040	22 45 18.53	−00 40 25.2	18.47	0.44	−0.17	0.6	0.04 ± 0.02
SDSS J2336−0051	23 36 47.00	−00 51 14.6	18.32	0.48	−0.20	0.7	0.05 ± 0.02

Table 7.2: Additional parameters of the 26 white dwarf candidates initially identified as variable sources and the three non-variable white dwarfs (below the dashed line) selected as "control" objects. Objects marked with † were later dropped as candidates. $T_{\rm eff}$ and $\log g$ are calculated using 1D atmospheric models. The initial class column shows the spectral classification we assigned to the object based on the available SDSS spectrum. "ZZ$_{\rm cand}$" are ZZ Ceti candidates (Sect. 7.4). The "LT obs" column shows the results of our LT time series follow up. Object which were not observed to vary (in our LT follow up or by Mukadam et al. 2004) are flagged as "NOV" followed by the non variability limit set by the observations.

Object	$T_{\rm eff}$ [a] [K]	$\log g$ [a] [cgs]	initial class	LT obs.	remarks
SDSS J0028−0012	14,590±480	7.99±0.07	DA	–	–
SDSS J0050−0001	21,120±570	7.59±0.08	DA	–	–
SDSS J0050−0023	11,170±90	8.84±0.05	ZZ$_{\rm cand}$	–	NOV0.6 %[b]
SDSS J0102−0033	11,110±170	8.37±0.09	ZZ$_{\rm cand}$	ZZ Ceti	ZZ Ceti[b]
SDSS J0106−0014	14,240±300	7.49±0.06	ZZ$_{\rm cand}$	–	eclipsing binary[c]
SDSS J0121−0028	10,447±30[d]	8.42±0.03[d]	ZZ$_{\rm cand}$	NOV1.4 %	–
SDSS J0134−0109	10,490±80	8.04±0.07	ZZ$_{\rm cand}$	ZZCeti	–
SDSS J0158−0000	13,020±440	8.29±0.09	ZZ$_{\rm cand}$	–	–
SDSS J0209+0050	24,910±510	7.94±0.07	DA	–	–
SDSS J0247+0003	19,362±120	8.05±0.019	DA	–	–
SDSS J0318+0030	11,450±120	8.33±0.05	ZZ$_{\rm cand}$	ZZ Ceti	ZZ Ceti[b]
SDSS J0321−0050	16,896±440[e]	8.00±0.09[e]	DAH	–	–
SDSS J0326+0002	21,710±320	7.93±0.05	DA	–	–
SDSS J0326+0018	12,570±90	8.17±0.03	ZZ$_{\rm cand}$	–	NOV0.5 %[b]
SDSS J0342+0024†	32,812±170[e]	8.52±0.03[e]	DAB	–	contam. (Sect.7.3.1)
SDSS J0349−0059	100,000±790[e]	5.00±0.01[e]	PG1159	–	known pulsator[f]
SDSS J2109+0111	20,530±340[e]	7.81±0.05[e]	DA	–	–
SDSS J2156−0046	10,940±150	8.20±0.09	ZZ$_{\rm cand}$	ZZ Ceti	–

Table 7.2: Continued from previous page.

Object	$T_{\rm eff}$ [a] [K]	$\log g$ [a] [cgs]	initial class	LT obs.	remarks
SDSS J2157+0037			no spec	–	see Sect. 7.5.8
SDSS J2157−0044†	60,420±5190	8.00±0.31	DA	–	pos. err (Sect. 7.3.2)
SDSS J2218−0000	12,239±440[e]	9.73±0.24[e]	MWD	–	–
SDSS J2220−0041	7730±40	7.98±0.07	DA	–	WD+BD[g]
SDSS J2237−0101	11,700±270	8.06±0.11	$\mathrm{ZZ_{cand}}$	ZZ Ceti	–
SDSS J2318−0114	21,470±790	7.83±0.11	DA	–	–
SDSS J2330+0100	6660±60	8.23±0.13	DA	–	–
SDSS J2333+0051	22,857±890[e]	8.09±0.07[e]	$\mathrm{V777\,Her_{cand}}$	NOV2.1 %	–
SDSS J0327+0012	16,800±220	8.59±0.03	DA	NOV1.2 %	
SDSS J2245−0040	13,260±300	8.12±0.07	DA	NOV4.2 %	
SDSS J2336−0051	12,860±330	7.80±0.09	DA	NOV3.0 %	NOV0.5 %[b]

[a] Tremblay et al. (2011);[b] Mukadam et al. (2004); [c] Kleinman et al. (2004); [d] Kepler et al. (2015);
[e] Kleinman et al. (2013); [f] Woudt et al. (2012); [g] Steele et al. (2009)

7.3.1 Source contamination

If two sources in Stripe 82 happen to be spatially very close ($\lesssim$ 2"), some of the measurements may suffer from poor deblending during variable seeing conditions, resulting in apparently variable multi-epoch photometry. Inspecting the SDSS images of the 26 variable white dwarf candidates, we found that SDSS J0342+0024 has a close, potentially contaminating neighbour (Fig. 7.4). We therefore decided to drop this star from our candidate list.

7.3.2 Errors in source extraction

While inspecting the light curves of our variable candidates, two objects stood out for having some extremely faint detections. SDSS J0106−0014 has two g-band magnitude measurements of 25.5 mag and 24.6 mag, while SDSS J2157−0044 has one g-band magnitude measurement of 24.7 mag. All these values are much fainter than the nominal g-band limit of SDSS, implying that the objects were most likely just at the edge of detection in those nights. In both cases these magnitudes diverge dramatically from the median magnitude of the object ($g = 18.63$ for SDSS J2157−0044, $g = 18.15$ for SDSS J0106−0014), strongly contributing to the high reduced χ^2 values calculated for these objects. We decided to further verify the reliability of these measurements by checking the coordinates of the detections.

Figure 7.5 clearly shows that, in the case SDSS J2157−0044, the apparent dimming is due to an error in the position at which the source was extracted. However for SDSS J0106−0014 the coordinates of bright and faint detections are consistent, and we have to conclude that a genuine dimming was observed (see Sect. 7.5.3).

7.4 ZZ Cetis candidates

Since the ZZ Ceti instability strip is defined by a narrow range in temperature and surface gravity, a $u-g, g-r$ colour projection of the $T_{\rm eff}/\log g$ strip can be used to select ZZ Ceti candidates (Mukadam et al., 2004; Greiss et al., 2014). By inspecting the colour-colour locus of known ZZ Cetis we selected from our variable candidate list ten stars most likely belonging to this class (Fig. 7.6, Table 7.2). However, as we discuss later, $u-g, g-r$ colours alone are not very efficient at discriminating between ZZ Ceti and non pulsating white dwarfs (see Sect. 7.4.3).

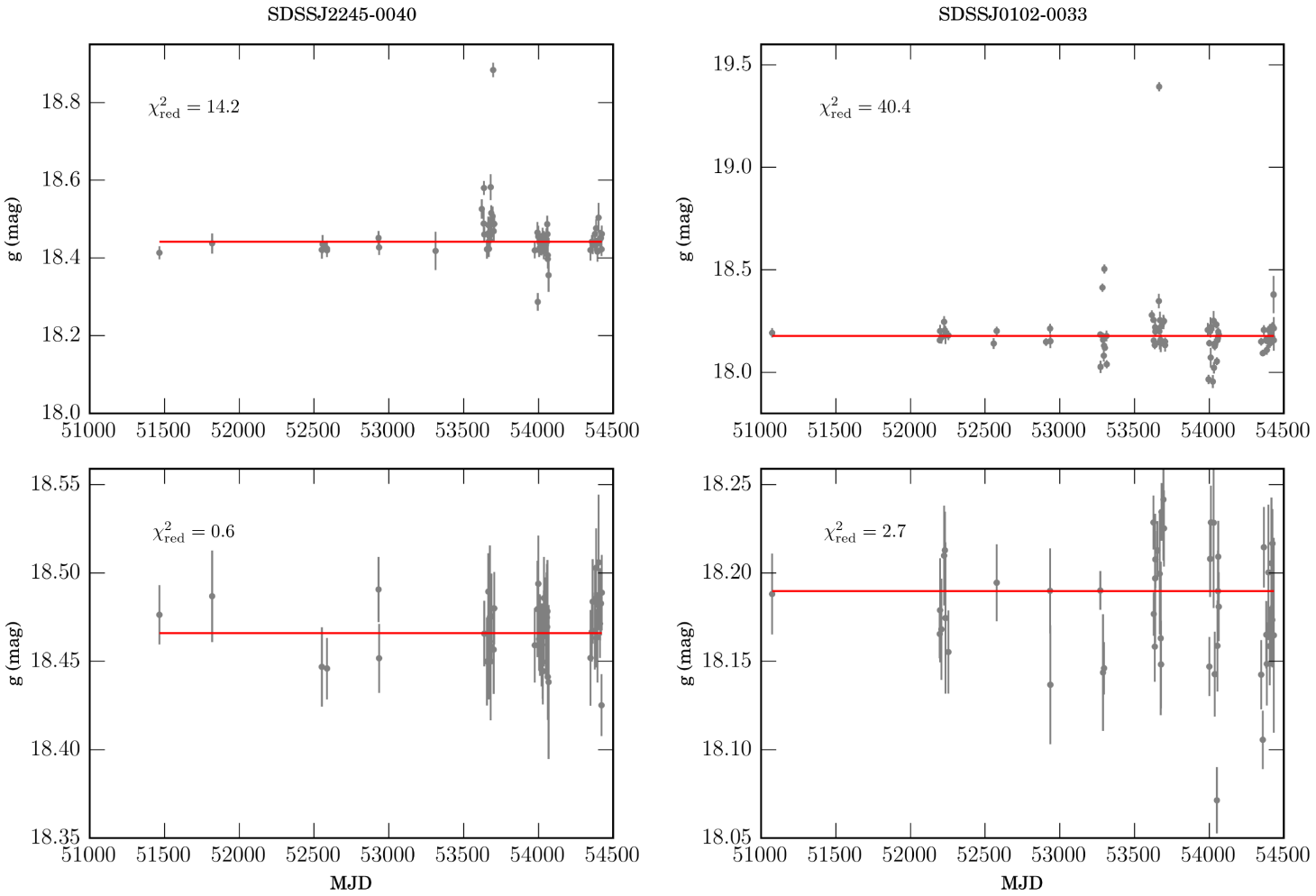

Figure 7.2: Multi-epoch light curves of the "control" white dwarf SDSS J2245−0044 (*left*) and the confirmed ZZ Ceti SDSS J0102−0033 (*right*). *Top panels:* all available Stripe 82 data with the default calibration. *Bottom panels:* Multi-epoch light curves of the same stars after re-calibrating the photometry and discarding unreliable nights. The red line indicates the median magnitude values.

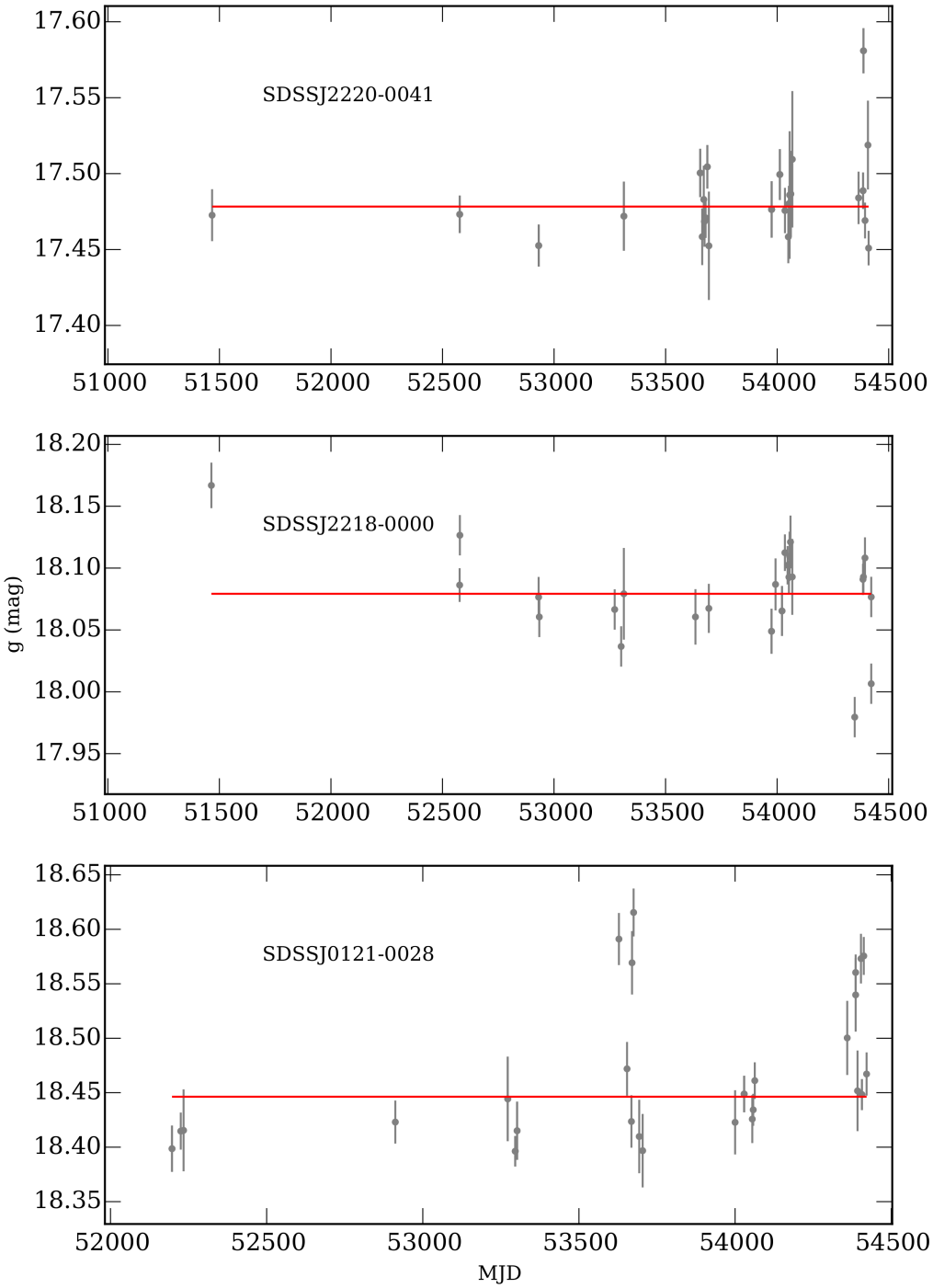

Figure 7.3: Multi-epoch light curves of the candidate variable white SDSS J2220−0041, SDSSJ 2218-0000 and SDSSJ 0121-0028, constructed using re-calibrated photometry and discarding unreliable data. The red line indicates the median magnitude values.

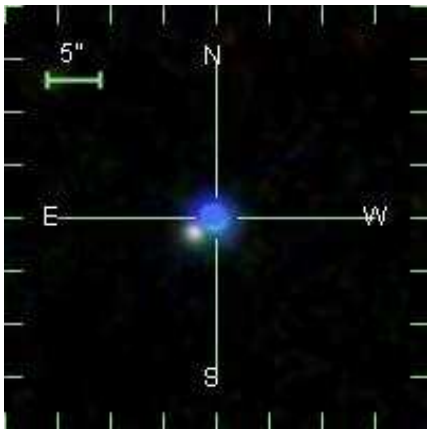

Figure 7.4: SDSS image of SDSS J0342+0024 showing possible contamination from nearby source.

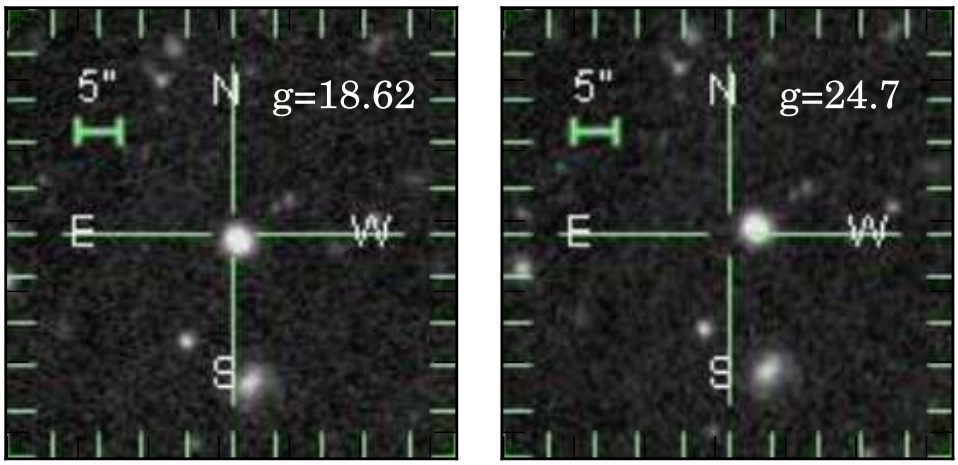

Figure 7.5: SDSS images of SDSSJ 2157−0044 centred at the position of one of the detections close to the median magnitude (*left panel*) and at the position of the faint detection (*right panel*).

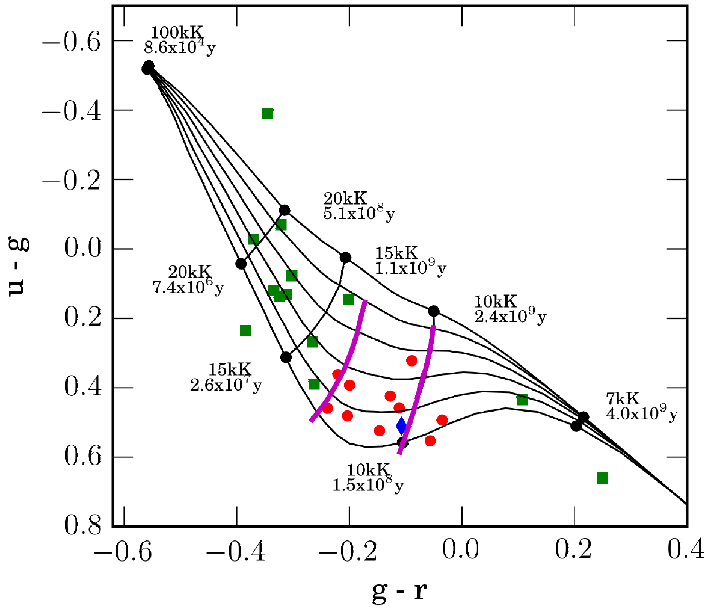

Figure 7.6: $u-g, g-r$ colour-colour distribution of our sample of Stripe 82 variable white dwarfs candidates: ZZ Ceti candidates as red circles, one candidate with no SDSS spectroscopy (see Sect. 7.5.8) as the blue diamond and remaining candidates as green squares. The magenta lines show the empirical boundary of the ZZ Ceti instability strip from Gianninas et al. (2014). White dwarf cooling tracks from Holberg & Bergeron (2006) are shown in the overlay. The colours of our variable candidates have been computed using the median magnitude values.

7.4.1 Follow up observations

We obtained high-speed photometry for six of our ten ZZ Ceti candidates and one V777 Her candidate (see Sect. 7.5.5) in order to confirm their pulsating nature. We used the optical imaging component of the IO (Infrared-Optical) suite of instruments (IO:O) [1] on the Liverpool Telescope (LT) on the island of La Palma. Each target was observed with 30s exposures for $\simeq 2$ hours. In order to verify the robustness of our multi-epoch variability selection we also observed three "control" white dwarfs which have colours compatible with those of ZZ Cetis, but for which we found no evidence of variability in multi-epoch data (i.e. $\chi^2_{\rm red} \leq 1.0$; Table 7.1).

7.4.2 Analysis and results: three new ZZ Cetis

We extracted sky-subtracted light curves from our LT observations and computed Fourier transforms (FT) for our six ZZ Ceti candidates, the three "control" DAs and one candidate V777 Her (see Sect. 7.5.5). We classified a candidate as a con-

[1] http://telescope.livjm.ac.uk/TelInst/Inst/IOO/

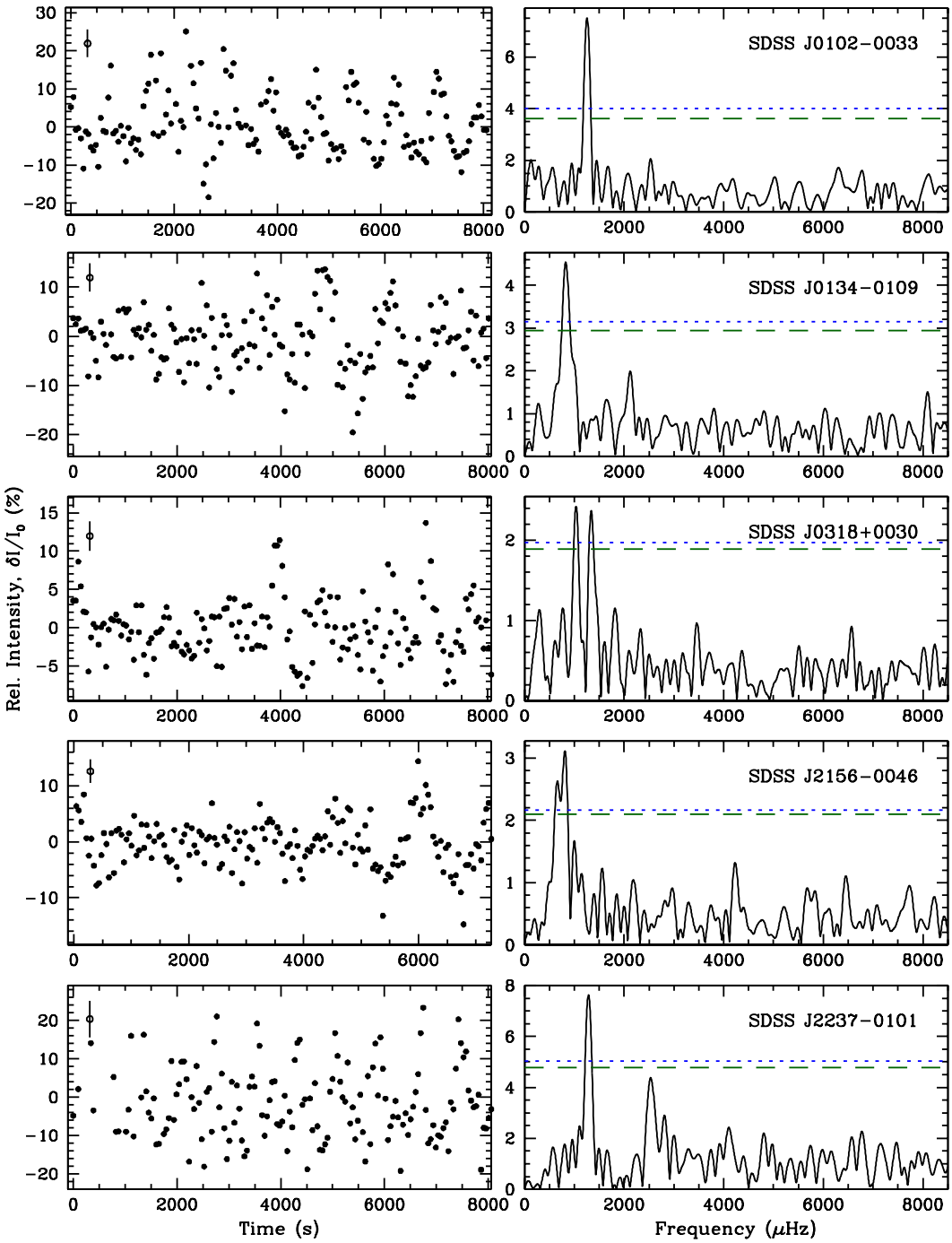

Figure 7.7: LT ligthcurves (left) and corresponding Fourier transforms (right) for the five ZZ Ceti candidates which where confirmed as pulsating white dwarfs. Typical photometric uncertainties are indicated in the top left of each panel. The green dashed line marks 4 times the average amplitude of the entire Fourier transform; the blue dotted line marks the 3-sigma significance threshold, as determined by 10,000 bootstrap shuffles of the light curve (for more details see Greiss et al. 2014). SDSS J0134−0109, SDSS J2237−0101 and SDSS J2156−0046 are new high-amplitude ZZ Ceti discoveries.

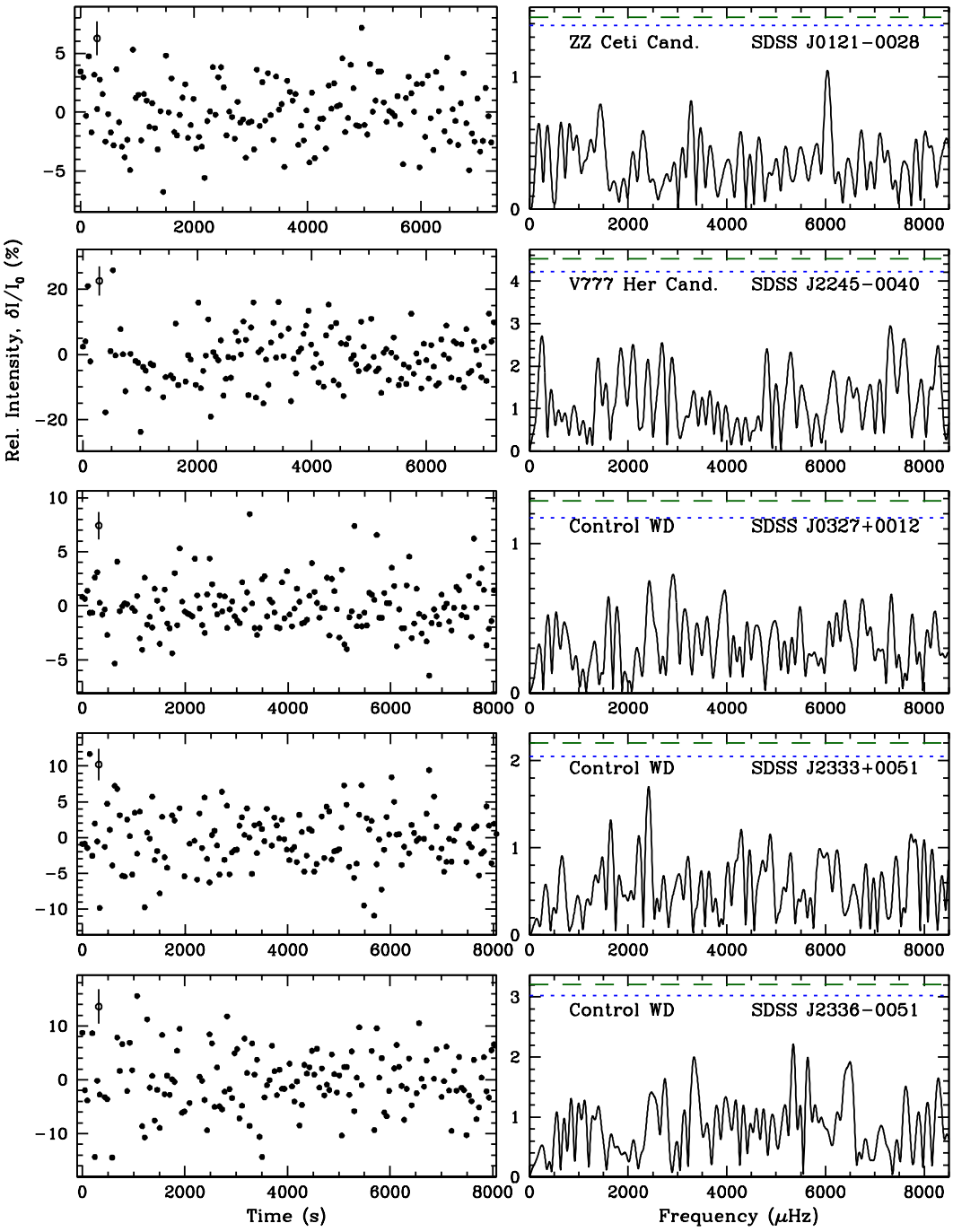

Figure 7.8: As Figure 7.7 for the five objects for which we detected no variability in our LT observations. SDSS J0327+0012, SDSS J2245−0040 and SDSS J2336−0051 have colours compatible with those of ZZ Cetis, but show no evidence of variability in their Stripe 82 data ("control" white dwarfs). Our observations do not completely rule out the presence of pulsations, as all objects may vary at smaller amplitudes; the maximum pulsation amplitude of known ZZ Cetis has a median of 1.5 per cent in the SDSS g band.

firmed pulsating white dwarf if its FT shows a peak larger than 4 times the average amplitude of the entire FT and above a $3\,\sigma$ threshold (Greiss et al., 2014). Of the six ZZ Ceti candidates observed we detect pulsations for five of them. Two (SDSS J0102−0033 and SDSS J0318+0030) had already been identified as ZZ Ceti stars by Mukadam et al. (2004), while the remaining three (SDSS J0124−0109, SDSS J2157−0044 and SDSS J2237−0101) are new discoveries (Fig. 7.7). We designate the remaining five objects (three "control" white dwarfs, one ZZ Ceti candidate and one V777 Her candidate) as "not observed to vary" (NOV) and estimate percentile non variability limits (Fig. 7.8). These results are reported in Table 7.2.

7.4.3 The ZZ Ceti instability strip

As mentioned in Section 7.4 we picked our ZZ Ceti candidates by selecting the Stripe 82 variables which were closest to the $u-g, g-r$ projection of the ZZ Ceti instability strip. However, Fig. 7.9 reveals that many known NOVs are within the $u-g, g-r$ boundaries used; and vice versa, confirmed ZZ Cetis lie significantly outside the strip. Several studies have shown that a candidate selection purely based on colours yields a success rate of only $13-30$ per cent (see Voss et al. 2006; Fontaine et al. 1982; Mukadam et al. 2004). Even though $u-g, g-r$ colours are good indicators of white dwarf temperature it appears that the narrow range of $T_{\rm eff}$ and $\log g$ that defines the ZZ Ceti instability strip does not unambiguously project to the observed colours. Furthermore, the *ugriz* magnitudes of SDSS are not acquired simultaneously, but in the sequence *riuzg*, with observations in each filter separated by 71.72 s. As a result u and g band observations are performed roughly 143 seconds apart and g and r observation nearly 290 seconds apart. Cool pulsating white dwarfs can vary in brightness by up to 20 percent on such timescales, implying that the SDSS colours of these objects may be taken during different pulsation phases and are not, therefore, reliable indicators of temperature. Figure 7.10 clearly illustrates this effect, i.e. multi-epoch colours of confirmed ZZ Cetis exhibit much larger scatter in colour-colour space than those of confirmed NOVs. Reddening too, though often considered to be a minor effect for relatively nearby white dwarfs, may still contribute to the observed discrepancy between temperatures and colours.

If optical spectra are available, $T_{\rm eff}$ and $\log g$ can be measured from fitting the Balmer lines of DA white dwarfs. (Koester et al. 1979, Bergeron et al. 1995, Koester 2009, Tremblay et al. 2011). ZZ Ceti candidates can then be reliably selected on the basis of the atmospheric parameters (Bergeron 2001, Mukadam et al. 2004, Gianninas et al. 2011). Figure 7.9 illustrate that the majority of known ZZ Cetis (including the five confirmed as part of this work) lie within the boundaries of the

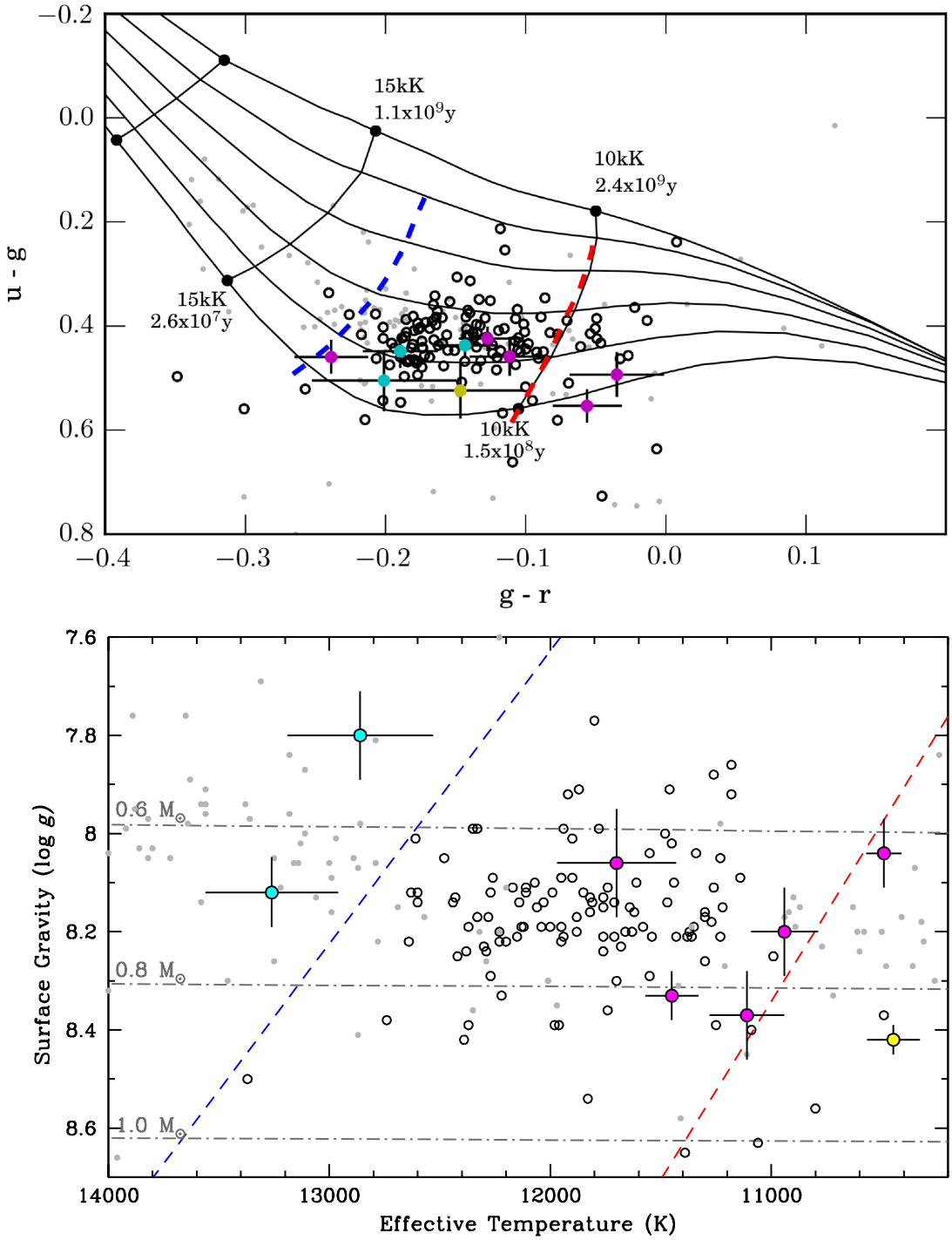

Figure 7.9: Colour distribution (*top panel*), and $T_{\rm eff}$-$\log g$ distribution (*bottom panel*) of known ZZ Cetis (empty circles) and NOVs (grey dots). $\log g$ and $T_{\rm eff}$ values were taken from Tremblay et al. (2011) and Gianninas et al. (2011) and are calculated using 1D atmospheric models. The empirical blue and red edge of the ZZ Ceti instability strip are shown as a blue and a red dashed line, respectively. We include our confirmed ZZ Cetis as magenta dots and our "control" white dwarf confirmed as NOVs as cyan dots (Table 7.2) and the ZZ Ceti candidate SDSS J0121−0028 (Sect. 7.5.1) as a yellow dot. The "control" white dwarf SDSS J0327+0012 is outside the range of the plot in the bottom diagram.

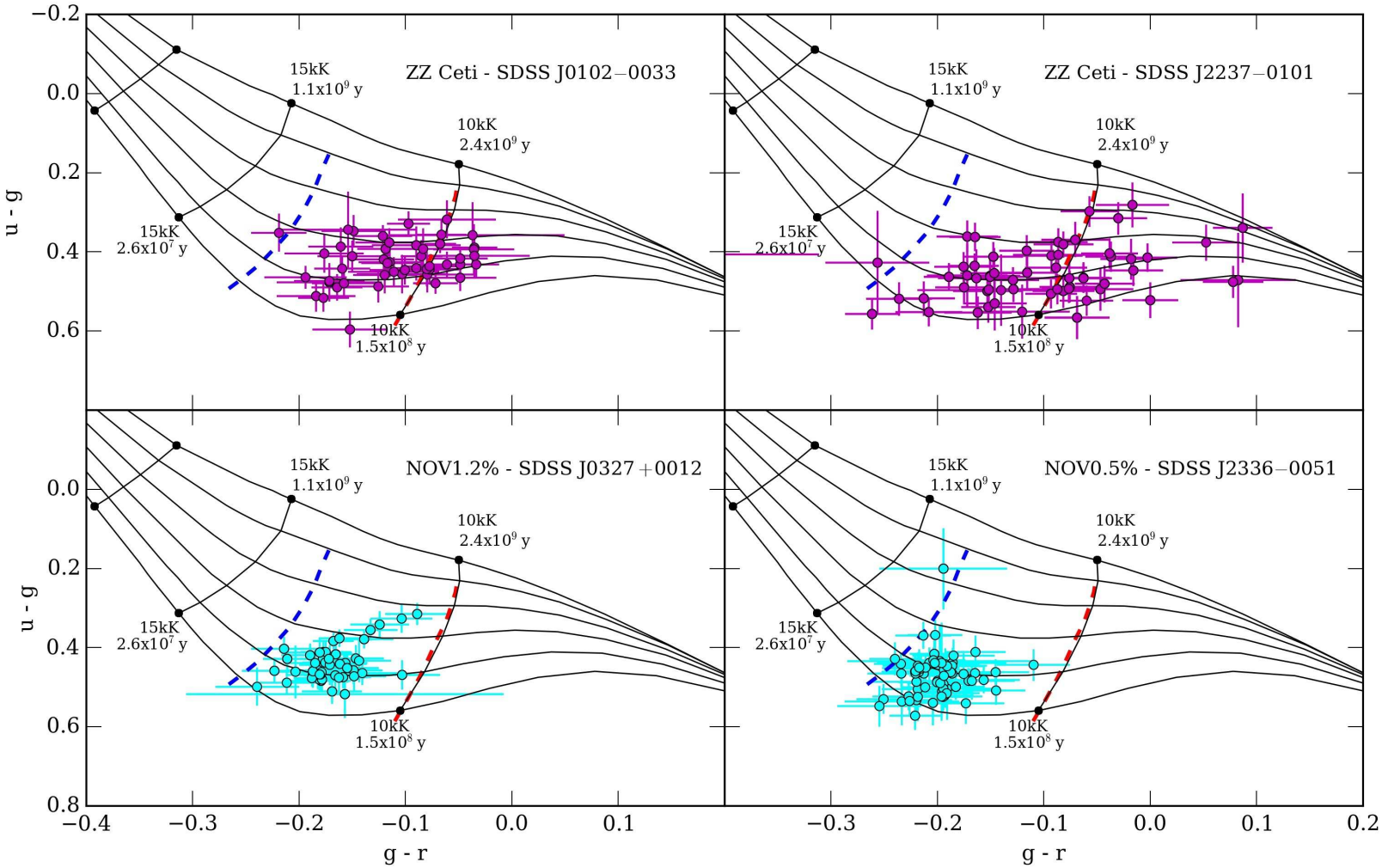

Figure 7.10: Colour-colour distribution of all reliable recalibrated Stripe 82 epochs of two confirmed ZZ Cetis (SDSS J0102−0033, SDSS J2237−0101, *top panels*, magenta points) and two confirmed NOV, "control" white dwarfs (SDSS J2245−0040 and SDSS J2336−0051, *bottom panels*, cyan points). The empirical blue and red edge of the ZZ Ceti instability strip are shown as a blue and a red dashed line, respectively.

Table 7.3: Pulsation properties of the five confirmed ZZ Cetis. Three new ZZ Ceti discovered as part of this work are marked with *.

name	period (s)	amplitude (%)
SDSS J0102−0033	796.1±3.7	7.51±0.65
SDSS J0134−0109*	1212±13	4.54±0.59
SDSS J0318+0030	969±11	2.18±0.35
	746.4±6.7	2.11±0.35
SDSS J2156−0046*	1234±15	3.14±0.41
	1478±21	2.70±0.35
SDSS J2237−0101*	774.4±4.6	8.01±0.85
	392.3±2.2	4.47±0.83

empirical instability strip, with little contamination from NOVs. Even though the spectroscopic method can achieve efficiency upwards of 80 per cent, the required large samples of spectroscopically confirmed DAs are observationally expensive.

In this pilot study we selected ZZ Ceti candidates without relying on spectroscopy and combining colour selection with the evidence of multi-epoch variability. Five out of the six candidates followed-up with high speed photometry, were confirmed to be ZZ Cetis (see Sect. 7.4.2), implying an efficiency $\simeq 83$ per cent. Even though limited to sparse data over only the $300\,\mathrm{deg}^2$ of Stripe 82, we showed that, using multi-epoch data, it is possible to achieve an efficiency similar to that of the spectroscopic selection method. However it is important to keep in mind that our statistics is limited to only the six ZZ Ceti candidates we followed up with LT observations. Our selection method is biased in favour of cool, high-amplitude ZZ Cetis (see Sect. 7.4.4) and our three newly identified ZZ Cetis are among the coolest ever discovered. With their identification we empirically constrain the red edge of the instability strip. Applying this selection to other current and future time domain surveys (e.g. PanSTARSS, LSST) will provide very large samples of high-confidence ZZ Ceti candidates, paving the way for global ensemble asteroseismology of white dwarfs.

7.4.4 Pulsation properties of the ZZ Ceti variables

We list the dominant periods found for the five confirmed ZZ Cetis in Table 7.3. All five ZZ Cetis undergo large amplitude pulsation with periods longer than 600s, which are normally associated with cool ZZ Cetis ($T_{\mathrm{eff}} \simeq 11,000\,\mathrm{K}$). Fig. 7.9 clearly shows that all our confirmed ZZ Cetis are indeed cool pulsators, with three of them lying on the red edge of the instability strip. This selection effect is caused by the

fact that pulsation amplitude increases with decreasing $T_{\rm eff}$. Since variability with amplitudes $\lesssim$0.03 mag would not be detectable in the Stripe 82 data, we are biased to preferentially select cool, large-amplitude ZZ Cetis.

Mukadam et al. (2004) report periods for SDSS J0102−0033 (926.1 s, 830.3 s) and SDSS J0318+0030 (826.4 s, 587.1 s, 536.1 s) compatible with cool ZZ Cetis, but significantly different from the period reported here. Such changes in pulsation periods over long time scales are not uncommon, as cool ZZ Cetis are known to undergo amplitude and frequency variations (e.g. G29−38, McGraw & Robinson 1975; Kleinman et al. 1998; GD 1212, Hermes et al. 2014a).

7.5 Notes on single objects

7.5.1 SDSS J0121−0028

Based on its $u-g; g-r$ colours, SDSS J0121−0028 was selected as a ZZ Ceti candidate, but in our two hours high-speed photometric follow-up we did not observe any pulsation to a limit of 1.39 per cent. The amplitude of the variation calculated from the Stripe 82 data (8-10 per cent, Table 7.1) is above this non-variability threshold, possibly implying that our LT observations were taken during a period of destructive interference of the pulsation modes (e.g. Castanheira et al. 2006). Nonetheless, Fig. 7.9 shows that SDSS J0121−0028 lies outside the ZZ Ceti instability strip, redward of the the red edge. If SDSS J0121−0028 is indeed a ZZ Ceti it would be a rare, though not unprecedented, outlier (e.g. WD J0940+0050, Castanheira et al. 2013). Another possibility is that SDSS J0121−0028 undergoes some other type of magnitude variation on timescales longer than 2 hours.

To further investigate the nature of SDSS J0121−0028, we retrieved all available ultraviolet and mid-infrared photometry of SDSS J0121−0028. The spectral energy distribution of SDSS J0121−0028 (Fig. 7.11) shows a marked infrared excess which is not consistent with a single, isolated white dwarf. The presence of a close, low-mass companion could explain the observed infrared excess and companions may also cause some degree of optical variability in white dwarfs (Littlefair et al. 2014; Casewell et al. 2015; Maoz et al. 2015).

However the infrared excess in SDSS J0121−0028 becomes apparent only in the UKIDSS K band, rising towards longer wavelengths. A blackbody fit to this infrared emission, adopting the photometric distance of the white dwarf, suggests a $T_{\rm eff} \simeq 1100$ K and radius $\simeq 2.1$ Jupiter radii ($\rm R_J$), i.e. more than twice the radius of a typical brown dwarf (0.83 $\rm R_J$, Sorahana et al. 2013). It therefore seems unlikely that the infrared excess is caused by a brown dwarf companion. An alternative ori-

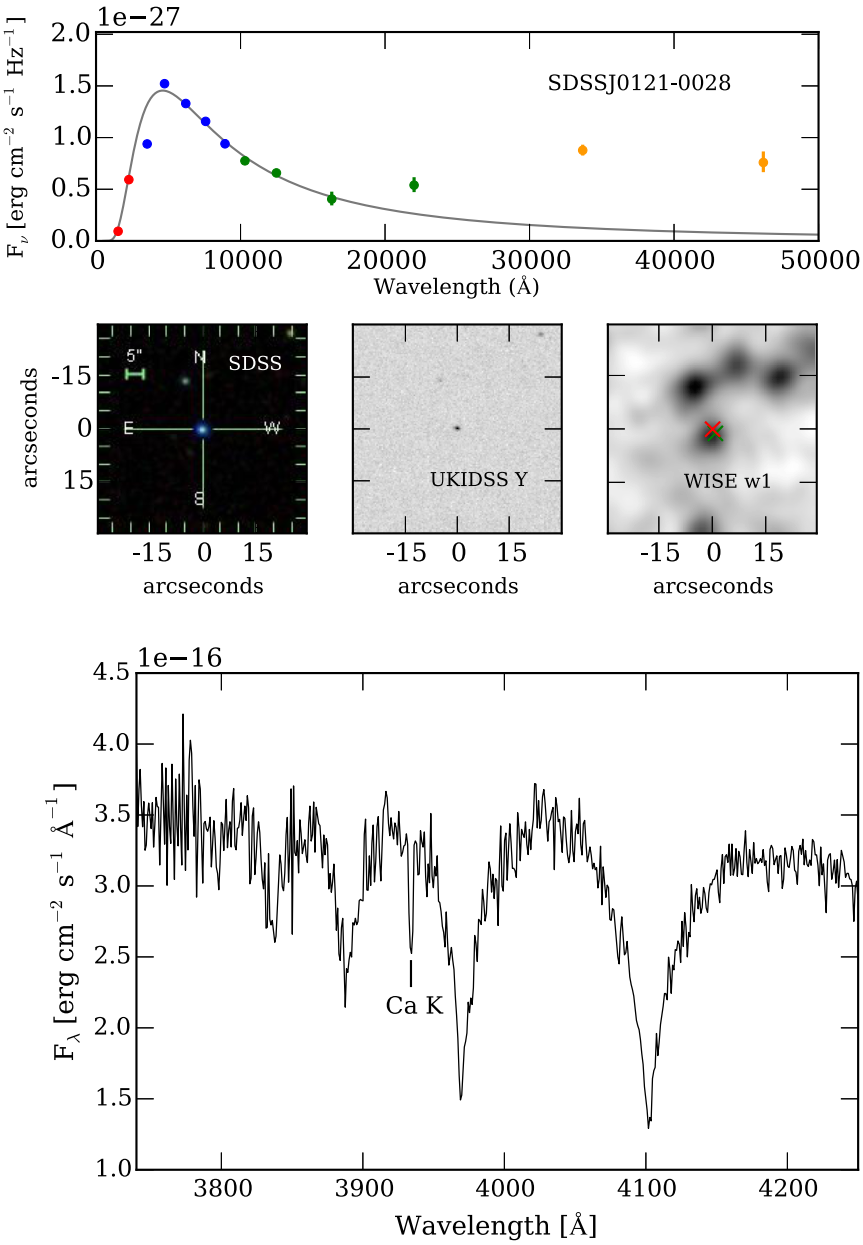

Figure 7.11: *Left panel*: Spectral energy distribution of SDSS J0121−0028. Galex fuv, nuv fluxes are plotted in red, SDSS Stripe 82 recalibrated median $ugriz$ fluxes in blue, UKIDSS $YJHK$ fluxes in green and WISE $w1, w2$ fluxes in yellow. The grey solid line shows a blackbody model of the white dwarf fitted to the g and r fluxes. *Right panel*: SDSS spectrum of SDSS J0121−0028 showing the presence of Ca K absorption line.

gin of the infrared excess could be a circumstellar debris discs resulting from tidal disruption of rocky planetesimals (Graham et al. 1990; Jura 2003), and $\simeq 1-3.5$ per cent of all white dwarfs exhibit infrared excesses consistent with the presence of such discs (Farihi et al., 2009; Girven et al., 2011; Rocchetto et al., 2015). In all cases the presence of these discs is accompanied with metal pollution of the white dwarf atmosphere. Close inspection of the SDSS spectrum of SDSS J0121−0028 reveals a strong calcium absorption line at 3933.7Å, identifying it as a metal polluted DAZ white dwarf (Fig. 7.11). The presence of metals in the photosphere of SDSS J0121−0028 strongly supports the hypothesis that the observed infrared excess is due to a debris disc. There is growing evidence of variability in some white dwarf debris discs, including changes in the optical line profiles (Gänsicke et al., 2008; Wilson et al., 2015) and line fluxes (Wilson et al., 2014) from gaseous discs, as well as changes in the infrared flux from the dust (Xu & Jura, 2014). However, to date, optical variability in white dwarfs with debris discs has only been observed at amplitudes much lower than what we measured for SDSS J0121−0028.
The data at hand does not allow to unambiguously determine the nature of the variability of SDSS J0121−0028 and we recommend further observations of this object.

7.5.2 SDSS J0050−0023 and SDSS J0326+0018

Two of our ZZ Ceti candidates had already been observed by Mukadam et al. (2004) and found not to vary: SDSS J0050−0023 and SDSS J0326+0018. We did not acquire more observations, but the NOV limits calculated by Mukadam et al. (2004) are considerably smaller than the amplitudes of the variability detected in the Stripe 82 data (> 0.1 mag; Table 7.1). Again this implies that these white dwarfs may vary on longer timescales.

SDSS J0050−0023 is known massive white dwarf with spectroscopic mass above a $1 M_{\odot}$ (Castanheira et al., 2010). At the temperatures around the ZZ Ceti instability strip, stars with such mass are expected to be up to 90 per cent crystallized (Kanaan et al., 2005). Crystallization has significant effect on the pulsation properties of a white dwarfs since pulsations cannot propagate into the crystallized region (Montgomery & Winget, 1999). Pulsating massive white dwarfs can therefore experience dramatic changes in their pulsation amplitudes (e.g. BPM37093, McGraw 1976; Kanaan et al. 1998).

SDSS J0050−0023 was classified as NOV6 by Mukadam et al. (2004) and NOV3.7 by Castanheira et al. (2010), however Castanheira et al. (2010) also report possible, lower-amplitude pulsations with a period of 584s. The multi-epoch variability observed in Stripe 82 seems to validate the hypothesis that SDSS J0050−0023

is a massive pulsator with highly variable pulsation amplitudes. It is possible that all high-cadence monitoring to date was carried out during a phases of pulsation dampening and consequently failed to identify pulsations. We encourage further, long-term monitoring of SDSS J0050−0023 to determine if the star is truly variable.

7.5.3 SDSS J0106−0014: an eclipsing binary

In Sect. 7.3.2 we mentioned that the Stripe 82 data of SDSS J0106−0014 contains two extremely faint, but reliable detections. Literature research revealed that SDSS J0106−0014 is a known eclipsing binary system (Kleinman et al., 2004). Previous observation of this objects reported a period of 0.085 days with a mid-eclipse time at MJD 55059.051 (Parsons et al., 2015). This ephemeris confirms that the dim detection of SDSS at MJD 53697.271 and 52522.362 indeed correspond to observations taken in eclipse.

7.5.4 Magnetic White Dwarfs

Nearly half a century ago, Kemp et al. (1970) detected circularly polarized light from the white dwarf GJ 742 proving that the star harboured a magnetic field. Since then hundreds of magnetic white dwarfs have been identified via spectropolarimetry (e.g. Friedrich et al. 1996; Vennes et al. 2003; Kawka et al. 2007) or detection of Zeeman splitting (e.g. Hagen et al. 1987; Reimers et al. 1996; Kleinman et al. 2013). Wide-area spectroscopic surveys have played a pivotal role in these searches, with SDSS in particular being responsible for the discovery of the majority of known magnetic white dwarfs (Gänsicke et al., 2002; Schmidt et al., 2003; Külebi et al., 2009; Kleinman et al., 2013; Kepler et al., 2015). The actual fraction of white dwarfs with magnetic fields is hard to estimate because of the lack of a well defined, homogeneous, large spectroscopic sample of white dwarfs. Magnitude limited censuses suggest that 3−4 per cent of all white dwarfs harbour strong ($\gtrsim 2$ MG) magnetic fields (Liebert et al., 2003; Kepler et al., 2013). However, since hotter white dwarfs are visible at larger distances, magnitude limited samples are inevitably biased towards hotter systems. In contrast, the fraction of magnetic white dwarfs in a volume limited sample should reflect more accurately the true incidence of these objects. Kawka et al. (2007) closely examined the local sample of white dwarfs and found 10 to 30 per cent of the objects to be magnetic. But again sever biases may effect this statistics as the local sample is not representative of the entire white dwarfs population (Hollands et al., 2015).

Another important open question about magnetic white dwarfs concerns the

origin of the magnetic field. Several scenarios have been put forward:

- Fossil field left over from the evolution of magnetic, peculiar Ap and Bp stars (Angel et al., 1981; Wickramasinghe & Ferrario, 2000). As these stars evolve off of the main sequence the magnetic flux is conserved and the contraction of the stellar radius can amplify the surface field by a factor $\sim 40,000$. This single star formation channel can successfully explains the observed field strengths, but the low space density of Ap and Bp stars is not sufficient to account for the incidence of magnetic white dwarfs (Kawka & Vennes, 2004).

- Common envelope magnetic dynamo during binary evolution. In binary systems, the evolution and consequent expansion of one of the two stars may lead to a common envelope phase (Webbink, 1984). Within this envelope the stars lose angular momentum and spiral inward towards each other. Eventually the common envelope is ejected leaving behind a close binary or a single star resulting from a merger. Tout et al. (2008) suggested that within the common envelope a magnetic dynamo may be generated and the resulting magnetic field may survive after the expulsion of the envelope remaining bound to the newly formed white dwarf. This formation mechanism could generate magnetic fields $\geq 1\,\mathrm{MG}$. Furthermore empirical evidence seems to suggest that magnetic white dwarfs have, on average, higher masses than non-magnetic ones (Liebert, 1988). Indeed the binary formation scenario proposed by Tout et al. (2008) would generate more massive white dwarfs.

  On the other hand, recent work by Hollands et al. (2015) showed that a significant number of cool DZ white dwarfs harbour magnetic fields. Assuming a binary formation scenario it is hard to justify the presence of accreted planetary material in the magnetic white dwarf's atmosphere.

- Magnetic dynamo generated during planetary engulfment. Some studies have suggested that a similar scenario to the common envelope one may occur if during its evolution, the white dwarf progenitor engulfs a giant gaseous planet or a brown dwarf. In this case the magnetic dynamo would be generated within the expanded shells of the star as the low-mass companion spirals inward (Farihi et al., 2011b; Nordhaus et al., 2011). This formation mechanism would not justify the higher average mass of magnetic white dwarfs, but it would explain the high incidence of magnetic fields in cool DZs (Hollands et al., 2015)

Some magnetic white dwarfs also exhibit period brightness variability. The origin of this variability is still matter of debate, but the most likely causes are stellar

rotation combined with localized magnetic dichroism (Brinkworth et al., 2013) or, in the case on convective white dwarfs (i.e $T_{\rm eff} < 14,000$K for DAs), the presence of star-spots (Lawrie et al., 2013). The period of these brightness modulation should, therefore, correspond to the rotation period of the white dwarf. The rotation period can provide valuable informations on the history of the white dwarf and, most importantly it can help distinguish between different evolutionary scenarios (Brinkworth et al., 2013; Lawrie et al., 2013). For example, single stars evolutionary channel should produce white dwarfs with relatively low rotation rates while white dwarfs resulting from mergers in binary systems should be very fast rotators.
Inspecting the SDSS spectra available for our 26 Stripe 82 variable candidates, we identify two magnetic white dwarfs: SDSS J2218−0000 and SDSS J0321−0050. The Zeeman splitting of Hα in SDSS J0321−0050 is very weak (Fig. 7.12). In fact, this star was previously classified as a non-magnetic DA (Eisenstein et al., 2006; Kleinman et al., 2013; Gentile Fusillo et al., 2015). Following Reid et al. (2001), we estimate the average surface magnetic field strength, Bs, according to the equation:

$$B\mathrm{s/MG} = \frac{\Delta(1/\lambda)}{46.686}, \tag{7.1}$$

where $\Delta(1/\lambda)$ is the inverse wavelength separation in cm^{-1} between the components of a Zeeman triplet (Reid et al., 2001); and find $B\mathrm{s} = 1.36 \pm 0.04$ MG. In contrast, SDSS J2218−0000 was already identified as a magnetic white dwarf and has a field sufficiently strong to smear out most of the Balmer lines ($B\mathrm{s} \simeq$ 225 MG, Schmidt et al. 2003; Külebi et al. 2009)

7.5.5 The V777 Her candidate SDSS J2333+0051

Among our variable candidates we identified one DB white dwarf (SDSS J2333+0051). With only $\simeq$ 20 V777 Her stars known to date, a robust definition of a DB white dwarfs instability strip, both empirical and theoretical, is still an ongoing challenge (Kilkenny et al. 2009, Nitta et al. 2009). Current evidence suggests that canonical 0.6 $M_\odot$ DB white dwarfs undergo pulsation as they cool between roughly 29,000 K and 21,000 K (Nitta et al., 2009). SDSS J2333+0051 has $T_{\rm eff} =$ 22,857 K and $\log g = 8.09$ (Kleinman et al. 2013; Table 7.2) and is therefore a likely V777 Her candidate. As for our ZZ Ceti candidates, we obtained high-speed photometry of SDSS J2333+0051 and carried out the required Fourier space analysis (Sect. 7.4.1). We did not detect pulsations in SDSS J2333+0051 to a limit of 2.1 per cent. Based only on this result we cannot conclusively exclude that SDSS J2333+0051 is a V777 Her, as it may have lower amplitude pulsations. However the multi-epoch

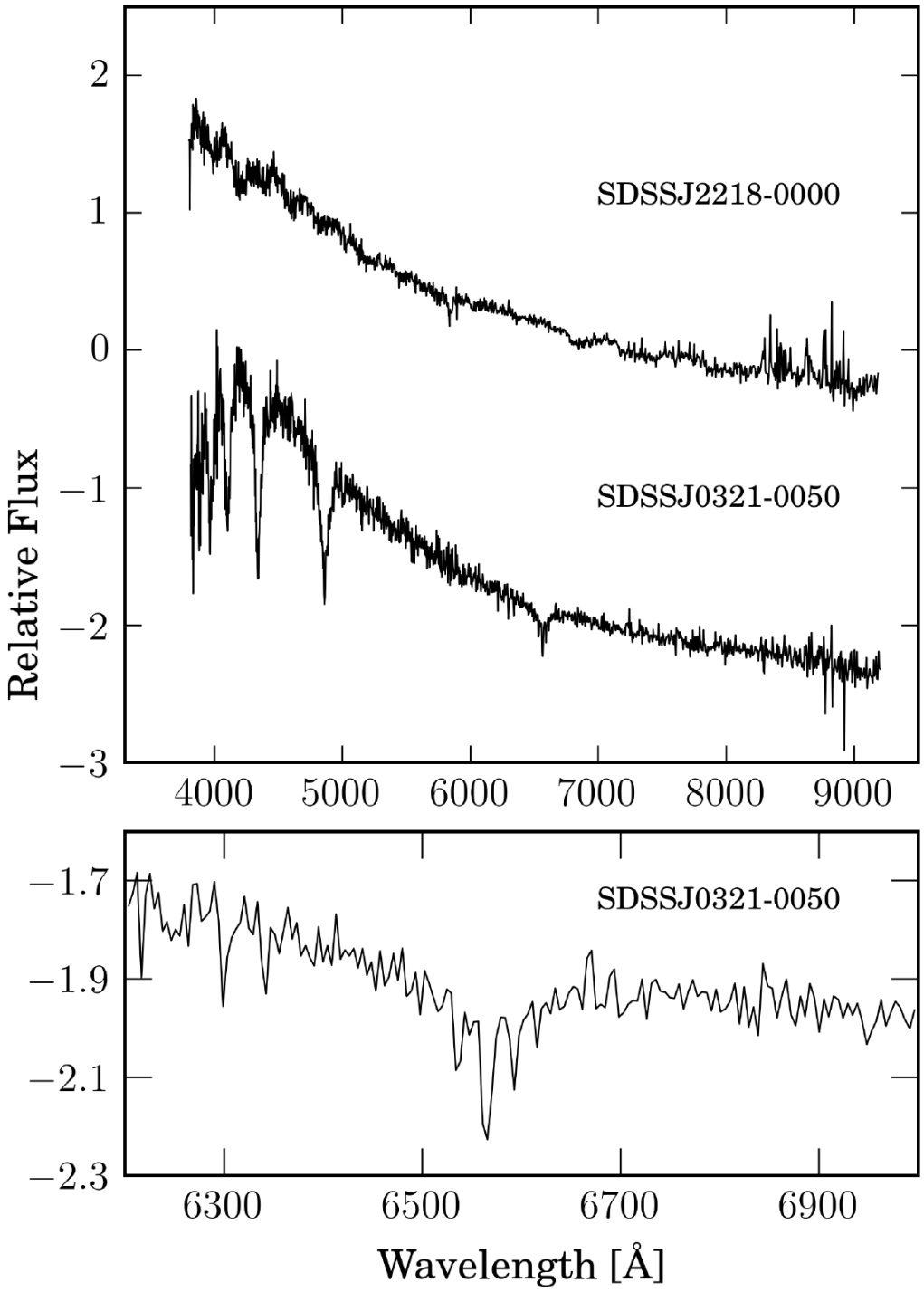

Figure 7.12: SDSS spectra of SDSS J2218−0000 and SDSS J0321−0050. In SDSS J2218−0000 the high magnetic field ($\simeq$ 225 MG) splits and significantly blurs the Balmer lines beyond recognition. In the case of SDSS J0321−0050 the presence of a weak field ($\simeq$ 1.4 MG) is revealed by Zeeman splitting of the Hα absorption line (*bottom panel*).

Stripe 82 variability observed for SDSS J2333+0051 has a larger amplitude (0.16 ± 0.02 mag, Table 7.1) than the limit obtained by our LT observations. It is therefore possible that this white dwarfs probably undergoes larger amplitude variations on longer timescales and we therefore encourage further observations of this star.

7.5.6 The PG1159 star SDSS J0349−0059

By inspecting the available SDSS spectra we identified one of our variable candidate, SDSS J0349−0059, as a PG1159 star (Table 7.2). SDSS J0349−0059 is a well studied object and a known pulsator (Woudt et al., 2012). Being able to independently recover a pulsating PG1159 star further proves the reliability of our selection method.

7.5.7 SDSS J2220−0041, a white dwarf plus brown dwarf binary

One of our variable candidates, SDSS J2220−0041, is a known white dwarf plus brown dwarf binary (PHL 5038, Steele et al. 2009). The presence of a low mass companion can, in some cases, cause some optical variability. Such variability is normally the result of irradiation of a tidally locked brown dwarf or ellipsoidal modulations (Littlefair et al. 2014; Casewell et al. 2015; Maoz et al. 2015). Both these mechanisms require the stars in the binary to be very close, but SDSS J2220−0041 is instead a wide binary system. The two stars in the system are spatially resolved at an angular separation of 0.94"; corresponding to an orbital separation of $\simeq$ 55 AU (Steele et al., 2009). The Stripe 82 data alone does not allow to identify the nature of the variability or to speculate on a possible connection with the presence of the brown dwarf companion.

7.5.8 The white dwarf candidate SDSS J2157+0037

Stripe 82 has been the subject of many diverse studies and, consequently, it is one of the areas of the SDSS footprint with highest spectroscopic completeness. Indeed, of the 400 white dwarf candidates in our initial sample only 69 do not have a SDSS spectrum, and of the final 26 variable candidates found by our selection algorithm only one object, SDSS J2157+0037, lacks SDSS spectroscopy. We can therefore only speculate about the nature of the observed variability. Its $u - g\,(0.51)$ and $g - r\,(-0.11)$ colours are compatible with those of ZZ Ceti stars (Fig. 7.6). Furthermore, the amplitude measured from its Stripe 82 lightcurve is similar to those of the confirmed ZZ Cetis in our sample. Again we encourage further observation of this object.

7.6 Conclusions

We have developed a method to select variable white dwarfs in large-area time domain surveys. Starting from a sample of white dwarf candidates, our method allows to correct and select reliable photometry using observations of neighbouring non-variable objects. Using this recalibrated photometry we then selected variable white dwarf candidates. We test our selection algorithm with a pilot search for pulsating white dwarfs in the SDSS Stripe 82.

From a sample of 400 white dwarf candidates taken from Gentile Fusillo et al. (2015), we identified 24 variable candidates. From these 24 objects we further selected ZZ Ceti candidates using $u-g, g-r$ colours and acquired high-speed photometric follow up of six targets. We confirm five of our candidates as cool ZZ Cetis, three of which are new discoveries. Selection purely based on colour typically yields a success rate of only 13−30%. We show that non simultaneous multi-band photometry is one of the causes of this low efficiency as it leads to unreliable colours for cool pulsating white dwarfs. However, we show that colour selection, combined with evidence of multi-epoch variability, significantly improves the quality of the ZZ Cetis candidates, without recourse to spectroscopy, achieving an efficiency of more than 80 per cent. Among our candidates we also recover one known pulsating PG1159 star and one known eclipsing binary. We speculate on the most likely cause for the observed variability of the remaining candidates. Even though we recommend further observations to confirm beyond any doubt the variable nature of all our candidates, this pilot study already reveals the ability of our method to efficiently identify different types of variable white dwarf from eclipsing binaries to cool, large-amplitude-pulsating white dwarfs.

SDSS Stripe 82 proved a useful resource for testing our selection method, but it only covers only 300 deg^2, with sparse observations taken under variable observing conditions. Upcoming time-domain surveys will cover much larger areas with more continuous cadence (eg. PTF, Law et al. 2009; Pan-STARRS, Morgan et al. 2014; Gaia, Walton 2014; LSST, Ivezic et al. 2011). The application of our selection method to these surveys will lead to identification of variable white dwarfs on industrial scale and provide very large samples of high-confidence ZZ Ceti candidates. In this pilot study we were aided by the high spectroscopic completeness of Stripe 82, but given the large area coverage of future time-domain surveys, such intense spectroscopic follow-up may not always be available. The photometric selection method presented in Chapter 4 will perfectly complement future searches for variable white dwarfs providing large samples of high-confidence white dwarf candidates.

Chapter 8

Planetary remnants around white dwarfs.

8.1 Metal pollution and debris discs.

Nearly a century ago the American astronomer Adriaan van Maanen discovered a new high proper motion star (van Maanen 2, van Maanen 1917). The strong calcium H & K absorption features in its spectrum led to its initial classification as an F star. Only years later the star was correctly identified as the third known white dwarf and the first one to be metal polluted (Kuiper, 1934, 1941). Today, mainly thanks to large area surveys, we know thousands of white dwarfs and the latest studies indicate that 25 to 50 per cent of them show traces of metal pollution (Zuckerman et al., 2003; Koester et al., 2005b; Zuckerman et al., 2010; Koester et al., 2014; Barstow et al., 2014). The very existence of metal polluted white dwarfs is somewhat puzzling as the high surface gravity should cause such heavy elements to sink out of the photosphere on timescales much shorter than the white dwarf's cooling age (see Chapter 1, Sect. 1.2.2; Fontaine & Michaud 1979; Muchmore 1984; Paquette et al. 1986; Koester 2009). The only viable explanation for the atmospheric composition of these objects is ongoing, or recent, accretion from an external source (Sion et al., 1990). Initially, the origin of metals had been explained in terms of episodic accretion from the interstellar medium (ISM; e.g. Dupuis et al. 1993a,b; Dufour et al. 2007b). However, the high abundances and accretion rates of the polluting material (Aannestad et al., 1993; Farihi et al., 2010b), and, most notably, the apparent lack of accreted hydrogen in DBZ white dwarfs could not be reconciled with the ISM accretion hypothesis (e.g Koester 1976; Koester & Wolff 2000; Friedrich et al. 2004). At about the same time when astronomers started to question the ISM accretion hypothesis, Zuckerman & Becklin (1987) discovered an

infrared (IR) excess around the metal-polluted white dwarf G29-38. Initially this was suggested to be a brown dwarf companion, but further observation demonstrated that it was in fact caused by emission from a dusty disc in orbit around the white dwarf (Graham et al., 1990). Koester et al. (1997) later discovered the presence of metals in the atmosphere of G29-38 and concluded that the star was currently accreting those heavy elements from an external source. A few years later Jura (2003) formally proposed that the circumstellar debris disc around G29-38, and the metals in photosphere of the star, were the result of the tidal disruption of one or more asteroids. As more metal polluted white dwarfs (DxZs) with debris discs were discovered, accretion of debris resulting from the tidal disrupted planetary remnants became the widely accepted explanation for metal pollution (Zuckerman et al., 2003; Farihi et al., 2009, 2010a). Further support for this theory came from the discovery, via the detection of emission lines of the 8600 Å CaII triplet, of DxZs with gaseous discs (Gänsicke et al., 2006a, 2007, 2008; Melis et al., 2012). The double-peaked nature of the CaII emission allowed to constrain the location of the gas to a disc located within Roche radius of the white dwarf, where an asteroid would be tidally disrupted. Today we can say that, in hindsight, the first real observational evidence of the existence of an extrasolar planetary system was van Maanen's discovery of the first metal polluted white dwarf (Zuckerman, 2015).

In recent years the number of known DxZs has greatly increased thanks to large area surveys, most notably the Hamburg Schmidt survey (Heber et al., 1991), Hamburg/ESO survey (Christlieb et al., 2001; Friedrich et al., 2000), the ESO supernovae Ia progenitor survey (SPY Koester et al. 2001, 2005b) and the Sloan Digital Sky Survey (SDSS) (e.g. Eisenstein et al. 2006; Dufour et al. 2007b; Koester et al. 2011; Kleinman et al. 2013). Over 30 new white dwarfs with debris discs have also been discovered largely via dedicated studies using the *Spitzer Space Telescope* (e.g. Fig.8.1; Jura et al. 2007a,b; von Hippel et al. 2007; Farihi et al. 2008b,a; Jura et al. 2009; Farihi et al. 2010b; Chu et al. 2011; Girven et al. 2012; Barber et al. 2012; Bilíková et al. 2012; Brinkworth et al. 2012; Farihi et al. 2012; Bergfors et al. 2014; Rocchetto et al. 2015). Over the last five years the large area IR surveys UKIDSS and the *Wide-field Infrared Survey Explorer* (WISE) have also started to play an increasingly important role in the discovery of these systems (Girven et al., 2011; Steele et al., 2011; Debes et al., 2011a,b, 2012; Barber et al., 2014). Today we know that all white dwarfs with circumstellar dust show some degree of metal pollution (with the only possible exception of PG 0010+280; Xu et al. 2015), and current estimates suggest that 1−3 per cent of all white dwarfs possess such discs (Farihi et al., 2009; Girven et al., 2011; Rocchetto et al., 2015).

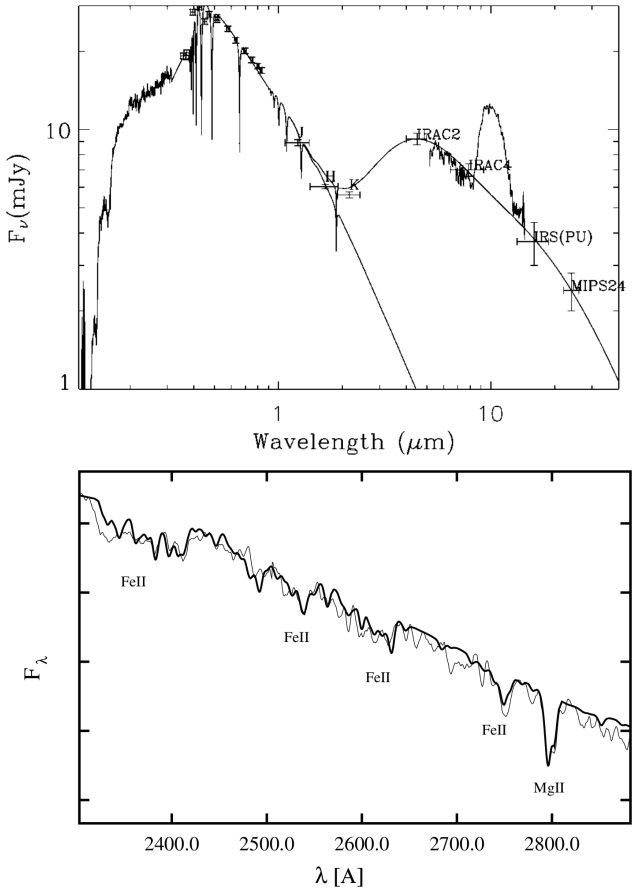

Figure 8.1: *Top panel:* SED of the white dwarf G29-38 (Reach et al., 2005). The infrared excess is fitted with a circumstellar dust disc model. The solid line represents the sum of the stellar and circumstellar model fluxes. The infrared spectrum also shows a strong $9-11\,\mu m$ emission feature characteristic of silicate minerals. *Bottom panel:* HST FOS UV spectrum of G29-38 showing absorption from Mg and Fe (Koester et al., 1997).

The realisation that DxZs are accreting remnants of a planetary system meant that accurate spectral analysis of these objects can reveal the chemical composition and bulk abundances of exo-planetary material. In DA white dwarfs with radiative atmospheres ($T_{\rm eff} \gtrsim 14,000\,{\rm K}$) metals can only be detected in the photosphere of the star. Timescales for metal diffusion in these objects are of the order of days, and increase to a few thousands years as the white dwarf cools down and develops a convective atmosphere. Consequently the detection of metals in DA white dwarfs implies ongoing or very recent accretion, and accretion rates for each element can therefore be accurately calculated from the observed metal abundances. On the other hand DBs have deep convection zones and accreted metals can be detected until they sink out at the bottom of the convection zones. In these white dwarfs

diffusion timescales are of the order of $10^5 - 10^6$ yr and, since different elements diffuse downwards with speeds dependent on their atomic weight and charge, the observed abundance ratios may not reflect the actual composition of the accreted debris. Consequently accretion rates have the meaning of averages over the diffusion timescales and are less reliable than those of DAs. However the total mass of metals in convective zones of DB white dwarfs can be used to place a lower limit on the mass of the accreted body.

To date several studies have shown that the accreted material is rocky in nature and often has compositions close to that of the bulk of Earth or, more generally, that of inner solar system bodies (Zuckerman et al., 2007; Klein et al., 2010; Vennes et al., 2010; Jura et al., 2012; Gänsicke et al., 2012). However, with the growing number of accurately studied systems, a certain degree of diversity is also starting to emerge. A number of recent studies claimed that some metal polluted white dwarfs accreted differentiated bodies (i.e. objects which had compositionally distinct layers like planets, Jura et al. 2009; Farihi et al. 2011a) or even water. The origin of this water is still object of debate and the possibilities include accretion of water-rich moons, entire water-worlds or multiple water-rich asteroids or comets (Jura et al., 2009; Farihi et al., 2011a; Veras et al., 2014; Raddi et al., 2015).

Detection of transits and radial velocity observations have proven extremely successful in discovering extra solar planets, but they can only provide information on the planet radius, mass (i.e. bulk density), and some insight into its atmospheric composition (e.g. Grillmair et al. 2008; Valencia et al. 2010). Today metal polluted white dwarfs are the only venue available to directly probe the bulk composition of rocky exo-planets, moons and asteroids. Unfortunately this new, challenging and exciting field is still limited by the small number of well studied systems. The majority of DxZs only show pollution from one or two elements (usually Ca and/or Mg) offering only a limited insight into the nature of the accreted material. Furthermore detailed abundance studies require high-resolution spectroscopy which is both time consuming and difficult to acquire for faint targets like white dwarfs. In conclusion, we have only scratched the surface of what this field has to offer and it is of utmost importance to identify more heavily polluted white dwarfs.

In this chapter I present the results of our high-resolution follow up of 15 newly identified metal polluted white dwarfs and our subsequent search for debris discs via detection of IR excess.

8.2 Metal Polluted white dwarfs in SDSS DR9/10

As part of the work described in Chapter 4, we identified 62 metal polluted white dwarfs which were followed-up spectroscopically for the first time by SDSS as part of DR9 and 10. For the majority of these objects, and indeed for the majority of all metal polluted white dwarfs, Ca appears to be the only heavy element visible in the SDSS spectra. The strong CaII H and K absorption lines are the unmistakable signature of external pollution, but on their own they only provide limited informations. We decided to carry out a high-resolution spectroscopic follow-up campaign of SDSS DxZs prioritising objects which showed traces of pollutants other than Ca in their SDSS spectrum (mostly Mg) and He atmosphere white dwarfs which also show traces of H (DBAZ and DABZ). The latter type are of particular interest as the H may be a signpost of water accretion (Raddi et al., 2015). To date we have acquired high-resolution spectroscopy of 15 DxZs.

8.2.1 Observations

Between April and August 2014 we observed seven of our targets with the X-shooter spectrograph at the VLT observatory (Vernet et al., 2011). The observations were carried out during photometric conditions using a $1''$ slit aperture for the UVB arm and $0.9''$ for the VIS arm. By measuring the full with at half maximum (FWHM) of the skylines in the spectra, we estimated the resolution of to be $R \simeq 4000 - 5500$ in the UVB arm and $R \simeq 6500 - 8000$ in the VIS arm. The acquired spectra were reduced using the standard procedures within the REFLEX[1] reduction tool developed by ESO. Seven additional targets were observed between December 26^{th} and 29^{th} 2013 using the double-armed Intermediate Resolution Spectrograph[2] (ISIS) on the William Herschel Telescope (WHT) on the island of La Palma. We observed under 1" seeing conditions and used the R600R and R600B gratings, in the ISIS blue and red arms respectively, with a 1" slit. The blue spectra and red spectra covered the total wavelength range $\simeq 3700 - 5000$Å and $\simeq 5700 - 7200$Å, respectively, with resolutions of $R \simeq 2300$ and $R \simeq 3900$. The spectra were de/biased and flat-fielded using the standard STARLINK[3] packages KAPPA, FIGARO and CONVERT. We carried out optimal spectral reduction using the package PAMELA[4] (Marsh, 1989). On more target, SDSS J0149+2400 or GD 17, was observed on September 4^{th} 2013

[1] http://www.eso.org/sci/software/reflex/

[2] http://www.ing.iac.es/Astronomy/instruments/isis/

[3] The STARLINK Software Group homepage website is http://starlink.jach.hawaii.edu/starlink.

[4] PAMELA was written by T. R. Marsh and can be found in the STARLINK distribution Hawaiki and later releases.

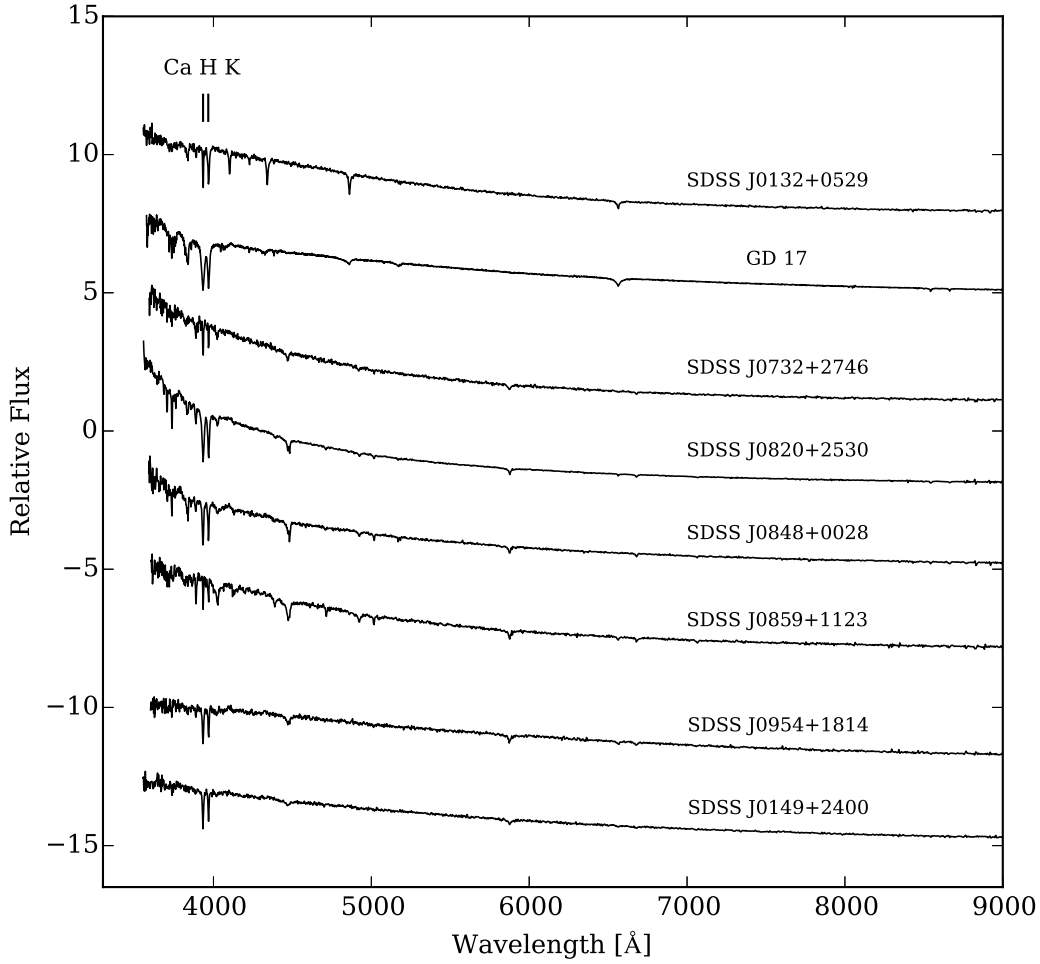

Figure 8.2: SDSS spectra of the 15 metal polluted white dwarfs for which we obtained high-resolution follow up. Continues in Fig 8.3.

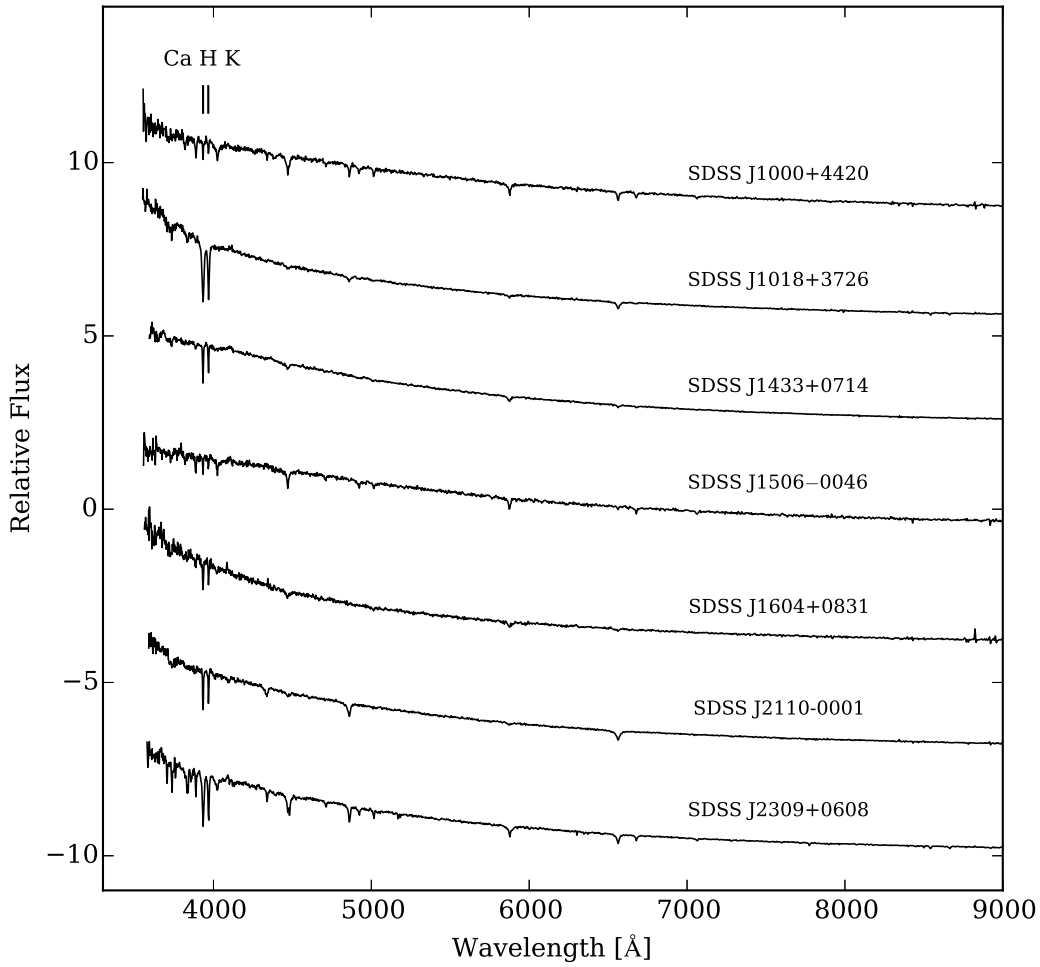

Figure 8.3: SDSS spectra of the 15 metal polluted white dwarfs for which we obtained high-resolution follow up. Continues from Fig 8.2.

at the MMT Observatory on Mt. Hopkins. We used 1″ slit on the Blue Channel Spectrograph facility instrument and the Echellette grating, providing a nominal simultaneous coverage of 3100–7200 Å. The resulting spectrum had a resolution of $R \approx 8200$ at 5577 Å. The spectra were reduced manually using the ECHELLE package within IRAF and the data were extracted using a median sky subtraction, variance weighting, and a cleaning algorithm for outliers (e.g. cosmic rays).

8.2.2 Spectral analysis

The SDSS spectra of the stars were fitted with DB/DBA model grids with varying H to He abundance ratios ([H/He]). Since it isn't possible to reliably determine surface gravity in the temperature range of these objects (Friedrich et al., 2000), we fixed the $\log g$ values at 8.0. The best fitting models were selected minimizing chi^2, and were then verified by detailed visual inspection. The resulting $T_{\rm eff}$ and [H/He] were used as starting values for a detailed analysis of the higher resolution spectra, including the additional elements O, Mg, Al, Si, Ca, Ti, Cr, Fe, Ni. It should be noted that the hydrogen Balmer lines as well as the He I lines are broadened by neutral He atoms. The broadening data for this process are poorly determined and the profile fits are therefore not fully satisfactory. Whenever some of the above mentioned elements could not be detected, we assumed Bulk Earth ratios relative to Ca, or an upper limit, whichever was the smaller number. The diffusion time-scale, diffusion velocity, and the accretion rates for each of the polluting elements (Koester, 2009) were calculated assuming a steady-state phase of the accretion (i.e. equilibrium between accretion and diffusion) following the procedure described in Gänsicke et al. (2012) and Koester et al. (2014). With the exception of the DAZ SDSS J0132+0529, all the white dwarfs in our sample have He dominated atmospheres. The accretion rates we present are, therefore, averaged over each element diffusion timescale (see Sect.8.1) and may be affected by large uncertainties. The analysis of the spectra including construction of the models, spectral fitting and calculation of elemental abundances and accretion rates, was carried out by Prof. Detlev Koester at the Institute for Theoretical Physics and Astrophysics at the University of Kiel. All the subsequent work presented in this chapter was performed personally by myself. Calculating accurate photospheric element abundances, diffusion timescales and accretion rates is an extremely complex and time-consuming procedure. Each objects has to be treated separately and the element ratios need to be adjusted manually before the best models can be calculated. What we present in this chapter can, therefore, only be considered the preliminary results of our spectral analysis as our work on these white dwarfs is still ongoing. The results of our analysis for objects which only

Table 8.1: J2000 coordinates, SDSS magnitudes and instrument used for the follow-up for the 15 metal polluted white observed.

Name	Ra [deg]	Dec [deg]	u mag	g mag	r mag	i mag	z mag	instrument
SDSS J0132+0529	01 32 22.87	05 29 23.70	18.92 (0.03)	18.38 (0.03)	18.24 (0.01)	18.22 (0.02)	18.22 (0.03)	X-shooter
GD 17	01 49 34.45	24 00 46.75	16.24 (0.02)	15.99 (0.01)	16.07 (0.01)	16.16 (0.01)	16.32 (0.01)	MMT
SDSS J0732+2746	07 32 17.01	27 46 41.53	18.58 (0.03)	18.60 (0.02)	18.81 (0.02)	19.02 (0.02)	19.11 (0.05)	ISIS
SDSS J0820+2530	08 20 19.49	25 30 35.39	17.54 (0.02)	17.53 (0.02)	17.77 (0.01)	17.95 (0.02)	18.20 (0.03)	ISIS
SDSS J0848+0028	08 48 57.87	00 28 34.83	18.45 (0.02)	18.38 (0.01)	18.63 (0.01)	18.82 (0.02)	18.97 (0.04)	X-shooter
SDSS J0859+1123	08 59 34.16	11 23 09.44	18.88 (0.04)	18.98 (0.02)	19.21 (0.02)	19.55 (0.04)	19.78 (0.07)	ISIS
SDSS J0954+1814	09 54 49.30	18 14 54.87	18.60 (0.02)	18.49 (0.2)	18.72 (0.02)	18.93 (0.02)	19.11 (0.04)	ISIS
SDSS J0958+0550	09 58 54.96	05 50 21.39	18.29 (0.02)	18.22 (0.02)	18.39 (0.02)	18.52 (0.02)	18.76 (0.03)	ISIS
SDSS J1000+4420	10 00 01.21	44 20 16.25	18.19 (0.02)	18.27 (0.03)	18.51 (0.03)	18.73 (0.02)	19.03 (0.05)	ISIS
SDSS J1018+3726	10 18 38.77	37 26 58.11	17.78 (0.01)	17.70 (0.02)	17.89 (0.01)	18.08 (0.01)	18.30 (0.02)	ISIS
SDSS J1433+0714	14 33 50.82	07 14 52.25	16.85 (0.02)	16.80 (0.02)	16.96 (0.01)	17.15 (0.02)	17.37 (0.01)	X-shooter
SDSS J1506−0046	15 06 57.27	−00 46 10.63	18.66 (0.02)	18.70 (0.02)	18.91 (0.02)	19.08 (0.02)	19.31 (0.05)	X-shooter
SDSS J1604+0831	16 04 01.31	08 31 09.06	18.62 (0.02)	18.56 (0.02)	18.73 (0.01)	18.90 (0.01)	19.12 (0.04)	X-shooter
SDSS J2110−0001	21 10 03.73	−00 01 52.70	18.00 (0.02)	17.96 (0.02)	18.11 (0.01)	18.29 (0.02)	18.46 (0.03)	X-shooter
SDSS J2309+0608	23 09 53.03	06 08 20.05	17.87 (0.02)	17.87 (0.02)	18.03 (0.02)	18.26 (0.2)	18.50 (0.03)	X-shooter

show pollution from Ca and Mg are given in Tables 8.2 and 8.3. The results of the analysis of the remaining objects are presented individually in Tables 8.4, 8.5, 8.6, 8.7 and 8.8.

8.2.3 Rocky bodies composition and oxygen budget.

Recent studies have shown that the elemental abundances of the debris in metal polluted white dwarfs can show substantial diversity, comparable at least to that seen across different meteorite classes in the solar system (e.g. Gänsicke et al. 2012). In Fig. 8.4 we compare the composition of the Earth (bulk, crust and core, Mcdonough 2000), with the accreted material on the well studied white dwarf PG1015+161 (Gänsicke et al., 2012). It is immediately evident that the parent body being accreted by PG1015+161 is mainly constituted by the same elements which make up the Earth, but the individual mass fractions are significantly different. In the case of PG1015+161 the higher relative Fe/O content seems to indicate a parent body with a metallic content higher than bulk Earth.

Fig. 8.4 also illustrates how in objects with enhanced water content, the mass fraction of O relative to other elements can be severely altered, suggesting that the presence of water can be observationally determined. However, the possible water content of an accreted body can only be estimated if the main rock forming elements (Ca, Al, Si, Mg, Cr and Fe) are detected. These elements naturally occur in the oxidized forms CaO, Al_2O_3, SiO_2, MgO, CrO, Cr_2O_3, FeO and Fe_2O_3, so much of the observed O in metal polluted white dwarfs is therefore the result of accretion of oxides. Only the O which is in excess of what accountable as oxide is likely to have originated from water.

8.2.4 Hydrogen

With the exception of SDSS J0132+0529 and SDSS J0848+0028, all of the metal polluted white dwarfs we followed up have He dominated atmospheres and also show traces of H (therefore are classified as DBAZ or DABZ). Various theories have been put forward to explain the origin of H in the atmosphere of DBs (e.g. spectral evolution and accretion from ISM, see Chapter 1, Sect. 1.2.2), but in the case of cool ($T_{\rm eff} \lesssim 15,000\,{\rm K}$) DB white dwarfs with large amounts H, the most likely origin scenario is accretion of water-rich debris (Farihi et al. 2010b; Jura et al. 2009; Raddi et al. 2015). This explanation becomes even more robust in the case of metal polluted DBs as these objects have certainly undergone, or are still undergoing, accretion of planetary debris (Veras et al., 2014). Since hydrogen

Table 8.2: Element abundances in the convection zone and diffusion data for the metal polluted white dwarfs in our sample which only show traces of pollution from Ca and Mg. Elements marked as (BE) were not detected and their abundance was determined as the bulk Earth ratio relative to Ca. Total assumed $M_{\rm Z}$ and $\dot{M}_{\rm Z}$ include upper limits and BE elements while observed $M_{\rm Z}$ and $\dot{M}_{\rm Z}$ only include detected elements. Continues in Table 8.3.

		SDSS J0732+2746	SDSS J0859+1123	SDSS J0954+1814	SDSS J0958+0550	SDSS J1000+4420
$T_{\rm eff}$ (K)		12830±400	15870±400	12690±400	11680±400	14150±400
Mass ($M_\odot$)		0.587	0.594	0.587	0.585	0.590
Radius ($R_\odot$)		0.01268	0.01276	0.01268	0.01266	0.01272
Z	Element			log n(Z)/n(He)		
1	H	−5.700±0.30	−4.70±0.30	−5.40±0.30	−5.70±0.30	−4.20±0.20
12	Mg	−7.190 (BE)	−5.49±0.30	−6.69±0.30	−6.99±0.30	−6.79±0.30
20	Ca	−8.400±0.20	−6.40±0.30	−7.80±0.30	−8.60±0.20	−8.20±0.20
$M_{\rm H}$ (10^{21} g)		3.14	5.87	6.63	5.06	54.06
$v_{\rm Mg}$ (10^{-8} cm s^{-1})		3.06	6.48	2.74	2.15	3.95
$\tau_{\rm Mg}$ (Myr)		2.83	0.95	3.20	4.37	1.95
$M_{\rm Mg}$ (10^{22} g)		<0.24	2.29	0.82	0.63	0.33
$\dot{M}_{\rm Mg}$ (10^{7} g s^{-1})		<3.22	76.99	8.17	4.56	5.48
$v_{\rm Ca}$ (10^{-8} cm s^{-1})		6.96	15.06	6.76	5.41	9.39
$\tau_{\rm Ca}$ (Myr)		1.25	0.41	1.30	1.74	0.82
$M_{\rm Ca}$ (10^{22} g)		0.02	0.47	0.10	0.03	0.02
$\dot{M}_{\rm Ca}$ (10^{7} g s^{-1})		0.64	36.33	2.58	0.46	0.83
tot. observed $M_{\rm Z}$ (10^{22} g)		0.02	2.76	0.92	0.66	0.35
tot. observed $\dot{M}_{\rm Z}$ (10^{7} g s^{-1})		0.64	113.32	10.75	5.12	6.31
tot. assumed $M_{\rm Z}$ (10^{22} g)		1.70	18.54	5.37	1.72	1.27
tot. assumed $\dot{M}_{\rm Z}$ (10^{7} g s^{-1})		21.83	1000.83	86.78	19.06	30.46

Table 8.3: Continued from Table 8.2. Element abundances in the convection zone and diffusion data for the metal polluted white dwarfs in our sample which only show traces of pollution from Ca and Mg.

		SDSS J1018+3726	SDSS J1433+0714	SDSS J1506−0046	SDSS J1604+0831	SDSS J2110−0001
$T_{\rm eff}$ (K)		11590±400	11376±400	1389±4002	11376±400	11579±400
Mass ($M_\odot$)		0.585	0.585	0.590	0.585	0.585
Radius ($R_\odot$)		0.01266	0.01265	0.01271	0.01265	0.01266
Z	Element			$\log(n(\mathrm{Z})/n(\mathrm{He}))$		
1	H	−4.50± 0.30	−5.50 0.30	−5.50±0.30	−5.20±0.30	−3.70±0.30
12	Mg	−7.09±0.30	−8.19 (BE)	< -7.59	−8.59 (BE)	−7.99 (BE)
20	Ca	−8.20±0.20	−9.40 ±0.20	−8.40±0.20	−9.80±0.20	−9.20±0.20
$M_{\rm H}$ (10^{21} g)		69.90	8.99	3.04	17.70	406.37
$v_{\rm Mg}$ (10^{-8} cm s^{-1})		2.29	2.00	3.72	2.01	2.36
$\tau_{\rm Mg}$ (Myr)		3.96	4.80	2.11	4.76	3.75
$M_{\rm Mg}$ (10^{22} g)		0.43	<0.04	< 0.06	< 0.02	< 0.05
$\dot{M}_{\rm Mg}$ (10^7 g s^{-1})		3.48	<0.29	<0.90	<0.12	< 0.43
$v_{\rm Ca}$ (10^{-8} cm s^{-1})		5.71	5.06	8.88	5.09	5.90
$\tau_{\rm Ca}$ (Myr)		1.59	1.90	0.89	1.88	1.50
$M_{\rm Ca}$ (10^{22} g)		0.06	0.004	0.02	0.002	0.005
$\dot{M}_{\rm Ca}$ (10^7 g s^{-1})		1.11	0.08	0.55	0.03	0.11
tot. observed $M_{\rm Z}$ (10^{22} g)		0.49	0.004	0.02	0.002	0.005
tot. observed $\dot{M}_{\rm Z}$ (10^7 g s^{-1})		4.59	0.08	0.55	0.03	0.11
tot. assumed $M_{\rm Z}$ (10^{22} g)		2.84	0.24	0.72	0.09	0.27
tot. assumed $\dot{M}_{\rm Z}$ (10^7 g s^{-1})		38.31	2.65	17.26	1.05	3.81

Table 8.4: Physical parameters, photospheric element abundances and diffusion data of DAZ SDSS J0132+0529. Elements marked as (BE) were not detected and their abundance was determined as the bulk Earth ratio relative to Ca. Total assumed $\dot{M}_{\rm Z}$ includes upper limits and BE elements while observed $\dot{M}_{\rm Z}$ only includes detected elements.

SDSS J0132+0529					
$T_{\rm eff}$ (K)		7500±400			
Mass ($M_\odot$)		0.593			
Radius ($R_\odot$)		0.01275			
Z	Element	$\log(n({\rm Z})/n({\rm H}))$	v (10^{-6} cm s^{-1})	τ (10^3 yr)	$\dot{M}$ (10^7 g s^{-1})
8	O	−5.34 (BE)	3.906	6.64	<93.68
12	Mg	−6.30±0.20	7.67	3.38	30.71
13	Al	−7.10±0.20	9.55	2.71	6.73
14	Si	−6.40±0.30	9.77	2.65	35.91
20	Ca	−6.80±0.20	7.18	3.60	15.00
22	Ti	−8.17±0.30	9.55	2.72	1.02
24	Cr	< −8.06	11.97	2.16	<1.78
26	Fe	−7.20±0.30	10.92	2.37	12.65
28	Ni	< −7.96	11.48	2.25	<2.43
tot. observed $\dot{M}_{\rm Z}$ (10^7 g s^{-1})					102.02
tot. assumed $\dot{M}_{\rm Z}$ (10^7 g s^{-1})					199.92

never diffuses out of the atmospheres of white dwarfs, large amounts can accumulate over long timescales as a consequence of multiple accretion events. On the other hand, O diffuses on timescales ranging from days to 10^6 years (see Sect. 8.2.2) and is only visible in the case of ongoing or recent accretion events. Consequently, it is impossible to directly correlate the amount of H in the atmosphere to the observed amounts of O and therefore of accreted water.

In Fig 8.5 we compare the mass of H in the convective zones of our 13 DABZ/DBAZ white dwarfs with that of other known similar objects. With a few exceptions (see Sect. 8.2.5), most of our objects only have modest amounts of H and do not stand out compared to other metal polluted white dwarfs. Furthermore 10 of our objects only show pollution from Mg and/or Ca severely limiting any possible speculation on the nature of the accreted parent body.

8.2.5 Notes on single objects

Even though the analysis of our metal polluted white dwarfs is still in a preliminary stage, five objects already stand out in terms of their accretion rates, the amount of H in their envelope or their peculiar photospheric abundances. Below, we analyse

Table 8.5: Physical parameters, element abundances in the convection zone and diffusion data for GD17. Total assumed $M_{\rm Z}$ and $\dot{M}_{\rm Z}$ include upper limits, while observed $M_{\rm Z}$ and $\dot{M}_{\rm Z}$ only include detected elements.

GD17						
$T_{\rm eff}$ (K)		8300±500				
Mass ($M_\odot$)		0.579				
Radius ($R_\odot$)		0.01259				
Z	Element	$\log(n({\rm Z})/n({\rm He}))$	v (10^{-8} cm s^{-1})	τ (Myr)	M (10^{22} g)	$\dot{M}$ (10^{7} g s^{-1})
1	H	−2.80±0.50	–	–	288.01	–
8	O	< −4.70	1.74	4.07	<57.50	<336.71
12	Mg	−7.50±0.10	1.768	4.02	0.14	1.10
13	Al	< −7.80	1.87	3.80	<0.08	<0.65
14	Si	< −7.20	2.14	3.32	<0.32	<3.06
20	Ca	−8.75±0.10	4.61	1.54	0.01	0.27
22	Ti	−10.20±0.20	4.91	1.44	0.0005	0.01
26	Fe	−7.80±0.10	4.32	1.64	0.16	3.09
28	Ni	−9.00±0.20	3.98	1.78	0.01	0.02
tot. observed $M_{\rm Z}$ (10^{22} g)					0.32	
tot. assumed $M_{\rm Z}$ (10^{22} g)					58.22	
tot. observed $\dot{M}_{\rm Z}$ (10^{7} g s^{-1})						4.66
tot. assumed $\dot{M}_{\rm Z}$ (10^{7} g s^{-1})						345.07

Table 8.6: Physical parameters, element abundances in the convection zone and diffusion data of SDSS J0820+2530. Elements marked as (BE) were not detected and their abundance was determined as the bulk Earth ratio relative to Ca. Total assumed $M_{\rm Z}$ and $\dot{M}_{\rm Z}$ include upper limits and BE elements while observed $M_{\rm Z}$ and $\dot{M}_{\rm Z}$ only include detected elements.

SDSS J0820+2530						
$T_{\rm eff}$ (K)		13540±400				
Mass ($M_\odot$)		0.589				
Radius ($R_\odot$)		0.01270				
Z	Element	$\log(n({\rm Z})/n({\rm He}))$	v ($10^{-8}\,{\rm cm\,s^{-1}}$)	τ (Myr)	M ($10^{22}\,{\rm g}$)	$\dot{M}$ ($10^{7}\,{\rm g\,s^{-1}}$)
1	H	−5.40±0.30	–	–	0.45	–
8	O	−5.14 (BE)	3.65	2.23	<13.08	<186.69
12	Mg	−6.09±0.20	3.37	2.42	2.23	29.38
13	Al	< −6.44	3.52	2.31	<1.11	<15.22
14	Si	−6.32±0.20	4.53	1.80	1.52	26.97
20	Ca	−6.60±0.20	8.16	1.00	1.14	36.35
22	Ti	−8.27±0.30	8.56	0.95	0.03	0.97
24	Cr	< −7.56	7.95	1.03	<0.16	<5.02
26	Fe	< −6.30	7.42	1.10	<3.16	<91.69
28	Ni	< −6.76	6.82	1.20	<1.15	<30.68
tot. observed $M_{\rm Z}$ ($10^{22}\,{\rm g}$)					4.91	
tot. assumed $M_{\rm Z}$ ($10^{22}\,{\rm g}$)					23.57	
tot. observed $\dot{M}_{\rm Z}$ ($10^{7}\,{\rm g\,s^{-1}}$)						93.46
tot. assumed $\dot{M}_{\rm Z}$ ($10^{7}\,{\rm g\,s^{-1}}$)						422.76

Table 8.7: Physical parameters, element abundances in the convection zone and diffusion data of SDSS J0848+0028. Elements marked as (BE) were not detected and their abundance was determined as the bulk Earth ratio relative to Ca. Total assumed $M_{\rm Z}$ and $\dot{M}_{\rm Z}$ include upper limits and BE elements while observed $M_{\rm Z}$ and $\dot{M}_{\rm Z}$ only include detected elements.

SDSS J0848+0028						
$T_{\rm eff}$ (K)		13790±400				
Mass ($M_\odot$)		0.590				
Radius ($R_\odot$)		0.01271				
Z	Element	$\log(n({\rm Z})/n({\rm He}))$	v ($10^{-8}\,{\rm cm\,s^{-1}}$)	τ (Myr)	M ($10^{22}\,{\rm g}$)	$\dot{M}$ ($10^{7}\,{\rm g\,s^{-1}}$)
1	H	< -6.00	–	–	<0.10	–
8	O	−5.3 (BE)	3.85	2.07	<7.44	<114.28
12	Mg	−5.59±0.20	3.56	2.24	6.35	90.21
13	Al	−6.64 (BE)	3.71	2.15	<0.63	<9.32
14	Si	−5.92±0.20	4.69	1.70	3.43	64.33
20	Ca	−6.80±0.20	8.58	0.93	0.65	22.12
22	Ti	−8.57±0.30	8.99	0.89	0.01	0.47
24	Cr	−7.76±0.30	8.36	0.96	0.09	3.07
26	Fe	−5.69±0.30	7.81	1.02	11.60	361.55
28	Ni	−6.96 (BE)	7.17	1.11	<0.65	<18.74
tot. observed $M_{\rm Z}$ ($10^{22}\,{\rm g}$)					22.13	
tot. assumed $M_{\rm Z}$ ($10^{22}\,{\rm g}$)					30.86	
tot. observed $\dot{M}_{\rm Z}$ ($10^{7}\,{\rm g\,s^{-1}}$)						541.75
tot. assumed $\dot{M}_{\rm Z}$ ($10^{7}\,{\rm g\,s^{-1}}$)						684.89

Table 8.8: Physical parameters, element abundances in the convection zone and diffusion data of SDSS J2309+0608.Total assumed $M_{\rm Z}$ and $\dot{M}_{\rm Z}$ include upper limits while observed $M_{\rm Z}$ and $\dot{M}_{\rm Z}$ only include detected elements.

SDSS J2309+0608						
$T_{\rm eff}$ (K)		14563±400				
Mass ($M_\odot$)		0.591				
Radius ($R_\odot$)		0.01272				
Z	Element	$\log(n(\mathrm{Z})/n(\mathrm{He}))$	v ($10^{-8}\,\mathrm{cm\,s^{-1}}$)	τ (Myr)	M ($10^{22}\,\mathrm{g}$)	$\dot{M}$ ($10^{7}\,\mathrm{g\,s^{-1}}$)
1	H	−3.70±0.30	–	–	12.77	–
8	O	−4.94±0.20	4.80	1.50	11.66	246.70
12	Mg	−5.59±0.20	4.46	1.62	3.96	77.97
13	Al	−6.44±0.30	4.66	1.55	0.62	12.76
14	Si	−5.62±0.20	5.54	1.30	4.28	10.45
20	Ca	−6.10±0.20	0.11	0.68	2.02	94.43
22	Ti	−7.87±0.20	0.11	0.65	0.04	2.01
24	Cr	−7.31±0.30	0.10	0.70	0.16	7.38
26	Fe	−5.69±0.30	9.68	0.75	7.24	308.86
28	Ni	< -6.66	8.89	0.81	<0.81	<31.96
tot. observed $M_{\rm Z}$ ($10^{22}\,\mathrm{g}$)					29.98	
tot. assumed $M_{\rm Z}$ ($10^{22}\,\mathrm{g}$)					30.79	
tot. observed $\dot{M}_{\rm Z}$ ($10^{7}\,\mathrm{g\,s^{-1}}$)						854.56
tot. assumed $\dot{M}_{\rm Z}$ ($10^{7}\,\mathrm{g\,s^{-1}}$)						886.52

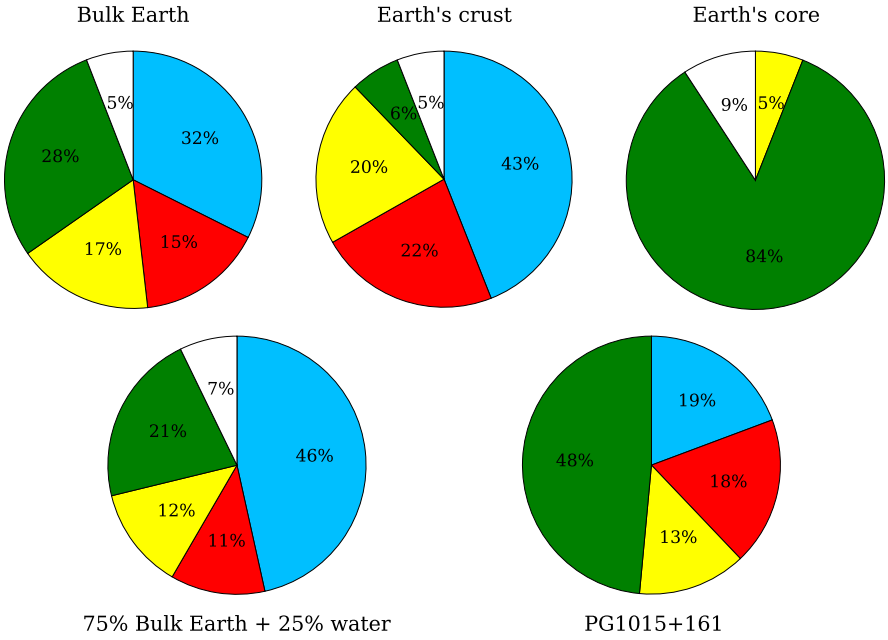

Figure 8.4: Mass fractions of the main constituents of Bulk Earth, Earth's crust, Earth's core (Mcdonough, 2000), of a hypothetical asteroid similar to Ceres (75 per cent of bulk Earth composition, but with an additional 25 per cent of water, Michalak 2000) and of the accreted material on the white dwarf PG1015+161 (Gänsicke et al., 2012). O, Mg, Si, Fe and remaining minor constituents are represented in light blue, red, yellow, green and white respectively.

in more detail the available data for these white dwarfs and put forward some speculations on their accretion history.

SDSS J0132+0529

SDSS J0132+0529 is the coolest white dwarf in our sample ($T_{\rm eff} = 7500\,{\rm K}$) and the only one with an H dominated atmosphere (i.e. a DAZ). Diffusion timescales for metals in the atmosphere of SDSS J0132+0529 are of the order of a few thousand years (Table 8.4). Consequently the mass of metals in the convective zone of this star does not provide a meaningful lower limit of the total mas of the accreted body. Nearly half of the total assumed accretion rate of SDSS J0132+0529 comes from O, which is not detected, but only included under our bulk Earth assumption (see Sect. 8.2.2). However even considering only the elements which are actually observed in its spectrum, SDSS J0132+0529 has the highest accretion rate ever measured in such a cool DAZ white dwarfs (1.02×10^9 g, e.g. Fig. 5 in Bergfors et al. 2014). SDSS J0132+0529 seems to accrete Ca and Al rich debris with Mg/Fe and Si/Fe ratios close to those of the Earth's crust ($\sim 2.5 - 3.3$, Table 8.4, Fig 8.6). Ca and

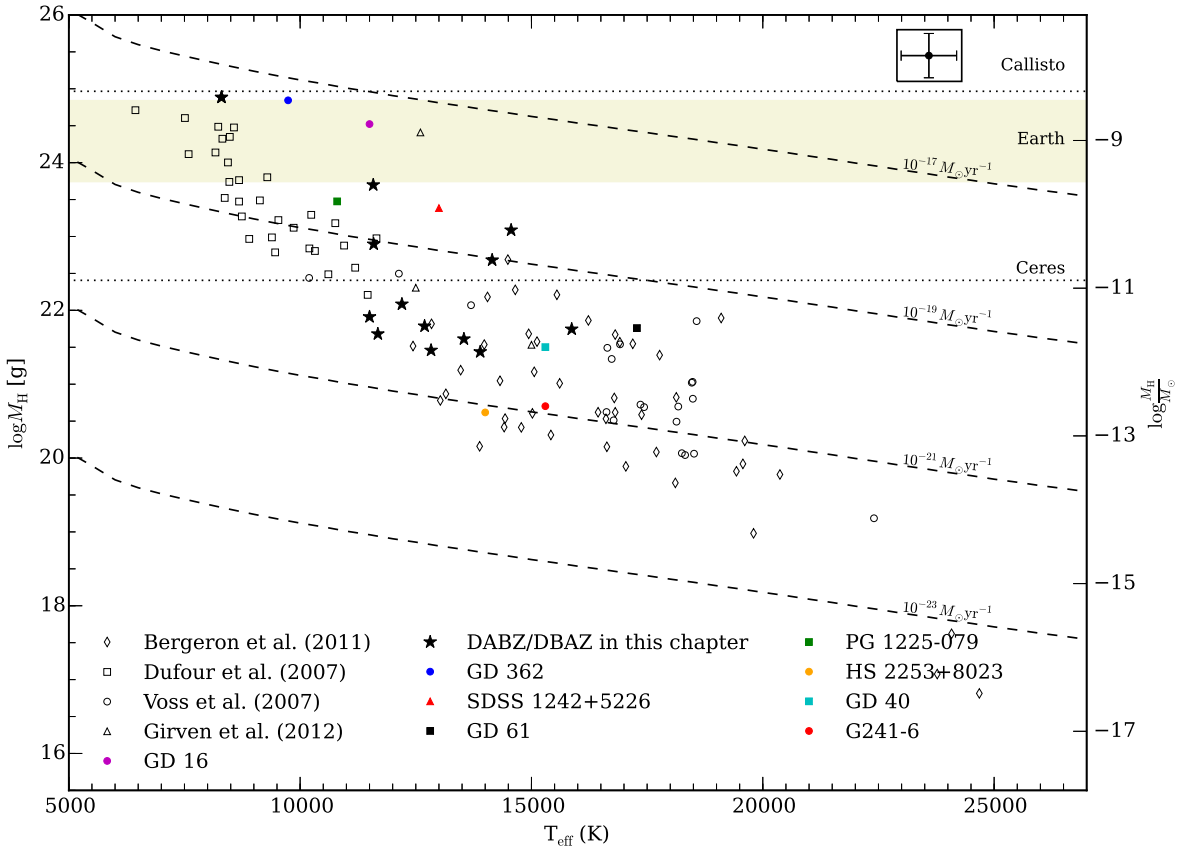

Figure 8.5: Total mass of hydrogen in the convection zones of helium-dominated white dwarfs as function of $T_{\rm eff}$. On the right axis, the hydrogen mass is given in units of solar masses. Hydrogen abundances of field DBA and DZA white dwarfs (open symbols, see legend for references) were converted into hydrogen mass adopting the evolutionary models of Bergeron et al. (2011), convection zone masses were calculated following Koester (2009). The hydrogen abundances of metal-polluted white dwarfs are taken from Jura & Young (2014) and references therein. For GD 362 (Gianninas et al., 2004), GD 61 (Farihi et al., 2013) and SDSS J1242+5226 (Raddi et al., 2015), we used the hydrogen mass supplied by the authors. The mass of hydrogen in water for Ceres, Callisto (ice mass fractions are 25 and 50 per cent, respectively, Michalak 2000; McCord & Sotin 2005; Canup & Ward 2002) and bulk Earth are plotted as dashed lines or shaded area. The dashed curves represent the cumulative mass of hydrogen for constant accretion rates during the white dwarf cooling ages. This plot was originally published in Raddi et al. (2015) and here we reproduce it with the addition of our 13 DABZ/DBAZ.

Al are two of the main refractory lithophiles: elements which sublimate only at very high temperatures and are therefore found mainly in the mantle and crust of differentiated objects (Grossman, 1972). Zuckerman et al. (2011) reported the discovery of another white dwarf which accretes Fe-poor and Al-Ca rich debris, NLTT 43806. Zuckerman et al. (2011) concluded that the debris accreted by NLTT 43806 were part of the crust and mantle of a large differentiated body, and must have been blasted off the planet by a collision with another rocky object. Such massive collision also offer a possible mechanism to drive material within the Roche radius of the white dwarf where it would then be accreted. The metal pollution of SDSS J0132+0529 is remarkably similar to that of NLTT 43806 with both objects having Ca/Mg ratio of $\sim 0.4 - 0.5$ and Ca/Si ratio of $\sim 0.3 - 0.4$. The main differences between the two objects are the Ca/Al ratio which is $\simeq 0.9$ in NLTT 43806 (close to that of silicate Earth) and only $\simeq 0.4$ in SDSS J0132+0529; and the fact that the Fe abundance compared to other elements in SDSS J0132+0529 is even lower than in NLTT 43806. In conclusion, the data currently at hand suggests that SDSS J0132+0529 accretes debris which was once part of the lithosphere of a planet, providing evidence for differentiation in extra solar rocky bodies and possibly large planet collisions (Veras et al., 2013; Mustill et al., 2014).

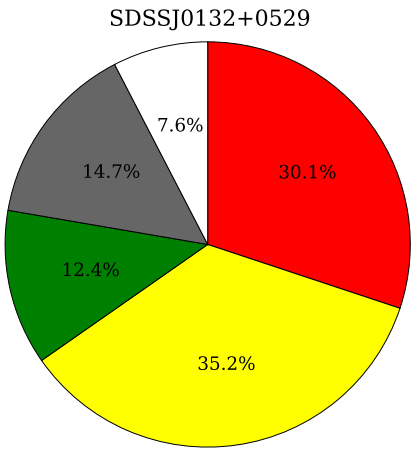

Figure 8.6: Mass fractions of the main constituents of the debris accreted onto the white dwarf SDSS J0132+0529. Mg, Si, Fe, Ca and remaining minor constituents are represented in light blue, red, yellow, green, grey and white respectively.

GD 17 or SDSS J0149+2400

By inspection of its SDSS spectrum, we initially classified GD 17 as a DAZ, but the clear asymmetric shape of the Hβ line suggested a more peculiar atmosphere composition than a "standard" DAZ. Our analysis revealed that GD 17 is, in fact, a He rich white dwarf with an atmosphere only seemingly dominated by H. Ironically, the archetypal example of this peculiar type of white dwarfs, discovered by Koester et al. (2005a), is called GD 16. Even among the other DB white dwarfs with accreted H, GD 16 stands out in terms of hydrogen mass in its atmosphere (Fig. 8.5). GD 17 is in many ways similar to GD 16 and, unsurprisingly, it too appears to have accreted an exceptionally high amount of H. We estimate the total H mass in its envelope to be $\simeq 2.9 \times 10^{24}$g, the highest value ever measured for any DBs (Fig. 8.5). Such a large amount of H leads to the tempting assumption that GD 17 must have accreted large amounts of water. However the newly acquired MMT spectra of GD 17 do not reveal any O absorption lines and our preliminary analysis only allows to place an upper limit on the accreted mass of O. Under the assumption that all the H was bound in water and was accreted from the same parent body as the observable Ti, Mg, Fe and Ca, the lack of observable O poses a problem. To explain these observations we have to assume that GD 17 must have experienced several distinct accretion episodes some of which involved water-rich planet bodies. However, over time, all accreted metals have diffused out of the convective envelope, leaving behind only a large amount of H. In this scenario the heavy pollutants we observe today (Ti, Mg, Fe, Ca and Ni) are not necessarily related to the H, and may, in fact, be the signature of a more recent accretion of dry asteroids. This recent accretion would have contributed very little in term of H and would have provided only O bound in oxides with the other metals. Adopting the common oxides of Mg, Ca, Ti and Ni, and assuming an equal amount FeO, Fe_2O_3, and Fe, the O accretion rate due to this dry asteroid would only be $1.8 \times 10^7\,\mathrm{g\,s^{-1}}$. This value is far below the upper limit provided by our model ($336.7 \times 10^7\,\mathrm{g\,s^{-1}}$, Table 8.5) and such small amount of O could easily not be detected. Indeed the high Fe and Ni content of the debris currently in the convective zone of GD 17 suggests that the parent body of the most recent accretion event could have been a metallic, dry, core-like asteroid.

SDSS J0820+2530

From our preliminary analysis, the atmosphere of SDSS J0820+2530 immediately stands out with a peculiar composition. The Mg/Si ratio in SDSS J0820+2530 is $\simeq 0.8$ and therefore consistent with that of most terrestrial rocky bodies, but we

detect no Fe and over a third of the total accretion rate is due to Ca alone. Since the debris is strongly Ca enhanced and Fe depleted, it would be tempting to assume that they originated from the crust and mantle of a differentiated body like in SDSS J0132+0529. However the Ca/Mg and Ca/Si ratios are $\simeq 1.2$, a value higher than expected in lithophile rich debris. Moreover the apparent lack of Fe is hard to reconcile with the detection of substantial amounts of Si and even traces of Ti. The current upper limit estimate for the accretion rate of Fe is also not very constraining as it is as high at the total accretion rate of the observed elements.

In conclusion, rather than venturing into any speculations, we limit ourself to note that SDSS J0820+2530 is a heavily metal polluted white dwarf with extremely peculiar composition. As illustrated in Fig. 8.7 the resolution of the ISIS spectrum of SDSS J0820+2530 is lower than the X-shooter ones, possibly inhibiting the detection of Fe and other metal species. Indeed further observation are required to establish the nature of the accreted material.

SDSS J0848+0028

SDSS J0848+0028 is the only DBZ in our sample, in other words the only object which does not show any H in its atmosphere. Compared to the bulk Earth composition, the material accreted by SDSS J0848+0028 is extremely Fe rich. In addition, we detect no Al in the atmosphere of this white dwarf and the other refractory litophiles, Ca and Ti have extremely low abundances in comparison to Fe, Si and Mg. Indeed SDSS J0848+0028 has the lowest Ca/Si, Ca/Mg, Ti/Si and Ti/Mg ratios of all the objects in our sample. We do not detect any O in SDSS J0848+0028, but even assuming a bulk Earth amount of O relative to Ca, the assumed accretion flux of O could only account for the oxides of Mg, Si and Ca. This extremely low O budget implies that a large portion of the Fe in SDSS J0848+0028 must have been accreted in metallic form, as typical for the core of differentiated bodies. Similarly, we find that Cr is also significantly overabundant in SDSS J0848+0028 with respect to the bulk Earth. The depletion of Cr in the silicate Earth is thought to be due to its partitioning into the Earths core (Moynier et al., 2011) and represents one more piece of evidence of differentiation. Finally, the lack of any trace of H in the atmosphere of SDSS J0848+0028 also indicates that the accreted material was mostly dry. While our analysis is still ongoing, it appears likely that the debris being accreted by SDSS J0848+0028 originated from the core of a differentiated planetesimal. The mass fractions of the polluting metals resemble those assumed for the core of terrestrial bodies and seen in primitive asteroids which have undergone partial melting (which leads to the separation of Fe from lighter elements). By calculating the mass

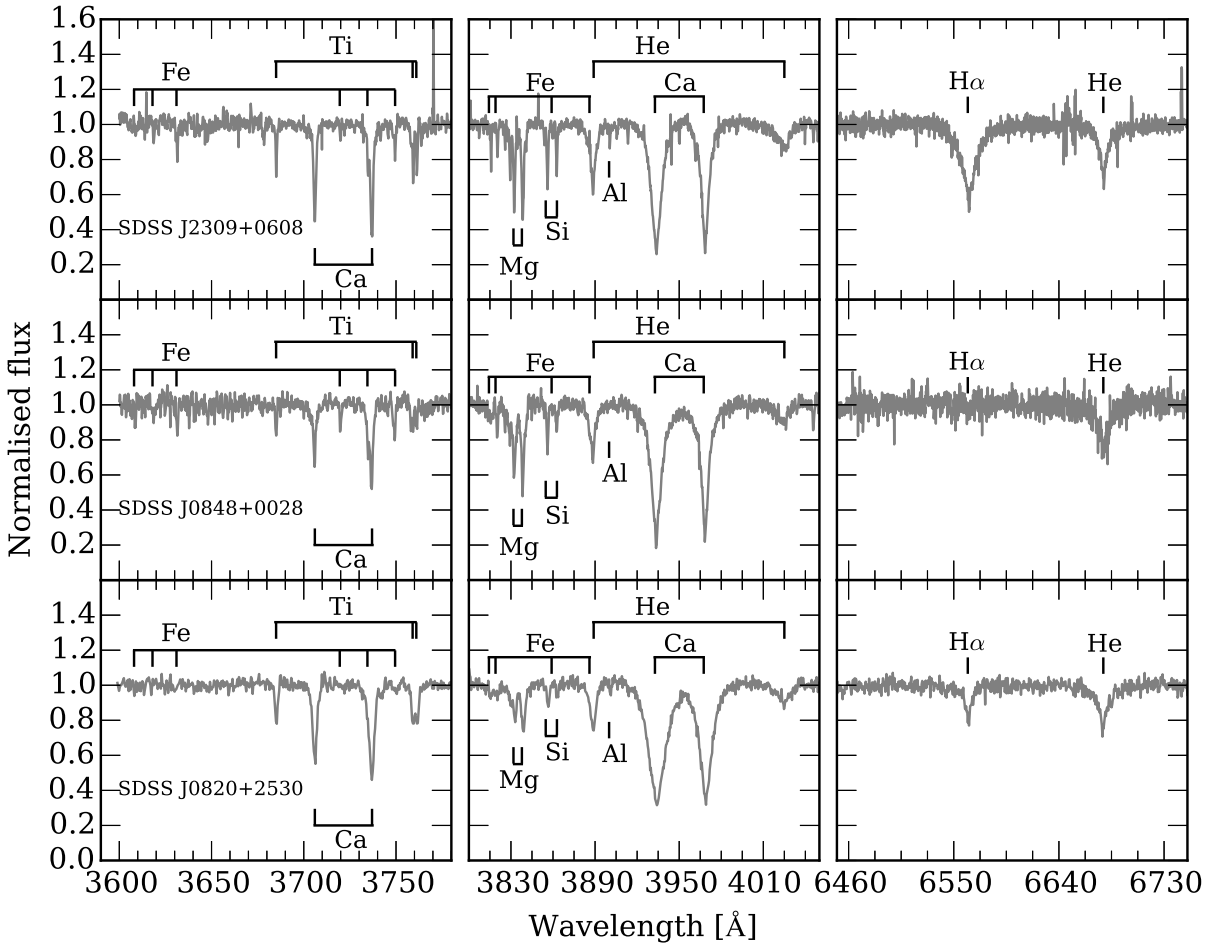

Figure 8.7: Comparison of some of the relevant absorption features in the X-shooter spectra of SDSS J0848+0028 and SDSS J2309+0608 and in the ISIS spectrum of SDSS J0848+0028 .

of the observed metals in the convection zone of SDSS J0848+0028 we can place a lower limit on the total mass of the accreted body. In Table 8.7 we report this limit to be 22×10^{22}g, a value comparable to the mass of Juno, one of the largest asteroids in our solar system.

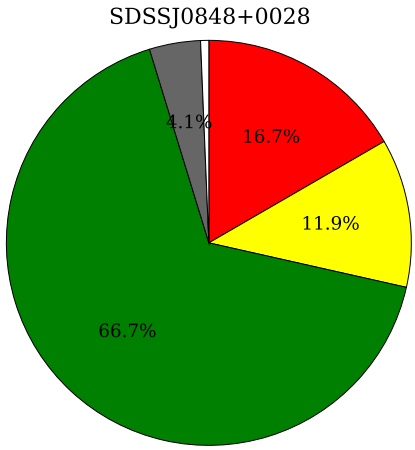

Figure 8.8: Mass fractions of the main constituents of the debris accreted onto the white dwarf SDSS J0848+0028. Mg, Si, Fe, Ca and remaining minor constituents are represented in red, yellow, green, grey and white respectively.

SDSS J2309+0608

SDSS J2309+0608 is the only white dwarf in our sample which shows the presence of O in its atmosphere. It also has the highest accretion rate and the highest total metal mass in its convection zone within our sample. Furthermore SDSS J2309+0608 is the only object in our sample with pollution from multiple elements which also shows an IR excess compatible with the presence of a debris disc (see Sect. 8.3.1, Fig. 8.11).

Despite being possibly the best-characterized white dwarf in our sample, the composition of the debris accreted by SDSS J2309+0608 is somewhat puzzling. In most terrestrial bodies (planets and asteroids) and metal polluted white dwarfs, the Mg/Si ratio seems to be within the range 0.5 to 2.0 (e.g Carter-Bond et al. 2012; Gänsicke et al. 2012; Jura et al. 2012; Zuckerman et al. 2011 and references therein). However, the debris in SDSS J2309+0608 are strongly calcium enriched, and with a Mg/Si ratio of $\simeq$ 7.4. Since Si and Mg have nearly the same diffusion times (Table 8.8) this peculiar ratio cannot be a consequence of differential gravitational settling and is therefore likely to reflect the actual composition of the parent body.

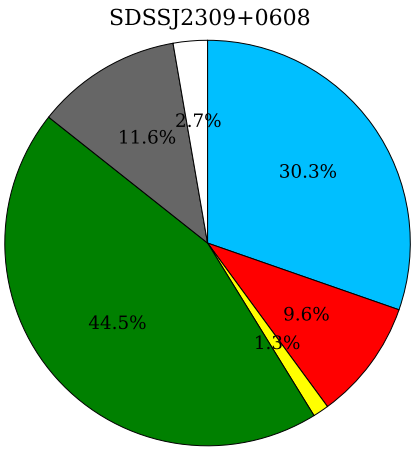

Figure 8.9: Mass fractions of the main constituents of the debris accreted onto the white dwarf SDSS J2309+0608. O, Mg, Si, Fe, Ca and remaining minor constituents are represented in light blue, red, yellow, green, grey and white respectively.

Furthermore, while the Fe/Mg fraction is close to that of core-like, metallic debris (e.g SDSS J0848+0028), the ratio of the lithophile Ca and Al to Mg is comparable to that of debris from the crust or mantle of planetesimals (e.g. SDSS J0132+0529 and NLTT 43806). A similar debris composition is seen in the white dwarf GD 40 (Klein et al., 2010) which accretes Si depleted debris (Mg/Si $\simeq$ 2.9), but with a high fraction of of refractive lithophiles (Ca, Al and Ti). Klein et al. (2010) explain that no objects in our solar system has a similar composition. They speculate that the Si depletion may be an effect of Mg to Si differentiation in the outermost crust of large asteroids (e.g. Vesta) while the somewhat paradoxical Ca, Al and Ti enhancement could be a consequence of intense heating occurred during the red giant phase or through the energy deposited by collisions. With the results of our preliminary analysis we cannot formulate a specific accretion history for SDSS J2309+0608, and we limit ourself to speculate that a scenario similar to that described for GD 40 by Klein et al. (2010) could also explain the debris composition of SDSS J2309+0608.

Another striking feature of SDSS J2309+0608 is its high O content. Assuming the most common oxidation states of the observed metals (see Sect. 8.2.3) and adopting a very conservative scenario in which all Fe occurs as Fe_2O_3, all O can be accounted as part of oxides. However, in a more realistic scenario in which Fe occurs in equal parts of Fe_2O_3, FeO and Fe, 20% of the accreted O would be in excess and could therefore have been accreted in the form of water. Indeed the presence of $\simeq 12.8 \times 10^{22}$ g of H in the convection zone of SDSS J2309+0608 corroborates the

idea that this white dwarfs has accreted or is accreting water-rich debris. Assuming all H was accreted in the form of water, the calculated H mass implies a total O mass of $\simeq 102.4 \times 10^{22}$ g. This is over 10 times the amount of O currently in the convective zone of SDSS J2309+0608. We therefore conclude that a significant fraction of H must be left over from older accretion events.

Finally, from the metal mass in the convective zone of SDSS J2309+0608 we estimate the lower limit of the mass of the accreted parent body to be $3{\times}10^{23}$g (Table 8.8). This value places the parent body toe-to-toe with Vesta, the second largest asteroid in the solar system.

8.3 A search for infrared excess

Large-area optical and IR surveys provide the opportunity to search for white dwarfs with IR excess on a large scale, as demonstrated by previous successful studies (e.g. Steele et al. 2011; Debes et al. 2011a; Girven et al. 2011). In this section I present the first results of our ongoing search for white dwarfs with IR excess in SDSS, ATLAS, UKIDSS, VHS and WISE.

8.3.1 Metal polluted white dwarfs with infrared excess.

Even excluding the possibility of contamination from background sources, the detection of an IR excess does not unambiguously correspond to the presence of a debris disc. Low-mass, close, unresolved companions (brown dwarfs, BD) to the white dwarfs may have an infrared signature similar to that of a debris disc and only far-infrared photometry and accurate SED modelling can discriminate between the two (e.g. Steele et al. 2011; Girven et al. 2011; Farihi et al. 2012). White dwarfs with close BD companions are per se very interesting systems: they are key to probe the parameter space spanned by BDs, and only ~ 6 have confirmed to date (Burleigh et al., 2006; Casewell et al., 2012; Steele et al., 2013; Littlefair et al., 2014). However, the targets of our search are debris discs and we aimed, where possible, to avoid WD+BD binaries. According to current theories all metal polluted white dwarfs have or must have had a circumstellar debris reservoir of pollutants. Therefore a debris discs is the most likely origin of any genuine (not caused by spurious photometric contamination) IR excess observed from a metal polluted white dwarf. In conclusion, a sample of spectroscopically confirmed metal polluted white dwarfs is the best starting point in a search for debris discs. Previous studies have extensively searched for possible IR excesses from the spectroscopically confirmed white dwarfs in SDSS DR7 using UKIDSS (Steele et al., 2011; Girven et al., 2011)

Table 8.9: Results of the cross matching of the newly identified SDSS DR9/10 metal polluted white dwarfs with UKIDSS and WISE.

new metal polluted white dwarfs in SDSS DR9/10	62
with at least one detection in UKIDSS $YJHK$	44
or in WISE $w1, w2$	
infrared excess candidates	4
of which with both UKIDSS and WISE photometry	2

and WISE (Debes et al., 2011b). Therefore a similar search using our sample of newly identified metal polluted white dwarfs from SDSS DR9/10 represent a natural progression in this type of work. We began by retrieving all available UKIDSS DR10 and WISE IR photomety for our 62 metal polluted white dwarfs. In their search for IR excess, Girven et al. (2011) compared the result of SDSS to UKIDSS coordinate cross matching as a function of matching radius. They determined that a radius of 2.5 arcseconds excluded nearly all spurious matches while missing only a handful of the highest proper motion objects. However the large proper motions of the white dwarfs and the now longer (few years since DR7) time interval between the two surveys can lead to some significant shifts in the coordinates of the objects. In our search we are striving for completeness and so decided to conduct our cross matching between SDSS ad UKIDSS using a matching radius of five arcseconds. Naturally this increased radius leads to higher chance of spurious matching so a great effort was later applied in manually eliminating those. Following a similar argument and taking into account the lower resolution of WISE (6"), we adopted a cross-matching radius of 10 arcseconds between SDSS and WISE.

Our cross-match results in a sample of 44 metal polluted white dwarfs with at least one detection in UKIDSS $YJHK$ or WISE $w1, w2$ (Table 8.9).

For all these objects we constructed SED using the available SDSS, UKIDSS and WISE photometry. In order to evaluate whether or not the IR detection corresponds to an excess we fit a blackbody model to the SDSS r and i magnitudes. In practice the SED of a white dwarfs is not a perfect blackbody, but the Rayleigh-Jeans tail of a blackbody curve can describe a white dwarf spectrum over regions with no significant absorption features; i.e. the equivalent wavelengths of r and i bands and the near and mid-infrared. We then proceeded to inspect the SEDs of our 44 objects with IR matches. We also closely inspected the available SDSS, UKIDSS and WISE images and discarded all objects for which the IR emission is likely caused by a contaminating source (e.g. Fig. 8.10).

We classified as a debris disc candidate all remaining objects with at least

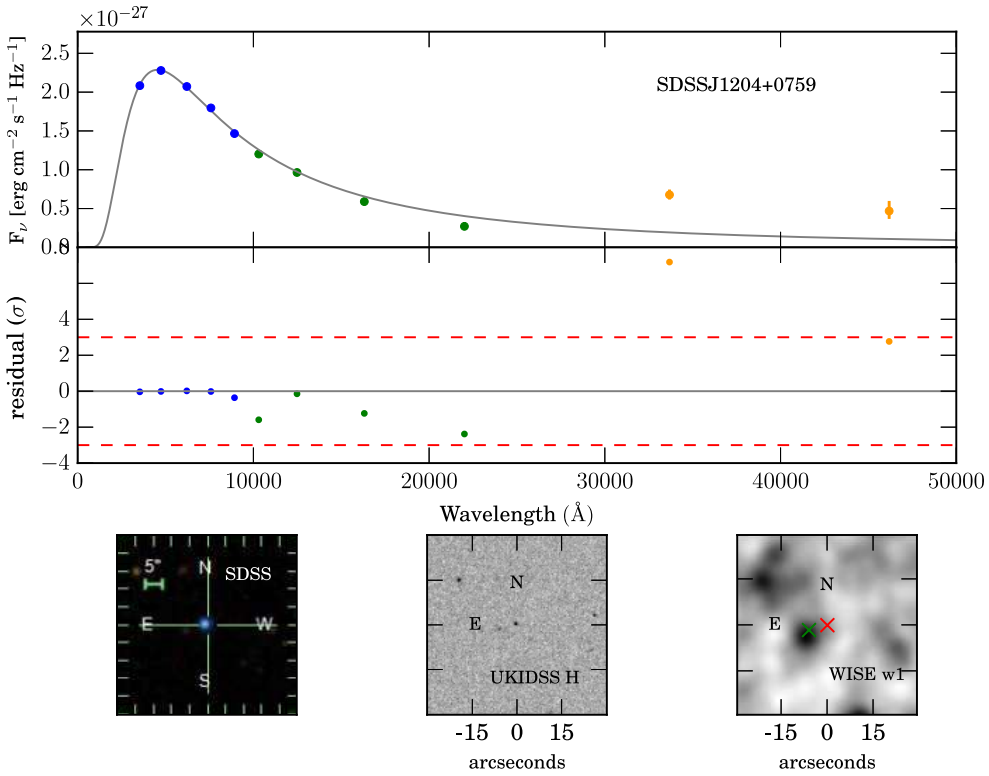

Figure 8.10: SED of the metal polluted white dwarf SDSS J1204+0759 showing a spurious infrared excess. SDSS *ugriz* , UKIDSS $YJHK$ and WISE $w1, w2$ photometric measurements are shown as blue, green ad yellow points respectively. The grey solid line in the top panel indicates a blackbody fit to the SDSS *ri* photometry. The dashed red lines in the middle panel indicate the 3σ threshold. SDSS, UKIDSS and WISE images are included in the bottom panels from left to right respectively. The red cross on the WISE image indicates the coordinates of the SDSS objects, while the green cross indicates the location of the WISE detection. The IR excess visible in the $w1, w2$ bands is most likely caused by a nearby source also faintly visible in the SDSS and UKIDSS image.

one IR measurement in the $H, K, w1, w2$ bands in excess by a minimum of 3σ with respect to the blackbody model (Fig. 8.11).

We conclude that four of our metal polluted white dwarfs are strong debris disc candidates (Table 8.10). As mentioned above such IR excess could be caused by a debris disc or a low mass companion, but the metal polluted nature of these white dwarf corroborates the debris disc origin. Further support for the disc scenario comes from the two candidates with both UKIDSS and WISE IR photometry. For these two objects the UKIDSS photometry is consistent with the flux from the isolated white dwarf and the IR excess becomes evident only in the $w1, w2$ bands (e.g. Fig. 8.11). Aside from debris discs, the only objects which could cause IR excess at such log wavelengths are very late-type (L or later) brown dwarfs. White

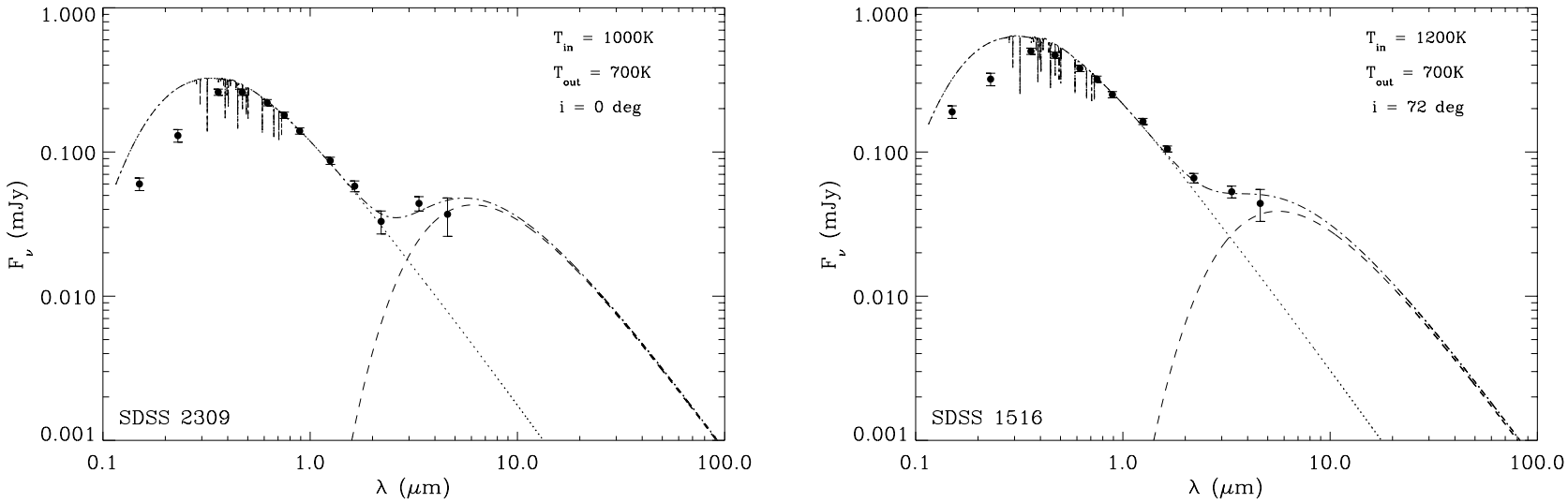

Figure 8.11: SEDs of SDSS J2309+0608 and SDSS J1516−0040 constructed from GALEX fuv, nuv, SDSS $ugriz$, UKIDSS $YJHK$ and WISE $w1, w2$ photometry. The dotted line represents the white dwarf model fitted to the GALEX and SDSS photometry, the dashed lines represent emission from optically thick, flat disc models, and the dotdashed lines represent the sum of the stellar and circumstellar model fluxes. The parameters of the disc models are given in the panel.

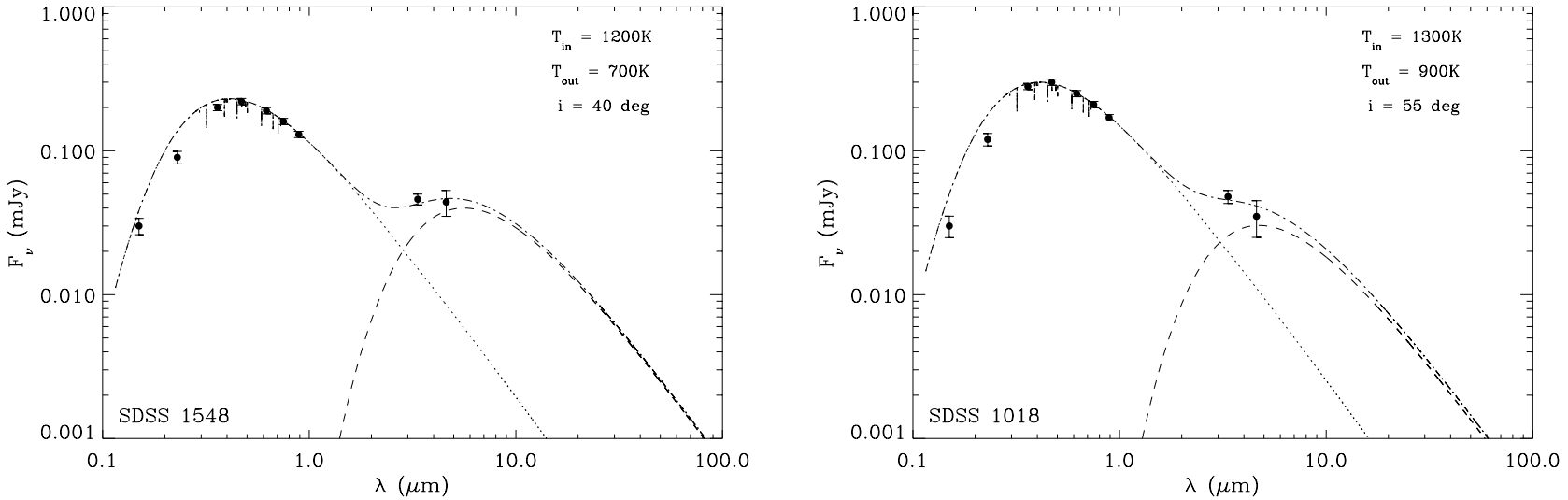

Figure 8.12: SEDs of SDSS J1548+2135 and SDSS J1018+3726 constructed from GALEX fuv, nuv, SDSS $ugriz$ and, WISE $w1, w2$ photometry. The dotted line represents the white dwarf model fitted to the GALEX and SDSS photometry, the dashed lines represent emission from an optically thick, flat disc model, and the dotdashed lines represent the sum of the stellar and circumstellar model fluxes. The parameters of the disc models are given in the panel.

Table 8.10: Four newly identified metal polluted white dwarfs from SDSS DR9/10 with infrared excess.

name	ra	dec	class	g(mag)	UKIDSS
SDSS J1018+3726	10 18 38.74	+37 26 57.5	DABZ	17.70±0.02	$----$
SDSS J1516−0040	15 16 42.96	−00 40 42.7	DBAZ	17.21±0.02	$YJHK$
SDSS J1548+2135	15 48 15.24	+21 35 28.5	DBAZ	18.05±0.02	$----$
SDSS J2309+0608	23 09 53.03	+06 08 20.0	DABZ	17.87±0.02	$YJHK$

dwarfs in close binaries with such low mass companions are extremely rare (Steele et al., 2011; Girven et al., 2011; Farihi et al., 2012) and the presence of a debris disc is a more likely explanation for the IR excess. For our four debris disc candidates we included Galex fuv and nuv photometry in the SEDs and attempted to fit the IR excess using the geometrically thin, optically thick disc model from Jura (2003). The free parameters in the disc model are the inner and outer disc temperature (T_{in}, T_{out}) and the disc inclination (i). Fig. 8.11 illustrates the result of our disc modelling and shows that the IR excess are consistent with the presence of flat, optically thick debris discs. However the best fits achieved are not fully satisfactory, implying that the data at hand could be not completely reliable or that background contamination may still be a factor. To ultimately discern the origin of the IR excess and correctly characterize the possible disc, it will be necessary to acquire more accurate IR photometry (e.g. Spitzer IRAC).

8.3.2 High-confidence white dwarf candidates with infrared excess.

Searching for an IR excess around known DxZs grants a certain degree of confidence that the detected IR emission is likely caused by a circumstellar debris disc. However, in current spectroscopic large area surveys white dwarfs are secondary if not completely serendipitous targets. This fact, combined with the rarity of DxZs and debris discs, means that among thousands of spectroscopic targets we can only hope to find a handful of metal polluted white dwarfs with IR excesses. A different approach which relies on targeted spectroscopic follow-up of high-confidence IR excess candidates could significantly increase the number of known DxZs with debris discs and enable better statistical studies of these objects. Thanks to our selection method for white dwarf candidates in SDSS and ATLAS we have, ready at hand, large samples of high-confidence white dwarf candidates, yet to be spectroscopically confirmed. By cross matching these candidates with large-area IR surveys (UKIDSS, VHS, WISE) we can produce a reliable sample of white dwarf candidates with IR excess.

Table 8.11: Results of the cross matching of SDSS and ATLAS white dwarf candidates with UKIDSS, VHS and WISE.

SDSS white dwarf candidates with $P_{\rm WD} \geq 0.9$ and no SDSS spectrum	9082
with at least one detection in UKIDSS $YJHK$ or WISE $w1, w2$	4367
infrared excess	252
only WISE data	200
ATLAS white dwarf candidates with $P_{\rm WD} \geq 0.95$ and no SDSS spectrum	1641
with at least one detection in VHS $YJHK$ or WISE $w1, w2$	1064
infrared excess	105
only WISE data	54

Candidate selection.

From our catalogue of SDSS white dwarf candidates we selected 9082 objects with $P_{\rm WD} \geq 0.9$ which have not yet received SDSS spectroscopic follow up (as of DR12). Using the procedure described in Sect. 8.3.1, we retrieved all available UKIDSS and WISE photometry for these white dwarf candidates, fitted their SEDs, and inspected both their fits and available images. We conclude that 252 of our white dwarf candidates display an IR excess consistent with the position of the white dwarf itself (Table 8.11).

We carried out an analogous search starting from our ATLAS DR2 white dwarf candidates. Accounting for the lower efficiency of the white dwarf selection method on ATLAS (Chapter 6, Sect 6.5 we decided to only select objects with $P_{\rm WD} \geq 0.95$. We also excluded all objects which, as a consequence of the overlap between ATLAS and SDSS, have SDSS spectrum. We retrieved available IR photometry for all 1641 suitable ATLAS candidates from VHS (instead of UKIDSS) and WISE. We find that 105 of these white dwarf candidates exhibit a reliable IR excess (Table 8.11). Three of these objects are also found in the SDSS sample of white dwarf candidates with IR excess.

Overall numbers

As the result of our large scale search for IR excess candidates we find that 5.4 per cent of our high-confidence SDSS white dwarf candidates and 6.4 per cent of the ATLAS ones have seemingly reliable IR excess. However a series of limitations affect these candidates samples. First of all, taking into account the efficiency of our selection method, we estimate that up to 5 per cent of these objects may not be white dwarfs, but some type of contaminants (e.g. main sequence A stars, subdwarfs or quasars). Without spectra, the data at hand does not allow us to determine

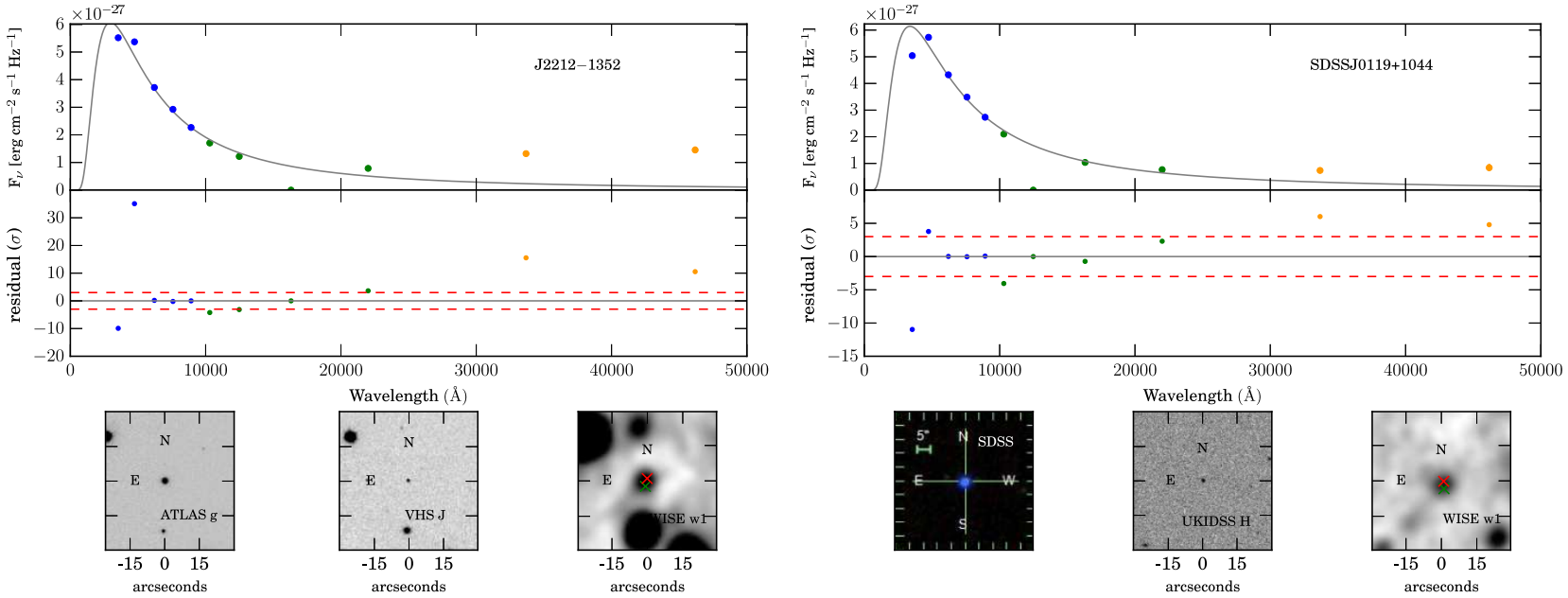

Figure 8.13: SEDs of a sample white dwarf candidates constructed from SDSS/ATLAS *ugriz* (blue points), UKIDSS/VHS $YJHK$ (green points) ans WISE $w1, w2$ (yellow points) photometry. The grey solid line in the top panel indicates a blackbody fit to the SDSS *ri* photometry. The dashed red lines in the middle panel indicate the 3σ threshold. SDSS/ATLAS, UKIDSS/VHS and WISE images are included in the bottom panels from left to right respectively. The red cross on the WISE image indicates the location of the SDSS objects while the green cross indicates the location of the WISE detection.

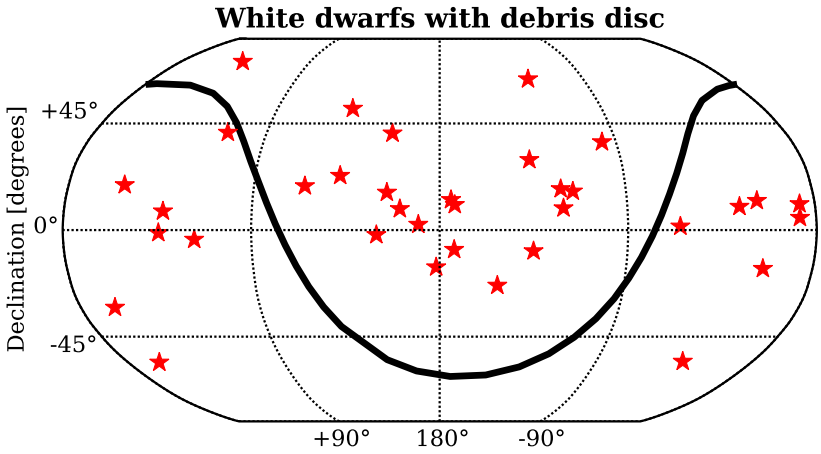

Figure 8.14: Sky distribution of the 35 metal polluted white dwarfs with debris discs confirmed to date (Rocchetto et al. 2015 and references therein). The majority of these objects are located in, or observable from, the northern hemisphere. This north-south gap emphasises the potential impact of our ATLAS+VHS IR-excess candidates. The solid black line indicates the galactic plane.

whether the IR excess is most likely caused by a debris disc or a substellar companion (BD). Furthemore, the majority of our IR candidates only have WISE IR data (Table 8.11). Without near-IR photometry it is impossible to tell if an excess in $w1$ and $w2$ corresponds to rising emission from a debris disc or BD, or to the tail of the emission from an M dwarf companion. M dwarf companions to white dwarfs are quite common (e.g. Rebassa-Mansergas et al. 2008) and are likely to be significant contaminants in our sample. Finally we cannot exclude the possibility that a fraction of the observed IR excesses are caused by unresolved background contamination. Nonetheless what we present is a sample of high-confidence white dwarfs candidates with IR excess; a catalogue of targets specifically tailored for a large scale search for metal polluted white dwarfs with debris discs, spanning both the northern and the southern hemisphere. Spectroscopic follow-up campaign of these objects could provide up to ~ 300 new spectroscopically confirmed white dwarfs the majority of which we predict to be host of debris discs or low mass companions. Even if just 1 in 10 of our IR excess candidates is in fact a metal polluted white dwarf, with only $\simeq 35$ DxZs with debris discs confirmed to date (mostly in the northern hemisphere Fig 8.14, (Rocchetto et al., 2015), our contribution would still double the number of such systems known.

Chapter 9

Summary and outlook

The main driving objective of the work described in these thesis was to efficiently exploit the enormous amount of data provided by large area surveys to identify various types of white dwarfs. I described in details the development of the selection methods and the results of some scientific applications to specific datasets. However, large scale exploration of the sky is a continuing effort and new, more advanced surveys publish their results every year. The selection routines described in the previous chapters can be applied to many of the next-generation surveys, opening up new and exiting research opportunities. In the following sections I summarise the content and the results of the previous chapters and describe some of the surveys which, in the near future, will have the greatest impact on many aspects of white dwarfs science.

9.1 Selecting white dwarfs from large area surveys

In Chapter 4 I presented a method that uses cuts in colour-colour and reduced proper motion-colour space to select white dwarfs without the recourse to spectroscopy while allowing an adjustable compromise between completeness and efficiency. Rather than just producing a list of white dwarf candidates, this method calculates a *probability of being a white dwarf* ($P_{\rm WD}$) for any object with available multi band photometry and proper motion. The application of the selection method to all objects in the SDSS DR10 photometric footprint results in a sample of $\simeq 66,000$ photometric sources with calculated $P_{\rm WD}$ from which it is possible to select a sample of $\simeq 24,000$ high-fidelity white dwarf candidates with $T_{\rm eff} \gtrsim 7000$ K and $g \leq 19$. In Chapter 5 the selection method was independently tested using on a sample of spectroscopically confirmed white dwarfs from the LAMOST (Large Sky Area Multi-Fiber Spectroscopic Telescope) survey. Cross matching the DR10 cata-

logue with the over 4 million spectra available in the third data release of LAMOST resulted in sample of 1673 white dwarf candidates with no previous SDSS spectroscopy. 309 of these objects were confirmed as genuine white dwarfs conclusively demonstrating that the calculated $P_{\rm WD}$ values can efficiently discriminate between confirmed LAMOST white dwarfs and contaminants. Even though it was developed using exclusively SDSS data, the selection routine for for white dwarf candidates can in principle be applied to any survey which provides multi-band photometry and proper motions. In Chapter 6 I describe the application of the algorithm to the second data release of the VST ATLAS survey using proper motions from PPMXL. I present a preliminary catalogue of $\simeq$ 9000 ATLAS sources with $P_{\rm WD}$ of which $\sim$ 2500 are estimated to high-confidence white dwarf candidates.

9.2 Variable white dwarfs in large area time-domain surveys

In Chapter 7 I presented a method to reliably select variable white dwarfs from large area time domain surveys and describe its application in a pilot study to search for pulsating white dwarfs in the Sloan Digital Sky Survey Stripe 82. From a sample 400 high-confidence white dwarf candidates from the SDSS DR10 catalogue (Chapter 4) 24 objects were selected on the basis on the variability they display in the multi-epoch Stripe 82 data. Follow-up observations confirmed five of these candidates as cool ZZ Cetis, three of which are new discoveries. Among the 24 candidates I also identify: one eclipsing binary, two magnetic white dwarfs and one pulsating PG1159 star. Even with sparse multi-epoch data over the limited area of Stripe 82, I demonstrate that this selection method can successfully identify various types of variable white dwarfs and efficiently select high-confidence ZZ Ceti candidates.

9.3 Planetary remnants around white dwarfs

As part of the work described in Chapter 4 I identified 64 new metal polluted white dwarfs which were observed in SDSS DR9/10. I acquired high-resolution spectroscopy of 15 of these objects and in Chapter 8 I presented the first results of this follow-up campaign. Using accurate spectral analysis we calculated the abundances of the polluting elements in the atmosphere of these white dwarfs and, where possible, we estimated the composition of the accreted parent bodies. In particular we focused on five white dwarfs which showed pollution from more elements than just Ca and Mg. The analysis of these objects is ongoing, but our preliminary

results show that the composition of the debris in these white dwarfs is broadly consistent with the main constituents of rocky objects in the solar system. However the mass fractions of the different polluting elements reveal a striking diversity in the nature of the accreted bodies. One of our white dwarfs, SDSS J0132+0529, appears to have accreted debris of the crust and mantle of a larger differentiated planetesimal. In contrast, the composition of the debris accreted by the white dwarfs SDSS J0848+0028 is consistent with that of the core of a differentiated body. Finally, I speculate that one more target, SDSS J2309+0608 may have accreted water rich debris.

I also documented my search for debris discs around white dwarfs via detection of infrared excess. By combining the available photometry from SDSS and the infrared surveys UKIDSS and WISE I constructed the SEDs of all newly identified metal polluted white dwarfs from SDSS DR9/10. Inspection of the SEDs and of the available images led to the identification of four metal polluted white dwarfs with significant infrared excess. In order to verify the origin of these excesses, they were fitted with debris disc models. I concluded that even though the infrared excesses examined are indeed consistent with the presence of dusty debris discs, further observations are still required to conclusively prove this theory. Lastly I presented the initial results of my ongoing effort towards a spectroscopic follow-up campaign of candidate white dwarfs with debris discs. By cross matching our high-confidence SDSS and ATLAS white dwarf candidates (Chapters 4, 6) with infrared data from UKIDSS, VHS and WISE I identified $\simeq$ 350 high-confidence white dwarf candidates with significant infrared excess. This target selection is still in its early stages and a fraction of these objects are likely white dwarfs with late-type or substellar companions (see Chapter 8, Section 8.3.2). Nonetheless, this sample represents the first catalogue of targets spanning both the north and the southern skies specifically tailored for a large scale search for metal polluted white dwarfs with debris discs.

9.4 Outlook

9.4.1 Gaia

Gaia is a cornerstone space mission of the European Space Agency (ESA) specifically designed to provide precise astrometry of around a billion objects. Gaia was launched on 19 December 2013 and began regular observing operations on August 21st 2014. During the nominal five years of mission Gaia will scan the entire sky on average 70 times. These repeated measurements will enable to precisely measure positions, parallactic distances and proper motions for approximately one per cent

Table 9.1: Gaia predicted end-of-mission parallax standard errors for unreddened B1V, G2V, and M6V stars.

	B1V	G2V	M6V
$V-I$ (mag)	−0.22	0.75	3.85
3 mag $< V <$12 mag	$5-16\mu as$	$5-16\mu as$	$5-16\mu as$
$V = 15$ mag	$26\mu as$	$24\mu as$	$9\mu as$
$V = 20$ mag	$600\mu as$	$540\mu as$	$130\mu as$

of all stars in the Milky Way brighter than $G = 20$, where G is the Gaia magnitude in a passband between about 400 and 1000 nanometres (Els et al., 2014). The trigonometric parallax uncertainties will depend both on the brightness and on the colour of the source (Table 9.1). Overall, the distance of about 20 million stars will be measured with a precision of 1%, while for 200 million more it will be about 10%.

The spacecraft is also equipped with a high-resolution spectrograph dedicated to radial velocity measurements and a blue and a red photometers. The radial velocity spectrograph will obtain spectra in the narrow near-infrared band (847−874 nm) and provide line-of-sight velocities to complement the proper motion measurements. The red and blue photometers will instead provide low-resolution spectra useful for intial source identification and on-ground calibration. The main aim of Gaia is to create a precise three-dimensional dynamical map of astronomical objects throughout the Milky Way. This unprecedented, massive stellar census will certainly have a revolutionary impact in many astronomical fields.

Thanks to Gaia precise distances and proper motions it will be possible to distinguish white dwarfs from other stellar populations with nearly perfect efficiency. Gaia will find a few hundred thousand white dwarfs, and effectively provide a complete sample within ≃50 pc from Earth. This vast sample will revolutionize every aspect of the field providing for first time a sound statistical basis to better constrain all properties of the global white dwarf population (Gänsicke et al., 2015). The multiple observations provided by Gaia will also enable to carry out searches for variable white dwarfs, similarly to that described in Chapter 7, harvesting thousands of objects over the entire sky. With Gaia, even rare types of white dwarfs (e.g. magnetic, metal polluted, with debris discs) will be in sufficiently large number to carry out large scale statistical studies. In particular the high resolution spectroscopy the wavelength range 847−874 nm could be extremely useful for identifying the signature Ca II triplet emission of white dwarfs with gaseous dusty discs (e.g. SDSS J1228+1040, Gänsicke et al. 2006a). However, though Gaia will provide the initial identification of the white dwarfs, the aforementioned science applications

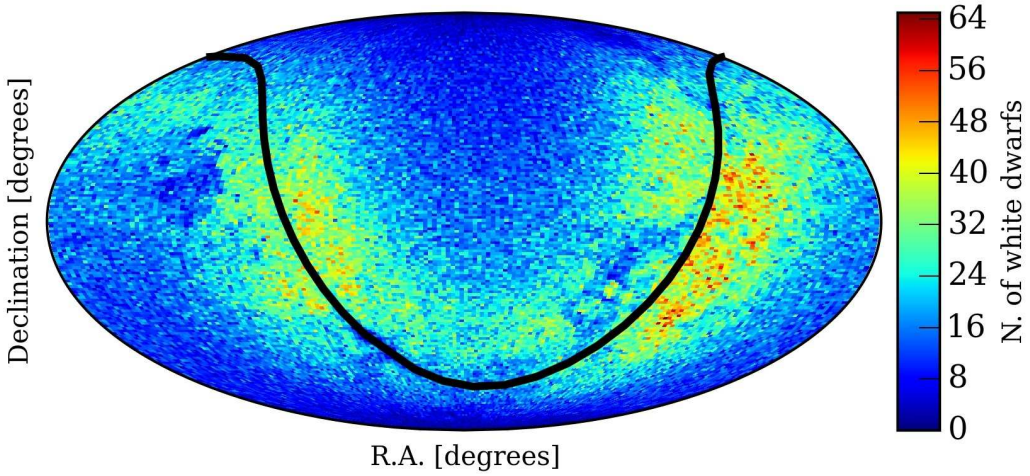

Figure 9.1: Sky distribution of a simulated sample of $\sim 500,000$ white dwarfs with G mag ≤ 20 which will potentially be identified by Gaia. Each bin on the plot represents one square degreee on the sky. The sample was created using the Gaia Universe Model Snapshot (GUMS, Robin et al. 2012). The black solid line indicates the galactic plane.

will necessarily require spectroscopic follow-up. Obtaining spectra for the millions of objects observed by Gaia is in itself a titanic project which will only be achievable thanks to the new upcoming multi-object spectrographs.

9.4.2 The next generation multi-object spectrographs: WEAVE and 4MOST

Multi-objects spectrographs are not a new idea and in the course of this work I made extensive use of data from this type of instruments (BOSS, LAMOST). However the next generation of these spectrograph will be significantly superior in many aspects (e.g. mirror size, multiplex capability, wavelength coverage and resolution, see below). Multi-object spectrographs are the logical answer to the increasing demand for large scale spectroscopic follow-up and several observatories around the world are planning to equip themselves with such instruments. Among the first to come online will be WEAVE and 4MOST. The WHT Enhanced Area Velocity Explorer (WEAVE, Dalton et al. 2014) is a multi-object spectrograph which will be mounted on the 4.2-m William Herschel Telescope at the Observatorio del Roque de los Muchachos, on La Palma in the Canary Islands. WEAVE will have a 2 degrees diameter field of view and will take up to 1000 spectra simultaneously in one exposure. The spectrograph will work in a low resolution mode ($R \simeq 5000$) covering the full wavelength range of 370-1000 nm and a high-resolution mode ($R \simeq 20000$) operating over a restricted wavelength range. WEAVE is estimated to see first light

in 2017 and to begin its ten years survey operations in 2018. During this time WEAVE will take up a minimum of 70 per cent of all WHT observing time and it will pursue two main science goals: spectroscopic follow-up of Gaia objects which will complement the map of the Milky Way with chemical abundance informations which Gaia cannot provide, and a galaxy evolution and cosmology project.

In the southern hemisphere the new era of large scale spectroscopic follow-up will begin with the 4m Multi-Object Spectrograph (4MOST, Depagne & 4MOST consortium 2014). 4MOST will be mounted on the VISTA telescope in Chile and, during the course of its initial five year survey operations, it will observe an area of 15,000−20,000 deg^2 at least two times. This instrument will have a 4.1 deg^2 field of view and will be able to acquire 2436 spectra simultaneously. Similarly to WEAVE, 4MOST will operate in two different resolution modes. 1624 fibers will be dedicated to low-resolution spectroscopy (R$> 5000 - 7000$) in the wavelength range 390−950nm, while the remaining 812 will be used for high-resolution spectroscopy (R$> 18,000$) in selected wavelength intervals. Starting from 2021, 4MOST will carry out a number galactic and extragalactic surveys with science goals raging from Gaia follow-up to constraining fundamental cosmological parameters. However ample observing time will also be awarded to the community via proposal applications.

Even though white dwarfs do not figure significantly in the main science goals for these new instruments, these spectrographs could still have an important impact on white dwarf science. Most of my work focused on developing reliable selection methods for white dwarf candidates or specific types of white dwarfs (variable white dwarfs and metal polluted white dwarfs), but spectroscopy follow-up is ultimately needed to confirm the nature of these candidates and carry out any further analysis. Furthermore the advent of Gaia will add thousands additional white dwarfs without spectra. With so many targets at hand, it is unthinkable to follow them up investing valuable time of single objects spectrograph at large observing facilities. The large multiplex capability of instrument like WEAVE and 4MOST will allow follow-up on an industrial scale and less than five per cent of the fibers will be sufficient to obtain spectra of effectively all white dwarfs with $g \leq 20$. Furthermore WEAVE and 4MOST will only be the first of these next generation facilities in the north and south hemisphere. In the next few years the Mayall telescope at Kitt Peak will equip the Dark Energy Spectroscopic Instrument (DESI) with its outstanding 5000 fibers, and the VLT will deploy the Multi-Object Optical and Near-infrared Spectrograph (MOONS). In the brief space of the next five years new multi-object spectrographs will revolutionize the way we perform spectroscopy and mark a turning point for the whole of astronomy .

9.4.3 Pan-STARRS

The Panoramic Survey Telescope and Rapid Response System (Pan-STARRS; Morgan et al. 2014) is constituted of a 1.8 m telescope with a 3.2 degree diameter field of view. The telescope is equipped with a 1.4 billion pixels CCD camera and the optical and near infrared filters g, r, i, z and y. A single observation in these broadband filters reaches a five σ depth of 24 magnitude, however co-adding images of observations taken of several years, Pan-STARRS should be able to reach a maximum depth of $\simeq 29.4$ mag. The main science survey carried out by Pan-STARRS, the 3π Steradian Survey (3π) covered the entire sky north of declination $-30°$ with a total of 60 epochs, twelve each in 5 filters, over the course of three years. The 3π has now been completed and all data will become publicly available in the immediate future. The second main, and still ongoing, Pan-STARRS survey is the Medium Deep Survey which comprises of ten fields spread across the sky observed of up to 4 times per night.

The deep, multi-band, multi-epoch photometry of PanSTARRS is a perfect dataset for large-scale searches for variability. The number of epochs of observation of the 3π survey, however, is not enough to replicate a study analogous the one presented in Chapter 7, but the high cadence fields of the Medium Deep survey will be the ideal starting point for a new, deeper search for variable white dwarfs.

9.4.4 LSST

The Large Synoptic Survey Telescope (LSST; Ivezic et al. 2011), is a 8.4 m survey telescope currently under construction at Cerro Pachón in Chile and estimated to see first light in 2019. LSST will have 3.5 deg field of view and over a 10 years survey it will cover 18,000 deg^2 (the entire visible sky) every few nights. LSST will carry out observations in 6 bands: u, g, r, i, z and y with an estimated accuracy of 0.01 mag and should achieve a 5 σ limiting magnitude of 23.9, 25.0, 24.7, 24.0, 23.3 and 22.1, respectively (potentially reaching 2.5 magnitudes deeper in co-added images). LSST will take 15 second exposure every 37 seconds providing high-cadence time domain data for approximately one billion sources. A further valuable resource of LSST will be precise proper motion measurement of faint sources with accuracies of 0.2 mas/yr at $r = 21$ and 1.0 mas/yr at r = 24.

LSST will represent a huge leap forward in the field of time domain astronomy and the potential science applications are vast and diverse. The large, deep sky coverage in multiple bands, combined with the proper motion will provide the necessary data to attempt a selection of white dwarfs among much fainter targets,

some even fainter than what Gaia will have identified. LSST time-domain data will allow to identify, on industrial scale, diverse variable phenomena which are beyond the capabilities of current time-domain surveys (e.g. low-amplitude hot pulsating white dwarfs or variable emission from debris disc).

My entire PhD work, from selection of big samples of white dwarfs candidates, to the identification of specific objects, was done by efficiently exploiting the ever increasing amount of data from large area surveys. However, we have only scratched the surface. The potential of current surveys like SDSS and ATLAS is still far from exhausted, and the next generation instruments and surveys will provide huge amount of data of unprecedented quality. In this new era of survey astronomy, techniques like the ones presented in this work will become of paramount importance.

Bibliography

Aannestad, P. A., Kenyon, S. J., Hammond, G. L., Sion, E. M., 1993, AJ, 105, 1033

Abazajian, K. N., et al., 2009, ApJS, 182, 543

Ahn, C. P., et al., 2012, ApJS, 203, 21

Ahn, C. P., et al., 2014, ApJS, 211, 17

Alam, S., et al., 2015, ArXiv e-prints

Alcock, C., Fristrom, C. C., Siegelman, R., 1986, ApJ, 302, 462

Althaus, L. G., Córsico, A. H., Isern, J., García-Berro, E., 2010, A&A Rev., 18, 471

Althaus, L. G., Miller Bertolami, M. M., Córsico, A. H., 2013, A&A, 557, A19

Angel, J. R. P., Borra, E. F., Landstreet, J. D., 1981, ApJS, 45, 457

Barber, S. D., Patterson, A. J., Kilic, M., Leggett, S. K., Dufour, P., Bloom, J. S., Starr, D. L., 2012, ApJ, 760, 26

Barber, S. D., Kilic, M., Brown, W. R., Gianninas, A., 2014, ApJ, 786, 77

Barstow, M. A., Jordan, S., O'Donoghue, D., Burleigh, M. R., Napiwotzki, R., Harrop-Allin, M. K., 1995, MNRAS, 277, 971

Barstow, M. A., Barstow, J. K., Casewell, S. L., Holberg, J. B., Hubeny, I., 2014, MNRAS, 440, 1607

Becker, A. C., Bochanski, J. J., Hawley, S. L., Ivezić, Ž., Kowalski, A. F., Sesar, B., West, A. A., 2011, ApJ, 731, 17

Bergeron, P., 2001, ApJ, 558, 369

Bergeron, P., Saffer, R. A., Liebert, J., 1992a, ApJ, 394, 228

Bergeron, P., Wesemael, F., Fontaine, G., 1992b, ApJ, 387, 288

Bergeron, P., Wesemael, F., Lamontagne, R., Fontaine, G., Saffer, R. A., Allard, N. F., 1995, ApJ, 449, 258

Bergeron, P., Ruiz, M. T., Leggett, S. K., 1997, ApJS, 108, 339

Bergeron, P., Fontaine, G., Billères, M., Boudreault, S., Green, E. M., 2004, ApJ, 600, 404

Bergeron, P., et al., 2011, ApJ, 737, 28

Bergfors, C., Farihi, J., Dufour, P., Rocchetto, M., 2014, MNRAS, 444, 2147

Bilíková, J., Chu, Y.-H., Gruendl, R. A., Su, K. Y. L., De Marco, O., 2012, ApJS, 200, 3

Bragaglia, A., Renzini, A., Bergeron, P., 1995, ApJ, 443, 735

Bramich, D. M., et al., 2008, MNRAS, 386, 887

Breedt, E., et al., 2014, MNRAS, 443, 3174

Brinkworth, C. S., Burleigh, M. R., Wynn, G. A., Marsh, T. R., 2004, MNRAS, 348, L33

Brinkworth, C. S., Gänsicke, B. T., Girven, J. M., Hoard, D. W., Marsh, T. R., Parsons, S. G., Koester, D., 2012, ApJ, 750, 86

Brinkworth, C. S., Burleigh, M. R., Lawrie, K., Marsh, T. R., Knigge, C., 2013, ApJ, 773, 47

Brown, W. R., Geller, M. J., Kenyon, S. J., Kurtz, M. J., 2006, ApJ, 647, 303

Brown, W. R., Geller, M. J., Kenyon, S. J., Kurtz, M. J., Bromley, B. C., 2007a, ApJ, 660, 311

Brown, W. R., Geller, M. J., Kenyon, S. J., Kurtz, M. J., Bromley, B. C., 2007b, ApJ, 671, 1708

Brown, W. R., Kilic, M., Allende Prieto, C., Kenyon, S. J., 2010, ApJ, 723, 1072

Brown, W. R., Kilic, M., Allende Prieto, C., Kenyon, S. J., 2012, ApJ, 744, 142

Burleigh, M. R., Hogan, E., Dobbie, P. D., Napiwotzki, R., Maxted, P. F. L., 2006, MNRAS, 373, L55

Canup, R. M., Ward, W. R., 2002, AJ, 124, 3404

Carlin, J. L., et al., 2012, Research in Astronomy and Astrophysics, 12, 755

Carter-Bond, J. C., O'Brien, D. P., Delgado Mena, E., Israelian, G., Santos, N. C., González Hernández, J. I., 2012, ApJ, 747, L2

Casewell, S. L., et al., 2012, ApJ, 759, L34

Casewell, S. L., et al., 2015, MNRAS, 447, 3218

Castanheira, B. G., Kepler, S. O., Kleinman, S. J., Nitta, A., Fraga, L., 2010, MNRAS, 405, 2561

Castanheira, B. G., Kepler, S. O., Kleinman, S. J., Nitta, A., Fraga, L., 2013, MNRAS, 430, 50

Castanheira, B. G., et al., 2004, A&A, 413, 623

Castanheira, B. G., et al., 2006, A&A, 450, 227

Catalán, S., Isern, J., García-Berro, E., Ribas, I., 2008, MNRAS, 387, 1693

Chandrasekhar, S., 1931, ApJ, 74, 81

Charpinet, S., Fontaine, G., Brassard, P., 2009, Nature, 461, 501

Chayer, P., Fontaine, G., Wesemael, F., 1995, ApJS, 99, 189

Chen, L., et al., 2012, Research in Astronomy and Astrophysics, 12, 805

Christlieb, N., Wisotzki, L., Reimers, D., Homeier, D., Koester, D., Heber, U., 2001, A&A, 366, 898

Chu, Y.-H., et al., 2011, AJ, 142, 75

Cojocaru, R., Torres, S., Isern, J., García-Berro, E., 2014, A&A, 566, A81

Cui, X.-Q., et al., 2012, Research in Astronomy and Astrophysics, 12, 1197

Dalton, G., et al., 2014, in Society of Photo-Optical Instrumentation Engineers (SPIE) Conference Series, vol. 9147 of *Society of Photo-Optical Instrumentation Engineers (SPIE) Conference Series*, p. 0

Dawson, K. S., et al., 2013, AJ, 145, 10

De Gennaro, S., von Hippel, T., Winget, D. E., Kepler, S. O., Nitta, A., Koester, D., Althaus, L., 2008, AJ, 135, 1

Debes, J. H., Hoard, D. W., Kilic, M., Wachter, S., Leisawitz, D. T., Cohen, M., Kirkpatrick, J. D., Griffith, R. L., 2011a, ApJ, 729, 4

Debes, J. H., Hoard, D. W., Wachter, S., Leisawitz, D. T., Cohen, M., 2011b, ApJS, 197, 38

Debes, J. H., Hoard, D. W., Farihi, J., Wachter, S., Leisawitz, D. T., Cohen, M., 2012, ApJ, 759, 37

Deng, L.-C., et al., 2012, Research in Astronomy and Astrophysics, 12, 735

Depagne, E., 4MOST consortium, t., 2014, ArXiv e-prints

Doherty, C. L., Gil-Pons, P., Siess, L., Lattanzio, J. C., Lau, H. H. B., 2015, MNRAS, 446, 2599

Drake, A., 2014, in Wozniak, P. R., Graham, M. J., Mahabal, A. A., Seaman, R., eds., The Third Hot-wiring the Transient Universe Workshop, p. 37

Drake, A. J., et al., 2009, ApJ, 696, 870

Drake, A. J., et al., 2014, MNRAS, 441, 1186

Dufour, P., Liebert, J., Fontaine, G., Behara, N., 2007a, Nature, 450, 522

Dufour, P., Kilic, M., Fontaine, G., Bergeron, P., Lachapelle, F., Kleinman, S. J., Leggett, S. K., 2010, ApJ, 719, 803

Dufour, P., et al., 2007b, ApJ, 663, 1291

Dunlap, B. H., Clemens, J. C., 2015, in Dufour, P., Bergeron, P., Fontaine, G., eds., 19th European Workshop on White Dwarfs, vol. 493 of *Astronomical Society of the Pacific Conference Series*, p. 547

Dupuis, J., Fontaine, G., Pelletier, C., Wesemael, F., 1993a, ApJS, 84, 73

Dupuis, J., Fontaine, G., Wesemael, F., 1993b, ApJS, 87, 345

Dupuis, J., Chayer, P., Vennes, S., Allard, N. F., Hébrard, G., 2003, ApJ, 598, 486

Dye, S., et al., 2006, MNRAS, 372, 1227

Dziembowski, W., Koester, D., 1981, A&A, 97, 16

Eisenstein, D. J., et al., 2006, ApJS, 167, 40

Els, S., Lock, T., Comoretto, G., Gracia, G., O'Mullane, W., Cheek, N., Vallenari, A., 2014, in Society of Photo-Optical Instrumentation Engineers (SPIE) Conference Series, vol. 9150 of *Society of Photo-Optical Instrumentation Engineers (SPIE) Conference Series*, p. 0

Falcon, R. E., Winget, D. E., Montgomery, M. H., Williams, K. A., 2010, ApJ, 712, 585

Farihi, J., Becklin, E. E., Zuckerman, B., 2005, ApJS, 161, 394

Farihi, J., Becklin, E. E., Zuckerman, B., 2008a, ApJ, 681, 1470

Farihi, J., Zuckerman, B., Becklin, E. E., 2008b, ApJ, 674, 431

Farihi, J., Jura, M., Zuckerman, B., 2009, ApJ, 694, 805

Farihi, J., Barstow, M. A., Redfield, S., Dufour, P., Hambly, N. C., 2010a, MNRAS, 404, 2123

Farihi, J., Jura, M., Lee, J., Zuckerman, B., 2010b, ApJ, 714, 1386

Farihi, J., Brinkworth, C. S., Gänsicke, B. T., Marsh, T. R., Girven, J., Hoard, D. W., Klein, B., Koester, D., 2011a, ApJ, 728, L8

Farihi, J., Dufour, P., Napiwotzki, R., Koester, D., 2011b, MNRAS, 413, 2559

Farihi, J., Gänsicke, B. T., Steele, P. R., Girven, J., Burleigh, M. R., Breedt, E., Koester, D., 2012, MNRAS, 421, 1635

Farihi, J., Gänsicke, B. T., Koester, D., 2013, Science, 342, 218

Ferrario, L., Wickramasinghe, D., Liebert, J., Williams, K. A., 2005, MNRAS, 361, 1131

Fontaine, G., Brassard, P., 2008, PASP, 120, 1043

Fontaine, G., Michaud, G., 1979, ApJ, 231, 826

Fontaine, G., Wesemael, F., 1987, in Philip, A. G. D., Hayes, D. S., Liebert, J. W., eds., IAU Colloq. 95: Second Conference on Faint Blue Stars, p. 319

Fontaine, G., Lacombe, P., McGraw, J. T., Dearborn, D. S. P., Gustafson, J., 1982, ApJ, 258, 651

Fontaine, G., Brassard, P., Bergeron, P., 2001, PASP, 113, 409

Fontaine, G., Brassard, P., Dufour, P., 2008, A&A, 483, L1

Friedrich, S., Oestreicher, R., Schweizer, W., 1996, A&A, 309, 227

Friedrich, S., Koester, D., Christlieb, N., Reimers, D., Wisotzki, L., 2000, A&A, 363, 1040

Friedrich, S., Jordan, S., Koester, D., 2004, A&A, 424, 665

Frieman, J. A., et al., 2008, AJ, 135, 338

Gänsicke, B., et al., 2015, ArXiv e-prints

Gänsicke, B. T., Euchner, F., Jordan, S., 2002, A&A, 394, 957

Gänsicke, B. T., Marsh, T. R., Southworth, J., Rebassa-Mansergas, A., 2006a, Science, 314, 1908

Gänsicke, B. T., Marsh, T. R., Southworth, J., 2007, MNRAS, 380, L35

Gänsicke, B. T., Koester, D., Marsh, T. R., Rebassa-Mansergas, A., Southworth, J., 2008, MNRAS, 391, L103

Gänsicke, B. T., Koester, D., Girven, J., Marsh, T. R., Steeghs, D., 2010, Science, 327, 188

Gänsicke, B. T., Koester, D., Farihi, J., Girven, J., Parsons, S. G., Breedt, E., 2012, MNRAS, 424, 333

Gänsicke, B. T., et al., 2006b, MNRAS, 365, 969

Ge, J., et al., 2015, in American Astronomical Society Meeting Abstracts, vol. 225 of *American Astronomical Society Meeting Abstracts*, p. 409.03

Gentile Fusillo, N. P., Gänsicke, B. T., Greiss, S., 2015, MNRAS, 448, 2260

Gentile Fusillo, N. P., et al., 2015, MNRAS, 452, 765

Giammichele, N., Bergeron, P., Dufour, P., 2012, ApJS, 199, 29

Gianninas, A., Dufour, P., Bergeron, P., 2004, ApJ, 617, L57

Gianninas, A., Bergeron, P., Ruiz, M. T., 2011, ApJ, 743, 138

Gianninas, A., Dufour, P., Kilic, M., Brown, W. R., Bergeron, P., Hermes, J. J., 2014, ApJ, 794, 35

Girven, J., Gänsicke, B. T., Steeghs, D., Koester, D., 2011, MNRAS, 417, 1210

Girven, J., Brinkworth, C. S., Farihi, J., Gänsicke, B. T., Hoard, D. W., Marsh, T. R., Koester, D., 2012, ApJ, 749, 154

Graham, J. R., Matthews, K., Neugebauer, G., Soifer, B. T., 1990, ApJ, 357, 216

Green, R. F., Richstone, D. O., Schmidt, M., 1978, ApJ, 224, 892

Greiss, S., Gänsicke, B. T., Hermes, J. J., Steeghs, D., Koester, D., Ramsay, G., Barclay, T., Townsley, D. M., 2014, MNRAS, 438, 3086

Grillmair, C. J., et al., 2008, Nature, 456, 767

Grossman, L., 1972, Geochimica et Cosmochimica Acta, 36, 597

Hagen, H.-J., Groote, D., Engels, D., Haug, U., Toussaint, F., Reimers, D., 1987, A&A, 183, L7

Hambly, N. C., Mann, R. G., Bond, I., Sutorius, E., Read, M., Williams, P., Lawrence, A., Emerson, J. P., 2004, in Quinn, P. J., Bridger, A., eds., Optimizing Scientific Return for Astronomy through Information Technologies, vol. 5493 of *Society of Photo-Optical Instrumentation Engineers (SPIE) Conference Series*, p. 423

Hambly, N. C., et al., 2008, MNRAS, 384, 637

Hayden, M. R., et al., 2015, in American Astronomical Society Meeting Abstracts, vol. 225 of *American Astronomical Society Meeting Abstracts*, p. 319.02

Heber, U., Jordan, S., Weidemann, V., 1991, in NATO ASIC Proc. 336: White Dwarfs, p. 109

Heger, A., Fryer, C. L., Woosley, S. E., Langer, N., Hartmann, D. H., 2003, ApJ, 591, 288

Hermes, J. J., et al., 2013, MNRAS, 436, 3573

Hermes, J. J., et al., 2014a, ApJ, 789, 85

Hermes, J. J., et al., 2014b, ApJ, 792, 39

Hewett, P. C., Warren, S. J., Leggett, S. K., Hodgkin, S. T., 2006, MNRAS, 367, 454

Holberg, J. B., Bergeron, P., 2006, AJ, 132, 1221

Holberg, J. B., Howell, S. B., 2011, AJ, 142, 62

Holberg, J. B., Oswalt, T. D., Sion, E. M., 2002, ApJ, 571, 512

Holberg, J. B., Sion, E. M., Oswalt, T., McCook, G. P., Foran, S., Subasavage, J. P., 2008, AJ, 135, 1225

Hollands, M. A., Gänsicke, B. T., Koester, D., 2015, MNRAS, 450, 681

Hurley, J. R., Pols, O. R., Tout, C. A., 2000, MNRAS, 315, 543

Iben, I. J., Ritossa, C., Garcia-Berro, E., 1997, ApJ, 489, 772

Ivezic, Z., Strauss, M. A., Tyson, J. A., Axelrod, T., Bloom, J. S., LSST Collaboration, 2011, in American Astronomical Society Meeting Abstracts #217, vol. 43 of *Bulletin of the American Astronomical Society*, p. 252.01

Jeans, J. H., 1902, Royal Society of London Philosophical Transactions Series A, 199, 1

Jura, M., 2003, ApJ, 584, L91

Jura, M., Young, E. D., 2014, Annual Review of Earth and Planetary Sciences, 42, 45

Jura, M., Farihi, J., Zuckerman, B., 2007a, ApJ, 663, 1285

Jura, M., Farihi, J., Zuckerman, B., Becklin, E. E., 2007b, AJ, 133, 1927

Jura, M., Farihi, J., Zuckerman, B., 2009, AJ, 137, 3191

Jura, M., Xu, S., Klein, B., Koester, D., Zuckerman, B., 2012, ApJ, 750, 69

Kanaan, A., Kepler, S. O., Giovannini, O., Winget, D. E., Montgomery, M., Nitta, A., 1998, Baltic Astronomy, 7, 183

Kanaan, A., et al., 2005, A&A, 432, 219

Kawka, A., Vennes, S., 2004, in Zverko, J., Ziznovsky, J., Adelman, S. J., Weiss, W. W., eds., The A-Star Puzzle, vol. 224 of *IAU Symposium*, p. 879

Kawka, A., Vennes, S., Schmidt, G. D., Wickramasinghe, D. T., Koch, R., 2007, ApJ, 654, 499

Kemp, J. C., Swedlund, J. B., Landstreet, J. D., Angel, J. R. P., 1970, ApJ, 161, L77

Kepler, S. O., et al., 2013, MNRAS, 429, 2934

Kepler, S. O., et al., 2015, MNRAS, 446, 4078

Kilic, M., Brown, W. R., Allende Prieto, C., Kenyon, S. J., Heinke, C. O., Agüeros, M. A., Kleinman, S. J., 2012, ApJ, 751, 141

Kilkenny, D., O'Donoghue, D., Crause, L. A., Hambly, N., MacGillivray, H., 2009, MNRAS, 397, 453

Klein, B., Jura, M., Koester, D., Zuckerman, B., Melis, C., 2010, ApJ, 709, 950

Kleinman, S. J., et al., 1998, ApJ, 495, 424

Kleinman, S. J., et al., 2004, ApJ, 607, 426

Kleinman, S. J., et al., 2013, ApJS, 204, 5

Koester, D., 1976, A&A, 52, 415

Koester, D., 2009, A&A, 498, 517

Koester, D., 2010, Memorie della Societa Astronomica Italiana,, 81, 921

Koester, D., 2013, White Dwarf Stars, p. 559

Koester, D., Knist, S., 2006, A&A, 454, 951

Koester, D., Wolff, B., 2000, A&A, 357, 587

Koester, D., Schulz, H., Weidemann, V., 1979, A&A, 76, 262

Koester, D., Provencal, J., Shipman, H. L., 1997, A&A, 320, L57

Koester, D., Napiwotzki, R., Voss, B., Homeier, D., Reimers, D., 2005a, A&A, 439, 317

Koester, D., Rollenhagen, K., Napiwotzki, R., Voss, B., Christlieb, N., Homeier, D., Reimers, D., 2005b, A&A, 432, 1025

Koester, D., Kepler, S. O., Kleinman, S. J., Nitta, A., 2009a, Journal of Physics Conference Series, 172, 012006

Koester, D., Voss, B., Napiwotzki, R., Christlieb, N., Homeier, D., Lisker, T., Reimers, D., Heber, U., 2009b, A&A, 505, 441

Koester, D., Girven, J., Gänsicke, B. T., Dufour, P., 2011, A&A, 530, A114+

Koester, D., Gänsicke, B. T., Farihi, J., 2014, A&A, 566, A34

Koester, D., et al., 2001, A&A, 378, 556

Kuiper, G. P., 1934, PASP, 46, 287

Kuiper, G. P., 1941, PASP, 53, 248

Külebi, B., Jordan, S., Euchner, F., Gänsicke, B. T., Hirsch, H., 2009, A&A, 506, 1341

Landolt, A. U., 1968, ApJ, 153, 151

Lasker, B. M., Hesser, J. E., 1971, ApJ, 163, L89

Laughlin, G., Bodenheimer, P., 1993, ApJ, 403, 303

Law, N. M., et al., 2009, PASP, 121, 1395

Law, N. M., et al., 2015, PASP, 127, 234

Lawrence, A., et al., 2007, MNRAS, 379, 1599

Lawrie, K. A., Burleigh, M. R., Dufour, P., Hodgkin, S. T., 2013, MNRAS, 433, 1599

Liebert, J., 1988, PASP, 100, 1302

Liebert, J., Bergeron, P., Holberg, J. B., 2003, AJ, 125, 348

Liebert, J., Bergeron, P., Holberg, J. B., 2005, ApJS, 156, 47

Limoges, M.-M., Lépine, S., Bergeron, P., 2013, AJ, 145, 136

Littlefair, S. P., et al., 2014, MNRAS, 445, 2106

Liu, X.-W., et al., 2014, in Feltzing, S., Zhao, G., Walton, N. A., Whitelock, P., eds., IAU Symposium, vol. 298 of *IAU Symposium*, p. 310

Luo, A.-L., et al., 2015, ArXiv e-prints

Mainzer, A., et al., 2011, ApJ, 731, 53

Maoz, D., Mazeh, T., McQuillan, A., 2015, MNRAS, 447, 1749

Marsh, T. R., 1989, PASP, 101, 1032

Marsh, T. R., Dhillon, V. S., Duck, S. R., 1995, MNRAS, 275, 828

Marsh, T. R., Nelemans, G., Steeghs, D., 2004, MNRAS, 350, 113

Martin, D. C., et al., 2005, ApJ, 619, L1

McCook, G. P., Sion, E. M., 1999, ApJ, 121, 1

McCord, T. B., Sotin, C., 2005, Journal of Geophysical Research (Planets), 110, 5009

Mcdonough, W., 2000, Earthquake Thermodynamics and Phase Transformation in the Earths Interior, Academic press, San Diego

McGraw, J. T., 1976, ApJ, 210, L35

McGraw, J. T., Robinson, E. L., 1975, ApJ, 200, L89

McMahon, R. G., Banerji, M., Gonzalez, E., Koposov, S. E., Bejar, V. J., Lodieu, N., Rebolo, R., VHS Collaboration, 2013, The Messenger, 154, 35

Melis, C., et al., 2012, ApJ, 751, L4

Mestel, L., 1952, MNRAS, 112, 583

Michalak, G., 2000, A&A, 360, 363

Montgomery, M. H., Winget, D. E., 1999, ApJ, 526, 976

Morgan, J. S., Burgett, W., Onaka, P., 2014, in Society of Photo-Optical Instrumentation Engineers (SPIE) Conference Series, vol. 9145 of *Society of Photo-Optical Instrumentation Engineers (SPIE) Conference Series*, p. 0

Morrissey, P., et al., 2005, ApJ, 619, L7

Moynier, F., Yin, Q.-Z., Schauble, E., 2011, Science, 331, 1417

Muchmore, D., 1984, ApJ, 278, 769

Mukadam, A. S., et al., 2004, ApJ, 607, 982

Mullally, F., Winget, D. E., Degennaro, S., Jeffery, E., Thompson, S. E., Chandler, D., Kepler, S. O., 2008, ApJ, 676, 573

Munn, J. A., et al., 2004, AJ, 127, 3034

Mustill, A. J., Veras, D., Villaver, E., 2014, MNRAS, 437, 1404

Nakajima, T., Oppenheimer, B. R., Kulkarni, S. R., Golimowski, D. A., Matthews, K., Durrance, S. T., 1995, Nature, 378, 463

Nitta, A., et al., 2009, ApJ, 690, 560

Nordhaus, J., Wellons, S., Spiegel, D. S., Metzger, B. D., Blackman, E. G., 2011, Proceedings of the National Academy of Science, 108, 3135

Orosz, J. A., Wade, R. A., 1999, MNRAS, 310, 773

Oswalt, T. D., Smith, J. A., Wood, M. A., Hintzen, P., 1996, Nature, 382, 692

Palla, F., 2013, Mem. Soc. Astron. Italiana, 84, 858

Paquette, C., Pelletier, C., Fontaine, G., Michaud, G., 1986, ApJS, 61, 177

Parsons, S. G., Marsh, T. R., Gänsicke, B. T., Drake, A. J., Koester, D., 2011, ApJ, 735, L30

Parsons, S. G., et al., 2015, MNRAS, 449, 2194

Pelletier, C., Fontaine, G., Wesemael, F., Michaud, G., Wegner, G., 1986, ApJ, 307, 242

Perlmutter, S., et al., 1999, ApJ, 517, 565

Pont, F., Zucker, S., Queloz, D., 2006, MNRAS, 373, 231

Prialnik, D., 2000, Stellar structure and evolution, Cambridge University Press, Cambridge

Probst, R. G., 1983a, ApJS, 53, 335

Probst, R. G., 1983b, ApJ, 274, 237

Quirion, P.-O., Fontaine, G., Brassard, P., 2007, ApJS, 171, 219

Raddi, R., Gänsicke, B. T., Koester, D., Farihi, J., Hermes, J. J., Scaringi, S., Breedt, E., Girven, J., 2015, MNRAS, 450, 2083

Reach, W. T., Kuchner, M. J., von Hippel, T., Burrows, A., Mullally, F., Kilic, M., Winget, D. E., 2005, ApJ, 635, L161

Rebassa-Mansergas, A., Gänsicke, B. T., Rodríguez-Gil, P., Schreiber, M. R., Koester, D., 2007, MNRAS, 382, 1377

Rebassa-Mansergas, A., Gänsicke, B. T., Schreiber, M. R., Koester, D., Rodríguez-Gil, P., 2010, MNRAS, 402, 620

Rebassa-Mansergas, A., Nebot Gómez-Morán, A., Schreiber, M. R., Girven, J., Gänsicke, B. T., 2011, MNRAS, 413, 1121

Rebassa-Mansergas, A., et al., 2008, MNRAS, 390, 1635

Rebassa-Mansergas, A., et al., 2015, MNRAS, 450, 743

Reid, I. N., Liebert, J., Schmidt, G. D., 2001, ApJ, 550, L61

Reimers, D., Jordan, S., Koester, D., Bade, N., Koehler, T., Wisotzki, L., 1996, A&A, 311, 572

Reindl, N., Rauch, T., Werner, K., Kepler, S. O., Gänsicke, B. T., Gentile Fusillo, N. P., 2014, A&A, 572, A117

Ren, J. J., et al., 2014, A&A, 570, A107

Renedo, I., Althaus, L. G., Miller Bertolami, M. M., Romero, A. D., Córsico, A. H., Rohrmann, R. D., García-Berro, E., 2010, ApJ, 717, 183

Richards, G. T., et al., 2002, AJ, 123, 2945

Riess, A. G., et al., 2000, ApJ, 536, 62

Robin, A. C., et al., 2012, A&A, 543, A100

Rocchetto, M., Farihi, J., Gänsicke, B. T., Bergfors, C., 2015, MNRAS, 449, 574

Roeser, S., Demleitner, M., Schilbach, E., 2010, AJ, 139, 2440

Rohrmann, R. D., 2001, MNRAS, 323, 699

Sako, M., et al., 2008, AJ, 135, 348

Schmidt, G. D., Liebert, J., Harris, H. C., Dahn, C. C., Leggett, S. K., 1999, ApJ, 512, 916

Schmidt, G. D., et al., 2003, ApJ, 595, 1101

Sesar, B., et al., 2007, AJ, 134, 2236

Shanks, T., et al., 2015, MNRAS, 451, 4238

Sion, E. M., Greenstein, J. L., Landstreet, J. D., Liebert, J., Shipman, H. L., Wegner, G. A., 1983, ApJ, 269, 253

Sion, E. M., Kenyon, S. J., Aannestad, P. A., 1990, ApJS, 72, 707

Sion, E. M., Holberg, J. B., Oswalt, T. D., McCook, G. P., Wasatonic, R., Myszka, J., 2014, AJ, 147, 129

Skrutskie, M. F., et al., 2006, AJ, 131, 1163

Smartt, S. J., Eldridge, J. J., Crockett, R. M., Maund, J. R., 2009, MNRAS, 395, 1409

Smith, A. M. S., et al., 2006, MNRAS, 373, 1151

Song, Y.-H., et al., 2012, Research in Astronomy and Astrophysics, 12, 453

Sorahana, S., Yamamura, I., Murakami, H., 2013, ApJ, 767, 77

Steele, P. R., Burleigh, M. R., Farihi, J., Gänsicke, B. T., Jameson, R. F., Dobbie, P. D., Barstow, M. A., 2009, A&A, 500, 1207

Steele, P. R., Burleigh, M. R., Dobbie, P. D., Jameson, R. F., Barstow, M. A., Satterthwaite, R. P., 2011, MNRAS, 416, 2768

Steele, P. R., et al., 2013, MNRAS, 429, 3492

Stoughton, C., et al., 2002, AJ, 123, 485

Strauss, M. A., et al., 2002, AJ, 124, 1810

Tout, C. A., Wickramasinghe, D. T., Liebert, J., Ferrario, L., Pringle, J. E., 2008, MNRAS, 387, 897

Tremblay, P.-E., Bergeron, P., 2008, ApJ, 672, 1144

Tremblay, P.-E., Bergeron, P., 2009, ApJ, 696, 1755

Tremblay, P.-E., Ludwig, H.-G., Steffen, M., Bergeron, P., Freytag, B., 2011, A&A, 531, L19

Tremblay, P.-E., Ludwig, H.-G., Steffen, M., Freytag, B., 2013, A&A, 559, A104

Valencia, D., Ikoma, M., Guillot, T., Nettelmann, N., 2010, A&A, 516, A20

van Maanen, A., 1917, PASP, 29, 258

Vennes, S., Kawka, A., 2008, MNRAS, 389, 1367

Vennes, S., Schmidt, G. D., Ferrario, L., Christian, D. J., Wickramasinghe, D. T., Kawka, A., 2003, ApJ, 593, 1040

Vennes, S., Kawka, A., Németh, P., 2010, MNRAS, 404, L40

Veras, D., Mustill, A. J., Bonsor, A., Wyatt, M. C., 2013, MNRAS, 431, 1686

Veras, D., Shannon, A., Gänsicke, B. T., 2014, MNRAS, 445, 4175

Vernet, J., et al., 2011, A&A, 536, A105

von Hippel, T., Kuchner, M. J., Kilic, M., Mullally, F., Reach, W. T., 2007, ApJ, 662, 544

Voss, B., Koester, D., Østensen, R., Kepler, S. O., Napiwotzki, R., Homeier, D., Reimers, D., 2006, A&A, 450, 1061

Voss, B., Koester, D., Napiwotzki, R., Christlieb, N., Reimers, D., 2007, A&A, 470, 1079

Walton, N., 2014, in Wozniak, P. R., Graham, M. J., Mahabal, A. A., Seaman, R., eds., The Third Hot-wiring the Transient Universe Workshop, p. 41

Warner, B., 1995, Cataclysmic Variable Stars, Cambridge University Press, Cambridge

Webbink, R. F., 1984, ApJ, 277, 355

Weidemann, V., 2000, A&A, 363, 647

Weidemann, V., Koester, D., 1984, A&A, 132, 195

Werner, K., 1991, A&A, 251, 147

Werner, K., Herwig, F., 2006, PASP, 118, 183

Wickramasinghe, D. T., Ferrario, L., 2000, PASP, 112, 873

Wilson, D. J., Gänsicke, B. T., Koester, D., Raddi, R., Breedt, E., Southworth, J., Parsons, S. G., 2014, MNRAS, 445, 1878

Wilson, D. J., Gänsicke, B. T., Koester, D., Toloza, O., Pala, A. F., Breedt, E., Parsons, S. G., 2015, MNRAS, 451, 3237

Winget, D. E., Kepler, S. O., 2008, ARA&A, 46, 157

Winget, D. E., van Horn, H. M., Hansen, C. J., 1981, ApJ, 245, L33

Winget, D. E., Robinson, E. L., Nather, R. D., Fontaine, G., 1982, ApJ, 262, L11

Winget, D. E., et al., 1991, ApJ, 378, 326

Wood, M. A., 1995, in Koester, D., Werner, K., eds., White Dwarfs, vol. 443 of *Lecture Notes in Physics, Berlin Springer Verlag*, p. 41

Woudt, P. A., Warner, B., Zietsman, E., 2012, MNRAS, 426, 2137

Wright, E. L., et al., 2010, AJ, 140, 1868

Xu, S., Jura, M., 2014, ApJ, 792, L39

Xu, S., Jura, M., Pantoja, B., Klein, B., Zuckerman, B., Su, K. Y. L., Meng, H. Y. A., 2015, ApJ, 806, L5

Yuan, H.-B., et al., 2015, MNRAS, 448, 855

Zhang, Y.-Y., et al., 2013, AJ, 146, 34

Zhao, G., Zhao, Y.-H., Chu, Y.-Q., Jing, Y.-P., Deng, L.-C., 2012, Research in Astronomy and Astrophysics, 12, 723

Zhao, J. K., Luo, A. L., Oswalt, T. D., Zhao, G., 2013, AJ, 145, 169

Zuckerman, B., 2015, in Dufour, P., Bergeron, P., Fontaine, G., eds., 19th European Workshop on White Dwarfs, vol. 493 of *Astronomical Society of the Pacific Conference Series*, p. 291

Zuckerman, B., Becklin, E. E., 1987, Nature, 330, 138

Zuckerman, B., Reid, I. N., 1998, ApJ, 505, L143

Zuckerman, B., Koester, D., Reid, I. N., Hünsch, M., 2003, ApJ, 596, 477

Zuckerman, B., Koester, D., Melis, C., Hansen, B. M., Jura, M., 2007, ApJ, 671, 872

Zuckerman, B., Melis, C., Klein, B., Koester, D., Jura, M., 2010, ApJ, 722, 725

Zuckerman, B., Koester, D., Dufour, P., Melis, C., Klein, B., Jura, M., 2011, ApJ, 739, 101